2010

Numerical Modeling Of The Shock Tube Flow Fields Before Andduring Ignition Delay Time Experiments At Practical Conditions

mouna lamnaouer
University of Central Florida

STARS Citation

lamnaouer, mouna, "Numerical Modeling Of The Shock Tube Flow Fields Before Andduring Ignition Delay Time Experiments At Practical Conditions" (2010). *Electronic Theses and Dissertations, 2004-2019*. 4208.
https://stars.library.ucf.edu/etd/4208

NUMERICAL MODELING OF THE SHOCK TUBE FLOW FIELDS BEFORE AND DURING IGNITION DELAY TIME EXPERIMENTS AT PRACTICAL CONDITIONS

by

MOUNA LAMNAOUER
B.S. of Aerospace Engineering,
University of Central Florida, 2004

A dissertation submitted in partial fulfillment of the requirements
for the degree of Doctor of Philosophy in Mechanical Engineering
in the Department of Mechanical, Materials, and Aerospace Engineering
in the College of Engineering and Computer Sciences
at the University of Central Florida
Orlando, Florida

Spring Term
2010

Major Professors: Alain J. Kassab
Eric L. Petersen

ABSTRACT

An axi-symmetric shock-tube model has been developed to simulate the shock-wave propagation and reflection in both non-reactive and reactive flows. Simulations were performed for the full shock-tube geometry of the high-pressure shock tube facility at Texas A&M University. Computations were carried out in the CFD solver FLUENT based on the finite volume approach and the AUSM+ flux differencing scheme. Adaptive mesh refinement (AMR) algorithm was applied to the time-dependent flow fields to accurately capture and resolve the shock and contact discontinuities as well as the very fine scales associated with the viscous and reactive effects. A conjugate heat transfer model has been incorporated which enhanced the credibility of the simulations. The multi-dimensional, time-dependent numerical simulations resolved all of the relevant scales, ranging from the size of the system to the reaction zone scale. The robustness of the numerical model and the accuracy of the simulations were assessed through validation with the analytical ideal shock-tube theory and experimental data. The numerical method is first applied to the problem of axi-symmetric inviscid flow then viscous effects are incorporated through viscous modeling. The non-idealities in the shock tube have been investigated and quantified, notably the non-ideal transient behavior in the shock tube nozzle section, heat transfer effects from the hot gas to the shock tube side walls, the reflected shock/boundary layer interactions or what is known as bifurcation, and the contact surface/bifurcation interaction resulting into driver gas contamination. The non-reactive model is shown to be capable of accurately simulating the shock and expansion wave propagations and reflections as well as the flow non-uniformities behind the reflected shock wave. Both the inviscid and the viscous non-reactive models provided a baseline for the combustion model

which involves elementary chemical reactions and requires the coupling of the chemistry with the flow fields adding to the complexity of the problem and thereby requiring tremendous computational resources. Combustion modeling focuses on the ignition process behind the reflected shock wave in undiluted and diluted Hydrogen test gas mixtures. Accurate representation of the Shock –tube reactive flow fields is more likely to be achieved by the means of the LES model in conjunction with the EDC model. The shock-tube CFD model developed herein provides valuable information to the interpretation of the shock-tube experimental data and to the understanding of the impact the facility-dependent non-idealities can have on the ignition delay time measurements.

In the name of God the most beneficent, the most merciful, and peace and blessings be upon his last messenger Mohammed

I dedicate this thesis to

God Almighty
Who has provided me with the strength and motivation to carry on this work

My mother, Habiba Abouhane
Who has dedicated her life to bring up the best in me

My father, Dr. Driss Lamnaouer
Who has been my role model and inspiration to achieve my goals

ACKNOWLEDGMENTS

I would like to express my deepest appreciation to the Committee chair Professor Alain Kassab for this guidance, support, and insight throughout the dissertation work and who along with Dr. Eduardo Divo allowed me generously to use the computational resource lab to conduct my research.

I would like to express my gratitude to Dr. Eric L. Petersen who introduced me to the shock-tube research at UCF. This thesis would not have been possible without your enthusiasm, motivation, and continuous support which had lasting effects. Thanks also go the students Rodrigo Garza-Urquiza and Nolan L. Polley from the research lab of Dr. Eric Petersen at Texas A&M University for providing the shock-tube experimental data which was used to validate part of this work.

Thanks go out to the other committee members, Dr. Ilie Marcel, Dr. Jay Kapat, and Dr. Mahmood Silieti for their valuable suggestions and comments. Also, I thank Steven Dick for the worthwhile technical assistance which made this work possible.

I convey my thanks and appreciation to my family and friends for their understanding, encouragements, and patience. Last but not least, I am thankful to all colleagues, staff and faculty in the Mechanical-Material-Aerospace Engineering department who made my academic experience at the University of Central Florida a memorable, valuable, and enjoyable one.

TABLE OF CONTENTS

LIST OF FIGURES

LIST OF TABLES

CHAPTER ONE: INTRODUCTION

The shock tube has found widespread use as an experimental device in which to investigate chemical kinetic behavior in reactive gas mixtures. A shock tube consists of a high-pressure driver section and low-pressure driven section initially separated by a diaphragm. The driver section is pressurized to energy high enough to cause the diaphragm to rupture and as a result, a shock wave is generated and travels down the driven tube. Simultaneously, an expansion fan propagates through the high-pressure side. Both waves reflect off the shock tube endwalls. Of interest herein is the endwall region behind the reflected shock wave where kinetic experiments take place. Ideally the flow properties behind the reflected shock are uniform and do not vary with time. In real shock tubes however, there is a slight deviation from this assumption due to viscous and non-ideal effects. As a result, some non-ideal effects occur that impact the test conditions, the magnitude of which depends on the tube diameter, pressure, and shock Mach number.

Outline of Study

As a first step towards modeling the complex mechanisms responsible for the non-uniform conditions and the reduced test times in the shock tube, the flow is modeled as inviscid and the focus is on developing a robust and accurate model capable of reproducing the major flow phenomena in the shock tube from the propagation of the shock wave and contact surface to the reflection of the expansion fan and incident shock. The inviscid model should serve as a baseline for the rather more complex viscous model which necessitates increased computational efforts. However, when shock-tube non-idealities need to be modeled to quantify their impact on the flow uniformity in the test region, viscous effects have to be taken into consideration. In this respect, a viscous model of the shock tube is introduced which simulates the major non-ideal mechanisms in the shock tube, including the reflected shock/boundary layer interaction or bifurcation, reflected shock/contact surface interactions, heat transfer from the hot test gas to the cold shock-tube walls, and driver gas contamination. Both the inviscid and viscous models should serve as a baseline for the reacting fluid model which incorporates detailed chemistry in order to model the ignition process behind the reflected shock wave.

The results from the axi-symmetric simulations of the shock-tube model are presented in this paper. The simulations were carried out with the commercial CFD solver FLUENT using the coupled explicit density solver and the finite-volume approaches. The accuracy, efficiency, and stability of the numerical model are investigated with 1st order, 2nd order, 1st/2nd order blending, and 3rd order MUSCL schemes. Adaption was used to assure mesh refinement in high-gradient regions to accurately resolve the shock and contact discontinuities. The shock-tube geometry is represented by a structured axi-symmetric mesh.

First, a description of the shock-tube facility being modeled in this study is provided followed by a background on the major mechanisms responsible for shock-tube non-idealities notably behind the reflected shock wave. The main motivation behind the shock tube study is laid out. Then a general overview of the model computational setup, including grid generation, numerical approach adopted, and dynamic grid adaption feature, is presented. Provided next, is the simulated inviscid solution of the temporal and spatial variation of the flow properties which are validated with the 1-D inviscid theory and with experimental data. Then the viscous solution is presented and the different mechanisms responsible for shock-tube non-idealities are identified and modeled. Finally, a reacting flow model is introduced and the ignition delay time behind the reflected shock is quantified and validated with experimental shock-tube data. Last, a summary is provided and main conclusions from the shock-tube modeling study are drawn.

The Shock tube Facility

A shock tube consists of a rigid cylinder in which a gas at high pressure, called the driver gas, is initially separated from a gas at lower pressure, called the test gas or the driven gas, by a diaphragm. The high and low pressure regions can also be referred to as compression and expansion pressure chambers respectively (1). When the diaphragm is suddenly burst, an incident shock wave generates and propagates through the test gas raising its temperature and pressure. As the shock wave moves through the test gas, a rarefaction wave moves back into the high-pressure gas at the speed of sound and reflects off the driver endwall once it reaches it. The test gas and the driver gas make contact at the "contact surface", which moves along the tube behind the shock front. The incident shock wave arrives at the end wall and reflects back raising the temperature and pressure of the shocked gas in the test region. As such, the energy release and chemical reaction starts resulting into an ignition event. The end of the experiment is dictated by the arrival of the expansion fan to the driven tube endwall or by the interaction of the reflected shock with the contact surface. Typical test times in the shock-tube experiments are on the order of few milliseconds. Figure 1 shows the ideal movement of the shock front, the contact surface, the rarefaction wave and the reflected shock wave in a distance-time diagram. The undisturbed low-pressure test gas is given by the subscript 1, and the initial temperature and pressure in this region are denoted as P_1 and T_1, respectively. The region between the shock front and the contact surface is denoted by the subscript 2 and the region between the contact surface and the rarefaction wave is indicated by the subscript 3. The initial conditions on the high-pressure side are given by the subscript 4. When the shock wave undergoes reflection at the end of the tube, the conditions in this region are given by the subscript 5.

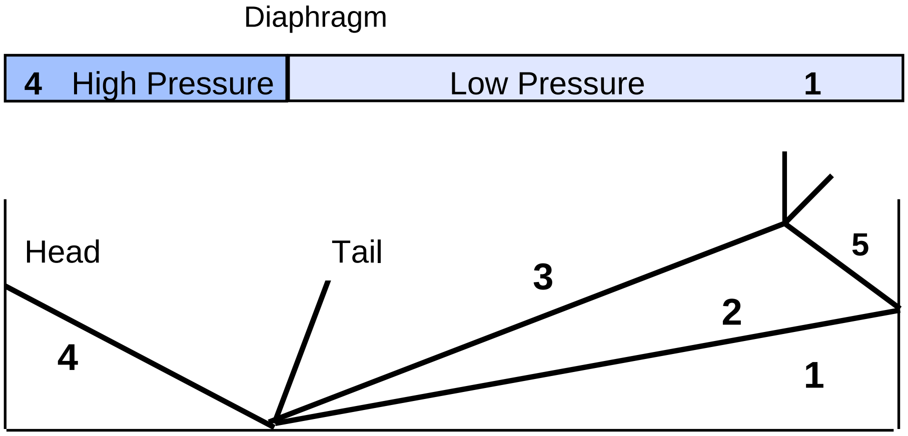

Figure 1: Time vs. distance diagram for a shock tube

The shock-tube facility being modeled herein is located in the combustion research laboratory at Texas A&M University. Pressures up to 100 atm and temperatures up to 2500 K can be generated in this facility. The shock tube consists of a 2.46-m long driver section with an internal diameter of 7.62 cm and a 4.72-m long driven section with an internal diameter of 15.24 cm. The shock-tube side wall and endwall thicknesses are 1.27 cm and 2.54 cm, respectively. The shock-tube facility is described in detail in De Vries et al. (2). A schematic of the experimental shock tube is given in Figure 2.

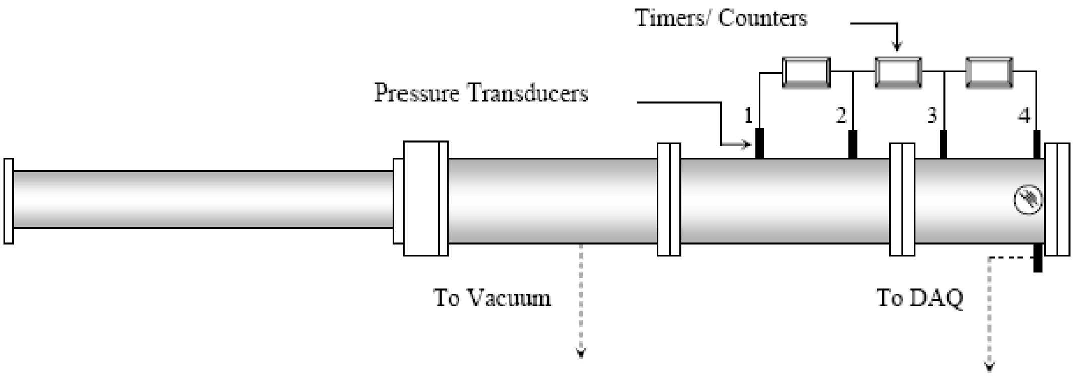

Figure 2: Shock Tube Facility at Texas A&M University

Target reflected-shock temperatures and pressures are achieved through the use of 1-mm Lexan diaphragms. Ignition measurements are performed in the reflected-shock region. Incident-shock velocities are measured at four different axial locations along the driven tube by using four PCB 113A pressure transducers in conjunction with four 120-MHz Fluke model PM6666 time-interval counters. The data acquisition system comprises of two 16-bit 10-MHz computer oscilloscope boards with a total of four channels. Temperatures and pressures in the reflected-shock region are determined from the standard 1-D shock-tube relations and the Sandia thermodynamic database. Ignition delay times are measured from the endwall location by monitoring the endwall pressure signal through a PCB 113A pressure transducer. The endwall emission trace is also used as a guide for ignition delay time determination and is acquired by monitoring the CH^* chemiluminescence through a 430±5 nm narrow band filter with a Hamamatsu 1P21 Photomultiplier tube (PMT) in a custom-built housing. Optical ports located on the side of the shock tube allow for additional non-intrusive optical access. Figure 3 and Figure 4 shows sample pressure and emission traces recorded from the endwall and the side wall ports respectively.

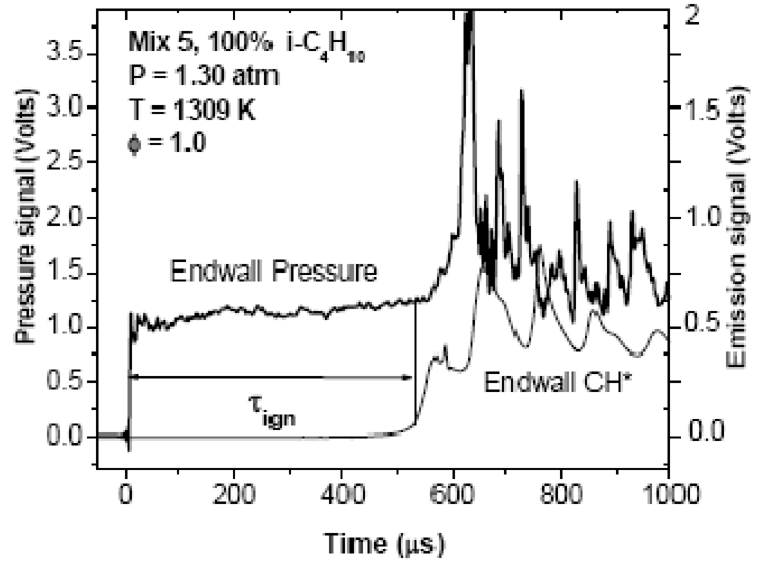

Figure 3: Typical endwall pressure and endwall emission traces.

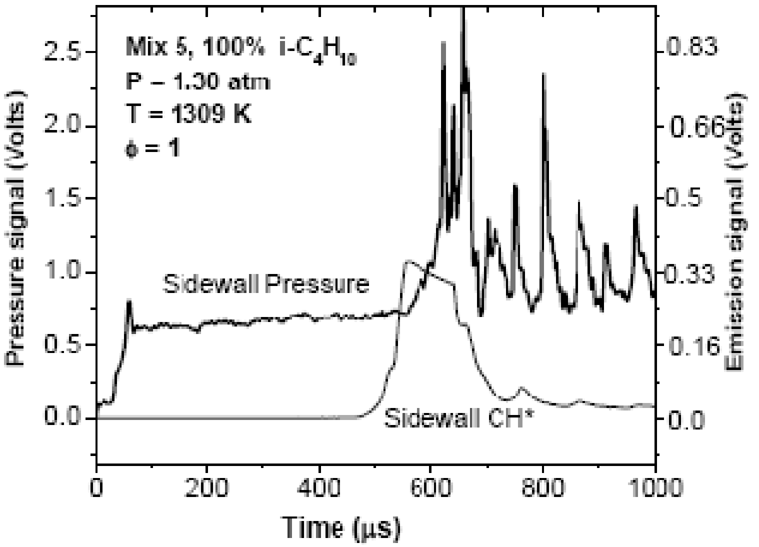

Figure 4: Typical sidewall pressure and sidewall emission traces

Background Shock-Tube Non-Idealities

There have been a number of experimental studies investigating the mechanisms responsible for non-ideal behavior in shock-tube facilities. These mechanisms include the non-ideal rupture of the diaphragm (3) (4) (5) (6) (7) (8), reflected shock/boundary layer interactions (9) (10) (11) (12) (13) (14) (15) (16)**,** driver gas contamination , contact surface instabilities (17) (18) (19) (20) (21) (22), and thermal boundary layer effects (23) (24) (25)**.**

Also, theoretical and analytical models have been developed that provide a reliable understanding of the non-idealities in the shock tube. In particular, Mark was the first to establish a theoretical treatment of the reflected shock/boundary layer interaction and the mechanism responsible for wall jetting of driver gas through the bifurcated structure (9). Since then, several empirical models have been developed in an attempt to quantify the disturbance level of the bifurcated zone (26) (12) (14). Davies and Wilson (27) and Stalker and Crane (28) used Mark's theory and developed analytical models for predicting the premature arrival of driver gas to the endwall region. Numerical simulations have also provided reliable information about the contamination process which is of great concern in high-enthalpy shock tunnels in particular (27) (28).

Ideally, the endwall region behind the reflected shock wave is assumed to be isothermal before chemical reaction takes place. However, in real shock-tube experiments and especially when the test times are relatively long, the isothermal assumption becomes invalid, and heat losses from the hot gas and the cold wall become important and should be accounted for in shock-tube modeling studies. Furthermore, the effect of the thermal boundary layer on the reflected-shock structure and the flow properties near the endwall region have been analyzed theoretically (29) (30) (31) (32) and numerically based on the gas kinetic models (BGK) (33) and the 1-D Navier-Stokes equations (34) (35).

Unfortunately, the shock tube is a transient test facility with unsteady and highly nonlinear physical processes that cannot be accurately modeled with simple 1-D models, but the investigation of complex phenomena associated with the shock tube can be enhanced considerably when done in concert with multi-dimensional numerical simulations. Such simulations are made possible with Computational fluid Dynamics (CFD) codes and the increased computational resources which have become quite powerful tools to highlight the flow physics in multi-dimensional complex and transient flow fields.

To that end, shock-tube non-idealities have been investigated during the last several decades. Multi-dimensional simulations have been performed to model the non-ideal rupture of the diaphragm to quantify the shock speeds, the structure of the developing flow downstream the diaphragm and the contact surface shape. For example, the opening of the diaphragm has been modeled as a slit in two dimensional simulations (8) (36)**,** versus an iris in axi-symmetric simulations (37) (38) (39) (40)**.** The reflected-shock bifurcation phenomenon has been simulated in a number of numerical studies (16) (41) (42) (43) (44) (45) (46) (47) (48) (49) (50) (51) and also has served as a test case for numerical method validations (51) (52) (53) (54) (55) (56). Multi-dimensional simulations have also aimed at modeling the interaction between the reflected shock and the contact surface in an attempt to predict the driver gas contamination in high-enthalpy shock tunnels in particular(38) (39) (40) (46) (57) (58) (41) (59) (41).

Motivation

While the studies mentioned above have given insight into the flow evolution in shock tubes and the various non-ideal phenomena that affect the test time and conditions, the inability to model the whole test facility geometry due to computational limitations necessitates various assumptions and consequently, the majority of the previously reported simulations focused on certain parts of the shock-tube facility such as the endwall region with the upstream inflow conditions derived from the Rankine–Hugoniot relations and the initial conditions set just before shock reflection upstream of the endwall. When viscous effects are taken into consideration, the initial flow field behind the incident shock is usually estimated from the boundary layer theory of Mirels (60) (61). Therefore the results depend greatly on the assumptions associated with modeling only part of the facility. Of particular interest in this study is the development of a fluid mechanics model of the reflected-shock process that can be applied to experimental conditions routinely seen in high-pressure chemical kinetic and ignition delay time experiments in undiluted fuel-air mixtures. With such a model, parametric studies can be performed that couple the shock-tube fluid mechanics with the chemical kinetics in an attempt to characterize the extent of non-ideal behavior in such experiments.

In this respect, accurate simulations of the complex spatial and temporal inter relations in the shock-tube flow are more likely to be achieved through modeling of the complete shock-tube geometry rather than just the endwall region of the shock tube. This approach is a challenging task because it requires the use of large mesh sizes in addition to time marching the solution over a large number of small time steps that allow the resolution of the flow-physics. Such large-scale computations can be made possible through the use of parallel processing.

CHAPTER TWO: COMPUTATIONAL MODEL

The simulations were carried out with the commercial CFD solver FLUENT. The model equations are discretized in space and time following the control volume approach and utilizing a density-based explicit solver. The flow domain is represented with a structured mesh of hexahedral cells. A grid adaption tool is used to resolve regions with the steepest gradients. The AUSM+ flux vector splitting scheme is used to compute the flux vectors. The convective terms are discretized in space following three schemes, 1/2nd order blending upwind, 2nd order upwind, and 3rd order MUSL schemes to investigate the impact of increasing scheme resolution on the accuracy and stability of the solution. An explicit time-stepping integration was performed using a four-stage Runge-Kutta scheme for unsteady flows. The time step was set by the Courant-Friedrichs-Lewy stability limit between 0.8 and 1.

Computational Grid

The computational domain represents the entire geometry of the high-pressure shock tube test facility at Texas A&M University described in detail in De Vries et al. (2). The shock tube consists of a 2.46-m long driver section with an internal diameter of 7.62 cm and a 4.72-m long driven section with an internal diameter of 15.24 cm. The shock-tube side wall and endwall thicknesses are 1.27 cm and 2.54 cm, respectively. Due to the axial symmetry of the shock tube, the flow domain is modeled with an axi-symmetric structured mesh as shown in Figure 5. The axi-symmetric approach is appropriate for the cylindrical geometry of the shock tube and is sufficient to render an accurate description of the real flow configuration. The boundary conditions of the shock-tube model when the conjugate heat transfer model is turned on are given in Figure 6.

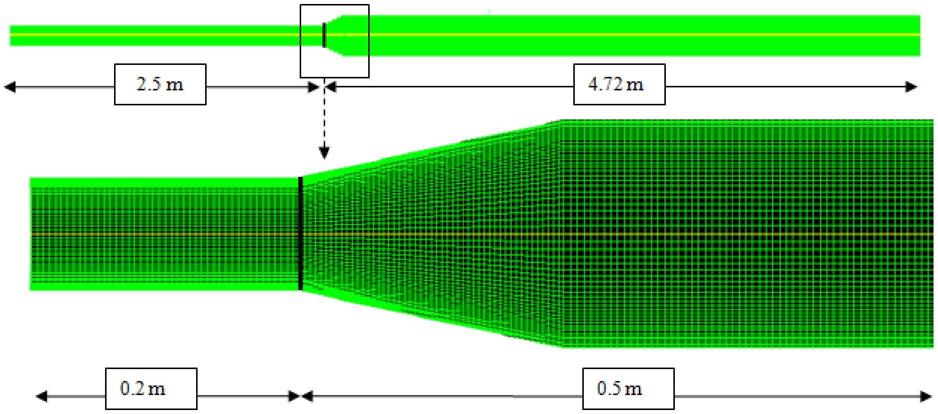

Figure 5: The axi-symmetric structured mesh showing the initial mesh before grid adaption is applied. Section shown is at the diaphragm location. Note the diverging section that mates the driver (left side) and the driven (right side) sections.

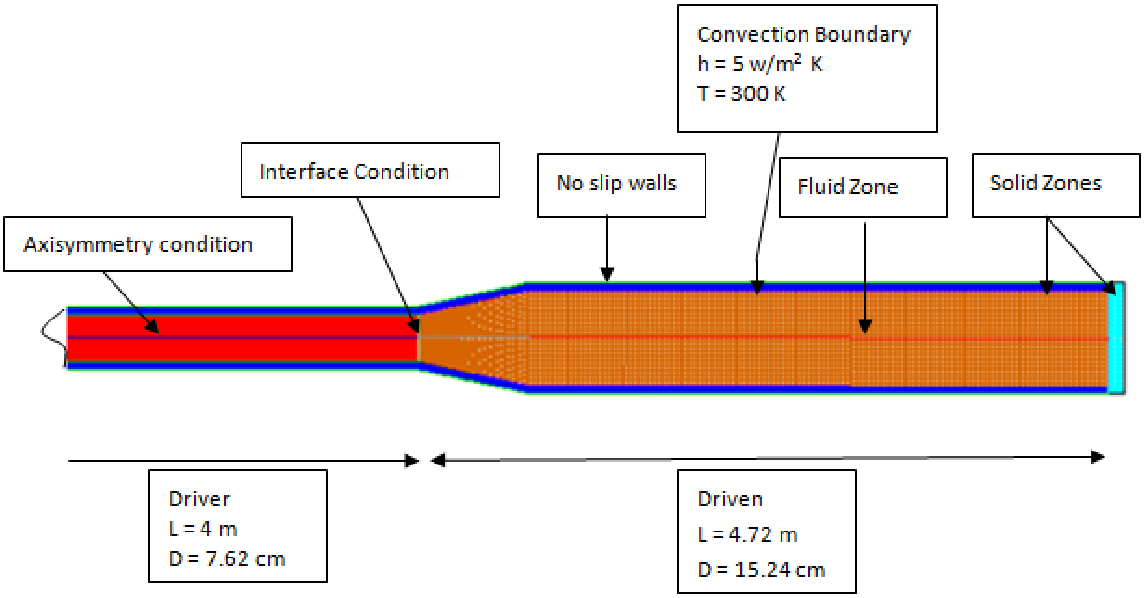

Figure 6: Axi-symmetric viscous/Conjugate heat transfer model boundary conditions

Numerical Model

Finite Volume Method

The density-based coupled-explicit algorithm is adopted with double precision. This algorithm solves the governing equations of continuity, momentum, energy and species transport simultaneously as a set of equations. The finite-volume-based discretization approach is used to solve numerically the Navier-Stokes equations. This is accomplished by first dividing the domain into discrete control volumes, then integrating the governing equations on the individual control volumes to construct algebraic equations for the discrete dependent variables and last linerazing the governing equation to produce a system of equations for the dependent variable. The governing equations can be illustrated by considering the unsteady conservation equation for transport of the scalar quantityφ. This is demonstrated by the following equation written in integral form for an arbitrary control volume V as follows,

$$\iiint \frac{\partial \rho\varphi}{\partial t} dV + \oint \rho\varphi\vec{v}.d\vec{A} = \oint \Gamma_\varphi \nabla\varphi.d\vec{A} + \iiint S_\varphi dV \tag{1}$$

Where, ρ is the density, $\vec{v}$ is the velocity vector, $\vec{A}$ is the surface area vector, Γ_φ is the diffusion coefficient for φ, $\nabla\varphi$ is the gradient of φ, and S_φ is the source of per unit volume. Discretization of Eq. (1) on a given cell yields,

$$\frac{\partial \rho\varphi}{\partial t} V + \sum_{f}^{N_{faces}} \rho_f \vec{v}_f \varphi_f.\vec{A}_f = \sum_{f}^{N_{faces}} \Gamma_\varphi \nabla\varphi_f.\vec{A}_f + S_\varphi V \tag{2}$$

Where N_{faces} are the number of faces enclosing the cell, φ_f is the value of φ convected through face *f*, $\rho_f \vec{v}_f.\vec{A}_f$ is the mass flux through the face *f*, $\vec{A}_f$ is the area of face *f*, $\nabla\varphi_f$ is the gradient of φ at face *f*, and V is the cell volume. Linearization of equation is performed as such,

$$a_p\varphi = \sum_{nb} a_{nb}\varphi_{nb} + b \tag{3}$$

Where the subscript *nb* refers to neighbor cells, and a_p and a_{nb} are the linearized coefficients for φ and φ_{nb}.

Spatial Discretization

The AUSM+ flux vector splitting scheme was used to compute the flux vectors. AUSM stands for Advection Upstream Splitting Method first introduced by Liou and Steffen (62) accurately captures shock and contact discontinuities by providing an exact resolution, free of "Carbuncle" phenomena and oscillations at stationary and moving shocks, and preserves the positivity of scalar quantities. The AUSM scheme was substantially improved to yield the generalized Mach number-based convection and pressure splitting functions. The new scheme termed AUSM+ is more robust and avoids using an explicit artificial dissipation (63) (64). First order can yield better convergence than higher order schemes especially in complex flows where shocks and discontinuities are present, however, especially when turbulence is dominant, first-order discretization is not recommended due to the increased numerical discretization error introduced by this scheme. First-order accuracy is obtained by simply setting the face value φ_f equal to the cell-center value of φ in the upstream cell as shown in Eq. (4). *fou* stands for first order upwinding.

$$\varphi_{f,fOU} = \varphi \tag{4}$$

In general, when shock discontinuities are present in the flow, it is almost impossible to achieve a stable solution, free of unphysical numerical oscillations and nonlinear instabilities without introducing some numerical dissipation. However, numerical dissipation can be reduced by increasing the mesh resolution at the shock and contact discontinuities by applying the adaptive grid refinement approach.

High resolution schemes such as 2nd order or higher schemes can yield more accurate results than the first order scheme. If second-order accuracy is desired, quantities at cell faces are computed using a multidimensional linear reconstruction approach by applying Taylor series expansion about the cell centroid. The face value φ_f is computed using the following equation:

$$\varphi_{f,SOU} = \varphi + \nabla\varphi . \vec{r} \tag{5}$$

Where *SOU* stands for second order upwinding, φ is the cell-centered value and $\nabla\varphi$ is its gradient in the upstream cell, $\vec{r}$ is the displacement vector from the upstream cell centroid to the face centroid. For second order schemes, oscillations creep up, notably at the discontinuities. A Total Variation Diminishing concept is applied and the gradient $\nabla\varphi$ is limited so that no new maxima or minima are introduced.

Another effective method to avoid the oscillations in the solution is by adding some diffusion to the 2nd order scheme by blending the second order $\varphi_{f,SOU}$ and first order $\varphi_{f,fOU}$ approximations as such,

$$\varphi_{blending} = \varphi_{f,fOU} + \beta(\varphi_{f,SOU} - \varphi_{f,fOU}) \tag{6}$$

Where β is a blending factor whose values lie between zero and one, $\beta = 0$ reduces the scheme to 1st order upwind, and $\beta = 1$ brings it back to pure 2nd order upwinding providing satisfactory results. Usually small amounts of the first order scheme (10-20%) is sufficient to get rid of the oscillations, and the accuracy is nearly as good as with 2nd order accurate scheme and the stability is nearly as good as the 1st order scheme.

Third order MUSCL Scheme (Monotone Upstream-Centered Schemes for Conservation Laws) (65) is achieved by blending a central differencing scheme and second order upwind scheme as such,

$$\varphi_{f,MUSCL} = \theta\varphi_{f,CD} + (1-\theta)\varphi_{f,SOU} \tag{7}$$

Where $\varphi_{f,CD}$ is determined using central differencing and $\varphi_{f,SOU}$ is computed using the second-order upwind scheme. Spatial accuracy is improved with the MUSCL scheme by reducing numerical diffusion, however the implemented scheme in the CFD solver FLUENT does not contain any flux-limiter and therefore produces undershoot and overshoot in the solution.

Temporal Discretization

Time marching is performed by evaluating the scalar φ at the current time level as such,

$$\frac{\varphi^{n+1} - \varphi^{n}}{\Delta t} = F(\varphi^{n}) \tag{8}$$

And φ^{n+1} is given by,

$$\varphi^{n+1} = \varphi^{n} + \Delta t\, F(\varphi^{n}) \tag{9}$$

Here, the time step Δt is restricted to the stability limit set by the Courant-Friedrich-Lewy condition CFL as shown as such.

$$\Delta t = \frac{2\, CFL.V}{\sum_f \lambda_f{}^{max} A_f} \tag{10}$$

Where V is the cell volume, A_f is the face cell, and $\lambda_f{}^{max}$ is the maximum of the local eigenvalues. To maintain time accuracy of the solution, the explicit time stepping employs the same time step in each cell of the domain. Explicit time stepping is primarily used in the cases of compressible transient flows in order to capture the shock and contact discontinuities while implicit time stepping is known to be more expensive and produces less accurate results. A four-stage Runge-Kutta scheme for unsteady flows is used by the CFD solver. The stability limit that was set between 0.8 and 1.

Dynamic Grid Adaption

Adaptive grid feature was used to cluster the grid around the shock and contact discontinuities. As with any numerical approximation of solution discontinuities, shocks will be somewhat smeared by grid resolution and numerical diffusion, adaption is an effective tool that can be used to resolve the discontinuities and reduce the numerical error in the digital solution with minimal numerical cost (66) (67). The adaption feature can also be used to achieve a grid-independent solution without regenerating the mesh. Adaption parameters can be tuned to effectively capture shock and contact discontinuities. Coarsen and refine thresholds are adjusted to achieve the desired level of adaption.

Adaption is performed by refining the mesh near high gradient regions and coarsening the mesh wherever else needed, thus providing better resolution of shock and contact discontinuities. The refine and coarsen limits are determined based on the normalized values of the density gradients. In this approach, the Euclidean norm of the gradient of the selected solution variable is multiplied by a characteristic length scale and the gradient function has the following form,

$$|e_{i1}| = (A_{cell})^{\frac{r}{2}}|\nabla f| \tag{11}$$

Where $|e_{i1}|$ is the error indicator, A_{cell} is the cell area, r is the gradient volume weight with $r = 1$ corresponding to full volume weighting, and $|\nabla f|$ is the Euclidean norm of the gradient of the desired field variable f. The normalized values are obtained by scaling the values of $|e_{i1}|$ by their maximum value in the domain as is shown in Eq. (12) so that the adaption rang, refine and coarsen thresholds, is between [0, 1]. The refine and coarsen threshold values depend on the strength of the shock and contact discontinuities. Dynamic grid adaption based on gradients of both density and pressure was performed every five iterations.

$$\frac{|e_{i1}|}{max|e_{i1}|} \tag{12}$$

Shown in Figure 7 is the computational model mesh with grid adaption based on gradients of density and pressure obtained with a) 1st order scheme, b) 2nd order scheme, and c) 3rd order MUSCL scheme. The mesh was adapted in regions with steep gradients where the contact discontinuities were present allowing for the resolution of the shock wave and contact surface. The 1st order solution produces a thick contact surface due to the numerical diffusion effect which smears the contact surface over a few cells. On the other hand, the high-resolution 2nd and 3rd order schemes sharply capture the contact surface with the 2nd order scheme yielding a better resolution than the 3rd order scheme. This is due to the fact that the implemented 3rd order MUSCL scheme in the current CFD solver is not TVD.

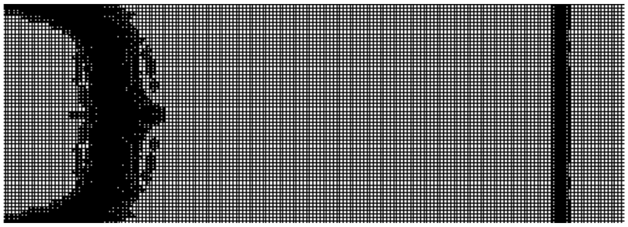

a)

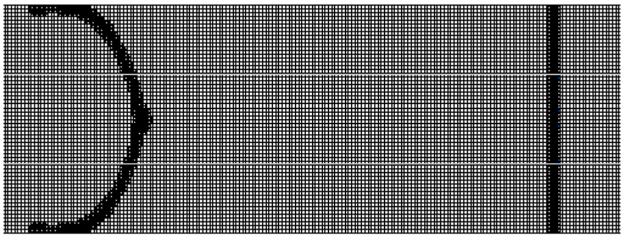

b)

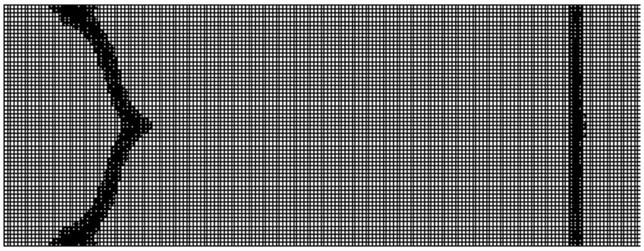

c)

Figure 7: Grid adaption based on pressure and density gradients show the resolved shock and contact discontinuities from three different schemes. a) 1st /2nd order blending, b) 2nd order, c) 3rd order MUSCL

Provided in Figure 8 are the profiles of a) density, b) temperature, and c) pressure from a 1st order solution generated with and without grid adaption. The test gas is Air and the driver gas is Helium. The initial pressure ratio across the diaphragm is equal to 10. Temperature and density profiles generated without grid adaption display a wrong prediction of the maximum temperature across the contact surface and a smearing of the solution over few cells. Grid adaption reduces this effect and resolves the contact surface, thus providing a more accurate solution.

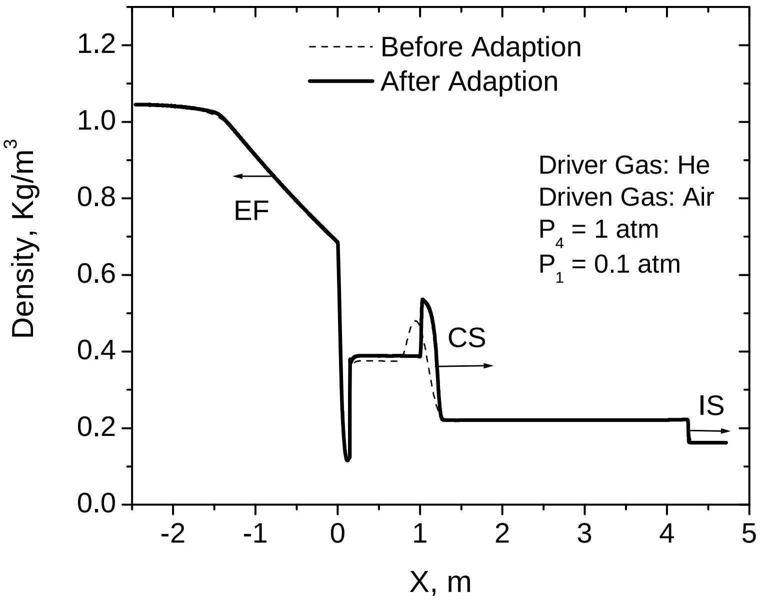

Before Adaption
After Adaption
Driver Gas: He
Driven Gas: Air
P_4 = 1 atm
P_1 = 0.1 atm
EF
CS
IS
Density, Kg/m^3
X, m
0.0
0.2
0.4
0.6
0.8
1.0
1.2
-2
-1
0
1
2
3
4
5

a)

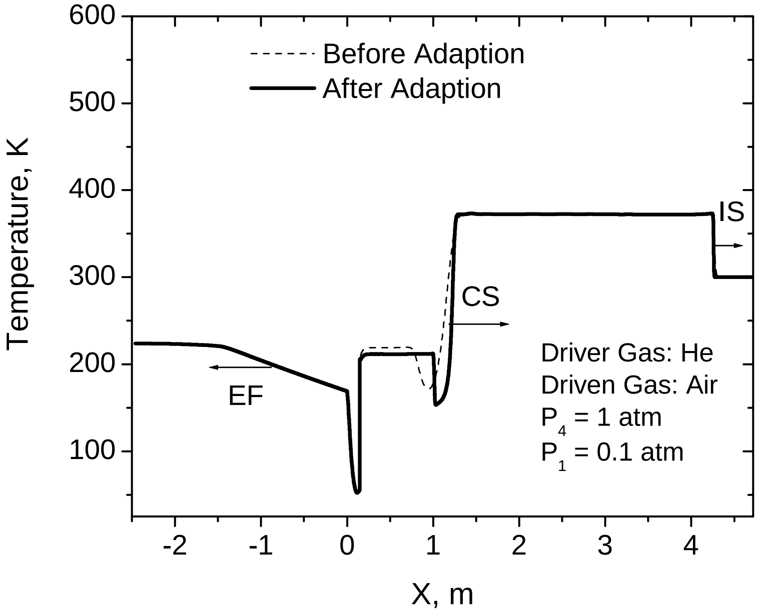

Before Adaption
After Adaption
Driver Gas: He
Driven Gas: Air
P_4 = 1 atm
P_1 = 0.1 atm
EF
CS
IS
Temperature, K
X, m
100
200
300
400
500
600
-2
-1
0
1
2
3
4

b)

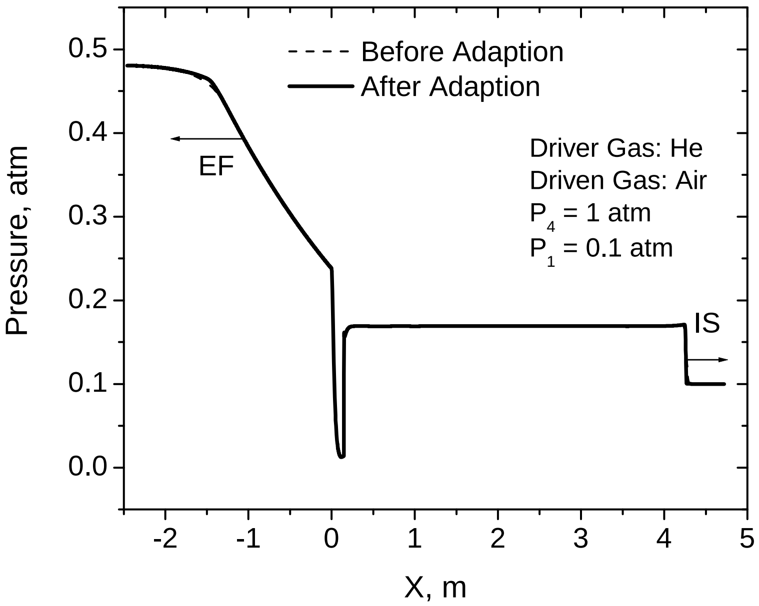

c)

Figure 8: a) Density, b) temperature, and c) pressure distribution along the tube axis before and after grid adaption. The simulations were performed with 1st/2nd order scheme. The smearing of the contact surface is reduced with grid adaption. The apparent sharp decrease in density, temperature, and pressure immediately after the diaphragm is due to the flow expansion through the diverging section at that location.

CHAPTER THREE: INVISCID SOLUTION

Introduction

As a first step towards modeling the complex mechanisms responsible for the non-uniform conditions and the reduced test times in the shock tube, the flow is assumed to be inviscid and this section focuses on developing a robust and accurate model capable of reproducing the major flow phenomena in the shock tube from the propagation of the shock wave and contact surface to the reflection of the expansion fan and incident shock. The inviscid model should serve as a baseline for the rather more complex viscous model which necessitates increased computational efforts. The modeling of the complex flow structure in the shock tube by solving the unsteady Euler equations under the assumption of inviscid flow have been successfully investigated in 1-D (68) (69) (70), 2-D (8) (36) (71) (72) (73), axi-symmetric (37)**,** and 3-D (74) (75) simulations. In addition, the axi-symmetric approach has proven to be an appropriate representation of the cylindrical geometry of the shock tube (37) (38) (39) (40) (46) (57) (58) (41) (59) (76) (49).

Background

Shock capturing methods have been widely used in the computation of inviscid flows with shock and contact discontinuities and they can be classified into two main categories, modern and classical. The classical methods including the McCormack method (77), the Lax-Wendrofff method (78), and Beam-Warming method (79) use symmetric or central discretization schemes, while modern methods employ upwind–type differencing schemes. Modern methods include higher order schemes such as the Total Variation Diminishing scheme (TVD) first introduced by Harten (80), Monotonic Upstream Centered Schemes for Conservation Laws (MUSCL) established from the Godunov approach (81) and introduced by Van Leer (65), the Flux-Corrected Transport (FTC) scheme introduced by Boris and Book (82), Essentially Non-Oscillatory schemes (ENO) proposed by Harten et al. (83), Piecewise Parabolic Method (PPM) proposed by Woodward and Colella (84), and the approximate Riemann solvers presented by Roe and Osher (85) (86).

In general, when shock discontinuities are present in the flow, it is almost impossible to achieve a stable solution, free of unphysical numerical oscillations and nonlinear instabilities without introducing some numerical dissipation. Modern shock capturing methods employ non-linear numerical dissipation, in a way that the amount of dissipation in any cell is adjusted according to gradients in neighboring cells which makes this scheme stable and accurate.

To avoid the generation of numerical oscillations associated with high order spatial discretization schemes such as 2nd order and higher, flux limiters are used. They operate when steep gradients in the form of shock and contact discontinuities are present in the solution and they have the effect of limiting the spatial derivatives near shocks and discontinuities to physically realistic values which makes the solution free from spurious numerical oscillations. In smooth regions of the solution, flux limiters do not operate and spatial derivatives are represented by higher order spatial accuracy (80) (87) (88). The numerical method is considered TVD when monotonicity is preserved such that the values of the local maximum and minimum are non-increasing and non-decreasing respectively. Godunov has shown that first order schemes preserve monotonicity and are therefore TVD. On the other hand, higher order schemes are not

TVD and introduce spurious oscillations. These drawbacks are overcome with flux limiters which make the numerical scheme TVD (89). TVD limiters have the ability to reduce the order of accuracy to 1st order in regions characterized with steep gradients. Away from the shocks and contact discontinuities, TVD simply do not operate and higher order discretization schemes are used in the majority of the flow while still capturing shock waves and strong gradients without obvious wiggles (80).

Previous studies which modeled the complex transient flow structures in shock tubes and captured the shock and contact discontinuities by solving the Euler equations have used different numerical approaches (68) (69) (70) (71) (72) (36) (73) (8) (37) (74) (75).

Argow (68) studied the evolution of non-classical flow fields in a conventional shock tube by solving the one-dimensional Euler equations. The equations were discredited by using the TVD-MacCormack (TVDM) predictor-corrector scheme, a finite volume variant of the MacCormack scheme which is second order accurate in space and time. A Minmod limiter was used and the courant condition was set to 0.6.

Loh and Liou showed that complicated shock and contact discontinuities can be accurately resolved when the streamwise marching Langrangian method is adopted (75). The steady Euler equations were discretized using the finite difference first order scheme which was upgraded to the high resolution TVD scheme by using the Minmod flux limiter. The scheme is a variation of Van Leer's MUSCL scheme (65) followed that given in Liou (63) and Liou and Hsu (90).

Cocchi et al. (70) proposed a correction to Godunov Type schemes that yields a perfect discontinuity. This method is based on a prediction step which makes use of any Euler scheme and a correction step based on a lagrangian approach. Two discretization methods were used; the first order Godunov scheme and the second order VanLeer scheme. The numerical diffusion was corrected for by the correction step which consists of interpolating the values at node points on both sides of the interface as function of values at neighboring points. Instabilities and oscillations were handled with the Total Variation Diminishing concept (TVD) and the Minmod limiter.

Petrie-Repar and Jacobs (37) employed a cell-centered finite volume code U2DE. The generalized MUSCL interpolation scheme was used to construct the left and right flow states and the Minmod limiter was applied to limit the oscillations in the flow domain. In addition, the Equilibrium flux Method (EFM) was used to calculate the flux array from the left and right edge flow states. EFM solves the Euler equations with added pseudo dissipation and in the hypersonic limit, becomes an upwind scheme. Grid adaption was implemented with the density and pressure gradient adaption performed every five time steps. Advancement in time was achieved by using the predictor-corrector explicit time scheme. The CFL condition was set to 0.5.

Burtschell and Zeitoun (49) investigated the interaction of two oblique axi-symmetrical shock waves in a supersonic flow by solving the Euler equations according to a cell-centered finite volume method on a two-dimensional structured grid. A second order accurate algorithm in space and time was used. The dissipative fluxes were replaced with central differences and the convective fluxes were computed by solving the Riemann problem replaced by the AUSM-M in the case of strong shocks. Instabilities were handled with both the Minmod and the Superbee-type limiters. The unsteady formulation of the discretized equation used a predictor corrector explicit time scheme with the CFL condition set to 0.8.

Jiang et al. (74) investigated the three-D propagation of the transmitted shock wave in a square cross section chamber numerically by solving the Euler equation. Discretization in space was accomplished using the dispersion-controlled scheme and the flux vector was split according to the Steger and Warming method with the help of the Minmod limiter. The time marching integration was performed using a 2^{nd} order accurate Range-Kutta algorithm with the courant number set to 0.5. The dispersion controlled scheme requires that shock capturing schemes must have leading or lagging phase errors to avoid non-physical oscillations near the shock and contact discontinuities which can be achieved without resorting to additional artificial viscosity.

Cocchi et al. (72) proposed a hybrid formulation of conservative and non-conservative forms to solve the Euler equations in order to correctly estimate the temperature across shock and strong rarefaction waves in two-dimensional flows. A finite volume formulation of a MacCormack (77) scheme with second order artificial viscosity was applied. Numerical results were compared to results from classical schemes such as the first order Godunov scheme (81) and the second order Godunov-MUSCL Hancock scheme (65) with an exact Riemann solver.

Takayama and Sun (91) performed numerical studies of shock diffraction phenomena in a two dimensional shock tube model by solving the Euler equations following a finite volume approach. The equations were discretized by the means of two 2^{nd} order in space and time schemes; a centered scheme based on the predictor-corrector Lax- Wendroff scheme with added nonlinear artificial viscosity and an upwind MUSL-Hancock scheme (88). A Minmod limiter was used to flatten slopes of primitive variables and the fluxes through interfaces were determined by solving the HLLC approximate Riemann problem.

Chang and Kim (71) investigated the dynamics of inviscid shock waves in an expansion tube. The simulation was performed on an axi-symmetric unstructured triangular mesh using the Finite volume Galerkin algorithm. The FCT (Flux-Corrected Transport) discretization scheme was adopted by blending the low order fluxes with the higher order ones under the monotonicity constraint. Excessive Anti-diffusion from the low order scheme was corrected for by blending the artificial dissipation and the area weighted differencing of higher order increment. A limiter function that computes the minimum between the density and the energy was chosen to prevent overshoots in the solution. Solution was marched in time following the 3-stage Runge-Kutta time integration. The H refinement adaptive method was used for grid adaption every 5 or 7 time steps.

Governing Equations

The first part of the study assumes the flow field as inviscid then the governing equations are the well known Euler equations for inviscid flows. For an axi-symmetric model, the continuity equation is given by,

$$\frac{\partial \rho}{\partial t}+\frac{\partial(\rho v_x)}{\partial x}+\frac{\partial(\rho v_r)}{\partial r}+\frac{\rho v_r}{r}=0 \tag{12}$$

The conservative form of the Euler equations is given by:

$$\frac{\partial U}{\partial t}+\frac{\partial E}{\partial x}+\frac{\partial G}{\partial y}+\alpha H=0 \tag{13}$$

Where $\alpha = 0$ for two-dimensional and $\alpha = 1$ for axi-symmetric problems. The vectors U, E, G, and H are defined as

$$U=\begin{bmatrix}\rho\\ \rho v_x\\ \rho v_r\\ \rho E\end{bmatrix} E=\begin{bmatrix}\rho v_x\\ \rho v_x v_x+P\\ \rho v_x v_r\\ (\rho E+P)v_x\end{bmatrix} G=\begin{bmatrix}\rho v_r\\ \rho v_x v_r\\ \rho v_r v_r+P\\ (\rho E+P)v_r\end{bmatrix} H=\frac{1}{r}\begin{bmatrix}\rho v_r\\ \rho v_x v_r\\ \rho v_r v_r\\ (\rho E+P)v_r\end{bmatrix} \tag{14}$$

Where ρ, v, P, and E are the density, velocity, pressure, and total energy per unit mass of the fluid, respectively. The total energy E is related to the equation of state for a perfect gas and is expressed with the following equation.

$$E = \frac{P}{\gamma - 1} + \frac{1}{2}\rho(v_x^2 + v_r^2) \tag{15}$$

Where $\frac{1}{2}\rho(v_x^2 + v_r^2)$ is the kinetic energy and γ is the specific heat ratio. The Total energy E is related to the total enthalpy H by

$$E = H - \frac{P}{\rho} \tag{16}$$

Where,

$$H = h + \frac{|v|^2}{2} \tag{17}$$

When the mixing and transport of chemical species are considered, the conservation equations describing convection, diffusion, with or without reaction sources for each component species have to be modeled. The conservation equation takes the following form,

$$\frac{\partial(\rho Y_i)}{\partial t} + \nabla.(\rho\vec{v}Y_i) = -\nabla.\vec{J}_i + R_i \tag{18}$$

Where R_i is the net rate of production of species i by chemical reaction when applicable. The local mass fraction of each species Y_i is predicted through the solution of a convection-diffusion equation for the i^{th} species. The conservation of energy is described by Eqn. (10) for an inviscid model as such,

$$\frac{\partial(\rho E)}{\partial t} + \nabla.\left(\vec{v}(\rho E + P)\right) = -\nabla.\left(\sum_j h_j J_j\right) \tag{19}$$

Where $\nabla.\left(\sum_j h_j J_j\right)$ is the transport of enthalpy due to species diffusion for multi-component mixing flows, J_j is the diffusion flux of species j, which arises due to concentration gradients, and h_j is the enthalphy of species j. The diffusion flux of species j is given by:

$$\vec{J}_j = -\rho D_{j,m} \nabla Y_j \tag{20}$$

Here $D_{j,m}$ is the diffusion coefficient for species j in the mixture. The transport of enthalpy becomes important and should be accounted for in the conservation of energy equation especially when the Lewis number is greater than 1. The Lewis number is given by,

$$Le_i = \frac{k}{\rho c_p D_{i,m}} \tag{21}$$

The equation of state for thermally and calorically perfect gas for multi-component mixtures is given by:

$$\rho = \frac{P}{RT \sum_i \frac{Y_i}{M_{w,i}}} \tag{22}$$

Where R is the universal gas constant, Y_i is the mass fraction of species i, $M_{w,i}$ is the molecular weight of species i, P and T are the local static pressure and temperature, respectively. The mixture's specific heat capacity is calculated as a mass fraction average of the pure species heat capacities as such

$$c_p = \sum_i Y_i c_{p,i} \tag{23}$$

$$c_v = \sum_i Y_i c_{v,i} \tag{24}$$

$$\gamma = \frac{\sum_i Y_i c_{p,i}}{\sum_i Y_i c_{v,i}} \tag{25}$$

$c_{p,i}$ is the specific heat of species i at constant pressure, and $c_{v,i}$ is the specific heat of species i at constant volume.

Numerical Simulations

Figure 9 shows the simulated flow fields in the shock tube. Initially, the high-pressure driver section (state 4) is separated from the low-pressure driven section (state 1) by a diaphragm which is modeled as an interface. The finite opening of the diaphragm is not accounted for in the present model, and at time 0 the diaphragm is assumed to rupture instantaneously. An illustration of the flow field after the rupture of the diaphragm is given Figure 9 (b) showing a left-running expansion wave and a right-running shock wave followed by the contact surface. The flow behind the incident shock wave is referred to as state 2. After the incident shock hits the endwall, as shown in Figure 9 c, it reflects and travels in the opposite direction towards the driver section creating high-temperature and -pressure conditions behind it (state 5).

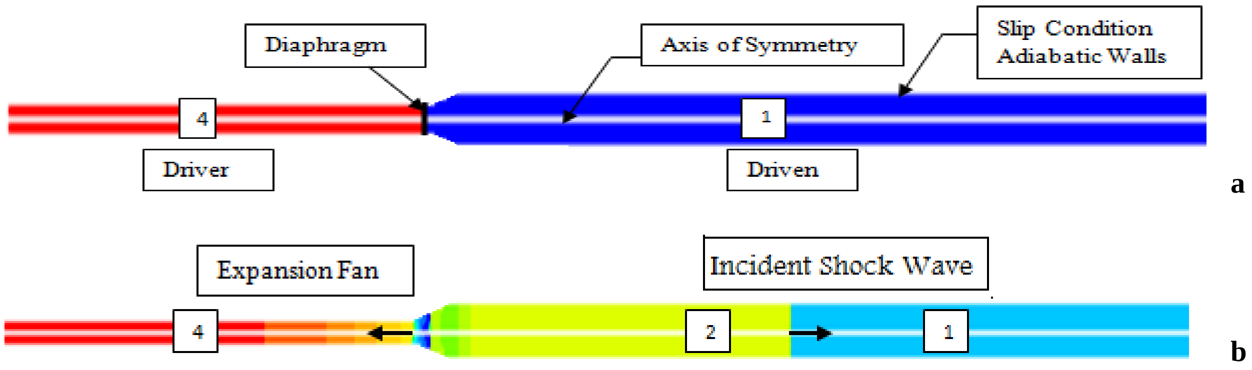

Figure 9: Pressure distribution showing the different flow states in the shock tube, a) before diaphragm rupture, b) after diaphragm rupture, c) after shock reflection.

Soon after the diaphragm rupture, the initial shape of the shock wave is spherical and the contact surface appears to be planar and stable. As the incident shock wave travels further downstream of the diaphragm, it becomes planar. The same observation has been reported in other studies (37) (38). The contact surface takes on a convex shape when viewed further along the tube. However, the contact surface can experience flow instabilities that could alter its shape to one of a complex nature. The contact surface is strongly influenced by the diaphragm rupture model used in the simulations. When an iris-diaphragm rupture is assumed, the driver gas appears as an annular tongue of material penetrating the driven gas (40). Petrie-Repar (37) observed the transformation of the contact surface from a convex shape to a concave shape when a gradually opening diaphragm model is used. The expanding driver gas interacts with the shock tube wall causing the development of an oblique shock which redirects the flow along the wall. As a result, the pressure and density are higher near the wall than the center causing the contact surface to take a concave shape (37). Cambier el al. (38) showed that the contact surface does not become planar with time and suggested that its fate could be dominated by the Rayleigh-Taylor instability. Taylor (17) showed that an accelerating contact surface when accelerated in a direction perpendicular to its plane is stable when the denser fluid is pushing the lighter fluid and is unstable when the converse is true.

Mesh Refinement study

Mesh refinement studies were performed at four mesh levels; 100000, 150000, 200000, and 250000 nodes. Figure 10 shows the temporal evolution of the endwall pressure obtained with four levels of refinement. The test conditions are set to an initial pressure ratio of 50, Helium is used as the driver gas, and Ar is used as the driven gas. Pressure profiles were obtained at conditions behind the reflected shock of 30 atm and 2500 K. Additional cells are added in the flow domain as necessary via grid adaption to maintain finer mesh around the shock and contact discontinuities. As such, the computational efforts are focused around high gradient flow fields all by keeping the overall computational time to a minimum. The total mesh size increased to approximately 500000 nodes with grid adaption. The solution is shown to be independent of the mesh size for a grid resolution consisting of 150000 nodes and above with grid adaption feature turned on.

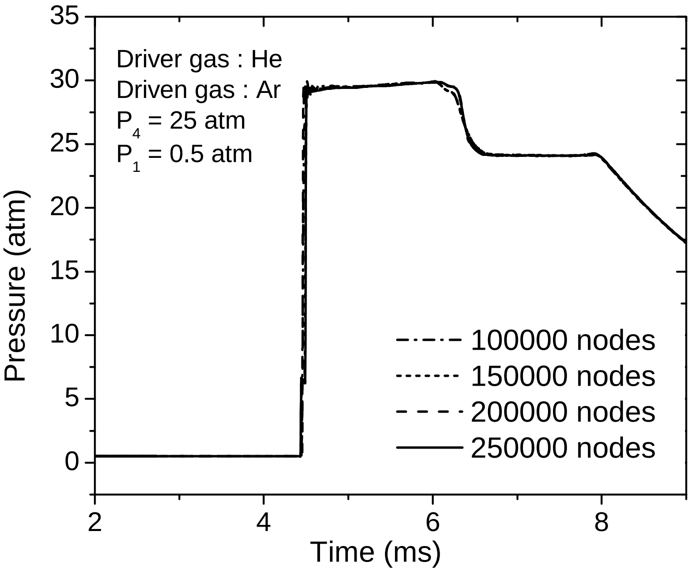

Figure 10: Grid convergence study performed with four mesh resolutions; 10×10^4, 15×10^4, 20×10^4, and 25×10^4 nodes. The pressure profile behind the reflected shock shows the solution is independent of the mesh size.

Accuracy of Numerical Scheme

The accuracy of the numerical model is investigated by comparing the numerical solution from three different schemes to the solution of the 1-D inviscid theory. Density, pressure, and temperature profiles along the shock-tube axis are provided for the 1st/2nd order blending scheme, 2nd order scheme, and 3rd order MUSCL scheme in Figure 11, Figure 12, and Figure 13 respectively. Figure 11 gives the profiles of a) pressure, b) density, and c) temperature obtained with the 1st/2nd order blending scheme along the shock-tube axis. Simulations are compared to the solution of the 1-D theory. The 1st/2nd order blending scheme yields results in agreement with the 1-D theory. The positions of the incident shock wave, the contact discontinuity, and the expansion waves agree with the analytical positions. It is also observed that the 1st/2nd order blending scheme generates some errors at the interface where the curve is slightly twisted on both sides of the interface. Simulation results obtained with the 2nd order accurate scheme are given in Figure 12.

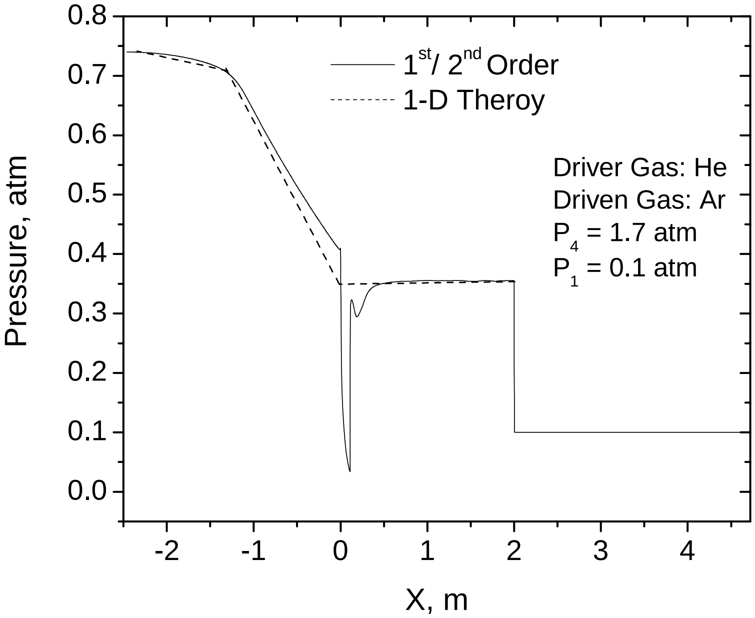

a)

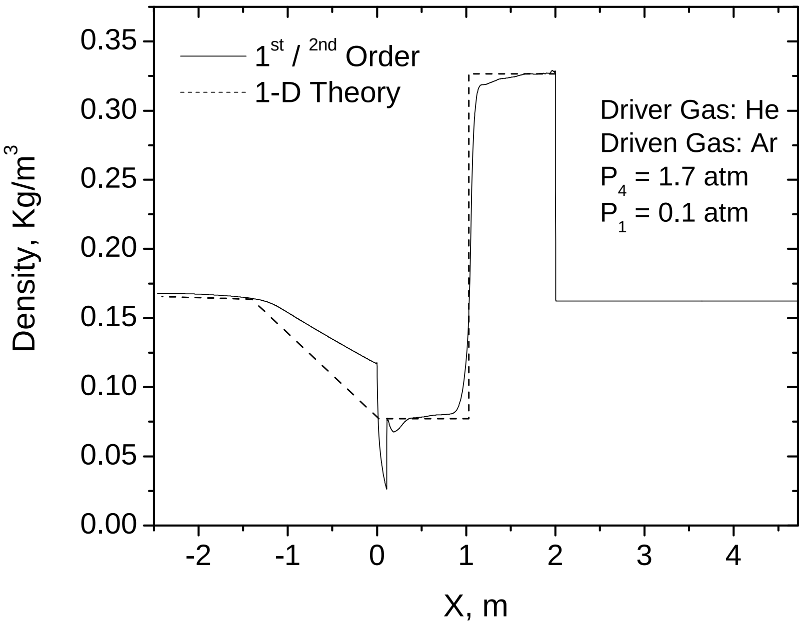

b)

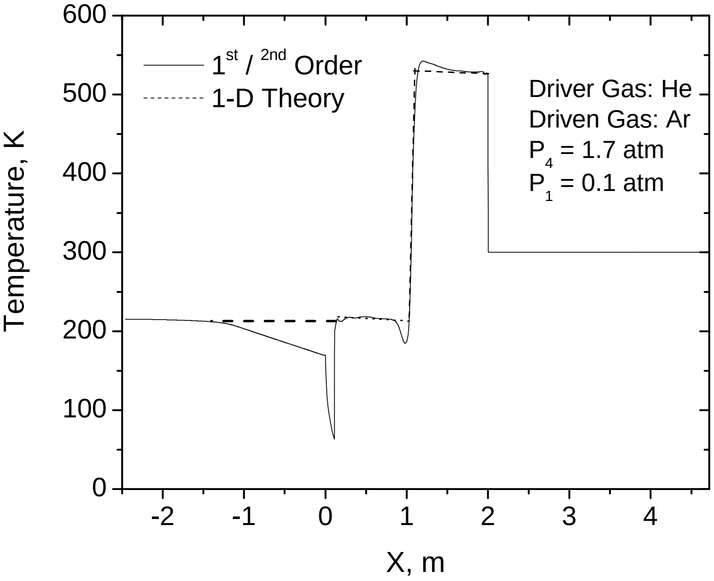

c)

Figure 11: a) Pressure, b) density, and c) temperature distribution along the tube axis. Simulations performed with 1st / 2nd order blending scheme. Comparison with 1-D inviscid theory is also shown.

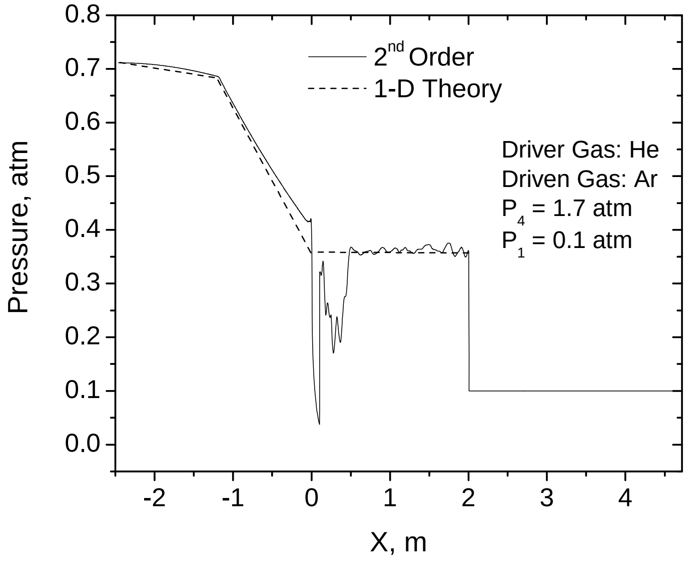
0.8
0.7
0.6
0.5
0.4
0.3
0.2
0.1
0.0
Pressure, atm
-2
-1
0
1
2
3
4
X, m
2nd Order
1-D Theory
Driver Gas: He
Driven Gas: Ar
P4 = 1.7 atm
P1 = 0.1 atm

a)

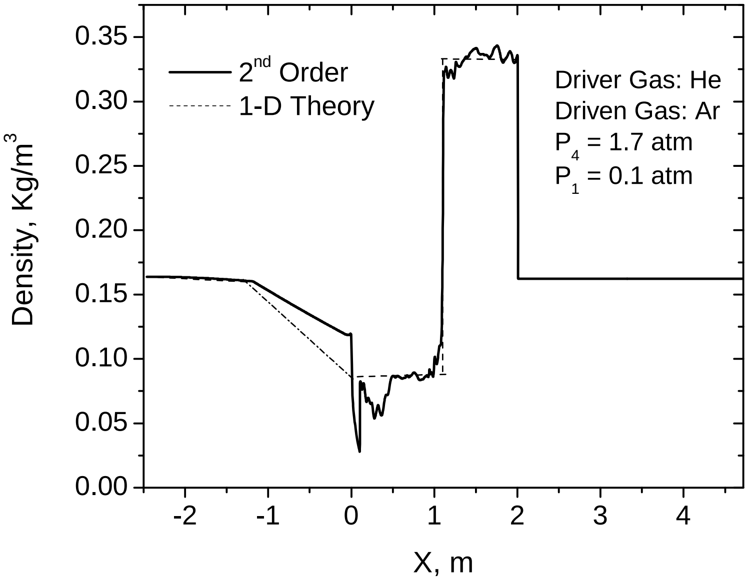
0.35
0.30
0.25
0.20
0.15
0.10
0.05
0.00
Density, Kg/m3
-2
-1
0
1
2
3
4
X, m
2nd Order
1-D Theory
Driver Gas: He
Driven Gas: Ar
P4 = 1.7 atm
P1 = 0.1 atm

b)

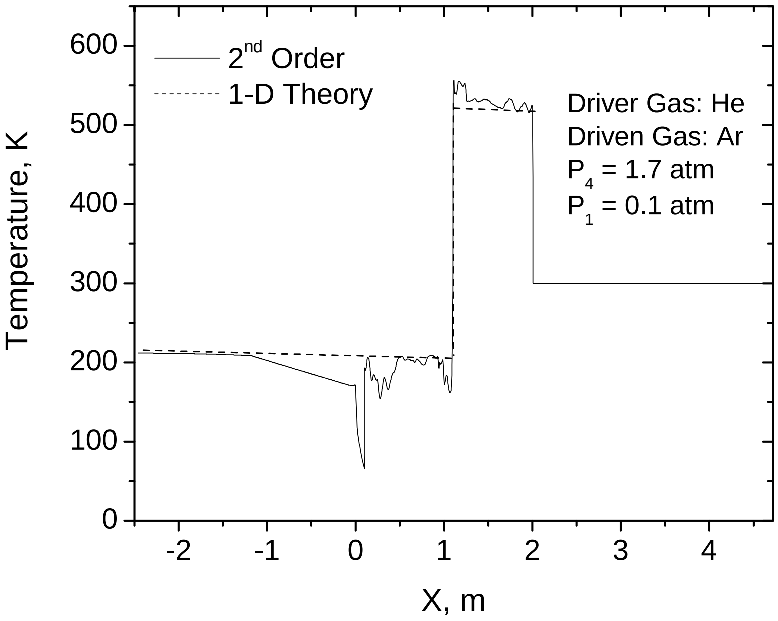

c)

Figure 12: a) Pressure, b) density, and c) temperature distribution along the tube axis. Simulations performed with 2^{nd} order scheme. Comparison with 1-D inviscid theory is also shown.

The high-resolution schemes correct the smearing effect at the contact surface but introduce unphysical behavior in the solution, across the shock and contact discontinuities. The oscillation disturbs the resolution of the flow field and generates further oscillations as the shock is propagating downstream. This phenomenon is attributed to the numerical issues associated with reconstructing higher-order gradients across the shock waves, contact discontinuities, and other varying parts of the solution which lead to overshoots and undershoots in the solution. The unphysical behavior is even more pronounced with the higher 3^{rd} order MUSCL scheme as shown in Figure 13.

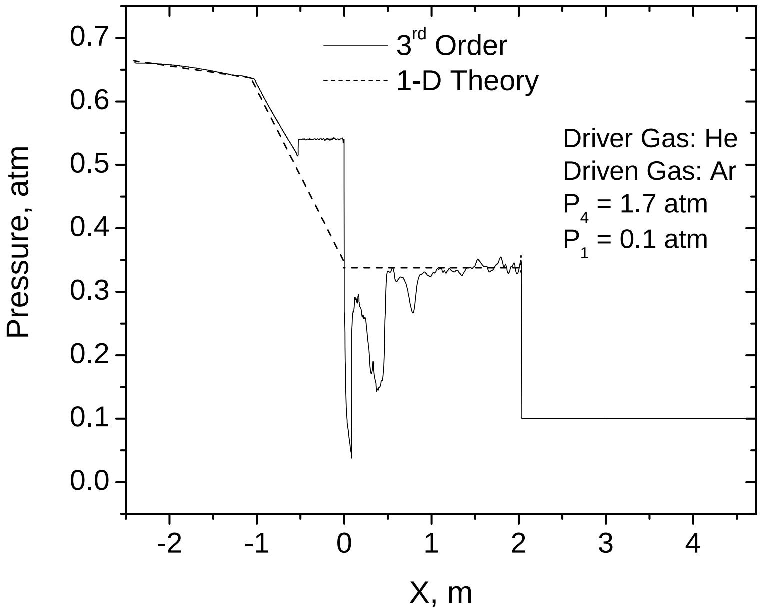
3rd Order
1-D Theory
Driver Gas: He
Driven Gas: Ar
P$_4$ = 1.7 atm
P$_1$ = 0.1 atm
Pressure, atm
0.7
0.6
0.5
0.4
0.3
0.2
0.1
0.0
-2
-1
0
1
2
3
4
X, m

a)

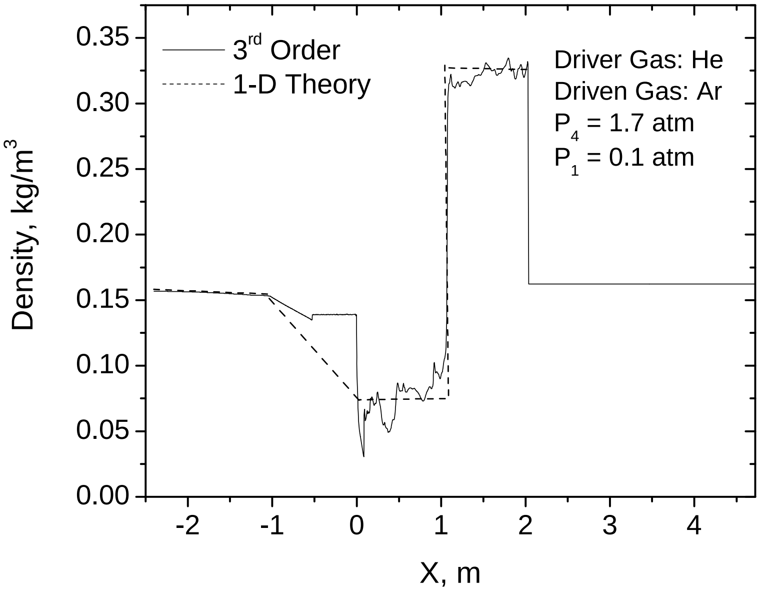
3rd Order
1-D Theory
Driver Gas: He
Driven Gas: Ar
P$_4$ = 1.7 atm
P$_1$ = 0.1 atm
Density, kg/m^3
0.35
0.30
0.25
0.20
0.15
0.10
0.05
0.00
-2
-1
0
1
2
3
4
X, m

b)

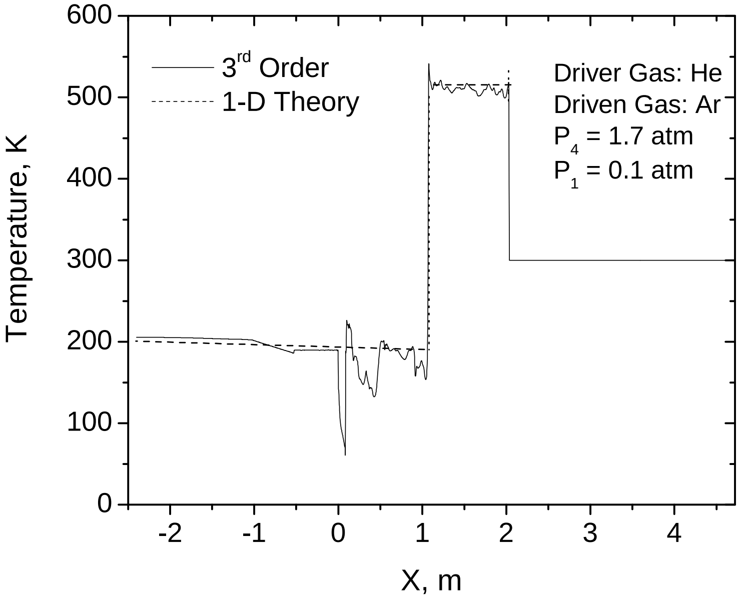

c)

Figure 13: a) Pressure, b) density, and c) temperature distribution along the tube axis. Simulations performed with 3rd order MUSCL scheme. Comparison with 1-D inviscid theory is also shown.

The oscillations seen in Figure 12 Figure 13 can be overcome with the use of flux limiters which make the numerical scheme TVD (81). TVD limiters are designed to switch the spatial discretization scheme down to a first-order accurate method in the vicinity of strong gradients. Away from the shocks and contact discontinuities, TVD simply does not operate, and higher-order discretization schemes are used in the majority of the flow while still capturing shock waves and strong gradients without obvious wiggles (80). The oscillations in the solution obtained with the 3rd order MUSCL scheme could be justified since the implemented scheme does not contain any TVD flux-limiter and therefore undershoot and overshoot in the vicinity of the contact discontinuities should be expected. However, when 2nd order accuracy is applied, TVD limiters are used by default, yet oscillations were present in the solution. It was speculated that these oscillations are not controlled properly with the inviscid model and a viscous model should resolve the flow fields better.

Parametric Shock-Tube Studies

Parametric Shock-Tube modeling studies were carried out in the inviscid baseline model for a wide range of test conditions behind the reflected shock wave as shown in Table 1. The numerical simulations for the inviscid model were performed with the 1st/2nd order blending scheme. This scheme was shown to be in good agreement with the 1-D inviscid theory compared to the high resolution schemes, in spite of a slight diffusion at the interface. In general, when shock discontinuities are present in the flow, it is virtually impossible to achieve a stable solution, free of unphysical numerical oscillations and nonlinear instabilities without introducing some numerical dissipation. A summary of the numerical simulations performed for the model validation study is given in Table 2, Table 3, and Table 4.

Table 1: Test gas mixtures and range of test conditions used in the validation study of the axi-symmetric model

Mixture number	Composition[a]	T_5 (K)	P_5 (atm)
1	100% Ar	683-2528	0.84-14.5
2	100% N_2	681-1980	0.7-1.2

[a] Driver gas is He

Table 2: Summary of numerical simulations performed with the axi-symmetric inviscid model. Conditions behind the reflected shock are $698 < T_5\,(K) < 2528$ and P_5 is near 1 atm. The driver gas is He and the driven gas is Ar.

T_5 (K)	P_5 (atm)	T_2 (K)	P_2 (atm)	P_1 (atm)	P_4 (atm)	P_4/P_1	Ms	Mr
698	0.99	481	0.416	0.141	1.5	10.64	1.6	1.45
701	1	482	0.417	0.141	1.6	11.35	1.6	1.45
706	1	484	0.42	0.141	1.7	12.06	1.61	1.46
719	1	490	0.43	0.141	1.8	12.77	1.628	1.472
800	1.31	525	0.45	0.141	2	14.18	1.73	1.526
900	0.99	568	0.346	0.086	1.9	22.09	1.85	1.583
918	1.03	577	0.35	0.086	2	23.26	1.87	1.59
980	1.91	600	0.5	0.141	2.5	17.73	1.91	1.62
1180	0.93	686	0.27	0.05	2	40.00	2.15	1.7
1187	1.62	690	0.45	0.086	2.5	29.07	2.16	1.7
1203	0.97	696	0.28	0.05	2.1	42.00	2.18	1.71
1214	0.98	701	0.284	0.05	2.15	43.00	2.19	1.71
1258	2.9	720	0.75	0.141	5	35.46	2.23	1.73
1480	1.35	810	0.35	0.05	2.5	50.00	2.44	1.79
1500	0.99	821	0.26	0.036	2.3	63.89	2.45	1.79
1568	1.06	849	0.28	0.036	2.5	69.44	2.51	1.81
1593	1.09	860	0.34	0.036	3	83.33	2.538	1.81
1596	1.51	860	0.39	0.05	3	60.00	2.54	1.817
1628	0.84	874	0.21	0.027	2	74.07	2.57	1.82
1690	2.84	900	0.6	0.086	6	69.77	2.62	1.83
1755	0.944	927	0.23	0.027	2.3	85.19	2.67	1.84
1783	0.96	939	0.239	0.027	2.4	88.89	2.697	1.854
1803	0.984	948	0.24	0.027	2.45	90.74	2.71	1.857
1953	1.1	1010	0.25	0.027	2.5	92.59	2.83	1.88
2097	1.22	1070	0.26	0.027	3	111.11	2.94	1.9
2528	1.58	1250	0.4	0.027	4	148.15	3.249	1.952

Table 3: Summary of numerical simulations performed with the axi-symmetric inviscid model. Conditions behind the reflected shock are $683 < T_5$ (K) < 1955 and $9.5 < P_5$ (atm) < 14.5. The driver gas is He and the driven gas is Ar

T_5 (K)	P_5 (atm)	T_2 (K)	P_2 (atm)	P_1 (atm)	P_4 (atm)	P_4/P_1	Ms	Mr
683	10.59	474	4.45	1.55	17	10.97	1.58	1.445
699	10.99	481	4.57	1.55	18	11.61	1.6	1.45
707	11.2	484	4.63	1.55	18.5	11.94	1.61	1.46
743	12.4	500	5	1.55	20	12.90	1.659	1.488
899	10.42	567	3.6	0.9	20	22.22	1.848	1.582
900	10.46	568	3.6	0.9	19.9	22.11	1.85	1.58
904	10.53	569	3.64	0.9	20	22.22	1.854	1.585
923	10.93	577	3.7	0.9	21	23.33	1.875	1.594
942	11.35	585	3.8	0.9	22	24.44	1.898	1.604
997	12.58	608	4	0.9	25	27.78	1.959	1.63
1094	14.8	650	4.5	0.9	30	33.33	2.064	1.671
1200	10	694	9.73	0.52	21.5	41.35	2.173	1.71
1206	10.1	697	2.95	0.52	22	42.31	2.179	1.712
1283	11.19	729	3.17	0.52	25	48.08	2.255	1.737
1337	11.95	752	3.32	0.52	27	51.92	2.306	1.752
1500	9.7	820	2.62	0.36	22.5	62.50	2.456	1.795
1510	14.49	825	3.8	0.52	35	67.31	2.465	1.797
1515	10	827	2.65	0.36	23	63.89	2.469	1.798
1550	10.4	841	2.72	0.36	24	66.67	2.5	1.8
1640	11.38	879	2.9	0.36	27	75.00	2.578	1.826
1735	12.39	919	3	0.36	30	83.33	2.658	1.845
1765	9.33	931.7	2.36	0.27	23	85.19	2.682	1.85
1800	9.8	946	2.41	0.27	24	88.89	2.711	1.856
1841	9.89	963	2.47	0.27	25	92.59	2.744	1.864
1889	13.93	980	3.37	0.36	35	97.22	2.775	1.87
1900	10.61	988	2.56	0.27	30	111.11	2.791	1.873
1916	10.44	994	2.58	0.27	27	100.00	2.803	1.876
1955	10.7	1011	2.64	0.27	28	103.70	2.834	1.882

Table 4: Summary of numerical simulations performed with the axi-symmetric inviscid model. Conditions behind the reflected shock are 681 < T_5 (K) < 1978 and P_5 near 1 atm. The driver gas is He and the driven gas is N_2

T_5 (K)	P_5 (atm)	T_2 (K)	P_2 (atm)	P_1 (atm)	P_4 (atm)	P_4/P_1	Ms	Mr
681	0.82	475	0.273	0.07	1.8	25.71	1.87	1.661
691	0.84	480	0.28	0.07	1.9	27.14	1.89	1.673
699	0.9	483	0.283	0.07	2.06	29.43	1.905	1.681
702	0.89	485	0.286	0.07	2.08	29.71	1.91	1.684
704	0.9	487	0.29	0.07	2.1	30.00	1.914	1.686
746	1	500	0.306	0.07	2.4	34.29	1.974	1.718
848	0.7	550	0.21	0.04	1.925	48.13	2.171	1.814
897	0.87	570	0.23	0.04	2.15	53.75	2.249	1.848
900	0.99	572	0.26	0.045	2.43	54.00	2.257	1.852
902	0.87	573	0.23	0.04	2.17	54.25	2.26	1.853
905	0.89	574	0.23	0.04	2.2	55.00	2.264	1.855
905	0.77	574	0.2	0.035	1.925	55.00	2.264	1.855
946	0.97	593	0.246	0.04	2.45	61.25	2.33	1.883
957	1	597	0.25	0.04	2.5	62.50	2.347	1.889
958	0.88	598	0.22	0.035	2.2	62.86	2.349	1.89
1077	0.94	650	0.218	0.03	2.4	80.00	2.529	1.959
1132	1.03	674	0.23	0.03	2.8	93.33	2.608	1.986
1136	1.04	676	0.234	0.03	3	100.00	2.614	1.988
1199	1.14	703	0.25	0.03	3.2	106.67	2.7	2.016
1214	1.17	710	0.254	0.03	3.3	110.00	2.722	2.023
1229	1.19	717	0.258	0.03	3.4	113.33	2.742	2.029
1433	0.98	807	0.2	0.02	3.2	160.00	3.006	2.105
1493	1.11	833	0.21	0.02	3.4	170.00	3.08	2.123
1500	1.11	837	0.219	0.02	3.42	171.00	3.088	2.125
1509	1.13	840	0.22	0.02	3.45	172.50	3.1	2.128
1525	1.14	847	0.223	0.02	3.5	175.00	3.118	2.133
1769	0.72	954	0.132	0.01	2.8	280.00	3.397	2.195
1800	0.74	967	0.135	0.01	2.92	292.00	3.43	2.2
1800	1.11	967	0.203	0.015	4.38	292.00	3.43	2.2
1809	0.75	971	0.136	0.01	2.95	295.00	3.44	2.2
1922	0.82	1021	0.146	0.01	3.4	340.00	3.56	2.226
1958	0.84	1036	0.149	0.01	3.55	355.00	3.598	2.233
1978	0.85	1045	0.15	0.01	3.65	365.00	3.619	2.237

Inviscid Model Validation

The numerical model is validated by comparing the flow properties predicted by the axi-symmetric model to the 1-D analytical solution of the ideal theory relations and the Sandia thermodynamic database. The ideal theory solution is based on the solution of multiple gas dynamics relations called the Rankine-Hugoniot relations. An example on how the flow properties in the shock tube can be calculated from the ideal theory is provided in the Appendix. Of most interest to the current study are the flow properties in the test region behind the reflected shock wave. Numerical simulations were performed for different initial conditions by varying the pressure ratio across the diaphragm to yield the incident-shock Mach number of interest. The flow properties behind the incident shock wave and subsequently in the test region behind the reflected shock are set by the strength of the incident-shock Mach number. The pressure ratio across the diaphragm, $P_4/P_{1,}$ versus Ms plots help guide future solutions and reduce the number of iterations needed to generate the test conditions of interest.

The incident-shock Mach number is determined from the shock velocity by recording the position of the shock front at two time steps. Figure 14 shows the pressure profiles behind the moving incident shock along the shock-tube axis at two time instances, t_1 and t_2. This method assumes no attenuation of the shock wave as is traverses the driven tube, which is valid for the inviscid solution herein.

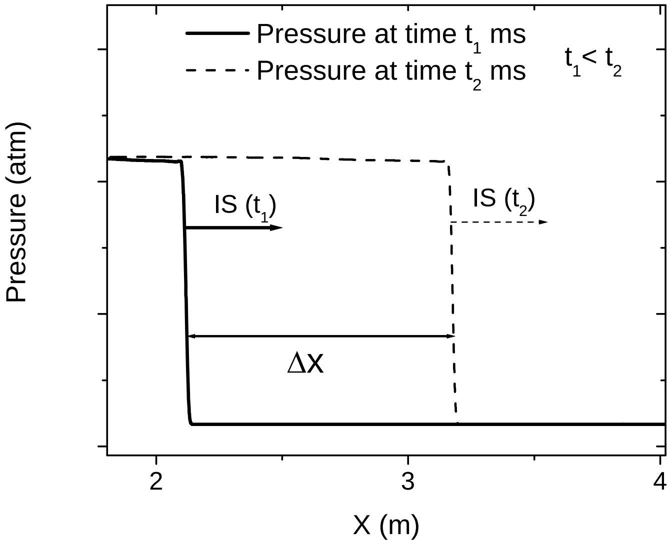

Figure 14: The incident-shock velocity is determined from the axial pressure profiles at two time instances t_1 and t_2. (IS : Incident Shock)

The shock velocity W_{IS} is calculated as such,

$$W_{IS} = \frac{\Delta x}{\Delta t} \tag{26}$$

The incident-shock Mach number is determined from,

$$M_{IS} = \frac{W_{IS}}{a_1} \tag{27}$$

The reflected-shock Mach number in the shock-fixed coordinate frame is given by,

$$M_{RS} = \frac{(W_{RS} + U_2)}{a_2} \tag{28}$$

Where U_2 is the gas velocity at state *2,* and a_1 and a_2 are the gas sound of speed at states *1* and *2*, respectively. Figure 15 reports the calculated incident-shock Mach numbers for different pressure ratios across the diaphragm in both a) Ar and b) N_2 test gases. In both cases, the driver gas is He. The axi-symmetric inviscid model predictions are compared to the solution of the 1-D ideal theory. Also shown in Figure 15 are the results of experiments from the shock tube of interest in the present study. The data points correspond to a range of diaphragms (aluminum and polycarbonate) and test pressures. The general trend between the data and inviscid model is quite good. As expected, the experimental data require more P_4/P_1 for a given Ms or T_5 due to viscous losses and real diaphragm opening times.

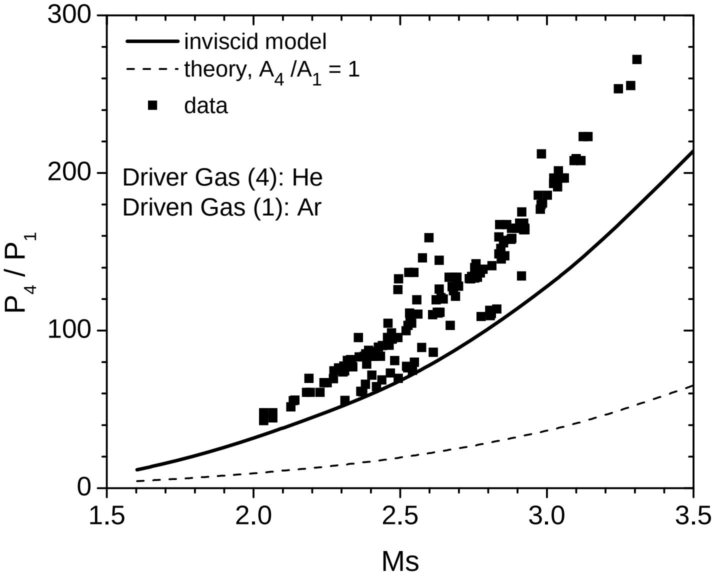

a)

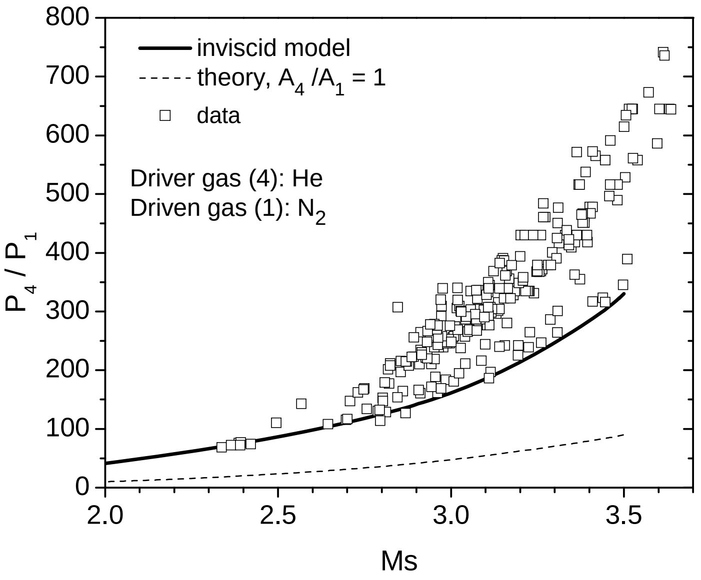

b)

Figure 15: Diaphragm pressure ratios P_4/P_1 required to generate incident-shock Mach numbers (Ms) between 1.6 – 3.5 in a) Ar and b) N_2 test gases. Data are from actual shock-tube experiments

The shock Mach numbers predicted by the axi-symmetric model are lower than the ideal theory by approximately 25% for a given pressure ratio across the diaphragm. As a result, the flow properties are also under-predicted. This is illustrated in Figure 16 which gives the P_4/P_1 ratio as a function of T_5, the temperature behind the reflected shock, in both a) Ar and b) N_2 test gases. As expected, the model under-predicts T_5 by 25%.

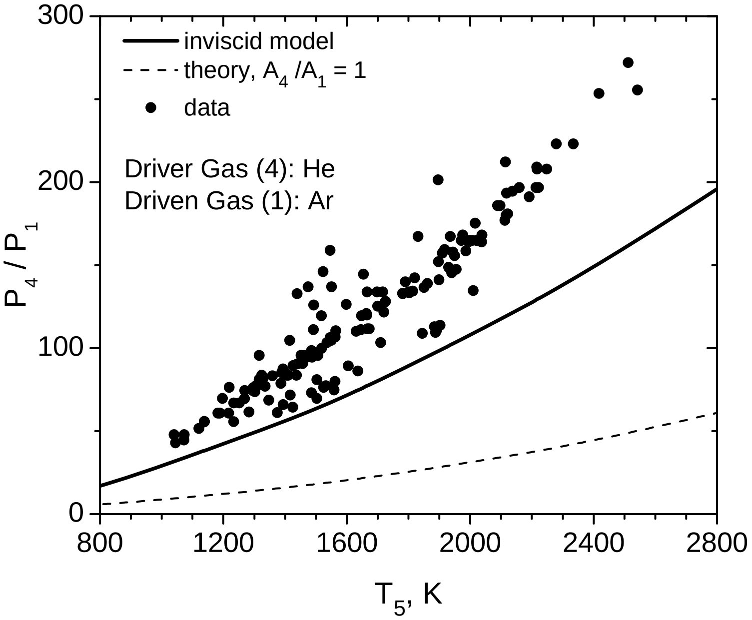

a)

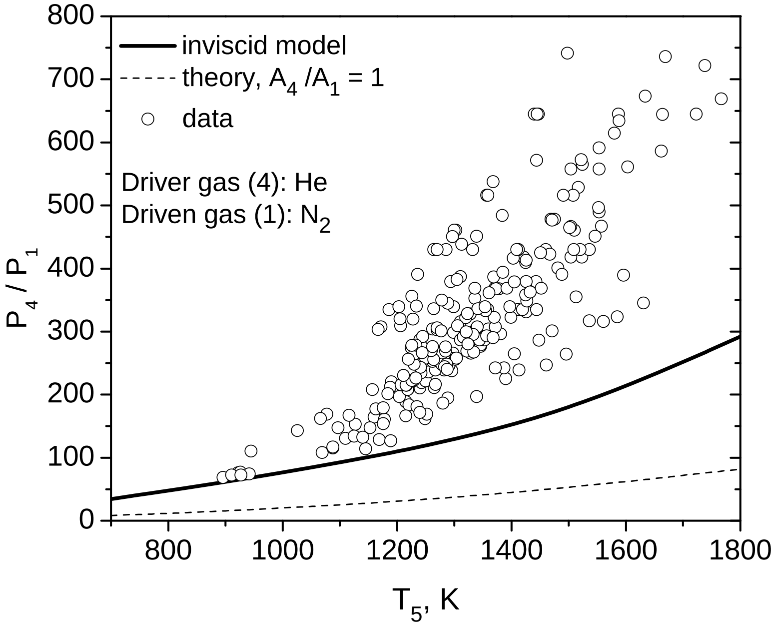

b)

Figure 16. Diaphragm pressure ratios P_4/P_1 required to generate temperature conditions of 650 K – 2800 K in a) Ar and b) N_2 test gases; driver gas is He. Data are from actual shock-tube experiments

In studies reported elsewhere (4) (5) (6) (7) (92), it was found that the modeled and experimentally measured shock velocities are in close agreement with the ideal theory for pressure ratios across the diaphragm below 10^3 while the ideal theory under-predicts the experimental velocities for pressure ratios above 10^3 by 20%. The high experimental velocities were associated with the wave processes which occur during the gradual opening of the diaphragm. White (4) and Ikui et al. (93) developed 1-D theory models for the constant-area shock tube which predict higher maximum shock speeds than the ideal shock tube model for pressure ratios above 10^3 and velocities in agreement with the ideal theory for pressure ratios below 10^3. The models were developed under the assumption that unsteady isentropic waves are formed in the driven section during the gradual opening of the diaphragm. The compression waves coalesce into a shock wave at some distance downstream of the diaphragm and the shock wave is successively accelerated by other compression waves.

The under-prediction of shock velocities by the ideal models was also reported in 1-D (94) and multi-dimensional (8) (36) (37) (38) (73) numerical studies which incorporated a finite time model for the opening of the diaphragm. The higher-than-ideal shock velocities were explained by a combination of mechanisms including heating of driver gas during pressurization, finite opening time of the diaphragm, multi-dimensional effects (5), and an entropy rise through the oblique shock structure which exists temporarily downstream of the diaphragm while it is opening (37).

In this study, the shock velocities predicted by the axi-symmetric model are below the ideal theory by up to 25% for pressure ratios raging from 5 to 100 for Ar test gas and from 25 to 300 for N_2 test gas. According to the one-D theories of White (4) and Ikui et al. (93), the shock velocities should be in close agreement with the ideal theory for pressure ratios below 10^3. The disagreement of the current model with the ideal theory and modeling results of other studies can be explained by the following. First, the current model does not take into account the gradual opening of the diaphragm which causes an acceleration of the shock wave downstream the diaphragm. Second, the ideal theories of White and Ikui et al. (93) and the experimental and simulation studies reported elsewhere (4) (5) (7) (8) (36) (38) (73) (92) (93) (94) were based on constant-area tubes, while the current shock-tube model is comprised of a diverging/conical section downstream of the diaphragm. Alpher and White (95)developed a modified ideal theory to account for unequal area changes in the diaphragm, however it was based on shock tubes with a converging section at the diaphragm and this model produces even stronger shocks and higher velocities than the constant area tubes. Therefore, to produce the same shock speed as the ideal theory, higher pressure ratios across the diaphragm have to be applied because of the area increase at the diaphragm section.

It is important to note when validating the model with the analytical solution or experimental data that the shock Mach number and flow properties predicted from the axi-symmetric model have to match the analytical solution and experimental measurements regardless of the pressure ratio across the diaphragm. It is not expected that the same pressure ratio between the model and the analytical solution or experiment will yield the same incident shock Mach number and therefore the same flow conditions. That is, regardless of the driver pressure required to produce a given shock Mach number, once the shock is formed, the properties behind it must match ideal theory.

Provided in Figure 17 are the predicted temperatures behind the reflected shock for a range of calculated incident-shock Mach numbers from the axi-symmetric model in a) Ar and b) N_2 test gases. The 1-D theory results are also given. The results show that there is a good agreement between the axi-symmetric inviscid model and the 1-D ideal theory as expected, so the curves are coincident.

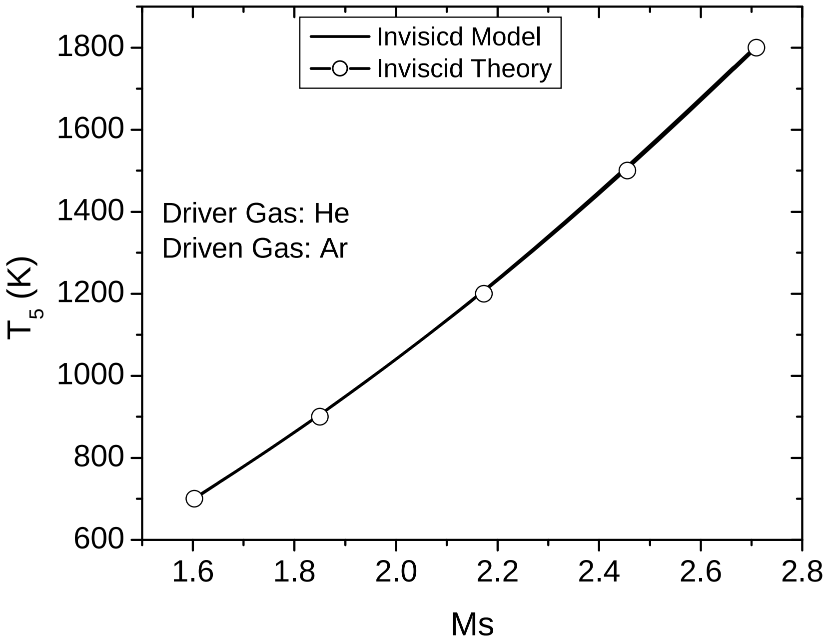

a)

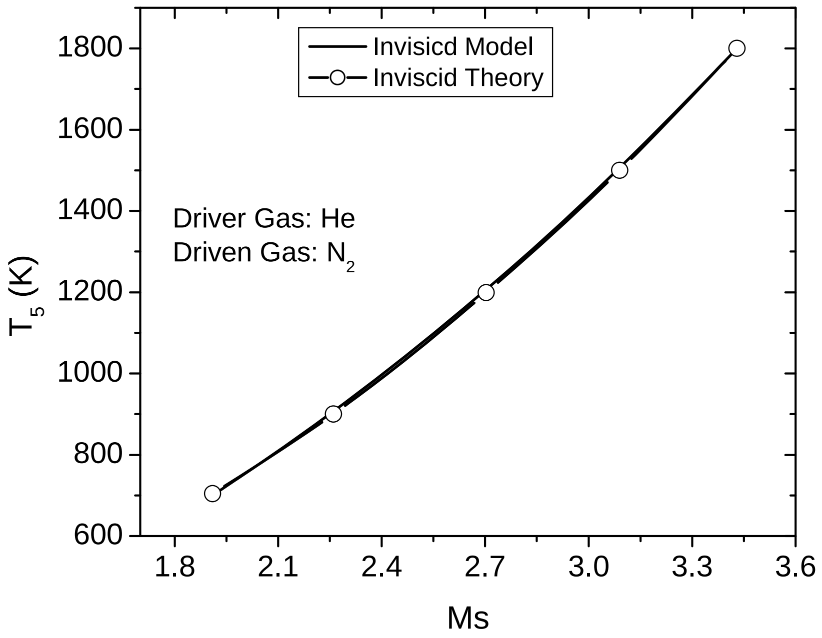

b)

Figure 17: Temperature behind reflected shock (T_5) versus incident shock Mach number (Ms). Numerical results are for a) Ar and b) N_2 test gases. The T_5 and Ms predicted by the model are in good agreement with the 1-D theory solution

CHAPTER FOUR: VISCOUS SOLUTION

Introduction

In the previous chapter, the flow was assumed to be inviscid, neglecting the effects of the viscous boundary layer. Overall, the inviscid model has proven to be capable of resolving the shock and contact discontinuities and accurately simulating the flow evolution from the rupture of the diaphragm all the way to the end of the shock-tube experiment. However, when shock-tube non-idealities need to be modeled to quantify their impact on the flow uniformity in the test region, viscous effects have to be taken into consideration. In this respect, this chapter introduces a viscous model of the shock tube which simulates the non-ideal behaviors in the shock-tube flow fields, the flow non-idealities in the shock-Tube nozzle, heat transfer effects from the hot gas to the shock-tube side wall, contact surface/reflected shock interactions, reflected shock/boundary layer interaction or what is known as bifurcation, and finally driver gas contamination.

As a first step towards modeling the non-idealities in the shock tube, the boundary layer is assumed as laminar, and a conjugate heat transfer model is incorporated to account for the heat losses from the test region hot gas to the cold shock-tube walls. The accuracy of the simulations is enhanced by modeling the boundary layer in the shock tube as turbulent and the k-ε realizable turbulence model was used in some cases. For the turbulent cases, the turbulent boundary layer mesh was carefully treated, and the enhanced wall treatments were utilized to ensure a y+ value close to 1 in order to guarantee the flow structure is resolved all the way to the viscous sub-layer.

Governing Equations

Navier-Stokes Equations

The conservation of momentum is described by:

$$\frac{\partial(\rho\vec{v})}{\partial t} + \nabla.(\rho\vec{v}\vec{v}) = -\nabla P + \nabla.(\bar{\bar{\tau}}) + \rho\vec{g} + \vec{F} \tag{29}$$

Where P is the static pressure, $\rho\vec{g}$ is the gravitational body force, $\vec{F}$ is the external body forces, and $\bar{\bar{\tau}}$ is the stress tensor which is given by:

$$\bar{\bar{\tau}} = \mu\left[(\nabla\vec{v} + \nabla\vec{v}^{T}) - \frac{2}{3}\nabla.\vec{v}\, I\right] \tag{30}$$

Where μ is the molecular viscosity, I is the unit tensor, and $\frac{2}{3}\nabla.\vec{v}\, I$ is the effect of volume dilation. For axi-symmetric models, the conservation of momentum in the axial and radial directions is described by Eqns. (31) and (32), respectively,

$$\begin{aligned} x - mom\text{:}\ & \frac{\partial}{\partial t}(\rho v_x) + \frac{1}{r}\frac{\partial}{\partial x}(r\rho v_x v_x) + \frac{1}{r}\frac{\partial}{\partial r}(r\rho v_r v_x) \\ & = -\frac{\partial P}{\partial x} + \frac{1}{r}\frac{\partial}{\partial x}\left[r\mu\left(2\frac{\partial v_x}{\partial x}\right) - \frac{2}{3}(\nabla.\vec{v})\right] + \frac{1}{r}\frac{\partial}{\partial r}\left[r\mu\left(\frac{\partial v_x}{\partial r} + \frac{\partial v_r}{\partial x}\right)\right] + F_x \end{aligned} \tag{31}$$

$$\begin{aligned} r - mom\text{:}\ & \frac{\partial}{\partial t}(\rho v_r) + \frac{1}{r}\frac{\partial}{\partial x}(r\rho v_x v_r) + \frac{1}{r}\frac{\partial}{\partial r}(r\rho v_r v_r) \\ & = -\frac{\partial P}{\partial r} + \frac{1}{r}\frac{\partial}{\partial r}\left[r\mu\left(2\frac{\partial v_r}{\partial r}\right) - \frac{2}{3}(\nabla.\vec{v})\right] + \frac{1}{r}\frac{\partial}{\partial x}\left[r\mu\left(\frac{\partial v_r}{\partial x} + \frac{\partial v_x}{\partial r}\right)\right] - 2\mu\frac{v_r}{r^2} \\ & + \frac{2}{3}\frac{\mu}{r}(\nabla.\vec{v}) + \rho\frac{{v_r}^2}{r} + F_r \end{aligned} \tag{32}$$

Where x is the axial coordinate, r is the radial coordinate, ϑ_x is the axial velocity, and $\vartheta_r$is the radial velocity.

When the flow is turbulent, the solution variables in the Navier-Stokes equations are decomposed into the mean and fluctuating components where the mean components are ensemble-averaged or time-averaged. The velocity component is then given by:

$$u_i = \bar{u}_i + u'_i \tag{33}$$

Where $\bar{u}_i$ and u'_i are the mean and fluctuating velocity components. Similarly, other scalar properties are expressed as such,

$$\emptyset = \overline{\emptyset} + \emptyset' \tag{34}$$

And $\emptyset$ represents any scalar quantity. The velocity component u_i is then substituted into the continuity and momentum equations to yield the ensemble-averaged momentum equations which can be written in Cartesian tensor form as follow,

$$\frac{\partial \rho}{\partial t} + \frac{\partial}{\partial x_i}(\rho u_i) = 0 \tag{35}$$

$$\frac{\partial(\rho u_i)}{\partial t} + \frac{\partial}{\partial x_j} = \frac{\partial}{\partial x_j}\left[\mu\left(\frac{\partial u_i}{\partial x_j} + \frac{\partial u_j}{\partial x_i}\right) - \frac{2}{3}\delta_{ij}\frac{\partial u_l}{\partial x_l}\right] + \frac{\partial}{\partial x_j}\left(-\rho\overline{u_i' u_j'}\right) - \frac{\partial P}{\partial x_i} \tag{36}$$

Eqs. (35) and (36) are called Reynolds-Averaged Navier-Stokes (RANS) equations. A new term appears on the right hand side of Eq. (36) given by $-\rho\overline{u_i' u_j'}$ and represents the Reynolds stresses. The Reynolds-averaged approach requires the modeling of the Reynolds stresses in order to close the momentum equation. This is achieved with the Boussineq hypothesis, proposed by boussinesq in 1877, which relates the Reynolds stresses to the mean velocity gradients:

$$-\rho\overline{u_i' u_j'} = \mu_t\left(\frac{\partial u_i}{\partial x_j} + \frac{\partial u_j}{\partial x_i}\right) - \frac{2}{3}\left(\rho k + \mu_t\frac{\partial u_i}{\partial x_k}\right)\delta_{ij} \tag{37}$$

Where μ_t is the turbulent viscosity or the eddy viscosity. A similar assumption can be used for the turbulent fluctuation terms that appear in the scalar transport equations. Consider a scalar property $\emptyset = \overline{\emptyset} + \emptyset'$,

$$-\rho\overline{u_i'\emptyset'} = \Gamma_t \frac{\partial \emptyset}{\partial x_i} \tag{38}$$

Where Γ_t is the turbulent diffusivity. The turbulent diffusivity is calculated from the turbulent viscosity μ_t, using a model constant called the turbulent Schmidt number σ_t,

$$\sigma_t = \frac{\mu_t}{\Gamma_t} \tag{39}$$

Experiments have shown that the turbulent Schmidt number is nearly constant with typical values between 0.7 and 1.

Energy Equation

The energy transport equation for viscous flows is given by:

$$\frac{\partial(\rho E)}{\partial t} + \nabla.[\vec{V}(\rho E + p)] = \nabla.[k_{eff}\nabla T - \sum_j h_j J_j + (\bar{\bar{\tau}}_{eff}.\vec{V})] + S_h \tag{40}$$

Where, $E = h - \frac{P}{\rho} + \frac{V^2}{2}$ is defined per unit mass in terms of pressure work and kinetic energy. The first three terms on the right hand side of equation represent energy transfer due to conduction, species diffusion, and viscous dissipation, respectively. The heat flux due to conduction is given by:

$$\nabla.(k_{eff}\nabla T) \tag{41}$$

Where k_{eff} is the effective thermal conductivity and is equal to the local thermal conductivity plus the turbulent thermal conductivity,

$$k_{eff} = k + k_t \tag{42}$$

For the standard and realizable κ–ε models, the effective thermal conductivity is given by,

$$k_{eff} = k + \frac{c_p \mu_t}{Pr_t} \tag{43}$$

The default value of the turbulent Prandtl number is 0.85 and μ_t is the turbulent viscosity. The viscous dissipation term is given by,

$$\nabla.(\bar{\bar{\tau}}_{eff}.\vec{V}) \tag{44}$$

Also called the viscous heating, describes the thermal energy created by viscous shear in the flow. The species diffusion term is given by,

$$\nabla.\sum_j h_j J_j \tag{45}$$

And includes the effect of enthalpy transport due to species diffusion. J_j is the diffusion flux of species j is given by Eq. (46) for laminar flows and by Eq. (47) for turbulent flows,

$$\vec{J}_j = -(\rho D_{j,m})\nabla Y_j \tag{46}$$

$$\vec{J}_j = -\left(\rho D_{j,m} + \frac{\mu_t}{Sc_t}\right)\nabla Y_j \tag{47}$$

Where $D_{j,m}$ is the mass diffusion coefficient for species j and Sc_t is the turbulent Schmidt number and is given by,

$$Sc_t = \frac{\mu_t}{\rho D_t} \tag{48}$$

μ_t is the turbulent viscosity, and D_t is the turbulent diffusivity. The default Sc_t is 0.7. The energy source S_h is only included when reactive flow is modeled. In the solid region, the conduction of heat is modeled by the following energy equation,

$$\frac{\partial(\rho h)}{\partial t} + \nabla.[\vec{V}(h)] = \nabla.(K\nabla T) + S_h \tag{49}$$

Where S_h is the volumetric heat source and h is the sensible enthalpy given by,

$$h = \int_{T_{ref}}^{T} c_p dT \tag{50}$$

With a T_{ref} of 300 K. The second term on the left hand side of equation 2 represents convective energy transfer due to the motion in the solid. In the model considered herein, the convective term in the solid does not apply.

Turbulence Modeling

The turbulence models which use the Boussineq hypothesis include the one equation Spalart-Allmaras model (96), the two-equation k-ε models including the standard k-ε model (97), the RNG k-ε model (98), and the Realizable k-ε model (99). Other improved two-equation models include the standard k-ω model (100) and the SST k-ω model (101). This approach is widely used due to the low computational cost associated with modeling the turbulent viscosity, however the Boussineq hypothesis assumes μ_t to be isotropic. This assumption is not necessarily true especially when strong separation and swirl are present in the flow. The alternative approach is to solve transport equations for each of the terms in the Reynolds stress tensor ending up with more transport equations to solve and thereby increasing the computational cost. The turbulent Reynolds-Stress model (102) adopts such approach and is often called a second order closure. Although it can model anisotropy turbulence, the increased computational efforts are not justified when simpler models which use the Boussineq Hypothesis yield accurate results except in the cases of highly swirling flows and stress driven secondary flows. Table 5 lists the different RANS turbulence models available in FLUENT and the characteristics of each model (103). It is important to note that all of the turbulence models displayed in Table 5 were adopted to investigate the impact of the different turbulence models on the shock tube flow field properties. Although the computational efforts increased with the SST and RSM models, the solution behaved independently of the turbulence models. It was then decided that the $\kappa-\varepsilon$ realizable model would be most appropriate for modeling the turbulence in the shock tube flow fields within an acceptable time frame.

Table 5: RANS turbulence models available in FLUENT (103)

RANS Model	**Characteristics**
Spalart-Allmaras	➢ One Equation Model
Standard k-ε	➢ Two Equation Model
RNG k-ε	➢ Variant of standard k-ε ➢ Additional term in ε equation for interaction between turbulence dissipation and mean shear ➢ Analytical formula for turbulent Prandtl number ➢ Differential formula for effective viscosity
Realizable k-ε	➢ Variant of standard k-ε ➢ New formulation for turbulent viscosity ➢ New transport equation for ε ➢ Variable C_μ instead of constant
Standard k-ω	➢ Two equation model ➢ Solves for k and ω, the specific dissipation rate
SST k-ω	➢ Variant of Standard k-ω model ➢ Acts as the k-ω in near wall region ➢ Acts as standard k-ε in the free stream

Reynolds Stress Model (RSM)	➢ Five equation model ➢ Accounts for history, transport, and anisotropy of turbulent stresses ➢ Accounts for streamline curvature, swirl, rotation and high strain rates

In addition to the Reynolds Stress Model (RSM) which models anisotropic turbulence, Large Eddy Simulation (LES) model is based on space filtered equations and directly resolves the large eddies. It requires extensive computational efforts in addition to a very fine mesh. Time dependent calculations are performed and the effect of the small eddies on the flow pattern is taken into account with a “subgrid model” of which many styles are available. Figure 18 shows the difference between RANS, LES and DNS approaches in resolving the eddies, the flux of energy, and the dissipation of energy. On the other hand, in Direct Numerical Simulation (DNS), the Navier Stokes equations are solved numerically and the range of the turbulent spatial and temporal scales are resolved from the large scale eddies all the way to the smallest dissipative scales. DNS requires the most computational efforts which makes it not practical in the computational fluid dynamics world, while RANS requires the least computational effort. RANS methods, although computationally affordable, provide averaged results which are inferior to LES results, for this reason, zonal approaches are often adopted with LES modeling where LES is adopted in the core region and RANS or other empirically-based models replacing LES in the wall region.

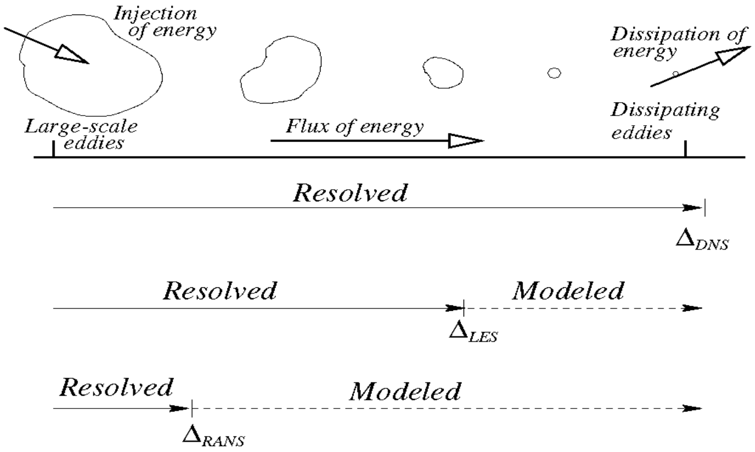

Figure 18: The difference between RANS, LES and DNS approaches in resolving the eddies, the flux of energy, and the dissipation of energy (104)

Wall treatment in turbulent modeling

The k-ε , RSM, and LES models are valid for turbulent flows far from the wall. Very close to the wall, near wall modeling procedures are required based on the region that needs to be resolved. The near-wall region in turbulent flows can be subdivided into three layers; The viscous sublayer which is the innermost layer where the flow properties are characterized by being quasi-laminar; the fully turbulent region or log layer characterized by equally important effects of molecular viscosity and turbulence; and finally the outer layer where turbulence plays a major role. Figure 19 illustrates these subdivisions of the near-wall region, plotted in semi-log coordinates.

There exist two different ways to model the near wall region. When the viscous sub-layer cannot be resolved, empirical formulas called wall functions are used to bridge the viscous region near the wall with the fully turbulent region away from the wall. The grid requirement for the near wall approach is such that the wall unit y+ falls between a value of 30 and 300. The first grid point should be placed in the log layer with at least ten points in the boundary layer. The y+ is given by,

$$y^+ = \frac{\rho \mu_\tau y}{\mu} \tag{51}$$

Where μ_τ is the friction velocity and it is defined by:

$$\mu_\tau = \sqrt{(\tau_w/\mu} \tag{52}$$

On the other hand, when the viscous sub-layer needs to be resolved, the enhanced or near-wall modeling approach is used such that the mesh is finer near the wall. In this case the y+ value needs to be close to 1 with an acceptable value of less than 5. The first grid point should be placed at y+ = 1 with at least ten grid points placed in the buffer and sub-layer. Figure 19 illustrates the different regions near the wall and their corresponding y+ values.

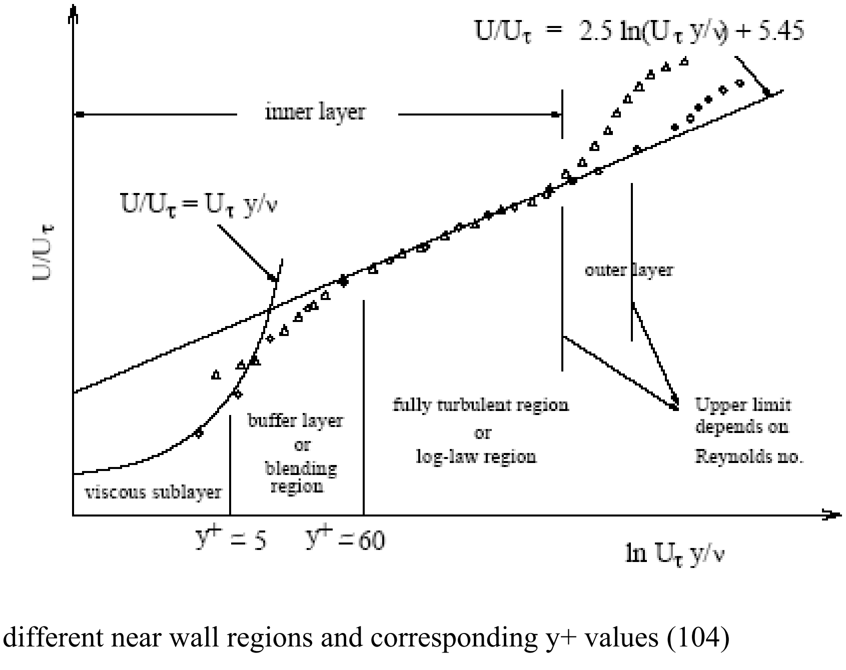

Figure 19: The different near wall regions and corresponding y+ values (104)

Simulations of Shock-Tube Non-Idealities

Shock-Tube Nozzle Section

There exist very few numerical studies which modeled the propagation of the shock wave in an area-changing shock tube (71) (105) (106) (107). In particular, Chang and Kim (55) performed numerical simulations in a circular shock tube suddenly expanded three times the original diameter. Upon the passage of the wave from the small diameter tube to the expanded tube, the flow structure became much more complicated due to the nonlinear interaction of the many flow elements confined in a limited flow passage, and a blast jet structure was produced. The complicated dynamics were associated with blast waves which then transformed into a planar shock wave further downstream. The pressure drop in the shock-tube nozzle illustrated in Figure 20 is attributed to the nonlinear transient interactions in the nozzle section of the shock tube, which are physical and not an artifact of the numerical scheme utilized herein.

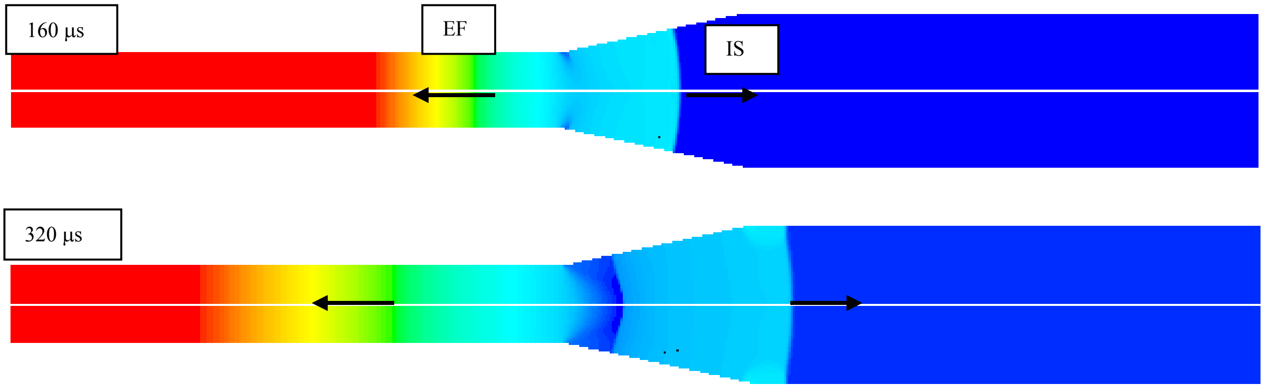

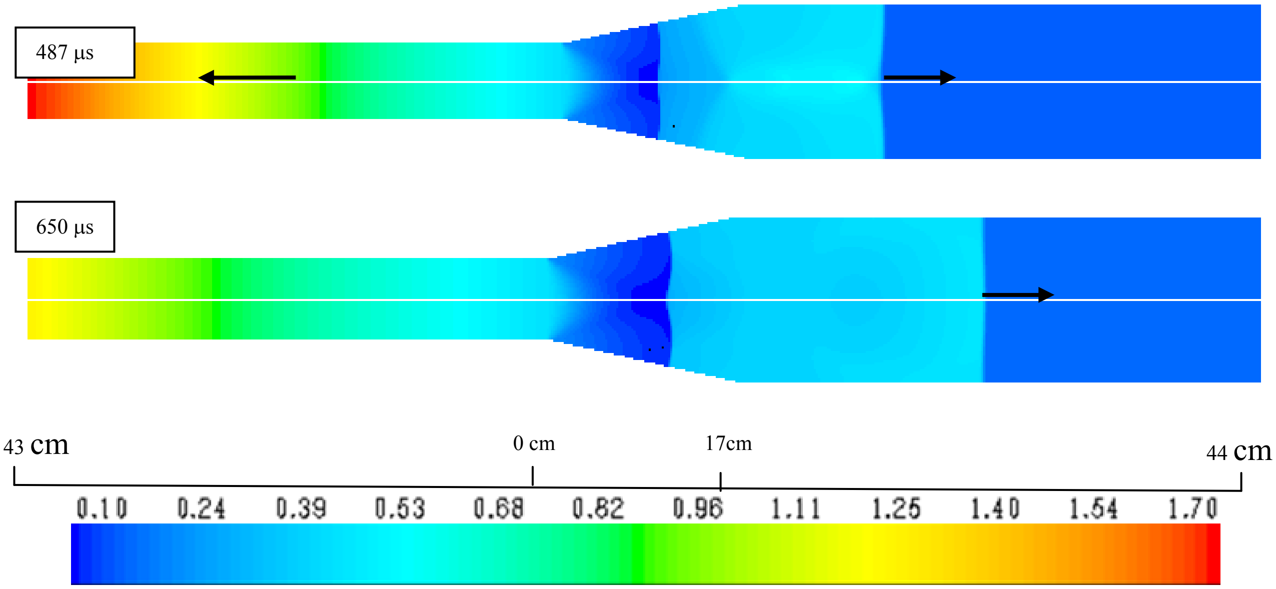

Figure 20: Sequence of pressure contours (atm) showing the propagation of the incident shock wave in the shock-tube nozzle. First, pressure in the nozzle increases due to passage of the incident shock wave and induced flow then pressure drops due to flow over-expansion in the nozzle. Time instances are given in the upper right corner of each frame. IS = Incident shock Wave, EF = Expansion Fan

The shock formation and transmission occur at a much faster rate than the pressure wave propagation leading to an over-expanded flow region lagging behind the incident shock wave. This causes a pressure drop in the nozzle section of the shock tube. The time-accurate solutions are able to reproduce this transient phenomenon and model the pressure drop accordingly. Figure 21 and Figure 22 illustrate this process and show the averaged static pressure and Mach number profiles, respectively, monitored versus time at a location 10 cm downstream of the diaphragm. The total length of the diverging nozzle is about 17 cm long. Immediately following the diaphragm rupture, the pressure rises to 0.48 atm due to the passage of the incident shock wave followed by a quasi-sharp drop to 0.07 atm due to the sudden over-expansion of the entrained flow behind the incident shock. This is equivalent to a pressure drop of 82%. The pressure in the conical nozzle remains constant until the expansion fan arrives at the diaphragm location at a time of 7 ms with an under-expanded flow relative to the existing flow in the conical nozzle. This causes the pressure to increase and the velocity to decrease and thus reducing the overall pressure drop in the conical nozzle section from 82% to 52%.

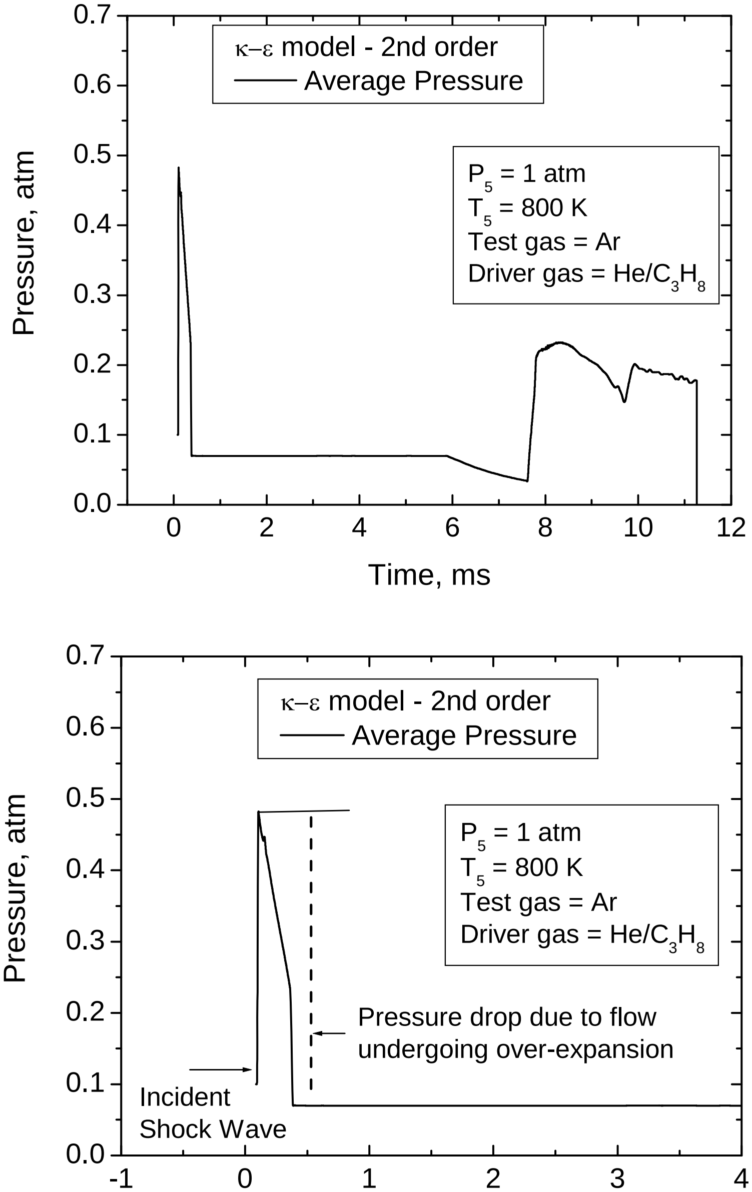

Figure 21: Monitored averaged static pressure at a location 10 cm downstream of the diaphragm. There is a pressure increase at Time = 0+ due to incident shock wave formation followed by a pressure drop due to flow undergoing expansion in the nozzle section. The bottom figure is a close-up of the top figure

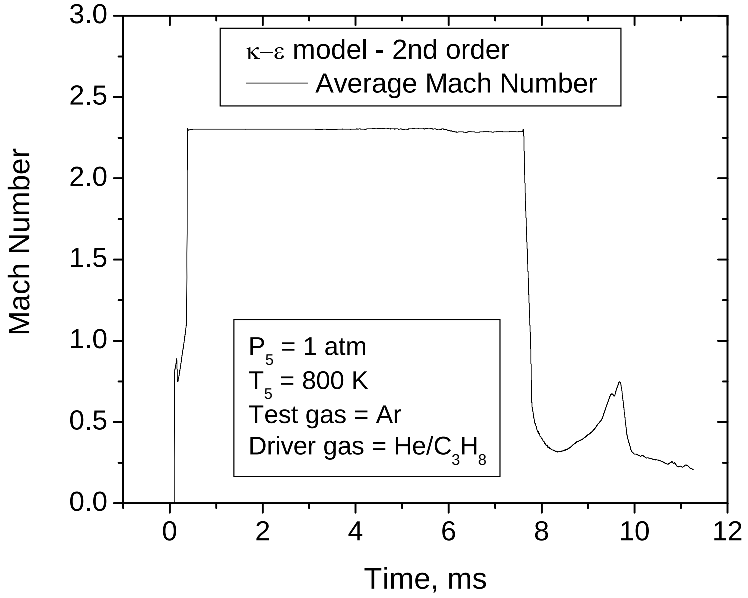

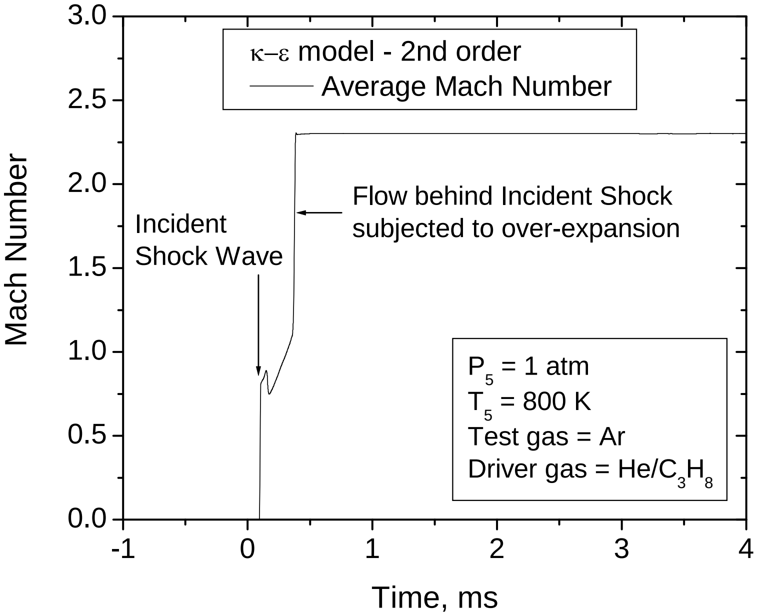

Figure 22: Monitored averaged Mach Number at a location 10 cm downstream of the diaphragm. Initially, the Mach number increases due to incident shock wave passage then the flow is further accelerated due to over-expansion in the nozzle downstream the diaphragm. The bottom figure is a close-up of the top figure

To further confirm that these flow instabilities in the nozzle section are related to the transient nonlinear flow physics in the nozzle section, numerical results were obtained for a constant-area tube with the 2nd order scheme. Figure 23 shows the density (a) and pressure (b) profiles along the shock-tube axis. Note that the solution is completely free of the transient nonlinear effects in the nozzle section, and the pressure drop previously noticed with the diverging-area shock tube is totally suppressed. This confirms that the pressure drop in the nozzle section is a physical behavior which should not be misinterpreted for the nonphysical spurious oscillations attributed to the accuracy of the numerical scheme employed.

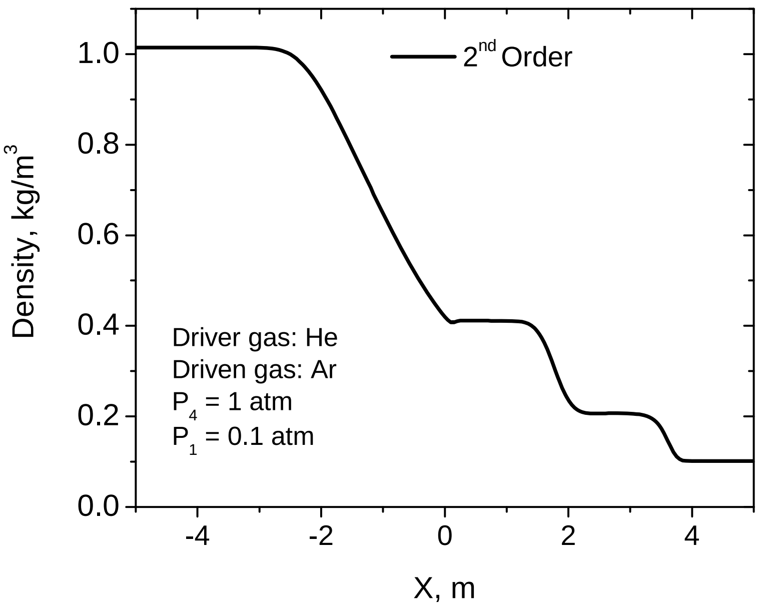

a)

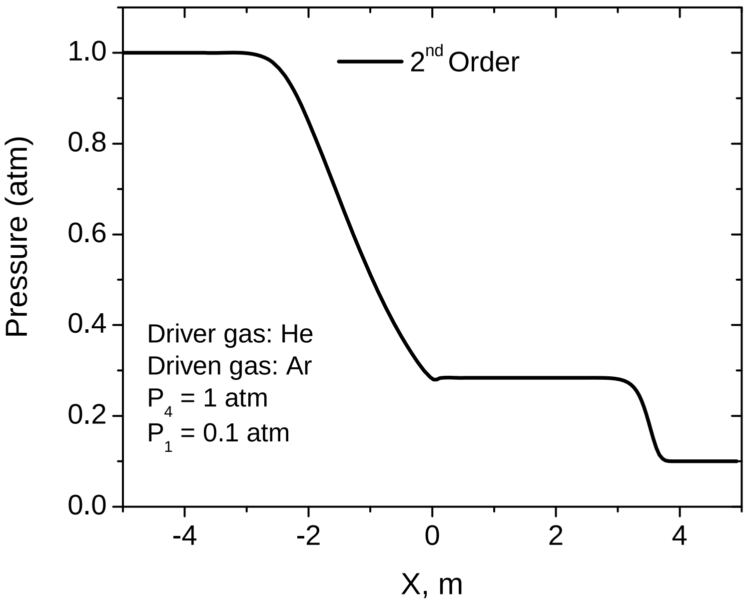

b)

Figure 23: a) Density and b) pressure distribution along the axis of a constant area shock tube.

Heat Transfer Effects

Ideally, the endwall region behind the reflected shock wave is assumed to be isothermal before chemical reaction takes place. However in real shock tube experiments and especially when the test times are relatively long, the isothermal assumption becomes invalid, and heat losses from the hot gas and the cold wall become important and should be accounted for in shock tube modeling studies.

Background

Heat transfer in shock tubes has been investigated experimentally (23) (24) (25) (108) (109) (110) and the effect of the thermal boundary layer on the reflected shock structure and the flow properties near the endwall region have been analyzed theoretically (29) (30) (31) (32) and numerically based on the gas kinetic models (BGK) (33) and the 1-D Navier Stokes equations (34) (35).

Corey Frazier studied heat loss from the hot gas to the cold shock-tube wall behind the reflected shock wave following a pure conduction solution. The flow behind the reflected shock was assumed to be stationary and effects of boundary layer reflected shock interactions were ignored. A two-dimensional model was used to analyze the heat transfer over the entire endwall region under long test times and high pressure conditions. Results showed that even at the worst test conditions of higher temperatures and low pressures where the boundary layer is the thickest and at test times as long as 20 ms, the boundary layer is well outside the hot gas endwall region (32).

The Modeling of the interaction of the incident shock with the endwall at varying temperatures has been investigated in a number of studies. All are based on the Navier-Stokes equations. Goldsworthy (29) made an analysis for the flow region behind the reflected shock waves using boundary layer theory. Clarke (30) modeled the interaction of the incident shock with the endwall and analyzed the thermal boundary problem by applying the method of matched asymptotic expansions. The temperature jump conditions with accommodation effects were included. In particular the Thermal Raleigh Problem (TRP) was investigated**.** It refers to the reaction of a compressible semi-infinite fluid adjacent to a solid impermeable wall. Equivalently, it is the reaction of the fluid to a step wise uniform isentropic expansion compression while keeping its temperature at x=0 fixed. The fluid will react by the formation of a compressible boundary layer, thereby inducing expansion waves and compression waves in the fluid, even formation of shock waves may occur. The thermal boundary layer problem has been analyzed in detail by Clarke (30) by applying the method of matched asymptotic expansions. Keck then came up with s simplified version of Clarke's theory (31). Mirels (60) (61) studied heat loss to the shock tube walls by convection from the moving gas behind the incident shock to the moving gas in the growing boundary layer with focus on boundary layer profile temperature rather than core flow temperature. Hanel and Gronig (34) modeled heat transfer effects behind the reflected shock using a finite difference scheme for strong shocks and matched asymptotic expansions for weak shocks. The temperature jump condition with accommodation effects was accounted for in addition to adsorption effects on the wall. Onishi (33) studied the interaction of the reflected shock with the endwall in order to quantify the velocity behind the reflected shock towards the wall. Ideally, the Euler equations predict zero and uniform velocity behind the wall. However, the thermal and viscous boundary layers resulting from the interaction process cause the shock to lose its energy. The weakened shock is not strong enough to cancel out the velocity induced by the incident shock wave and the magnitude of the velocity is several percent of velocity behind incident shock. The BGK model of the Boltzmann equation subject to the condition of diffuse-reflection at the wall was used for the study. The BGK model produces the same equations as the Navier-Stokes with the viscosity and thermal conductivity proportional to the local temperature of the continuum limit and the Prandtl number is assumed to be unity. Onishi stated that the interaction process should be modeled based on the kinetic theory because time and length scales under study are of the order of the collision time between the molecules and the mean free path. Luo et al. (35) studied the development of the thermal boundary layer as a result of interaction between the reflected shock and the endwall by solving the 1-D full Navier-Stokes equations based on CESE space time conservation element and solution element method. Results showed that shock-induced entropy disturbances can be neglected for disturbances more than 1mm from wall and also showed that shock trajectory is slightly affected by boundary layer development. For strong shocks, the accelerating reflected shock causes layer of varying entropy such that temperature and density are not uniform in the entropy layer. They also showed that thermal boundary layer at the driver endwall won't affect nucleation but may have some influence on droplet growth for low pressure conditions and He driver gas. The thermal boundary layer induced by shock reflection has also been extensively studied by Luo et al. (35) to obtain experimental information on the thermo-physical properties of gases such as thermal conductivities.

Conjugate Heat Transfer Model

To correctly predict the thermal field in the test region of the shock tube, the Conjugate Heat Transfer (CHT) approach is adopted. The heat transfer is computed by coupling the conduction of heat through the shock tube solid wall thickness with convective heat transfer in the fluid. Therefore two zones are specified in the grid generation, the solid and the fluid zones. Here the wall thickness must be meshed and the coupled thermal boundary condition is available on the wall zone which separates two cell zones. As such, the wall thermal resistance is directly accounted for in the energy equation. The boundary between the two zones is always a wall and a shadow zone is created automatically by FLUENT. Figure 24 illustrates the setup of the conjugate heat transfer model. The shock tube walls material is stainless steel with a density of 8030 kg/m^3, constant specific heat of 502.48 j/kg-K, and thermal conductivity of 16.27 W/m-K. The shock tube wall temperature is initially set to 300 K. Thermo-physical setup of the compressible flow assumes ideal gas density and uses the mixing law for constant specific heat. The thermal conductivity is set to 0.0454 W/m-K, the viscosity to 1.72×10^{-5} kg/m-s, and the mass diffusivity to 2.88×10^{-5} m^2/s.

The numerical simulations of the fluid flow and heat transfer in the shock tube were accomplished by solving the conservation equations of mass, momentum, energy and species. Of interest to the current study, is the energy transport equation for non-reacting flow given by the following,

$$\frac{\partial(\rho E)}{\partial t} + \nabla.[\vec{V}(\rho E + p)] = \nabla.[k_{eff}\nabla T - \sum_j h_j J_j + (\bar{\bar{\tau}}_{eff}.\vec{V})] \tag{53}$$

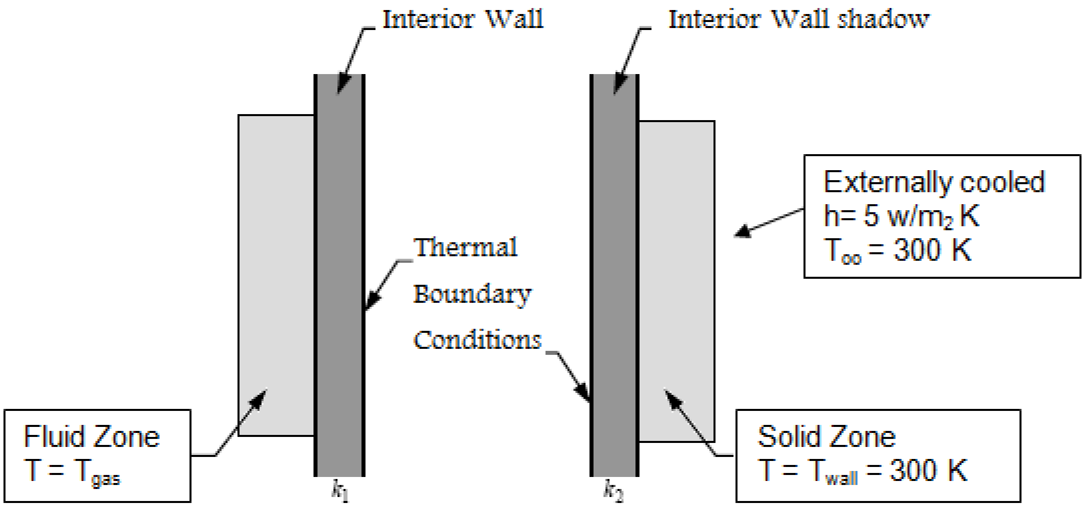

Figure 24: Conjugate Heat Transfer model setup. The thermal boundary conditions are supplied on the inner surfaces of uncoupled wall/shadow pairs

Shock Tube Simulations

For the CHT simulation, the primary goal was to set the shock-tube driver and driven initial conditions such that they would produce a long test time behind the reflected shock wave at the conditions that produced the most extreme change in average test temperature at long times for an 800-K test, which occurs at a 1-atm pressure condition in Argon. Viscous simulations were carried out in the entire shock tube geometry for multiple test conditions and driver gas compositions. Figure 25 shows the shock-tube flow field solution obtained with the conjugate heat transfer model.

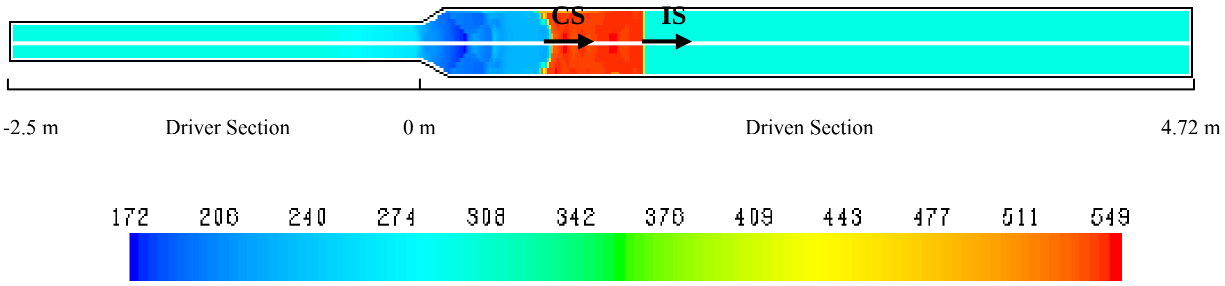

a) Temperature, K

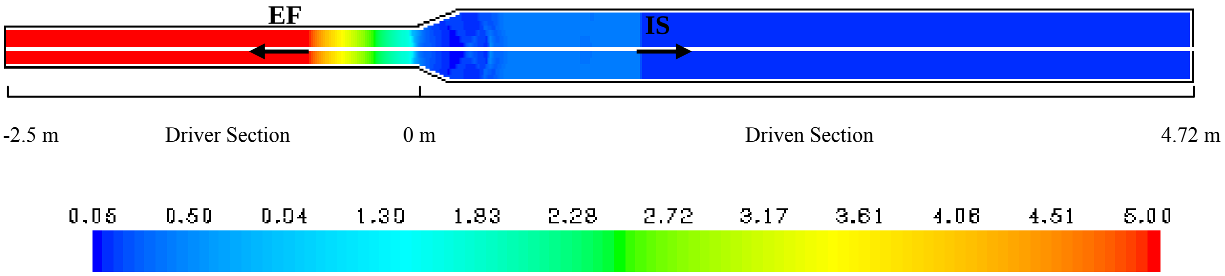

b) Pressure, atm

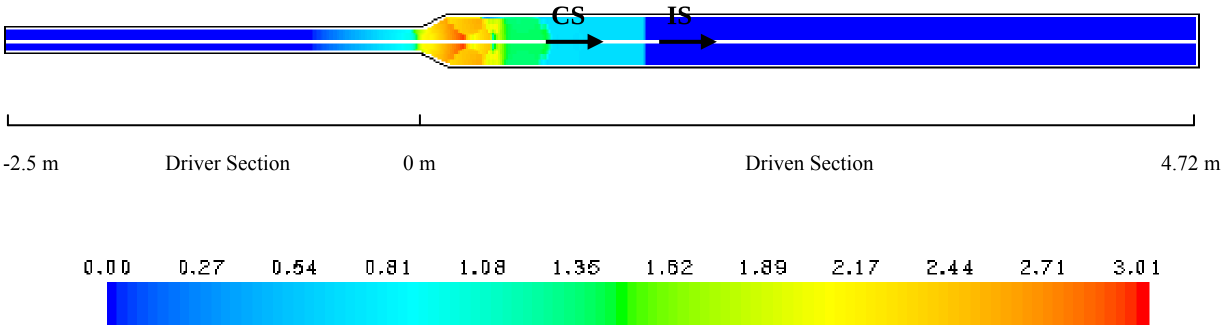

c) Mach numbers

Figure 25: Conjugate heat transfer solution of a) temperature, b) pressure, and c) Mach number flow fields at 2.5 ms of elapsed time from diaphragm rupture. Initial condition were carefully chosen to produce temperature and pressure behind the reflected shock of 800K and 1 atm respectively and in Ar test gas. Driver mixture comprised of Propane and He to tailor to longer test times up to 15 ms after the incident shock reflection. IS = Incident Shock, CS = Contact Surface, EF = Expansion Fan.

Driver Gas Tailoring

In conventional shock tubes, Helium is usually the driver gas of choice for it is known to produce strong shocks due to its high speed of sound and its low molecular weight. However, this results in fast-propagating expansion waves which reach the contact surface before the reflected shock does and then arrive at the endwall, thereby ending the test time. Helium produces test times on the order of 1-3 ms which are not sufficient for experimental measurements at lower temperatures. Figure 26 shows the endwall pressure trace obtained with a driver composition of 100% He and a test gas of 100% Ar. Note that the test time achieved behind the reflected shock tube and under which the conditions remain uniform is only about 1.6 ms which is not sufficient for autoignition studies at lower temperatures which require much longer test times. One way to avoid the early ending of the test time is to retard the arrival of the expansion wave at the endwall by extending the driver section length. Another way is to shorten the driven length to ensure the reflected shock reaches the contact surface before the expansion fan does. If it is not possible to modify the facility, tailoring with heavier driver gas mixtures such as Propane and Carbon Dioxide result in extended test times.

For example, Amadio et al. (111) performed non-reactive and reactive shock tube experiments performed using He/CO_2 and He/C_3H_8 driver mixtures in order to tailor the contact surface between the driver and driven gases to produce longer test times. Test times of the order of 15 ms were achieved for nonreactive cases, while ignition times over 5 ms were possible for shock reflected temperatures below 1000 K versus only 1 ms test times with 100% He driver-gases only. The last two approaches usually yield test times on the order of 10 ms for the facility dimensions utilized herein. When even longer test times are desirable, a combination of both shock-tube modifications and contact surface tailoring can produce test times as long as 20 ms.

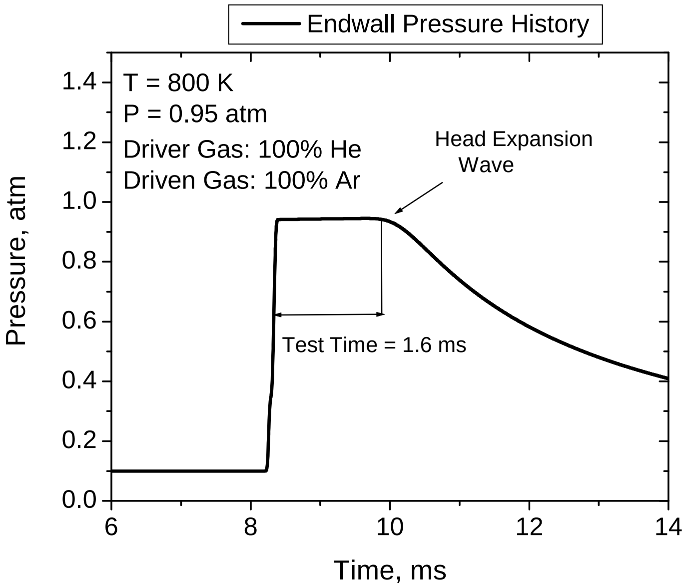

Figure 26: Typical endwall pressure trace at 800 K and 0.95 atm using a driver gas composition of 100% He and Ar as the test gas. He produced fast propagating expansion waves that reached the endwall sooner resulting in a test time of only 1.6 ms

A tailored condition is when there exists no pressure discontinuity at the point of interaction between the reflected shock and the contact surface. For that matter, the driver gas composition has to be adjusted until the same pressure is achieved on both sides of the discontinuity. Figure 27 shows the endwall pressure simulated with the laminar model at a quasi-tailored condition where the pressure non-discontinuity condition was enforced to be as close as possible to 1. As a result, the test time under which the flow properties in the test region are uniform was extended from 5.64 to 9.5 ms. Since it is difficult to judge the correct driver composition to yield a perfectly tailored condition, several viscous laminar simulations were performed with different driver gas mixtures. The majority of the simulations resulted in a pressure discontinuity upon the encounter of the reflected shock and the contact surface. When the pressure discontinuity is a sudden decrease, a shock wave forms and travels towards the endwall, increasing the test region pressure even further as shown in Figure 28. In case the pressure discontinuity is a sudden increase, an expansion wave forms and travel towards the endwall decreasing the test region pressure as displayed in Figure 29. Both the over-tailored and under-tailored conditions produce test times on the order of 5 ms.

There were also few cases in which the tailored driver composition resulted in expansion waves that reached the contact surface before the reflected shock did at a slower rate than using pure helium driver mixture resulting in test times on the order of 2.5-4 ms. This is illustrated in Figure 30 and Figure 31.

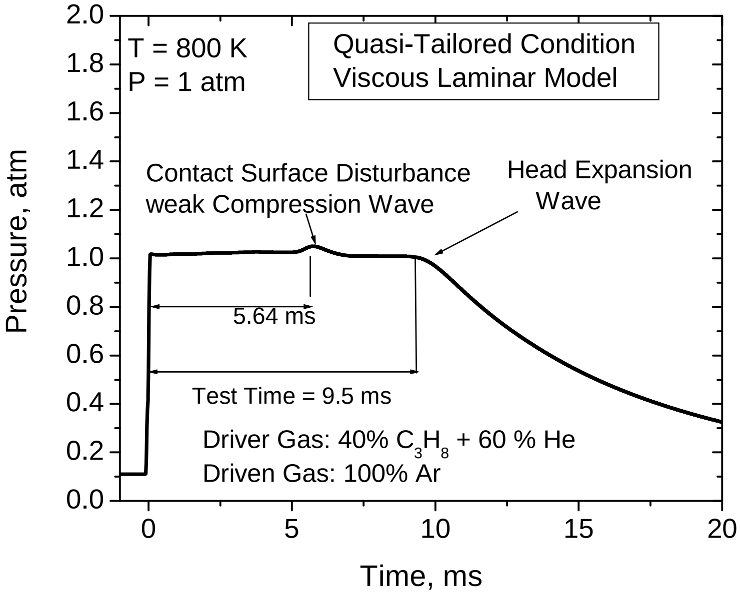

Figure 27: Quasi-tailored endwall pressure trace at 800 K and 1 atm using a driver gas composition of 40% propane + 60% helium and Ar as the test gas. The discontinuity in pressure from the compression wave is weak relative to the pressure behind the reflected shock allowing for test time extension up to 9.5 ms.

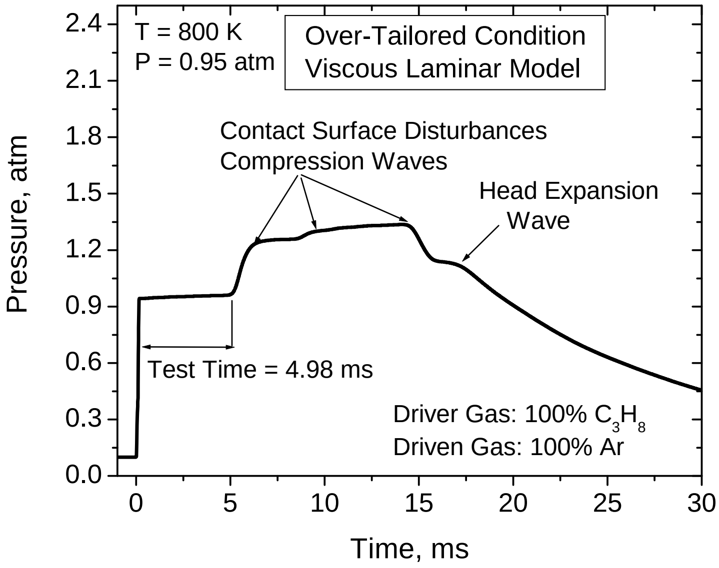

Figure 28: Over-tailored endwall pressure trace at 800 K and 0.95 atm using a driver gas composition of 100% propane and Ar as the test gas. The test time of 4.98 ms is ended by the pressure increase from the compression wave formed as a result of interaction between the contact surface and the reflected shock.

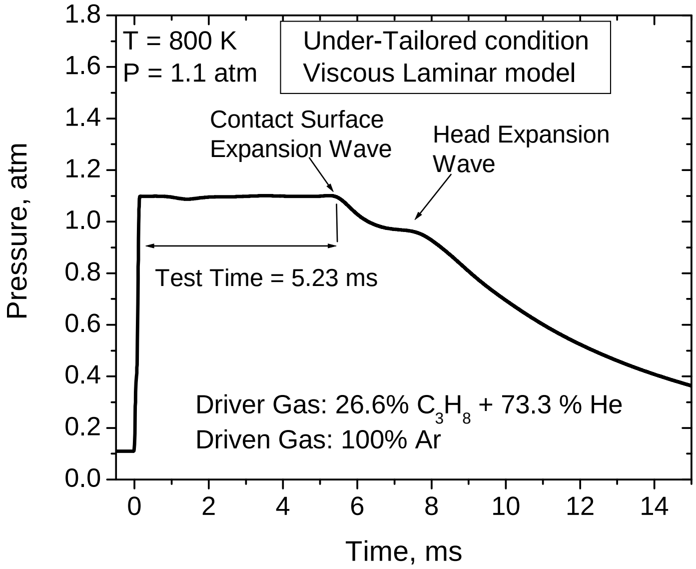

Figure 29: Under-tailored endwall pressure trace at 800 K and 1.1 atm using a driver gas composition of 26.6% propane + 73.3% helium and Ar as the test gas. The expansion wave from the contact surface arrives at the endwall after 5.23 ms of test time.

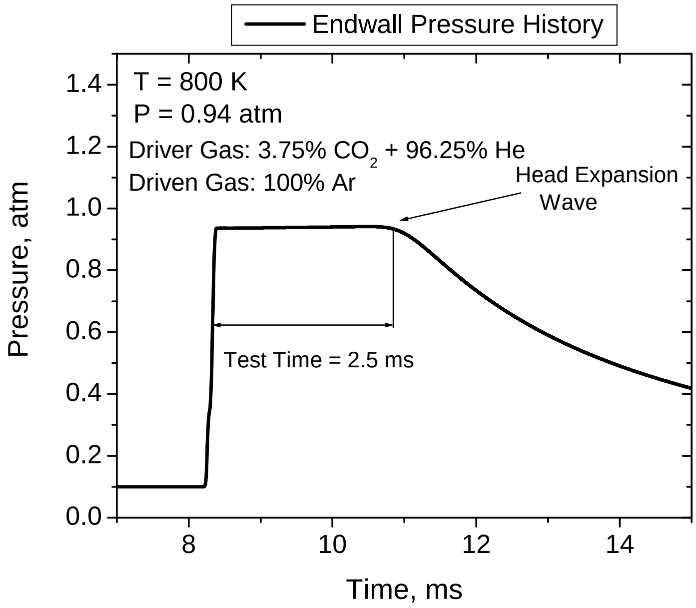

Figure 30: Non-tailored endwall pressure trace at 800 K and 0.94 atm using a driver gas composition of 3.75% CO_2 + 96.25% He and Ar as the test gas. The expansion wave reached the contact surface before the reflected resulting in a reduced test time of 2.5 ms.

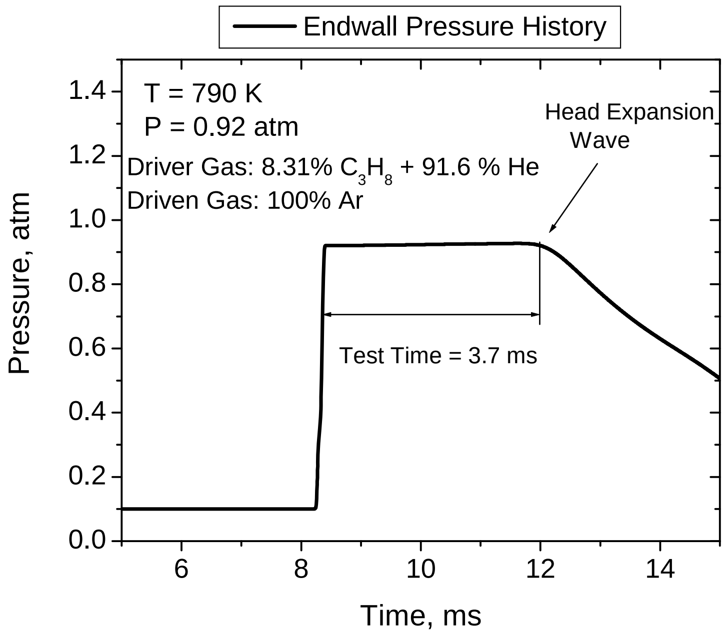

Figure 31: Non-tailored endwall pressure trace at 720 K and 0.92 atm using a driver gas composition of 8.31% C3H8 + 91.6% He and Ar as the test gas. The expansion wave reached the contact surface before the reflected resulting in a reduced test time of 3.7 ms.

Several runs were performed with different driver-gas mixture compositions to achieve the longest test time possible at the conditions of 800 K and 1 atm. Test times can be extended up to 20 ms by the use of unconventional driver gases such as C_3H_8/He, CO_2/ He, or a combination of C_3H_8/CO_2/He mixtures as have been shown by Amadio et al.(111). Table 6 and Table 7 give the simulation results for different test conditions ran with driver gas tailoring in the regular shock-tube geometry and in the modified driver length geometry respectively. The driver length in the shock-tube model was modified from 2.5 m to 4 m in order to delay the arrival of the expansion fan to the endwall thereby extending the test time further. The corresponding endwall pressure profiles for the longer driver tube are provided for the non-tailored (Figure 32), under-tailored (Figure 33, Figure 34, and Figure 35), over-tailored (Figure 36 and Figure 37), and quasi-tailored (Figure 38) conditions.

Table 6: The laminar/CHT simulations showing the test conditions used in driver gas tailoring. Driven gas is Ar

Driver Mixture*	T_5 (K)	P_5 (atm)	P_1 (atm)	P_4 (atm)	P_4/P_1	Test Time (ms)
100% He	850	1.07	0.1	2	20	1.6
	830	1.025	0.1	1.9	19	1.8
	800	0.94	0.1	1.7	17	2
	824	0.975	0.1	1.8	18	1.8
	780	0.9	0.1	1.6	16	2
3.75% C_3H_8 + 96.25% He	790	0.9	0.1	1.85	18.5	2.5
	800	0.93	0.1	1.9	19	2.5
3.75% CO_2 + 96.25% He	775	0.87	0.1	1.8	18	2.5
	785	0.9	0.1	1.9	19	2.5
	800	0.94	0.1	2	20	2.5
8.3% C_3H_8 + 91.6% He	760	0.85	0.1	2	20	3.5
	790	0.925	0.1	2.2	22	4
	825	1	0.1	2.5	25	4
	900	1.19	0.1	3	30	4
8.3% CO_2 + 91.6% He	730	0.8	0.1	2	20	3.5
	860	1.1	0.1	3	30	3.6
26.6% C_3H_8 + 73.3% He	800	1.11	0.11	3.19	29	5.2
40% C_3H_8 + 60% He	800	1.01	0.11	3.19	29	9.5
100% C_3H_8	605	0.52	0.1	1.85	18.5	8
	620	0.56	0.1	2	20	8
	800	0.95	0.1	4	40	5
100% CO_2	570	0.45	0.1	1.85	18.5	8
	578	0.475	0.1	2	20	8
	725	0.78	0.1	4	40	5

*Driver gas compositions are given in volumetric percentages

Table 7: The laminar/CHT model simulations showing the test conditions used in driver gas tailoring studies for the longer driver shock-tube model. Driven gas is Ar

Driver Mixture*	T_5 (K)	P_5 (atm)	P_1 (atm)	P_4 (atm)	P_4/P_1	Test Time (ms)
100% He	824	0.98	0.1	1.8	18.00	3.8
	800	0.94	0.1	1.7	17.00	4
1.41% C_3H_8 + 1.53% CO_2 + 97.05% He	925	1.22	0.1	3	30	4.8
	860	1.15	0.1	2.6	26	5
	807	0.96	0.1	2.2	22	5.1
8.3% C_3H_8 + 91.6% He	795	0.93	0.1	2.2	22.00	5
26.6% C_3H_8 + 73.3% He	925	1.21	0.1	3.7	37	5
	895	1.13	0.1	3.4	34	5
	850	1.05	0.1	3.1	31	5
	800	0.93	0.1	2.7	27	5.2
40% C_3H_8 + 60% He	800	0.95	0.1	2.9	29	15
	800	1.01	0.11	3.19	29	15
45% C_3H_8 + 50% He	800	0.94	0.1	3	30	5
100% C_3H_8	800	0.95	0.1	4	40	5

*Driver gas compositions are given in volumetric percentages

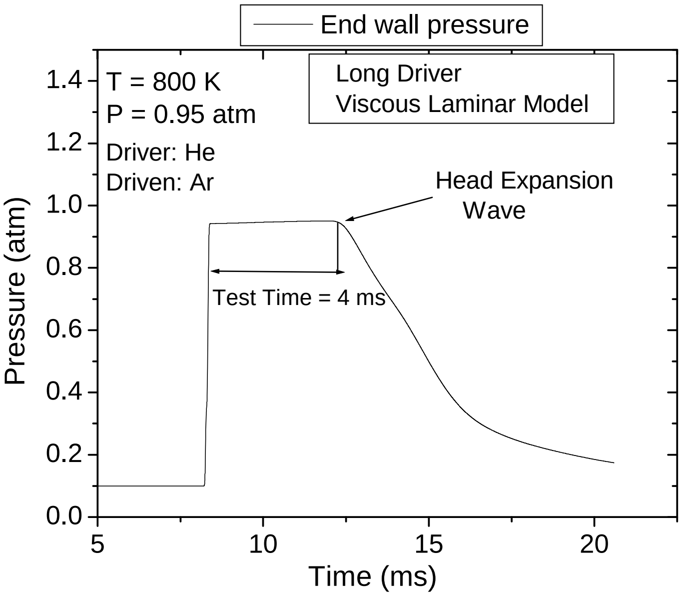

Figure 32: Endwall pressure trace in the longer driver shock tube at 800 K and 0.95 atm using a driver gas composition of 100% He and Ar as the test gas. The driver length extension from 2.5 to 4 m resulted in test time extension from 1.6 to 4 ms

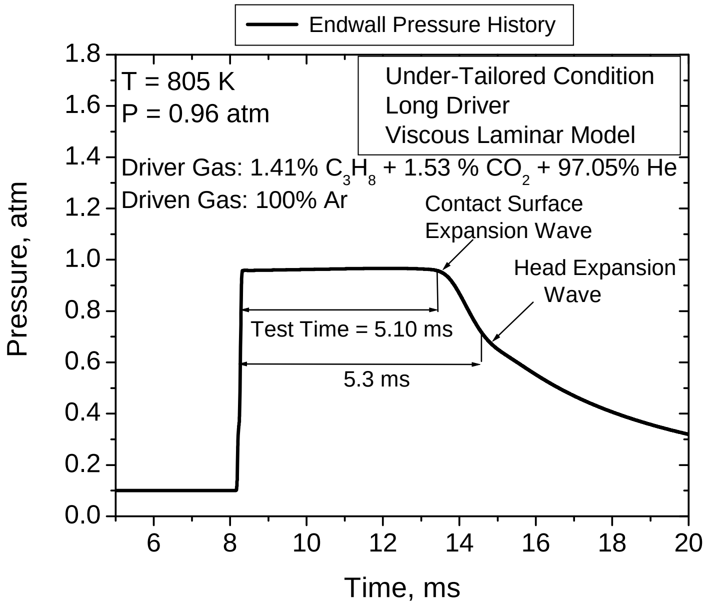

Figure 33: Under-tailored endwall pressure in the longer driver shock-tube trace at 805 K and 0.96 atm using a driver gas composition of 1.41% C_3H_8 + 1.53% CO_2 + 97.05% He and Ar as the test gas. The contact surface expansion wave arrives at the endwall after 5.1 ms of test time. The Head Expansion fan reaches the endwall after 5.3 ms

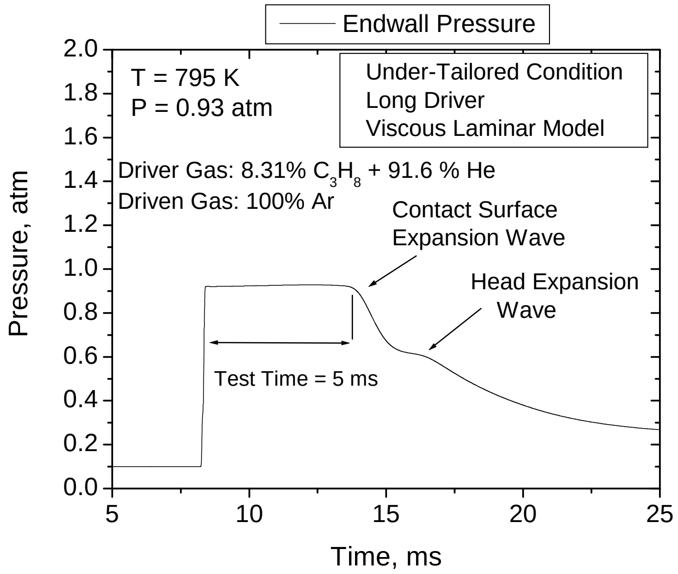

Figure 34: Under-tailored endwall pressure in the longer driver shock-tube trace at 795 K and 0.93 atm using a driver gas composition of 8.31% C_3H_8 + 91.6% He and Ar as the test gas. The contact surface expansion wave arrives at the endwall after 5 ms of test time. The Head Expansion fan reaches the endwall after 7 ms

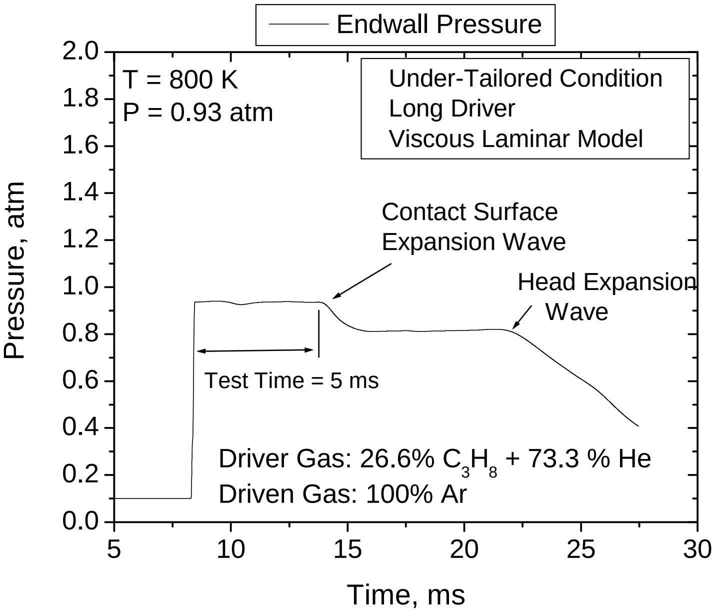

Figure 35: Under-tailored endwall pressure in the longer driver shock-tube trace at 795 K and 0.93 atm using a driver gas composition of 26.6% C_3H_8 + 73.3% He and Ar as the test gas. The contact surface expansion wave arrives at the endwall after 5 ms of test time. The Head Expansion fan reaches the endwall after 15 ms

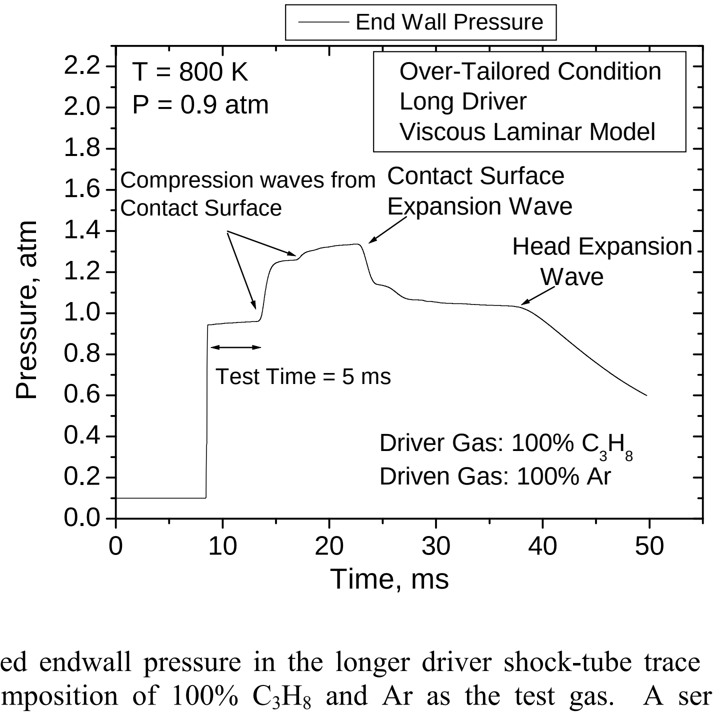

Figure 36: Over-tailored endwall pressure in the longer driver shock-tube trace at 800 K and 0.9 atm using a driver gas composition of 100% C_3H_8 and Ar as the test gas. A series of contact surface compression waves arrive at the endwall after 5 ms of test time

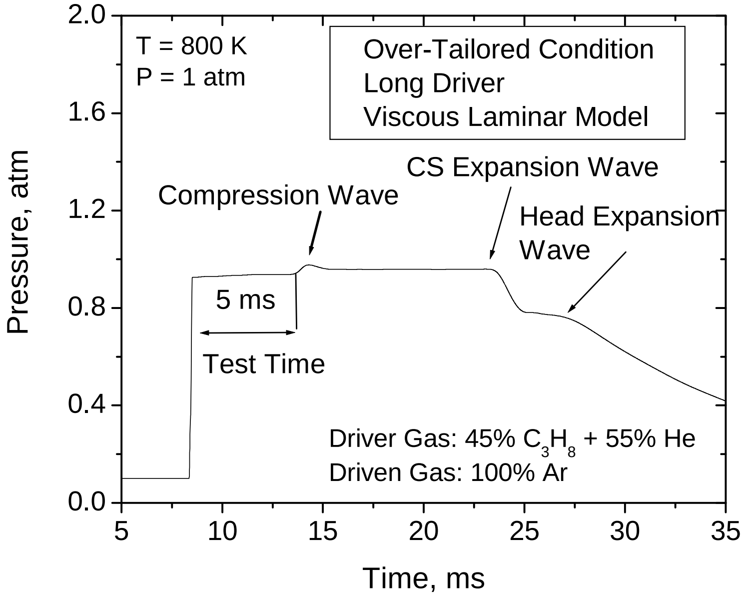

Figure 37: Slightly Over-tailored endwall pressure in the longer driver shock-tube trace at 800 K and 1 atm using a driver gas composition of 45% C_3H_8 + 55% He and Ar as the test gas. A weak compression wave resulted from the contact surface-reflected shock interaction allowing for only 5 ms of test time.

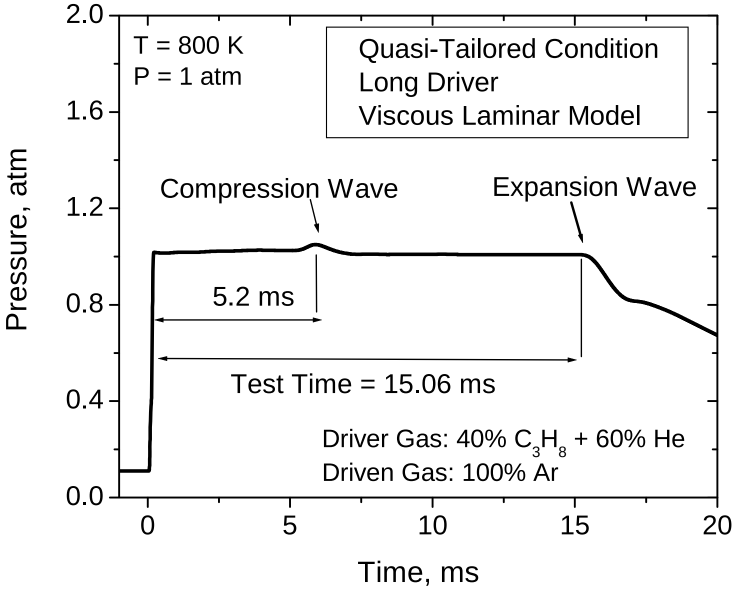

Figure 38: Laminar simulation of a quasi-tailored endwall pressure in the longer driver shock-tube trace at 800 K and 1 atm using a driver gas composition of 40% C_3H_8 + 60% He and Ar as the test gas. The discontinuity in pressure from the compression wave is weak relative to the pressure behind the reflected shock allowing for test time extension up to 15 ms

The number of test runs produced for the tailoring study allowed for the generation of pressure ratio across the diaphragm, P_4/P_1, versus T_5 plots which help guide future solutions and reduce the number of iterations needed to generate the test conditions of interest. Figure 39 and Figure 40 give the P_4/P_1 versus T_5 plots for the regular and modified driver geometry shock tube respectively.

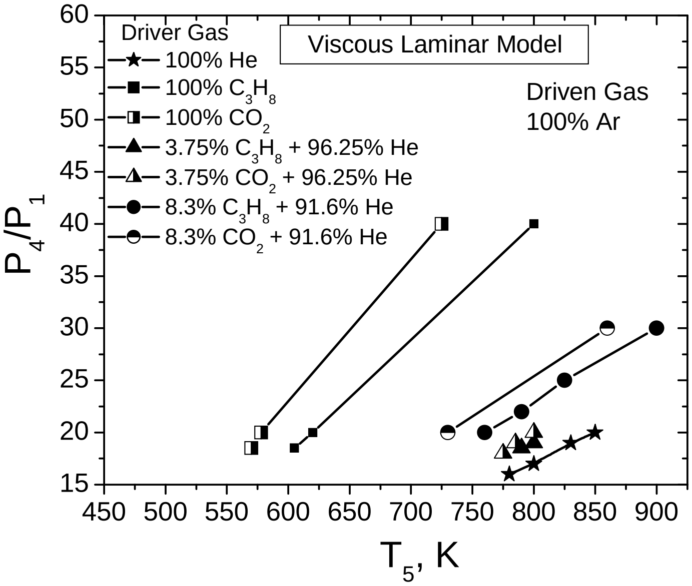

Figure 39: Diaphragm pressure ratios P_4/P_1 required to generate incident temperature behind the reflected shock T_5 between 550 and 950 K for different driver gas mixture compositions in the regular shock tube geometry with a driver length of 2.5 m

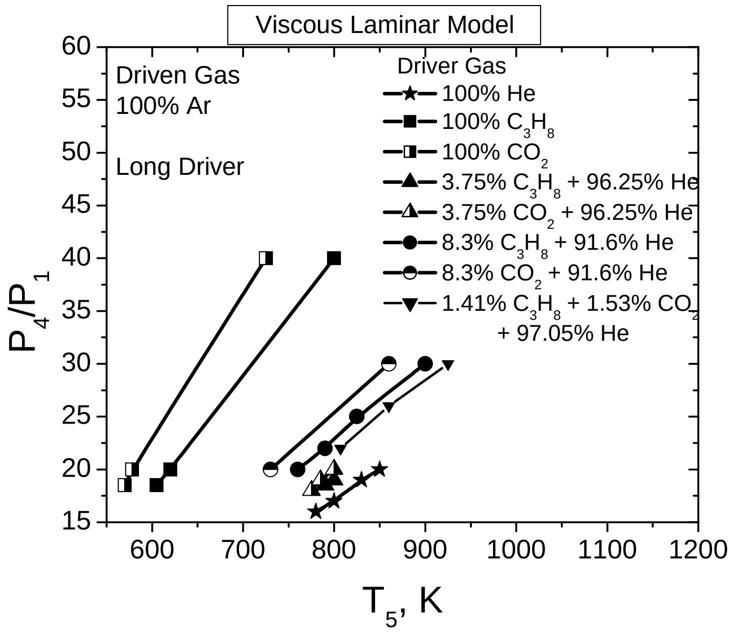

Figure 40: Diaphragm pressure ratios P4/P1 required to generate incident temperature behind the reflected shock T5 between 550 and 950 K for different driver gas mixture compositions in the modified driver shock tube geometry with the longer driver tube of 4 m

Turbulent simulations were performed with the κ–ε realizable model and enhanced wall treatments to allow for the resolution of the turbulent boundary layer all the way to the viscous sub-layer. Shown in Figure 41 are the temperature flow fields from the turbulent solution for an over-tailored condition achieved with a driver gas composition of 100% C_3H_8 at the conditions behind the reflected shock wave of 800 K and 1 atm. The turbulent temperature flow fields depict the incident-shock and contact surface propagation, the turbulent thermal boundary layer due to heat transfer to the shock tube side walls, the vortices shed from the contact surface due to the Ritch-Myer instability, the shock reflection from the endwall, and the interaction of the reflected shock with the contact surface. The time instances corresponding to each frame are given on the right. The interaction of the contact surface with the reflected shock results in a compression wave due to the sudden decrease in pressure. The pressure increase from the contact surface compression wave is evident at time = 10 ms where the compression wave coming from the contact surface compresses the gas behind the reflected shock and increasing its pressure. At time 13 ms, the compression wave which reflects off the endwall, interacts with the contact surface one more time to yield a second compression wave stronger than the first, increasing the endwall pressure even further. This process continues until the interaction between the contact surface and the reflected shock results in an expansion wave which brings the pressure and temperature at the endwall down. Finally the head expansion fan arriving from the shock-tube driver section cools down the endwall region and results in a further decrease of the properties behind the reflected shock.

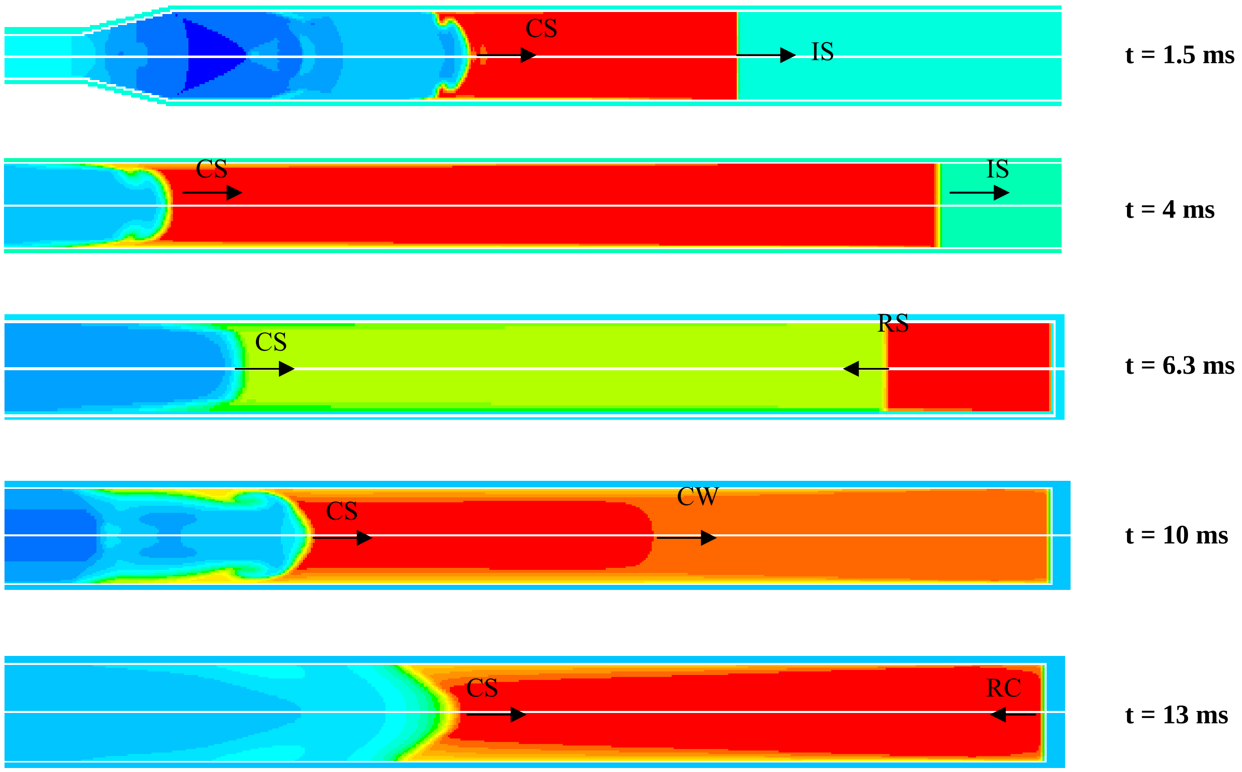

Figure 41: Turbulent solution for an over-tailored condition showing the temperature flow fields in the shock tube. The driver gas composition is 100% C_3H_8 and the driven test gas is Ar. Approximate times are shown on the right. CS: contact surface, IS: Incident Shock, RS: Reflected Shock, CW: Compression Wave, RCW: Reflected Compression Wave

The interaction of the reflected shock with the contact surface in the over-tailored case with 100% C_3H_8 driver gas is closely investigated. Figure 42 shows the axial distribution of temperature before, during, and after the contact surface-reflected shock interactions. The results show an increase in temperature at the contact surface location which can be quantified by approximately 50 deg K. This rise in temperature results from the pressure rise due to the compression wave passage from the overdriven condition and can be predicted from the isentropic temperature-pressure relation. As a result, the conditions behind the reflected shock wave become non-uniform. When driver gas tailoring is considered, it is recommended to avoid conditions that produce strong interaction between the contact surface and the reflected shock resulting in a temperature increase in the endwall region. It is speculated that the condition of 100% C_3H_8 driver gas composition produced the strongest interaction possible between the contact surface and the reflected shock and therefore the most increase in temperature. It is not expected to see a further temperature increase than 50 deg K when performing driver gas tailoring experiments with mixtures composed of combinations of C_3H_8 or CO_2 and Helium.

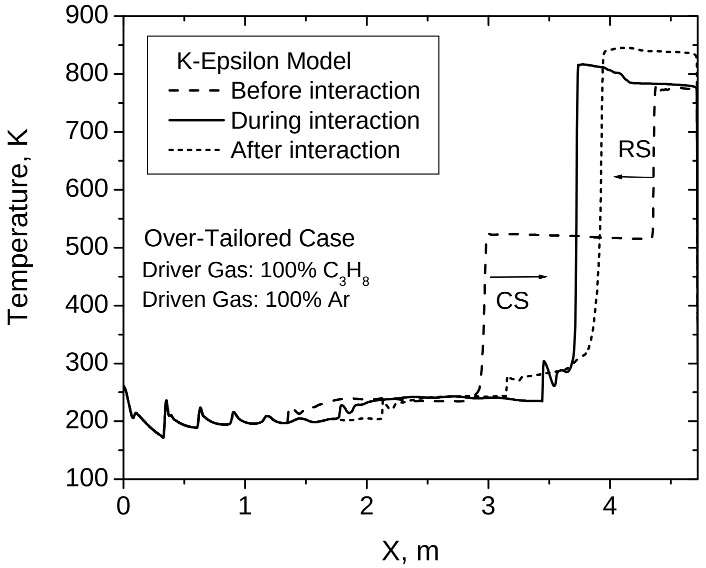

Figure 42: Turbulent solution of the axial distribution of temperature before, during, and after the interaction of the reflected shock with the contact surface for the over-tailored condition. The driver gas composition is 100% C_3H_8 and the test gas is Ar. The interaction results in about 50 deg K rise in temperature at the contact surface location first and propagates to the endwall region

Viscous simulations with the κ–ε turbulence model were generated at the driver gas composition which produced the longest test time of 15 ms for the laminar case. Figure 43 shows the endwall pressure profile obtained with a driver mixture of 40% C_3H_8 + 60 % He with the viscous laminar and turbulent K–ε models. The pressure ratio of 29 across the diaphragm was kept the same between both models. It is shown that the simulated endwall static pressure for the turbulent case has more discrete oscillations and is lower than the laminar case static endwall pressure. The resulting axial distribution of the density, pressure and temperature profiles along the entire shock-tube geometry is shown in Figure 44 a, Figure 44 b, and Figure 44 c respectively. The increased losses in the turbulent boundary layer result in reduced shock strength and therefore lower conditions behind the reflected shock wave than in the laminar case.

In order to produce a turbulent solution that matches the conditions of the turbulent model, a higher pressure ratio needs to be imposed across the diaphragm to produce a slightly stronger shock. The pressure ratio was slightly increased in the turbulent model which also required a slight adjustment of the driver gas mixture to 45 % C_3H_8 + 55% He. This condition provided a more uniform pressure profile with a test time of 17 ms as shown in Figure 46.

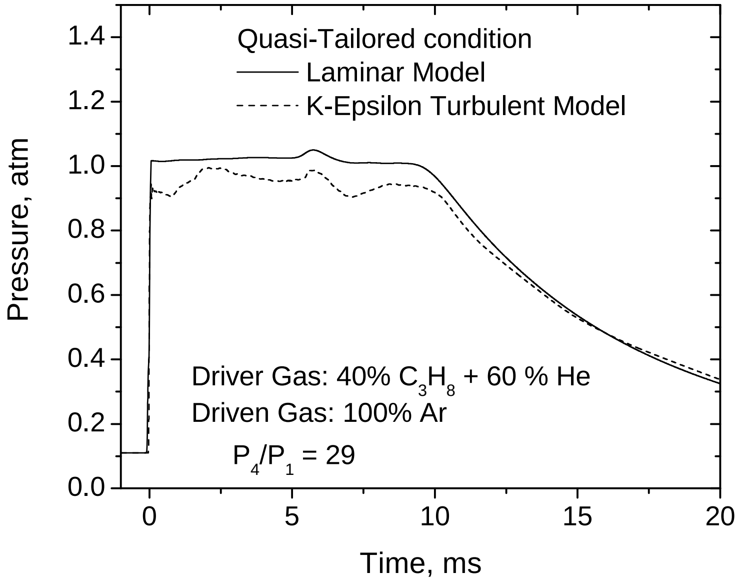

Figure 43: Endwall pressure history predicted by the laminar and turbulent viscous models at the quasi-tailored condition. At the same pressure ratio across the diaphragm, the turbulent solution yields a lower pressure behind the reflected shock due to the more pronounced losses in the turbulent boundary layer than in the laminar case

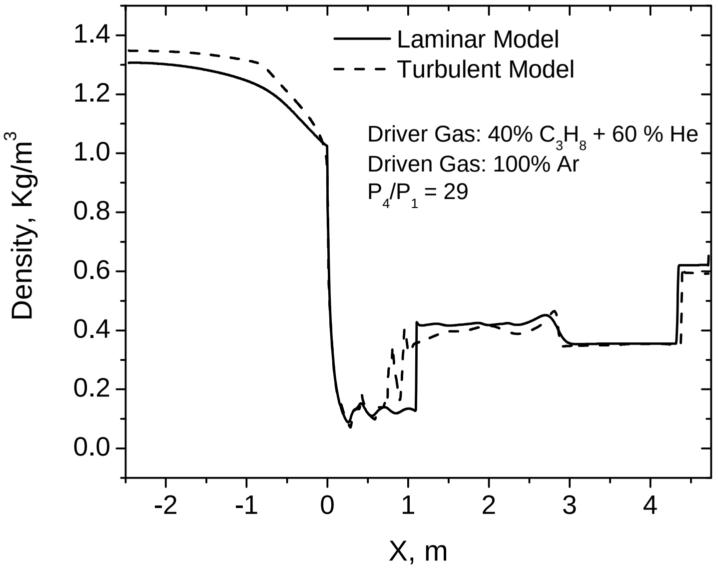
Laminar Model
Turbulent Model
Driver Gas: 40% C_3H_8 + 60 % He
Driven Gas: 100% Ar
P_4/P_1 = 29
Density, Kg/m^3
0.0
0.2
0.4
0.6
0.8
1.0
1.2
1.4
-2
-1
0
1
2
3
4
X, m

a)

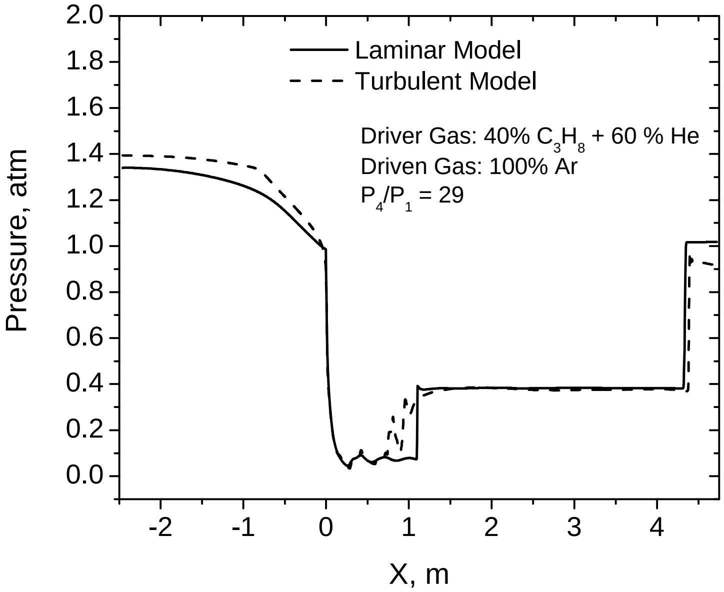
Laminar Model
Turbulent Model
Driver Gas: 40% C_3H_8 + 60 % He
Driven Gas: 100% Ar
P_4/P_1 = 29
Pressure, atm
0.0
0.2
0.4
0.6
0.8
1.0
1.2
1.4
1.6
1.8
2.0
-2
-1
0
1
2
3
4
X, m

b)

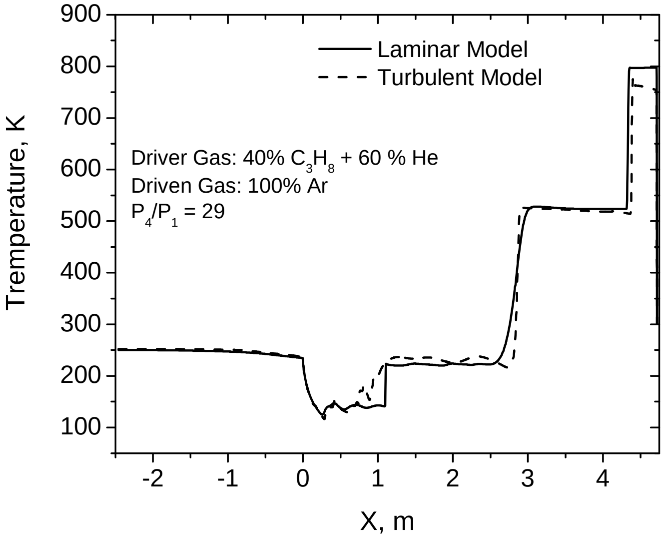

c)

Figure 44: Viscous laminar and turbulent solution along the axial distance of the shock tube showing a) density, b) pressure, and c) temperature profiles. The turbulent solution results in lower conditions than the laminar model due to increased losses in the turbulent boundary layer

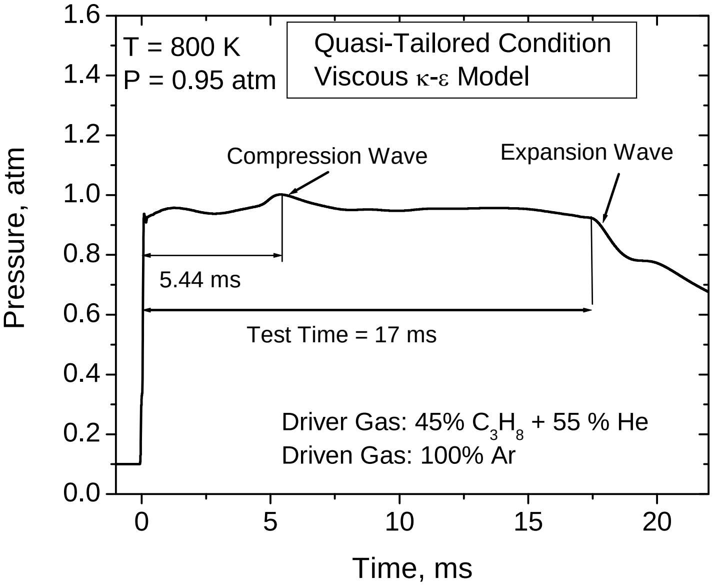

Figure 45: Turbulent simulation of a quasi-tailored endwall pressure in the longer driver shock-tube trace at 800 K and 0.95 atm using a driver gas composition of 45% C_3H_8 + 55% He and Ar as the test gas. The discontinuity in pressure from the compression wave is weak relative to the pressure behind the reflected shock allowing for test time extension up to 17 ms

Heat Transfer Modeling

The driver gas tailoring study resulted in test time extension up to 15 ms with a driver mixture composition of 40% C_3H_8 + 60 % He for the laminar solution and 17 ms with a driver gas composition of 45% C_3H_8 + 55 % He for the turbulent solution in the longer driver shock-tube. The modelled conditions behind the reflected shock are 800 K and 1 atm. Figure 46 displays the full turbulent conjugate solution of the shock-tube flow fields at four time instances of -3, 3, 6, and 15 ms after shock-reflection for the temperature, pressure, and Mach number solutions. By modeling the entire shock tube, the flow details such as the interaction of the reflected shock wave with the contact surface are fully resolved. Of most importance for the problem at hand are the test gas conditions near the endwall region.

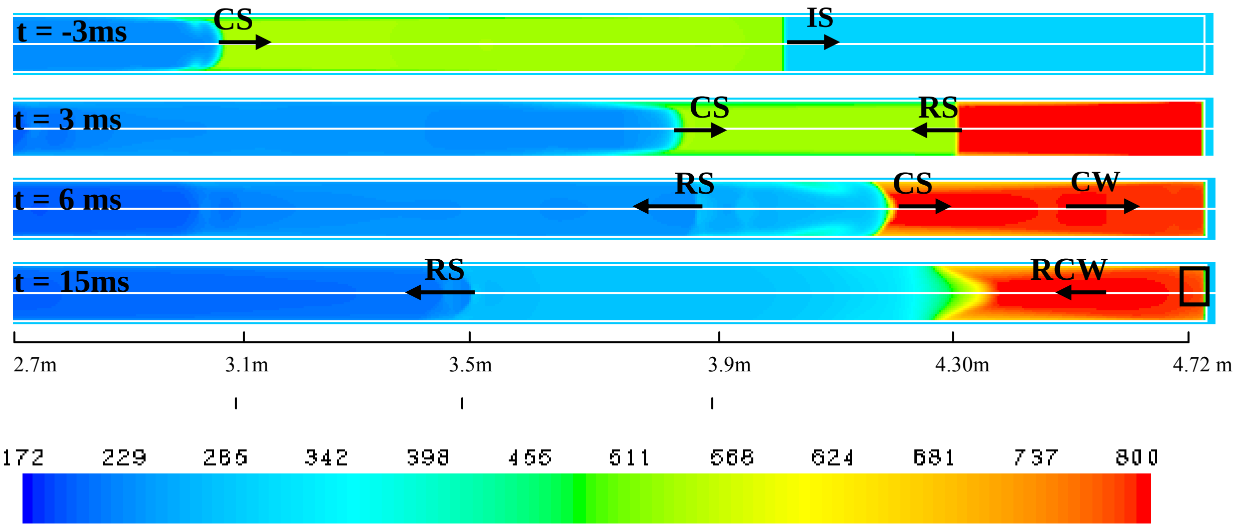

a) Temperature flow Fields, K

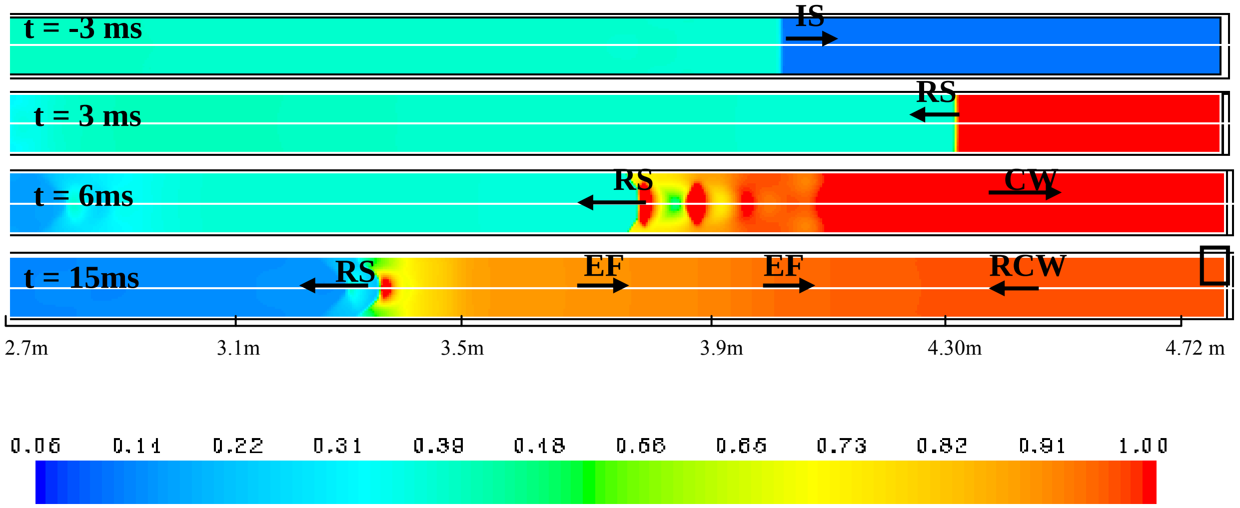

b) Pressure flow fields, atm

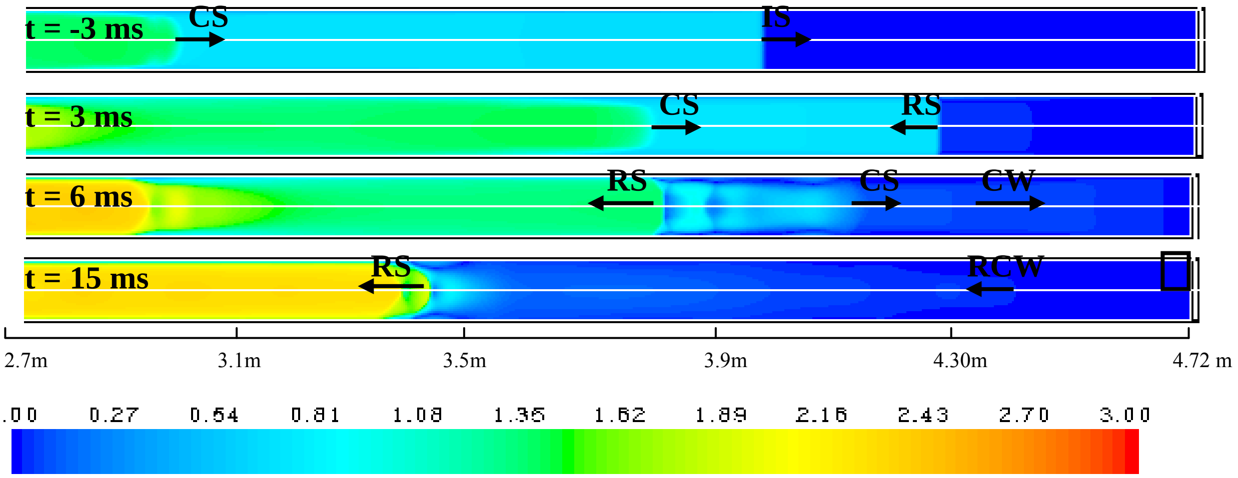

c) Mach number flow fields

Figure 46: Turbulent conjugate heat transfer solution showing a) temperature, b) pressure, and c) Mach number flow fields during shock propagation, reflection, interaction with the contact surface, and arrival of the expansion fan. Conditions behind the reflected shock are 800 K, 1 atm in Ar test gas. Corresponding times are given in the upper Left corner of each frame. Time zero is the moment the incident shock reflects off the endwall. IS = Incident Shock, CS = Contact Surface, RS = Reflected Shock, CW = Compression Wave, RCW = Reflected Compression Wave, EF = Expansion Fan

A close-up on the turbulent solution flow fields in the end wall region is shown in Figure 47 corresponding to the 15-ms solutions for temperature, pressure, and Mach number presented in Figure 46. The heat transfer from the hot gas to the walls is depicted by the thermal boundary layer present along the test region shock-tube walls (Figure 47 a) and appears similar to the predictions of the analytical heat conduction T (x, r, t) model. The temperature distribution shows that the thermal boundary layer is well outside of the test region indicating that heat transfer is not a concern for chemical kinetics measurements. This general result of the full CFD simulation confirms the results inferred from the conduction analysis presented above for the baseline shock-tube geometry with a 16.2-cm driven tube diameter. The endwall-region contours of pressure and Mach number in Figure 47 b and Figure 47 c show that the test gas has a nearly uniform pressure with essentially no bulk movement, even at the extreme test time of 15 ms.

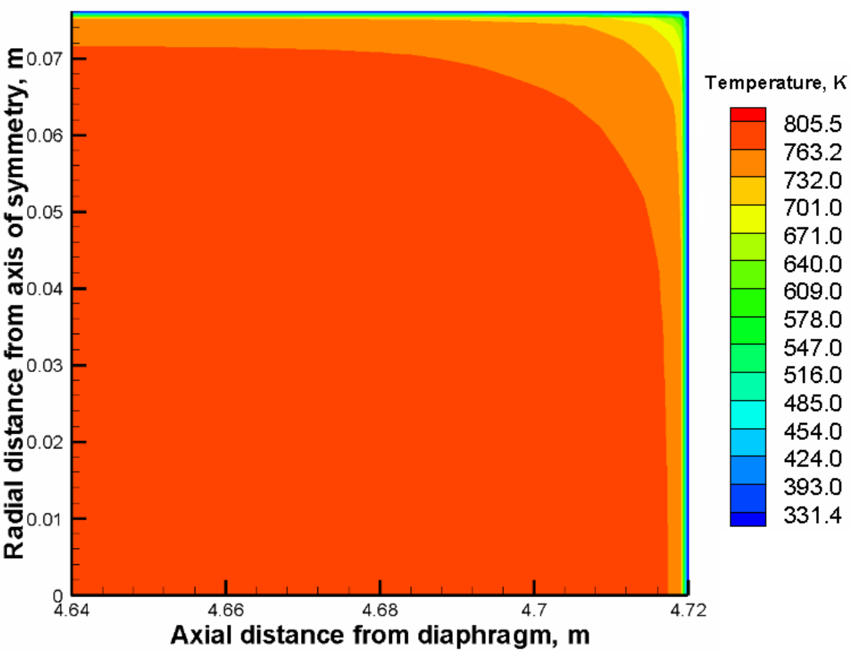

a) Temperature Flow fields, K

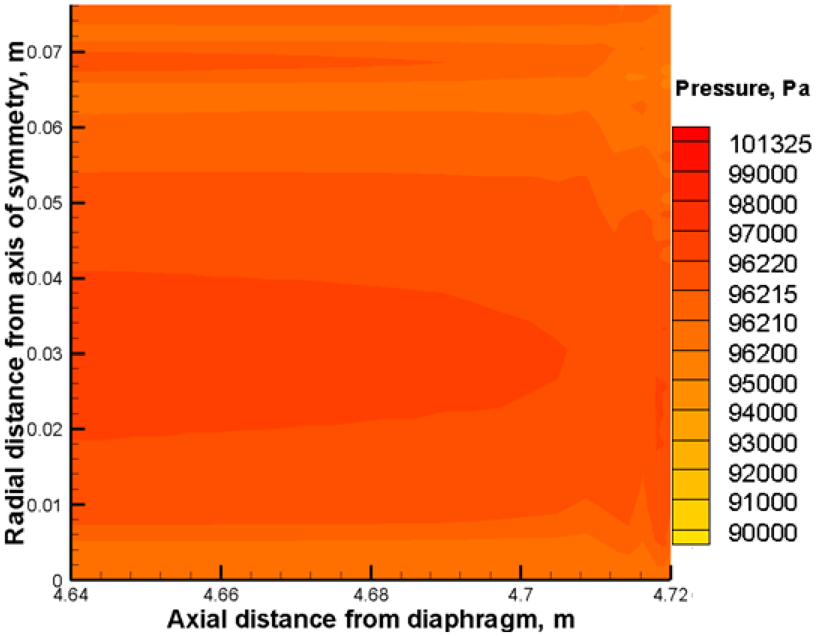

b) Pressure flow fields, Pa

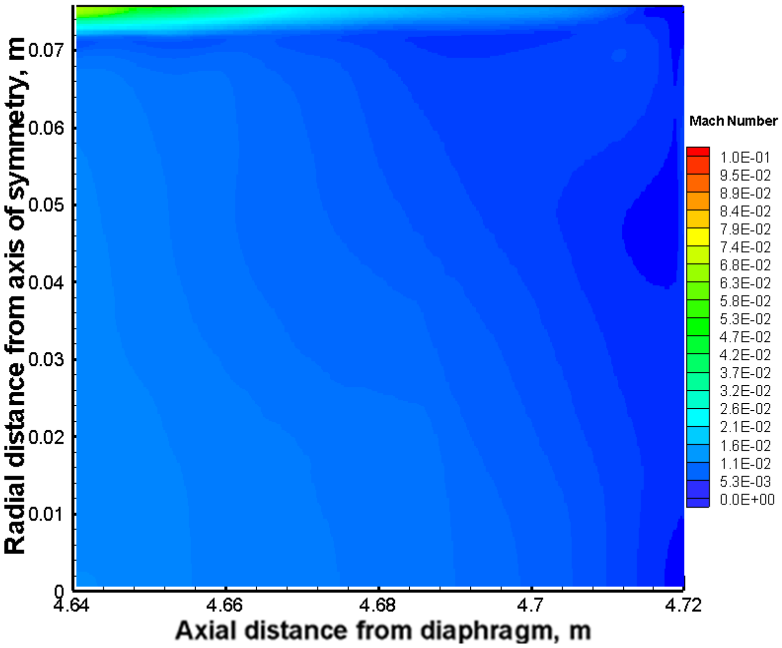

c) Mach number flow fields

Figure 47: A close-up on the turbulent conjugate heat transfer solution of a) temperature, b) pressure, and c) Mach number flow fields in the Ar hot gas test region at the conditions of 800 K, 1 atm, and 15 ms of test time

The test time is ended by the arrival of the contact surface expansion wave to the endwall followed by the head expansion wave denoted by the discontinuity in the slope of the pressure trace. The small compression bump near a test time of 5.2 ms in the laminar solution and 5.44 ms in the turbulent solution is from the interaction of the reflected shock wave with the contact surface, which emits a weak compression wave that travels back toward the endwall as shown in more details in Figure 38 and Figure 45. Heat transfer results are post-processed behind the reflected shock wave over the entire endwall test region. Figure 48 provides the average gas temperature solution for both the laminar and turbulent conjugate CFD models compared to the 1-D analytical conduction solution (32). The jump in the average gas temperature immediately after the shock tube walls come into contact with the hot gas is captured by both models, with the jump being more pronounced in the turbulent CFD solution. The conduction solution reports a higher decrease in the average gas temperature than the CFD conjugate solution.

The higher initial temperature jump at t = 0+ is due to the additional heat transfer between the hot gas and cold wall via the moving boundary layer that was formed initially behind the incident shock wave and which the conduction only solution does not model. Note also that the turbulent solution predicts a higher initial jump in temperature (by about 3 K) due to the stronger convective forces in the turbulent boundary layer when compared to the laminar one. The conduction model on the other hand exhibits more decrease in the average gas temperature and therefore more heat loss to the shock tube walls. Both models predict an average loss in temperature within a few K of each other, with the conduction solution being on the conservative side of over-estimating the heat loss. At 15 ms, the average gas temperature decreases by 19 K for the 1-D conduction solution versus only 13 K for the CFD conjugate solution. The difference in the average gas temperature between the two solutions is due to the presence of the viscous dissipation term in the energy equation which reduces the overall effect of heat transfer, notably after the passage of the reflected shock wave, resulting in a lower heat loss by the conjugate CFD models when compared to the conduction-only model.

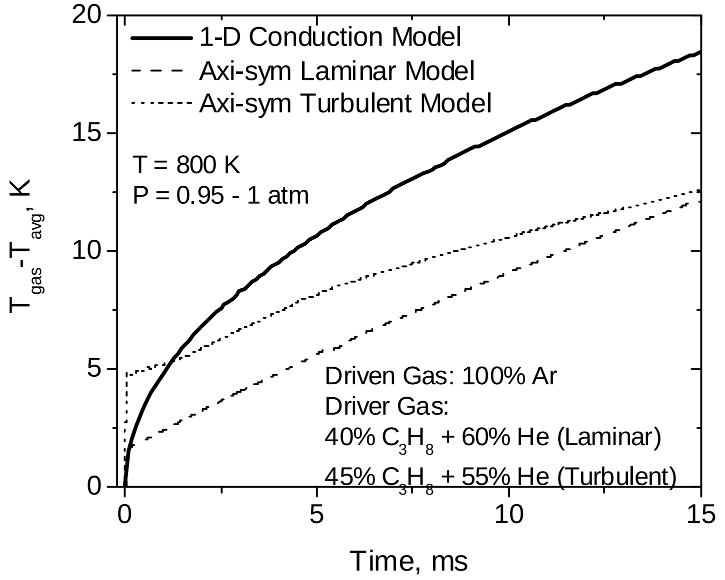

Figure 48: The difference between the maximum and the average bulk gas temperatures predicted by the viscous models. Results are compared to the 1-D analytical conduction model (32)

The heat transfer between the hot gas and the cold walls in viscous laminar and turbulent flow of shock-compressed argon test gas has been studied. The decrease in the average gas temperature predicted by the viscous CFD model is in reasonable agreement with the analytical conduction model. Both models exhibit the jump in temperature loss immediately after the hot gas comes into contact with the cold wall with the jump being more pronounced in the viscous model. However, the conduction model predicts slightly higher decrease in the average temperature than the viscous model indicating more heat loss to the shock tube wall. Both the laminar and turbulent CFD solutions produced average temperature losses that were about 5 K less than that predicted by the conduction model, implying that the simpler conduction model provides a somewhat conservative estimate of the heat loss. The energy equation solved in the CFD model accounts for the viscous dissipation term which reduces the rate of heat transfer resulting in less heat loss than the more conservative conduction model. Temperature contours showed that for the worst test condition of 800 K, 1 atm, and 15 ms of test time, the thermal boundary layer is well outside the endwall test region assuming that ignition initiation occurs far away from the shock-tube walls. In the case where ignition occurs near the corners of the endwall, the temperature gradient depicted by the thermal boundary layer can change the mechanism by which ignition is initiated. Overall, the conjugate CFD model accurately resolved the convective forces in the boundary layer and predicted an average gas temperature in the endwall region of 5 K less than the 1-D conduction solution, indicating that the latter solution is more conservative than the conjugate CFD solution.

Bifurcation

Shock bifurcation is suspected to be one of the major mechanisms responsible for non-ideal behavior in shock tubes for chemical kinetic studies. As the incident shock propagates down the shock tube, it leaves behind a boundary layer that grows in time, and when the shock reflects from the endwall, it interacts with the boundary layer it created and forms a bifurcated shock structure.

Background

There have been a number of numerical studies investigating Bifurcation in the shock tube (16) (41) (42) (43) (44) (45) (46) (47) (48) (49) (50) (51) and which also has served as a test case for numerical method validations (51) (52) (53) (54) (55) (56).

In particular, Sjogreen and Yee (54) studied grid convergence of several high order methods for the computation of bifurcation phenomenon in the shock tube. They developed adaptive numerical dissipation control high order methods referred to as the ACM and compared wavelet filter schemes with a fifth-order weighted ENO (WENO) scheme. Simulations with a standard second-order TVD scheme and a MUSCL scheme with limiters were used as reference solutions. The 2-D viscous laminar shock tube problem with complex shock/shear/boundary layer interactions was used for the validation of the higher order schemes. The computations were conducted on a uniform grid. It was found that the shock tube problem contains fine scale structures that are stiff and require extreme grid refinement and time step restrictions in order to resolve all the flow scales.

Satofuka (73) performed 2-D simulations of bifurcation and the reflected shock/contact surface interaction in the shock tube by adopting the ICE method proposed by Harlow and Amsden back in 1971 for solving time-dependent problems in multidimensional fluid dynamics. The simulation were performed for low Re numbers.

Daru (51) (52) simulated the Bifurcation phenomenon which served as a benchmark case for the evaluation of the accuracy of numerical schemes for unsteady viscous flow computations. The sensitivity of the results to different numerical schemes (a predictor corrector MacCormack scheme, a Harten-Yee second-order finite difference upwind scheme, and a MUSCL scheme), limiters (O3 and O3Sup limiters, Van Leer limiter, Minmod b4 limiter) the Reynolds number (Re = 200, 1000), and the grid refinement was reviewed. The Reynolds number was limited to 1000 in order to limit the grid size requirements. Convergence problems were encountered when classical shock capturing TVD schemes were used. The difficulty to obtain a converged solution for Reynolds number greater than few hundred was highlighted. It was demonstrated that the MacCormack-type scheme is more accurate for solving this kind of problem.

Daru and Tenaud in a more recent study (51) (53) used a high order coupled time-space scheme named OSMP7 (112) (113) to model the BL/ reflected shock interaction. The scheme was developed based on a coupled time and space approach and is seventh order accurate. The scheme guaranties monotonicity preserving properties as in TVD schemes but retains the original high order scheme in the vicinity of extrema at the difference of classical TVD schemes. As such, the OSMP7 scheme allows capturing sharp discontinuities without producing spurious oscillations and preserves high order accuracy in the smooth regions. The viscous fluxes were discretized by using a classical second-order centered scheme. Several Reynolds numbers were investigated (200, 500, 750, and 1000) in a square shock tube with dimensionless unit length $0<x, y<1$, incident Mach number of 2.37, Pr number of 0.73, and dimensionless dynamic viscosity of 1. Compared to classical WENO schemes, the OSMP7 exhibited a faster grid convergence, a sixth fold lower CPU cost than the WENO schemes.

Takano (45) conducted Finite-difference calculations using the flux-corrected-transport scheme, the diagonalized Beam-Warming scheme, and the Crank-Nicolson scheme to simulate the behavior of reflected-shock waves interacting with the shock-tube boundary-layers in Nitrogen and Argon gases. Computations were carried out in the end wall section of the shock tube for an indent shock Mach number of 4 and test gas conditions of 120 Pa and 298 K. It was observed that a bifurcation of the reflected-shock wave occurs and develops in Nitrogen gas but few interactions appeared for Argon gas. Takano (114) in a later study developed a finite-difference procedure which numerically solves the thin-layer Navier-Stokes equations with ionization reactions to predict ionizing non-equilibrium flows generated by strong shock waves. Simulations were carried out for bifurcated reflected-shock waves in ionizing argon in a shock tube with an incident shock Mach number of 14 in Argon at 400 Pa and 298 K. the computed flow fields agreed very well with experimental shadowgraphs for reflected-shock waves in ionizing Argon.

Kleine et al. (16) investigated the reflected shock/boundary layer interaction both experimentally and numerically using a numerical scheme based on the Euler equations. Color schlieren photographs were used to visualize the characteristic wave pattern. Good agreement was found between the simulated and the observed wave configuration.

Wilson et al. (43) investigated the reflected shock/BL interaction process both numerically and experimentally using quasi-one-dimensional and axi-symmetric numerical simulations of the complete shock tube flow. The numerical model incorporated a finite rate chemistry model, a laminar viscosity, and a moving mesh. Time-dependent simulations were compared with experimental pressure traces recorded at the NASA Ames electric-arc driven shock tube facility. The axi-symmetric simulations reproduced the bifurcation process which was found to also provide a mechanism for driver gas contamination in the stagnation region.

Burtschell and Zeitoun (49) investigated the interaction of two oblique axi-symmetrical shock waves in a uniform supersonic flow with a diverging shock both experimentally and numerically. Numerical simulations were performed by solving the Euler and Navier-Stokes equations using a second order accurate space and time scheme and AUSM+ for the viscous fluxes. It was found that the interaction between the boundary layer and the shock wave is highly affected by viscous effects and accurate modeling of the phenomenon was made possible by solving the Navier Stokes equations. The Euler approach was unsuccessful in reproducing the complicated flow structure even when the Re is very high.

Kim and Kim (55) developed a newly formulated AUSM type method named M-AUSMPW+ was developed for multi-dimensional flows. It is supposed to reduce the excessive numerical dissipation as well as preserves the monotonicity of the scheme. Kim and Kim (56) in the second part of the study developed 3rd and 5th order multi-dimensional limiting process (MLP) schemes developed in order to prevent oscillations across a multi-dimensional discontinuity. The schemes proved to be compatible with higher order interpolation schemes such as ENO type schemes. The shock boundary layer interaction phenomenon was chosen as a test case for the MLP schemes combined with the M-AUSMPW+ numerical flux. In addition, combinations of several limiters including the Super-bee, the minmod, and the van leer, MLP Super-bee, MLP3, and MLP5 limiters with M_AUSMPW+ and 2nd order TVD schemes such as ROE FDS were investigated.

This test problem was also studied by Daru and Tenaud (53) (52) (51) (41) and Sjogreen and Yee (54). The simulations were carried out in a 2-D square shock tube with a Reynolds number of 200 and a constant viscosity. It was shown that TVD with van Leer limiter scheme is very diffusive while MLP3 and MLP5 yielded almost the same results as MLP-Super-bee limiter. The results obtained with MLP5 with M-AUSMPW+ were more accurate than the results acquired with van Leer limiter with AUSMPW+. The height and angle of the primary vortex which is sensitive to numerical dissipation were accurately modeled, while the van Leer limiter with AUSMPW+ yielded a smaller vortex.

Bulovich et al. (50) simulated the interaction of the reflected shock wave from the flat end of a cylindrical shock tube with the boundary layer formed at the side wall. The entire shock tube geometry was represented as an axi-symmetric model and the Navier–Stokes equations were integrated in the thin layer approximation using a predictor–corrector scheme which is second order accurate in space and time.

Graur et al. (48) investigated the efficiency of three numerical approaches to describe the complex phenomenon of shock wave boundary layer interaction. Computations were carried out based on a kinetic approach (Direct Simulation Monte Carlo method) and on two continuum approaches (Navier-Stokes equations and quasi gas dynamic equations). The flow was assumed axi-symmetric, and the boundary layer was modeled as laminar. The Navier-Stokes approach was based on an exact Riemann solver coupled with the AUSMDV solver with second-order MUSCL extrapolation. It was found that among all three approaches, the slip condition improves the agreement with the experimental data for the continuum approach.

Narayanswami et al. (115) simulated the interaction between crossing shock waves and a flat plate turbulent boundary layer at Mach 8.3 by solving the full 3-D mean compressible Reynolds-averaged Navier-Stokes (RANS) equations incorporating the algebraic turbulent eddy viscosity model of Baldwin and Lomax. Pressure profile results agreed well with experimental data however surface heat transfer was significantly over-predicted due to limitations of the Baldwin Lomax turbulence model.

Bifurcation Modeling

Figure 49 shows a schematic of the bifurcated structure and the corresponding ideal side wall static pressure variation model reproduced from Petersen and Hanson (26) and originally developed by Mark (9). The terminology adopted by Petersen and Hanson (26) is employed herein to refer to the different instances of the bifurcated structure passage. As outlined by the ideal pressure model, the bifurcation structure is characterized by three main features. First, the static pressure rises at t_o as a result of the passage of the front foot or oblique shock wave (OA) followed by the second oblique shock (AC) whose main function is to render the flow parallel to the shock-tube side walls. The pressure remains constant until the passage of the separated bubble (CD) at time t_D. Then pressure rises again and reaches an overshoot at time t_p due to the arrival of the stagnation streamline. Lastly, after time t_e , the static pressure relaxes to the ideal pressure P_5 when the bifurcation structure has completely passed over the pressure port location.

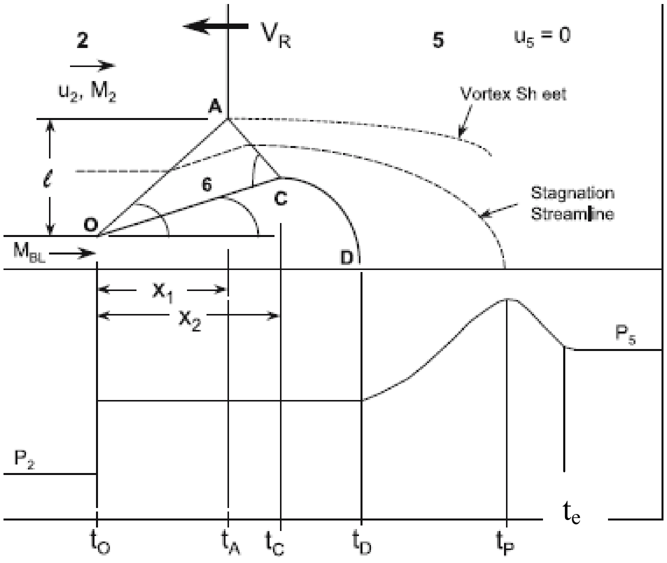

Figure 49: Schematic of the bifurcation structure and corresponding ideal side wall static pressure trace versus time (26)

In reality, between the first rise in pressure through the oblique shock and the passage of the separated bubble (CD), the pressure is not constant, and it is characterized by strong pressure gradients due to the embedded vortices and unstable shear layer in the separation zone adjacent to the side wall (44). This effect is evident in Figure 49 (a) where the side wall static pressure trace is shown for a non-ideal numerical simulation of bifurcation in an axi-symmetric, 15.2-cm diameter Helium-driven shock tube. The side wall pressure trace was monitored at a location 16 mm from the endwall. The conditions behind the reflected shock wave are a temperature of 950 K, pressure near 1 atm, and the test gas being Air. The deviation from the ideal theory is evident, and the pressure between instances t_o and t_D is no longer constant. Because the passage of the normal reflected shock cannot be detected from the side wall pressure trace alone, the endwall center port pressure was monitored and the time of passage of the normal reflected shock agrees with time t_A as shown in Figure 49 (b). We denote time zero, the time corresponding to the passage of the normal portion of the reflected shock. Other studies investigating bifurcation in shock tubes as in Petersen and Hanson (26) resorted to laser diagnostics to quantify the time of the main reflected-shock passage which was detected by a schlieren spike in the transmitted laser intensity. In their study, empirical correlations were also developed for the different time passages; Δt_{AO} the time of normal shock passage, Δt_{DO} the time of separation zone passage, Δt_{PO} the time of end of the stagnation streamline passage, and Δt_{EO} the time of the entire interaction zone passage, in addition to a correlation describing the height of the bifurcated foot as a function of the incident shock mach number, specific heat ratio, and the mixture molecular weight. The height of the bifurcated foot does not consider the thickness of the boundary layer which can be determined from experimental and numerical measurements. The correlations provided in Table 8 were developed for gas mixtures with molecular weights and specific heat ratios ranging between 14.7 and 44 and between 1.29 and 1.51 respectively and for pressures and temperatures behind the reflected shock covering a range of values between 11 to 265 atm and 780 to 1740 K, respectively. However, the bifurcation structure did not show any dependence on pressure, and extrapolation to lower values other than the range specified should not affect the validity of the correlation. Another important factor is the location at which the measurement was taken. Petersen and Hanson's study (26) used a location of 20 mm from the endwall. For locations relatively close to the endwall, the size of the bifurcated foot varies linearly with distance from the endwall and for locations relatively far from the endwall, the height of the bifurcated foot varies at a lower rate (26). The results indicate the bifurcation structure height is strongly dependent on the specific heat ratio γ_2 such that the bifurcated foot height increases with decreasing γ_2. Therefore it is expected to see a more defined bifurcation structure when diatomic and polyatomic are used in the test gas mixture as opposed to monatomic gases. The shock strength and mixture molecular weight have an influence on the bifurcation zone height as well, such that the bifurcated foot height increases with increasing shock strength and decreasing mixture molecular weight, however with a lesser intensity than specific heat ratio effect

Table 8: Empirical correlations describing the bifurcation structure main time and length characteristics (26)

Parameter	Description	Correlation	r^2	Uncertainty
Δt_{OA} (μs)	Time to normal shock passage	$4.6M_s^{0.66}\gamma_2^{-7.12}M^{0.57}$	0.985	± 1 μs
Δt_{DO} (μs)	Time to separation zone passage	$190 - 140\gamma_2 + 0.66M$	≥ 0.960	± 3 μs
Δt_{PO} (μs)	Time to end of stagnation streamline passage	$425 - 322\gamma_2 + 1.53M$	≥ 0.960	± 3 μs
Δt_{EO} (μs)	Time to entire interaction zone passage	$508 - 390\gamma_2 + 2.45M$	≥ 0.960	± 5 μs
l (mm)	Bifurcated foot height	$7.5M_s^{1.07}\gamma_2^{-2.662}M^{-0.37}$	0.980	± 0.2 mm

γ_2 is the specific heat ratio for conditions behind the incident shock wave Ms. M is the test gas mixture molecular weight.

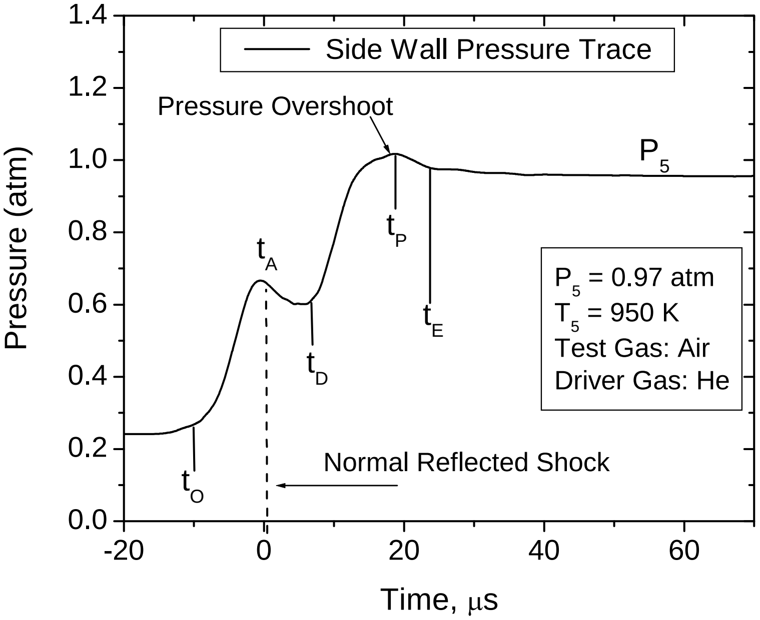

a) Side wall static pressure

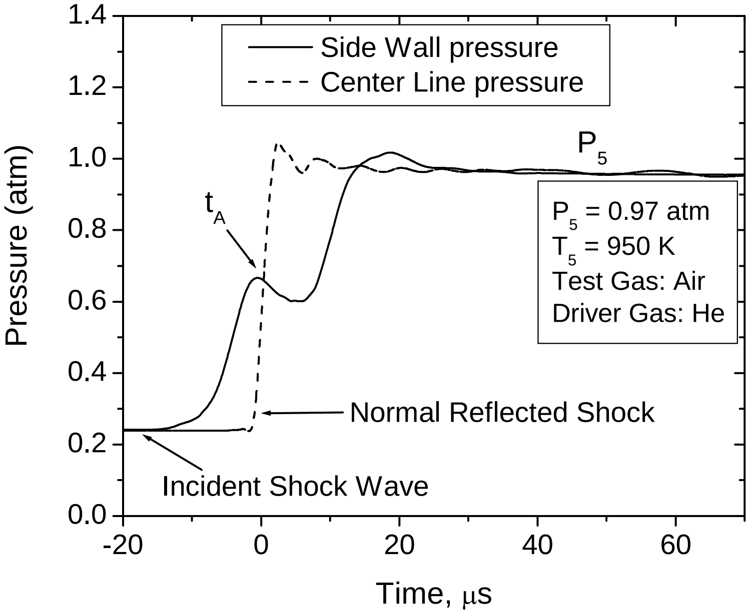

b) Axial static pressure

Figure 50: Viscous axi-symmetric simulation of a) the side wall and b) the center static pressure at a location of 16 mm from the endwall. Time = 0 corresponds to passage of the normal portion of the reflected shock wave.

Bifurcation Flow Fields

Provided in Figure 51 are the pressure contours in the shock tube endwall section describing the development of the bifurcation structure up to a distance of 22.5 cm from the endwall. The interaction is taking place in an air mixture with an average temperature and pressure behind the reflected shock of 950 K and 1 atm, respectively. The frames given in Figure 51 show the development of the bifurcation structure at different time instances. The time frame contours are given at intervals of approximately 50 μs. The corresponding time instances which are given on the right of each frame represent the elapsed time from the shock reflection.

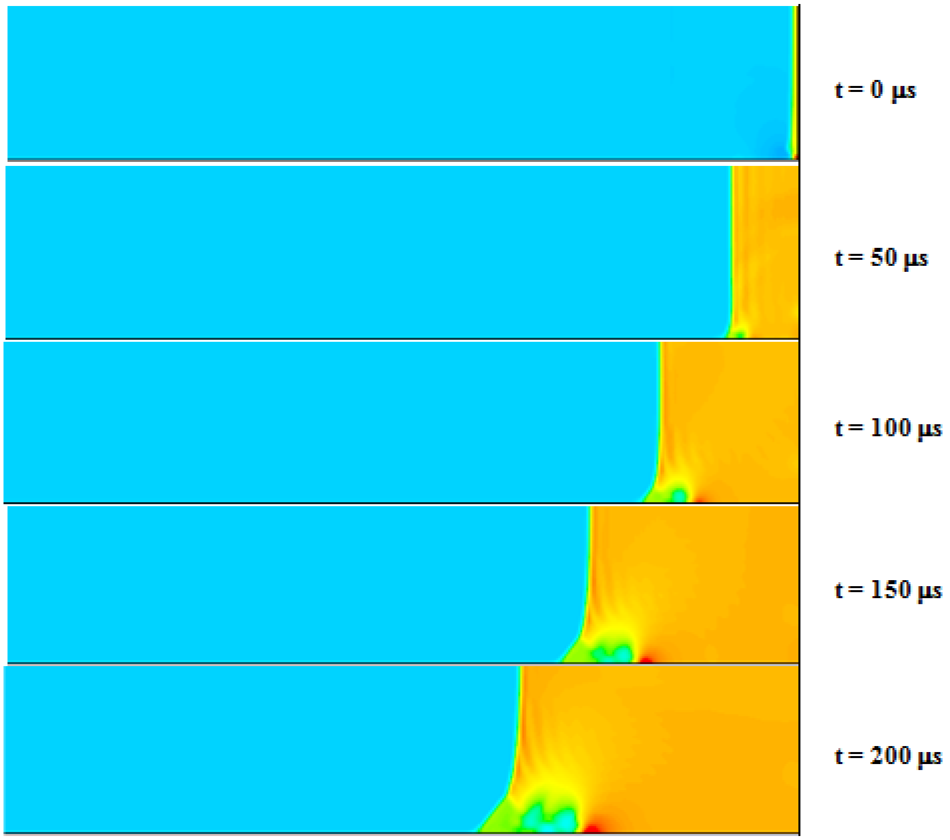

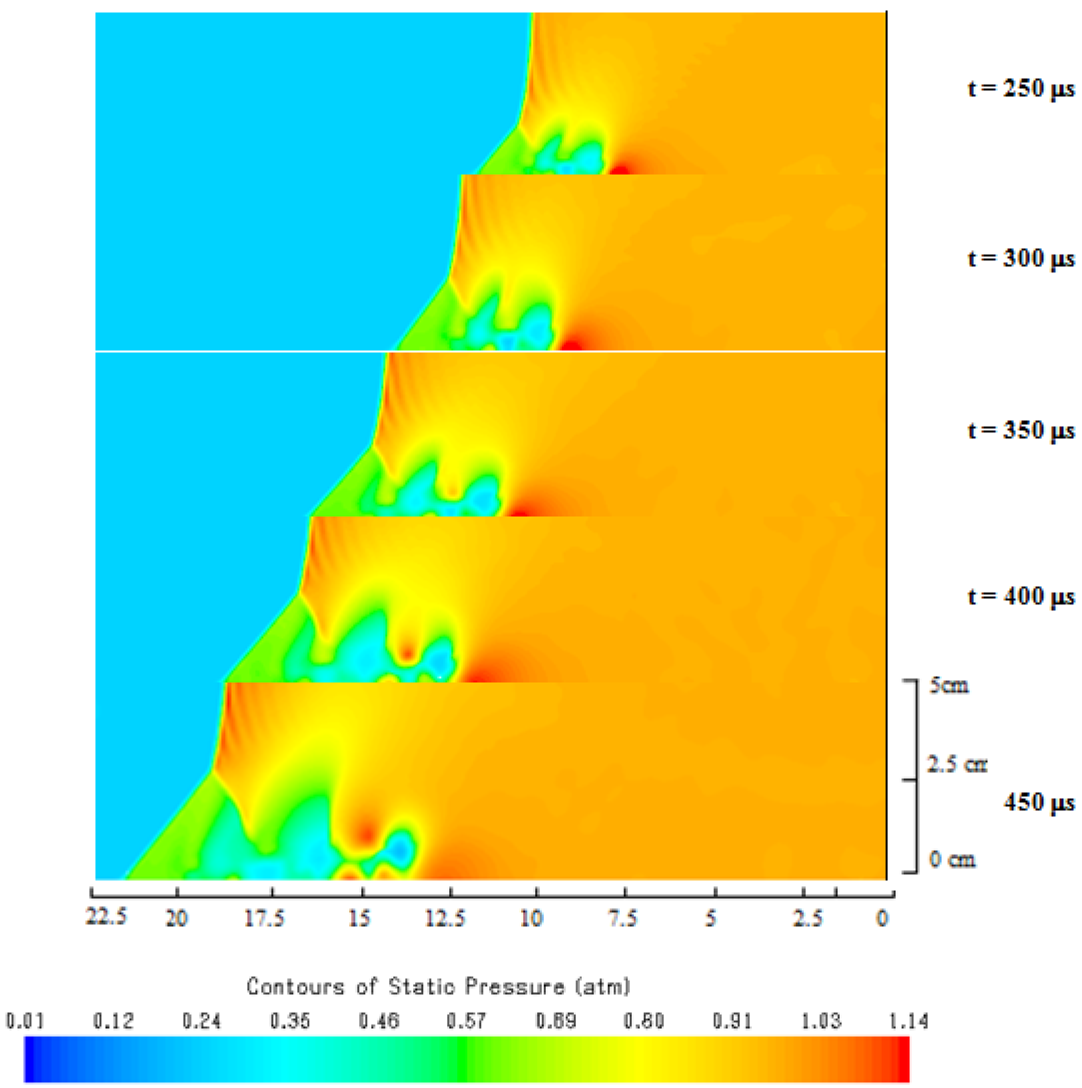
t = 250 µs
t = 300 µs
t = 350 µs
t = 400 µs
5cm
2.5 cm
450 µs
0 cm
22.5
20
17.5
15
12.5
10
7.5
5
2.5
0
Contours of Static Pressure (atm)
0.01
0.12
0.24
0.35
0.46
0.57
0.69
0.80
0.91
1.03
1.14

a)

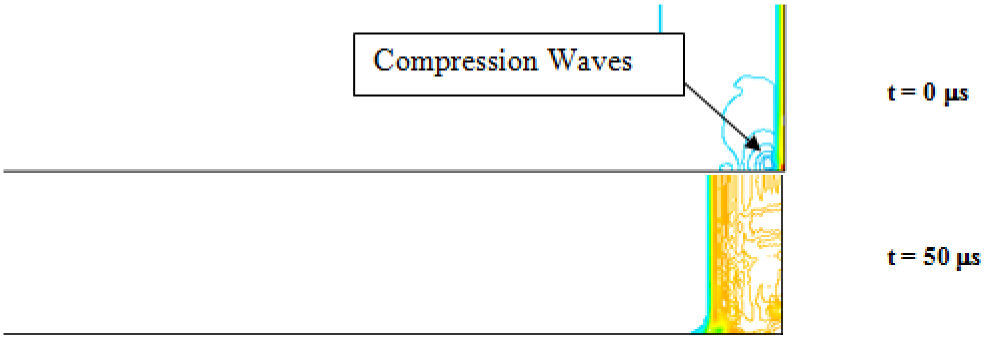
Compression Waves
t = 0 µs
t = 50 µs

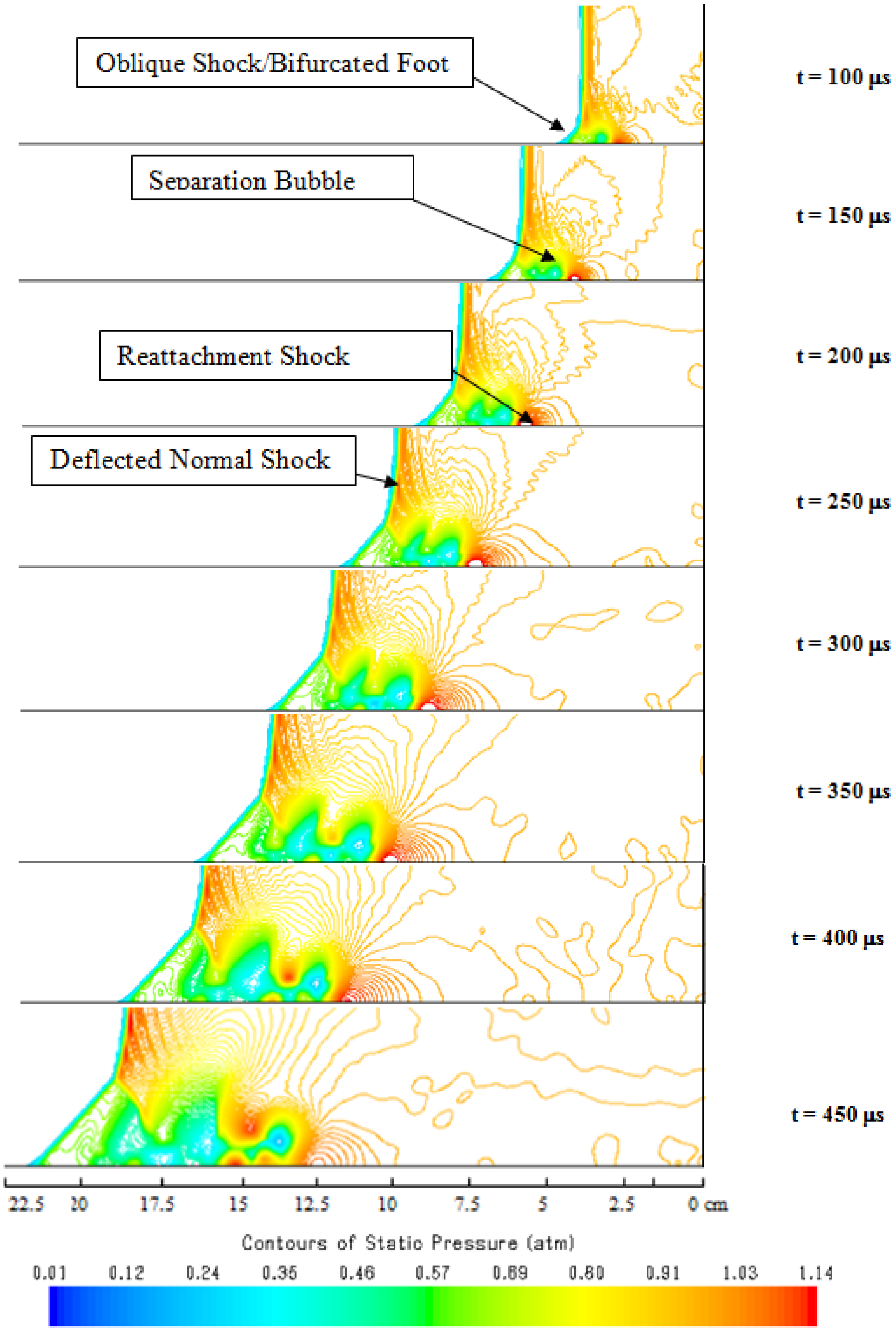

b)

Figure 51: The filled (a) and non-filled (b) static pressure contours showing the time evolution of the bifurcation structure in the endwall region of the shock tube at the conditions behind the reflected shock wave of T_5= 950 K and P_5 = 1 atm in Air Test Gas

Time 0 is denoted as the moment the incident shock wave hits the endwall. Initially, upon the first interaction of the reflected shock with the boundary layer, a very weak bifurcated structure forms such that the lambda-like shape is not well defined. This is true for a distance from the endwall up to 2.5 cm, then the bifurcation structure becomes more defined, and the triple-shock system can be clearly depicted. Also, important to note from the initial interaction, are the hot jets which form close to the endwall in the corners. These jest come from the sudden movement of the hot endwall fluid which gets displaced in a counterclockwise direction. This can be detected from the temperature contours given in Figure 52. The hot jets which look like hot pockets reach a temperature of 1050 K, about 100 degrees higher than the average flow temperature. This can potentially trigger local autoignition when the right thermodynamic conditions are available. Although this is not a concern when nonreactive flow is modeled, the flow fields in the endwall region need to be closely monitored and correctly represented. Any sign of non-ideal behavior in the endwall region is an indication that the kinetic behavior in a reactive shock-tube mixture may no longer be occurring ideally.

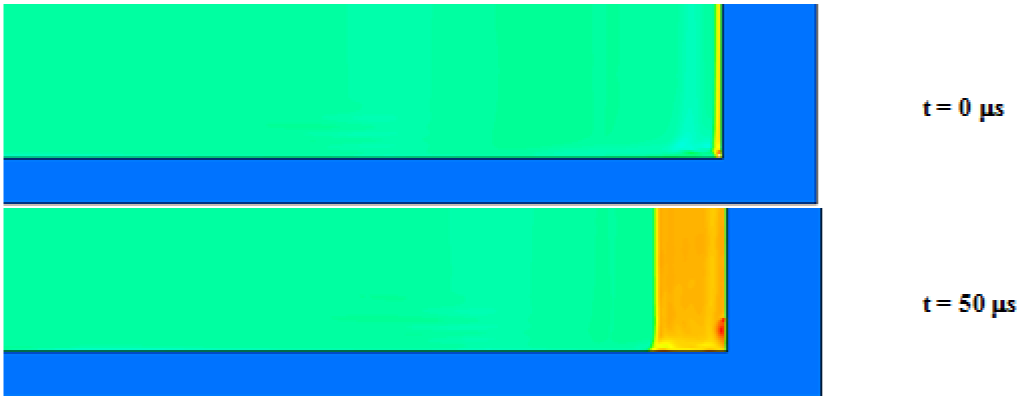

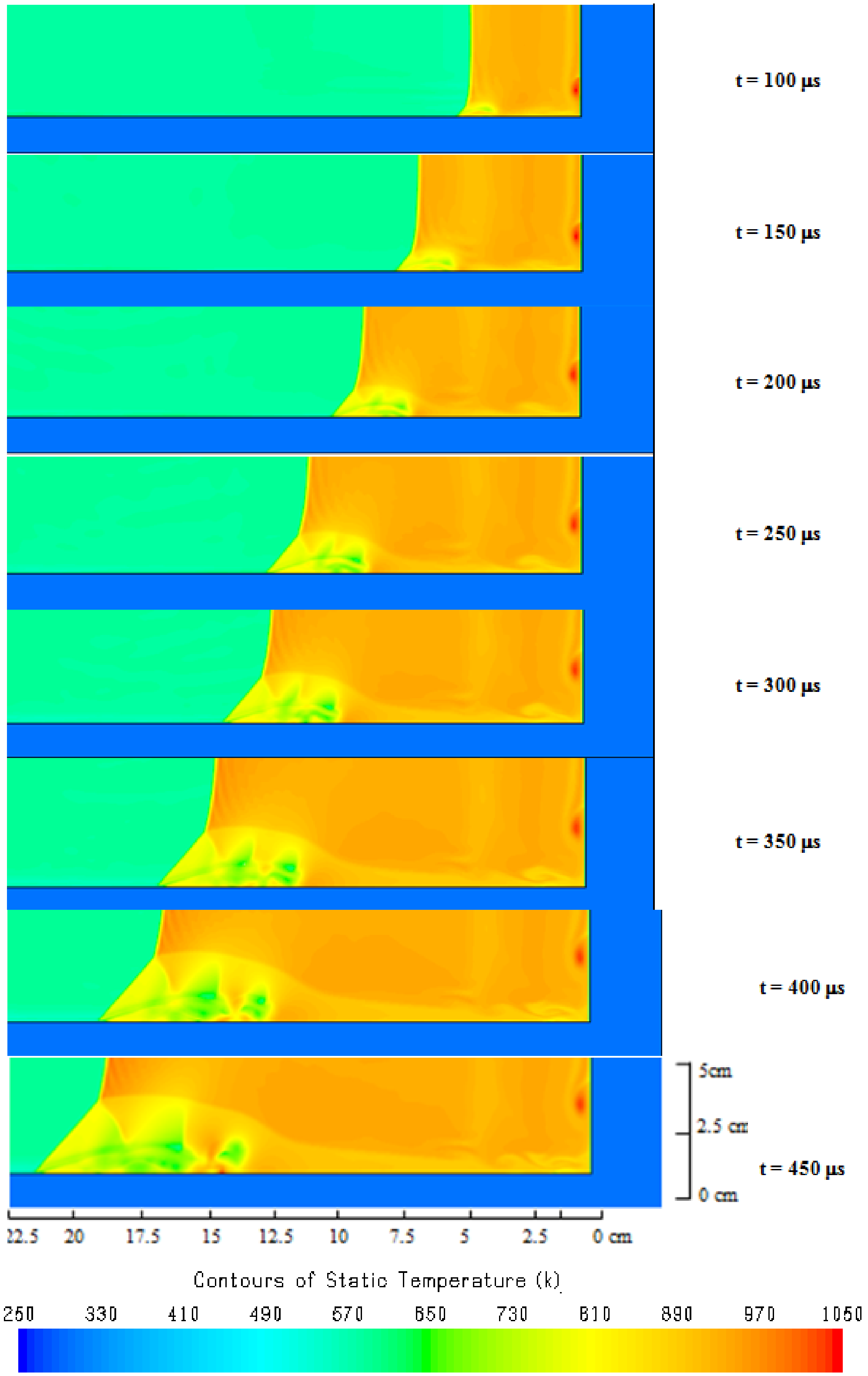
t = 100 µs
t = 150 µs
t = 200 µs
t = 250 µs
t = 300 µs
t = 350 µs
t = 400 µs
t = 450 µs
5cm
2.5 cm
0 cm
22.5
20
17.5
15
12.5
10
7.5
5
2.5
0 cm
Contours of Static Temperature (k)
250
330
410
490
570
650
730
810
890
970
1050

a)

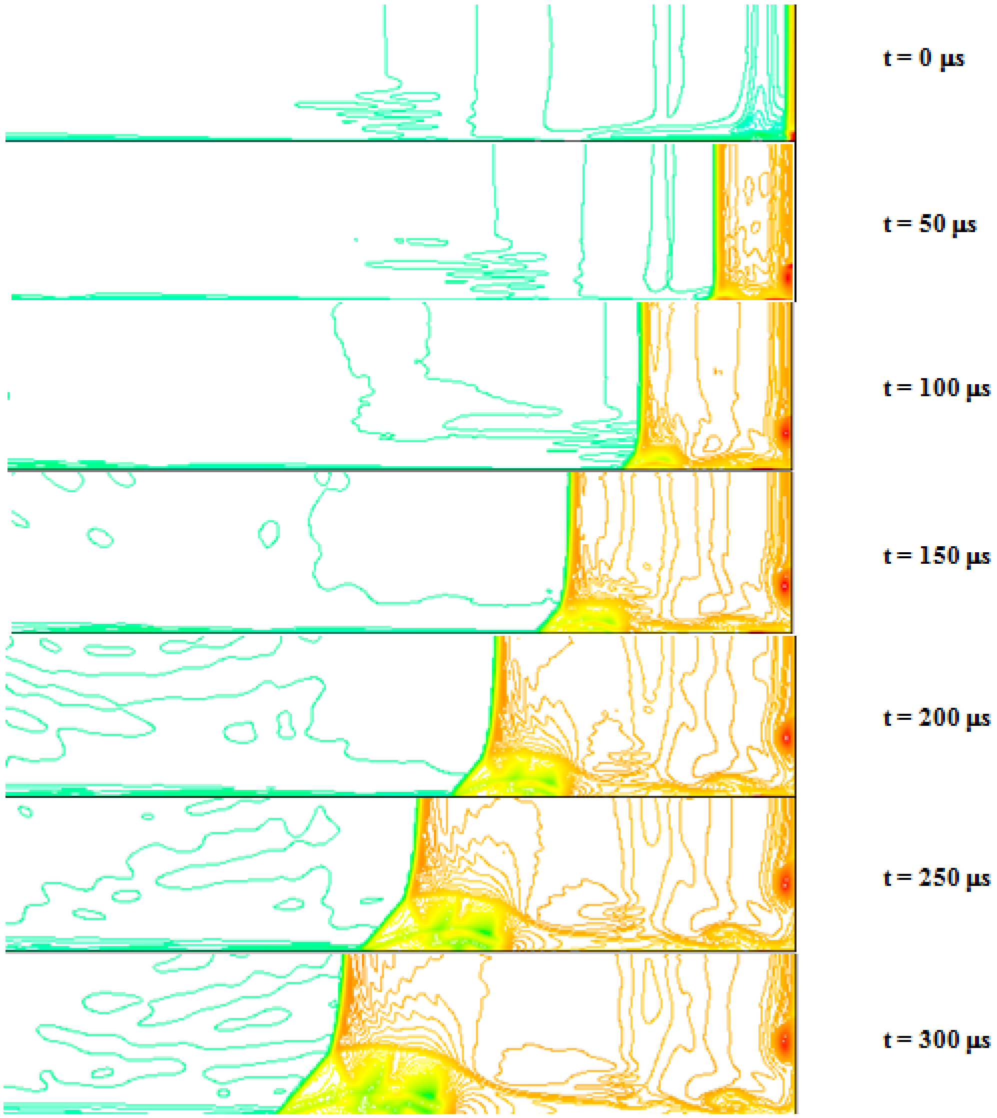
t = 0 µs
t = 50 µs
t = 100 µs
t = 150 µs
t = 200 µs
t = 250 µs
t = 300 µs

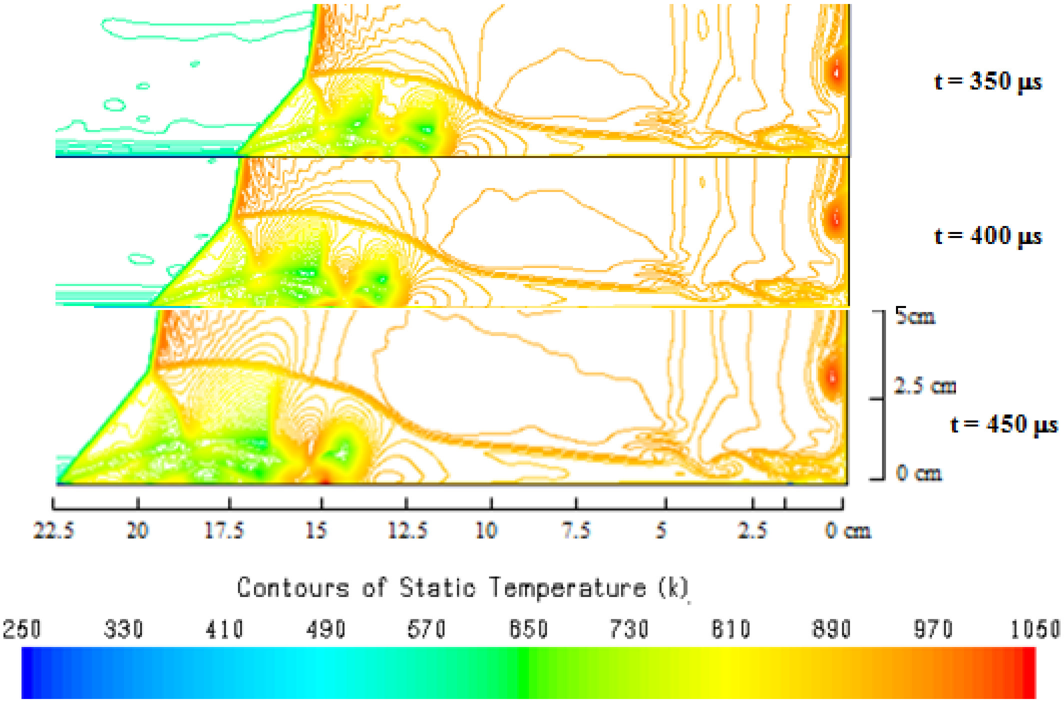

b)

Figure 52: The filled (a) and non-filled (b) temperature contours showing the time evolution of the bifurcation structure in the endwall region of the shock tube at the conditions behind the reflected shock wave of T_5= 950 K and P_5 = 1 atm in Air Test Gas

The interaction of the boundary layer with the reflected shock wave is due to the boundary layer flow induced by the incident shock which has a lower stagnation pressure than the flow behind the normal reflected shock wave and which is accompanied by compression waves. These compression waves can be seen in Figure 51 (b) from the pressure contours at time 0 µs which corresponds to the arrival of the incident shock to the shock-tube end wall. The interaction of the reflected shock with these compression waves result in the formation of the lambda-like shock structure which is made up of the bifurcation foot, the tail shock, and the triple point at which the slip line originates. The slip line is the separation point between the flow behind the normal reflected shock and the flow accumulated in the bifurcation zone due to their different residual velocities (44). As the reflected shock wave is advancing forward, the boundary layer fluid accumulates under the bifurcated foot and, according to Weber et al. (44) can travel up to 8 cm in the viscous region due to a favorable pressure gradient caused by the expansion of the flow following the area change under the bifurcated foot and the flow displacement in the viscous region. When the boundary layer fluid arrives at the reattachment shock, the rear of the interaction zone, it encounters an adverse pressure gradient causing the boundary layer flow to stagnate and to reverse direction. The motion of the boundary layer fluid in the forward and reversed direction results in the development of a viscous vortical region near the shock-tube side wall. Eventually, more fluid from the boundary layer is being entrained in the viscous region as the reflected shock is moving downstream. As a result, the bifurcation foot height increases linearly with distance from the endwall until it interacts with the contact surface, where the bifurcation structure loses its strength and the bifurcated foot height is greatly reduced. As a result of continuous displacement of the viscous region and the inviscid flow adjacent to the boundary layer, shock and expansion waves form; this is particularly evident in the reattachment shock, which is responsible for the pressure overshoot at time t_p as shown from the static side wall and center pressure traces in Figure 51 a and Figure 51 b .The reattachment shock whose main function, just like the second oblique shock wave (AC), is to turn the flow parallel to the wall resulted in a slight compression of the flow denoted by the pressure overshoot at time t_p followed by the reattachment of the flow to the side wall after the interaction zone has completely passed at time t_e . The relatively inviscid flow adjacent to the boundary layer that also has to flow through the bifurcation structure experiences a double compression effect, first by the first oblique shock (or the bifurcated foot) then by the second oblique shock or tail shock. Consequently, at the end of the interaction zone denoted by the pressure overshoot and shock reattachment, the flow is turned parallel to the shock-tube side wall and is of the same conditions as the flow compressed by the normal portion of the reflected shock.

As the bifurcation structure progresses forward, the boundary layer flow induced by the incident shock has a lower stagnation pressure than the flow behind the normal reflected shock wave and accumulates behind the bifurcated foot front, forming a recirculation zone which separates and forms a separation bubble. While the main flow adjacent to the boundary layer enters the region between the lambda shock and the separation bubble, flows past the bubble and rolls inwards towards the endwall corner. The energetic wall jet (112) bounded by the highly supersonic shear layer is carrying the cold flow from the boundary layer flow and impinges on the slip line and side and end walls in an oscillatory motion impacting the local properties of the flow. As a result, the flow temperature in the interaction zone drops significantly. The average, center and side wall temperature and pressure properties were monitored at a location 16 mm from the endwall, which is the location of interest for chemical kinetics experiment measurements herein, and are given in Figure 54 (a) and Figure 54 (b) respectively. The side wall temperature has significantly dropped as a result of both heat transfer effects and the cold boundary layer fluid accumulating under the bifurcation structure. The side wall pressure profile shows a very oscillatory behavior which is attributed to the continuous impingement of the energetic wall jet on the side wall even after the interaction zone has completely passed the endwall region, thereby impacting the local flow properties.

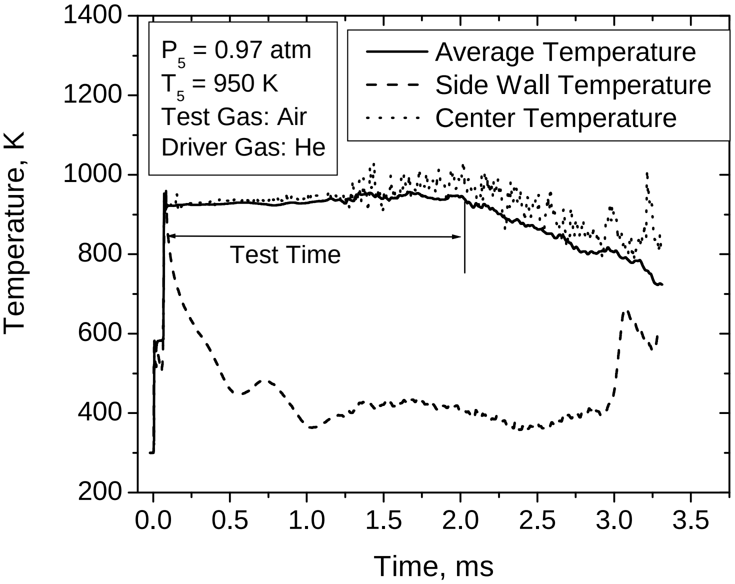

a) Temperature Profiles

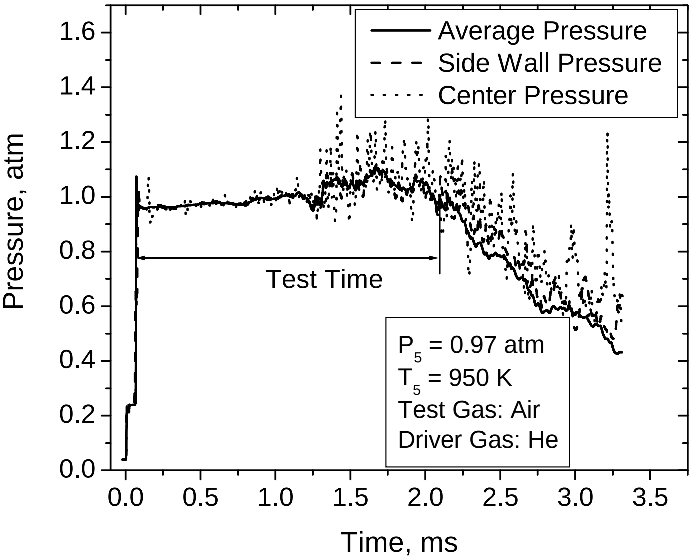

b) Pressure Profiles

Figure 53: Time evolution of the average, center, and side wall a) temperature and b) pressure profiles at the average conditions of 950 K and 0.97 atm. The test gas is air and the driver gas is Helium. The effect of the reflected shock/boundary layer interaction on the local and average flow properties is well represented

The supersonic shear layer as the name indicates reaches a Mach number of 3. This is illustrated in the Mach number contours provided in Figure 54. The reduced area of the viscous region causes the flow to expand and to accelerate. As a result, the shear layer Mach number increases to 3 and then decreases near the reattachment region where the flow is compressed again at the end of the interaction zone. The unstable supersonic shear layer has been reported in the studies of Weber et al. (44), Glowacki et al. (116), Havener et al. (117), and and Daru and Tenaud (52) (53) (51). Also important to note is the supersonic region right before the interaction of the boundary layer with the reflected shock wave. We previously mentioned that the boundary layer flow induced by the incident shock is accompanied by compression waves. This phenomenon is highlighted in the pressure contours in the early stages of the interaction which is also consistent with the high Mach number region.

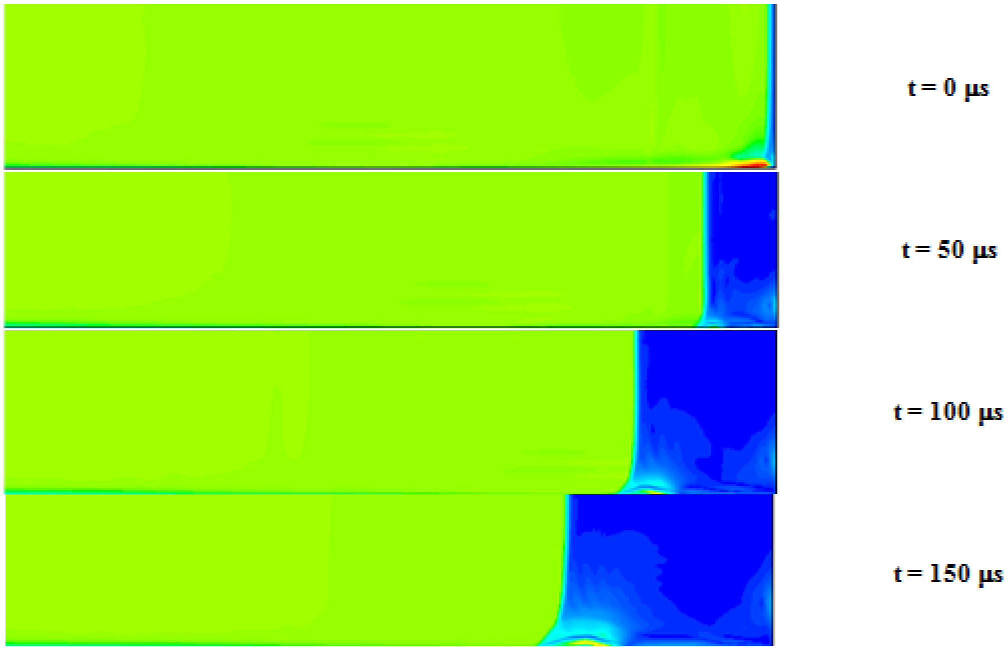

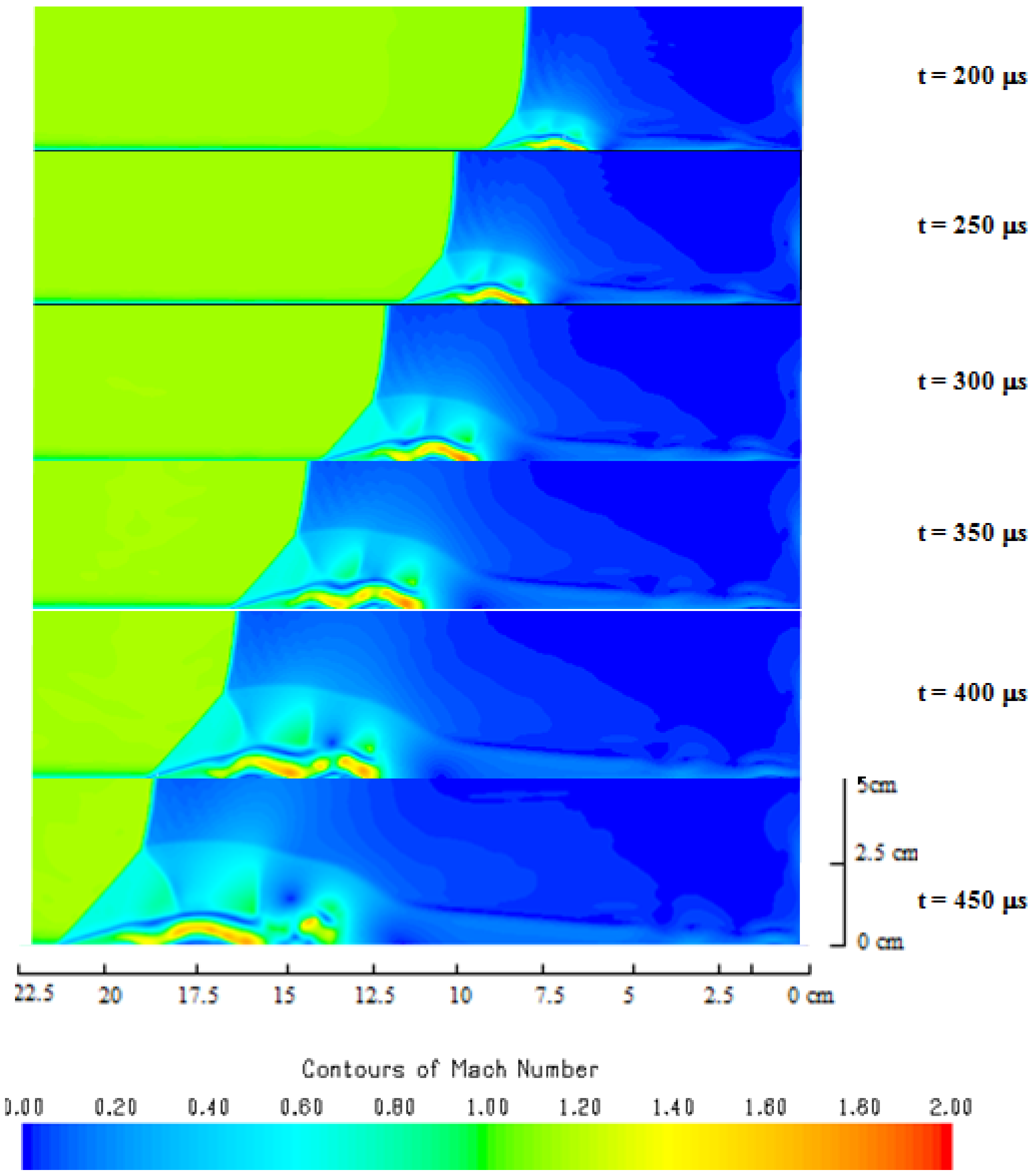
t = 200 µs
t = 250 µs
t = 300 µs
t = 350 µs
t = 400 µs
t = 450 µs
5cm
2.5 cm
0 cm
22.5
20
17.5
15
12.5
10
7.5
5
2.5
0 cm
Contours of Mach Number
0.00
0.20
0.40
0.60
0.80
1.00
1.20
1.40
1.60
1.60
2.00

a)

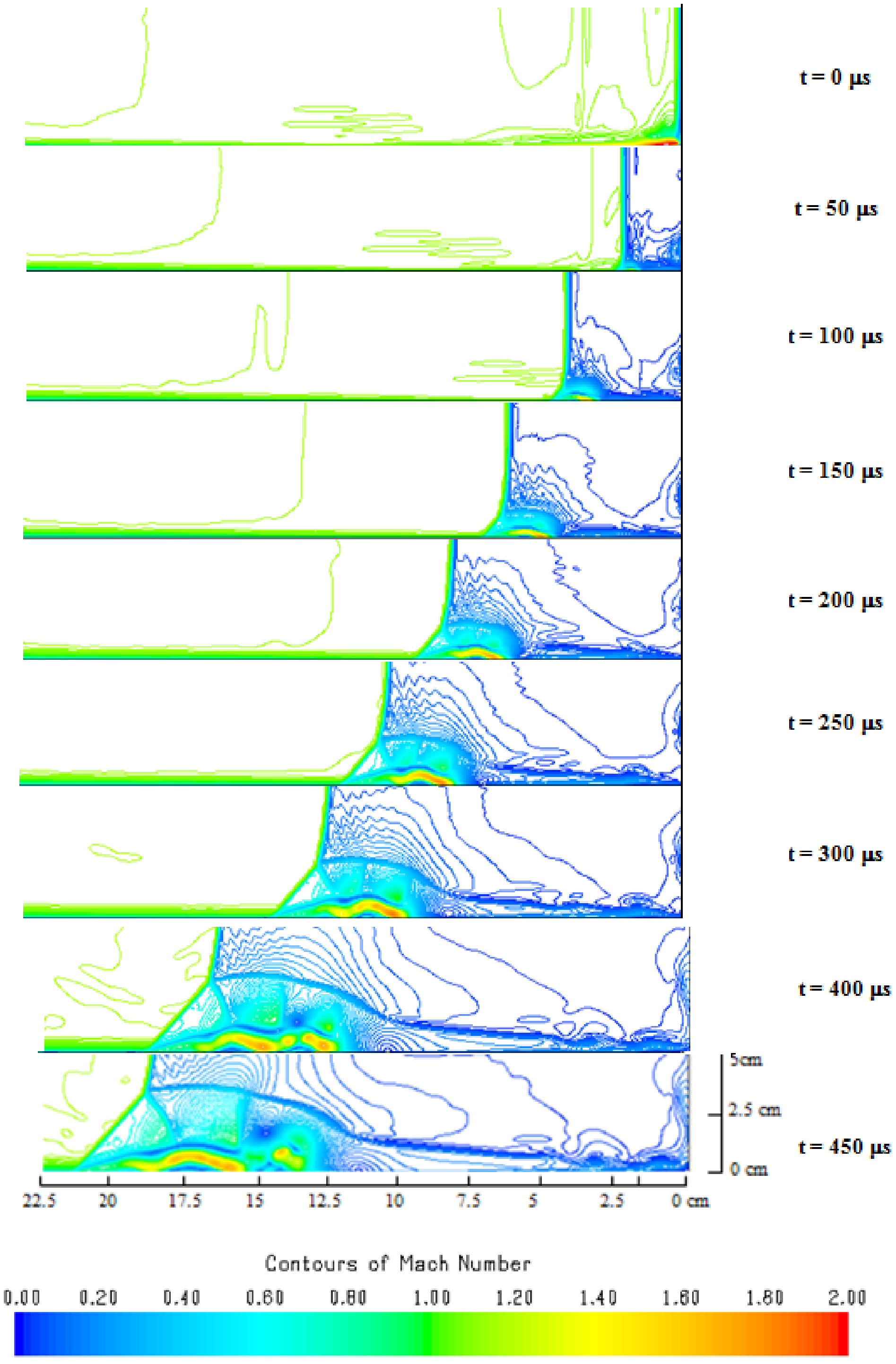

b)

Figure 54: The filled (a) and non-filled (b) Mach number contours showing the time evolution of the bifurcation structure in the endwall region of the shock tube at the conditions behind the reflected shock wave of T_5= 950 K and P_5 = 1 atm in Air Test Gas

The oscillatory motion of the jet between the side wall and the slip line due to the viscous stresses results in the formation of the counter-rotating vortices of positive and negative vorticity as has been reported by Daru and Tenaud (51). Figure 55 shows the vorticity contours and the embedded vortices between the side wall and the shear layer which grow in size and in number as the reflected shock moves away from the end wall. According to Daru and Tenaud the number of counter-rotating vortices is proportional to the velocity of the jet and becomes more pronounced at the lower Re numbers (53).

These vortices of both small and large scales appear to be made up of three layers of fluid with different temperatures, as Daru and Tenaud pointed out in their simulation results (51). The first layer is in the center and is comprised of the hot, shocked fluid; the next layer of fluid is colder and comes from the boundary layer and the third layer is the coldest due to the cold flow around it in the recirculation zone. The vorticity flow fields are similar to the results obtained by the numerical studies of Daru and Tenaud (52) (53) (51).

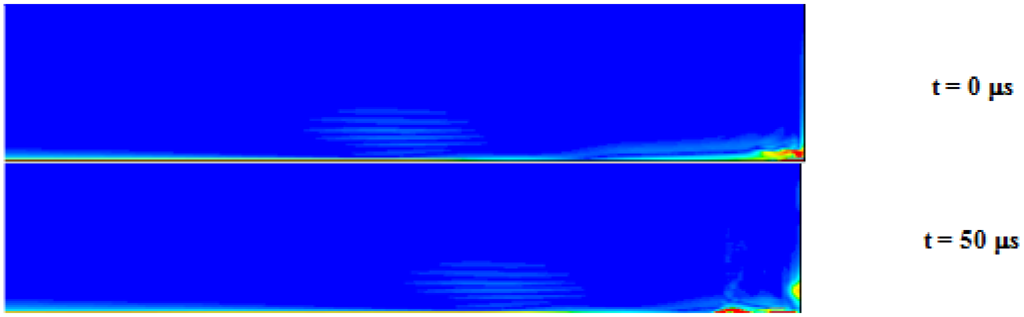

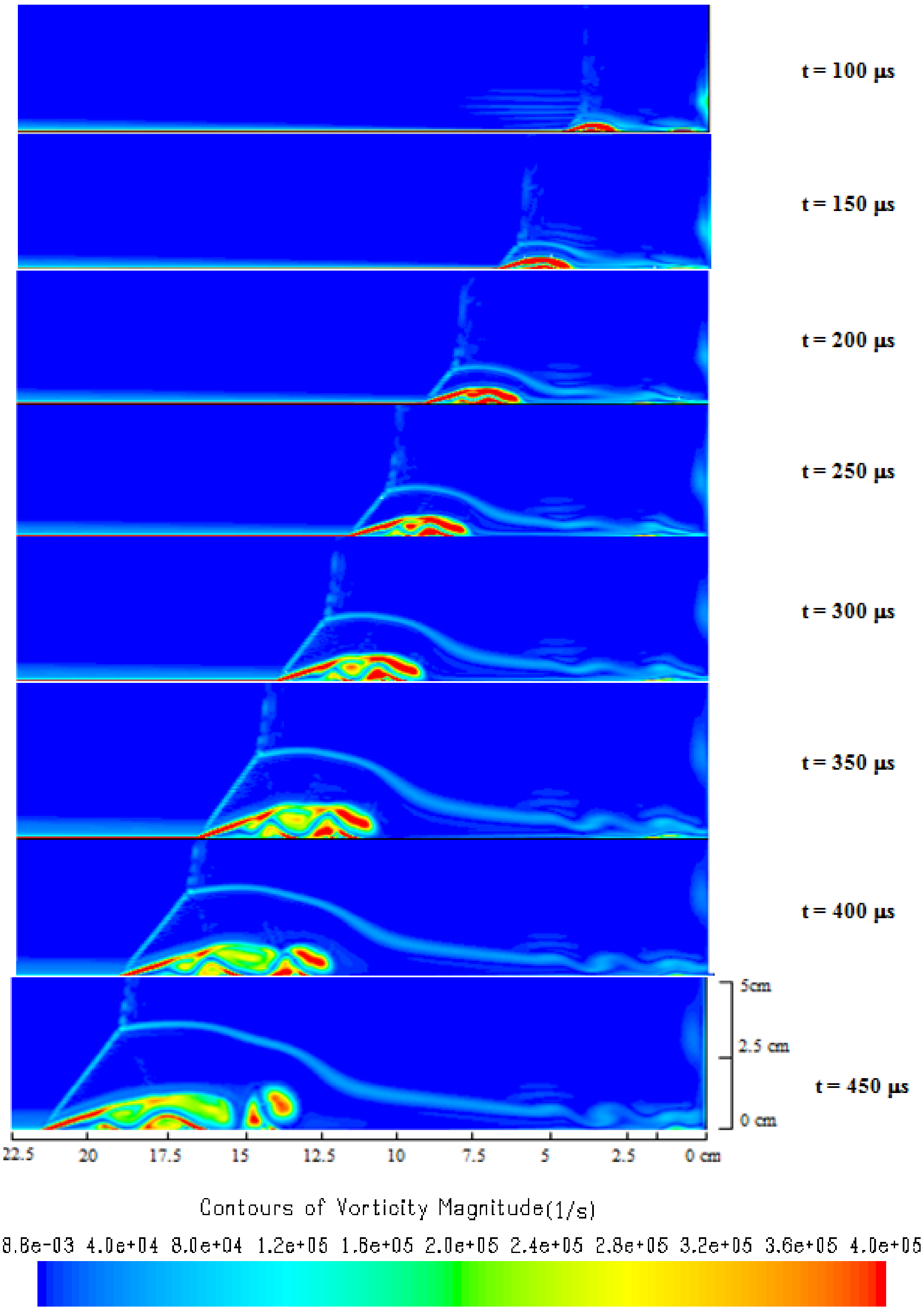
t = 100 μs
t = 150 μs
t = 200 μs
t = 250 μs
t = 300 μs
t = 350 μs
t = 400 μs
5cm
2.5 cm
t = 450 μs
0 cm
22.5
20
17.5
15
12.5
10
7.5
5
2.5
0 cm
Contours of Vorticity Magnitude(1/s)
8.6e-03
4.0e+04
8.0e+04
1.2e+05
1.6e+05
2.0e+05
2.4e+05
2.8e+05
3.2e+05
3.6e+05
4.0e+05

a)

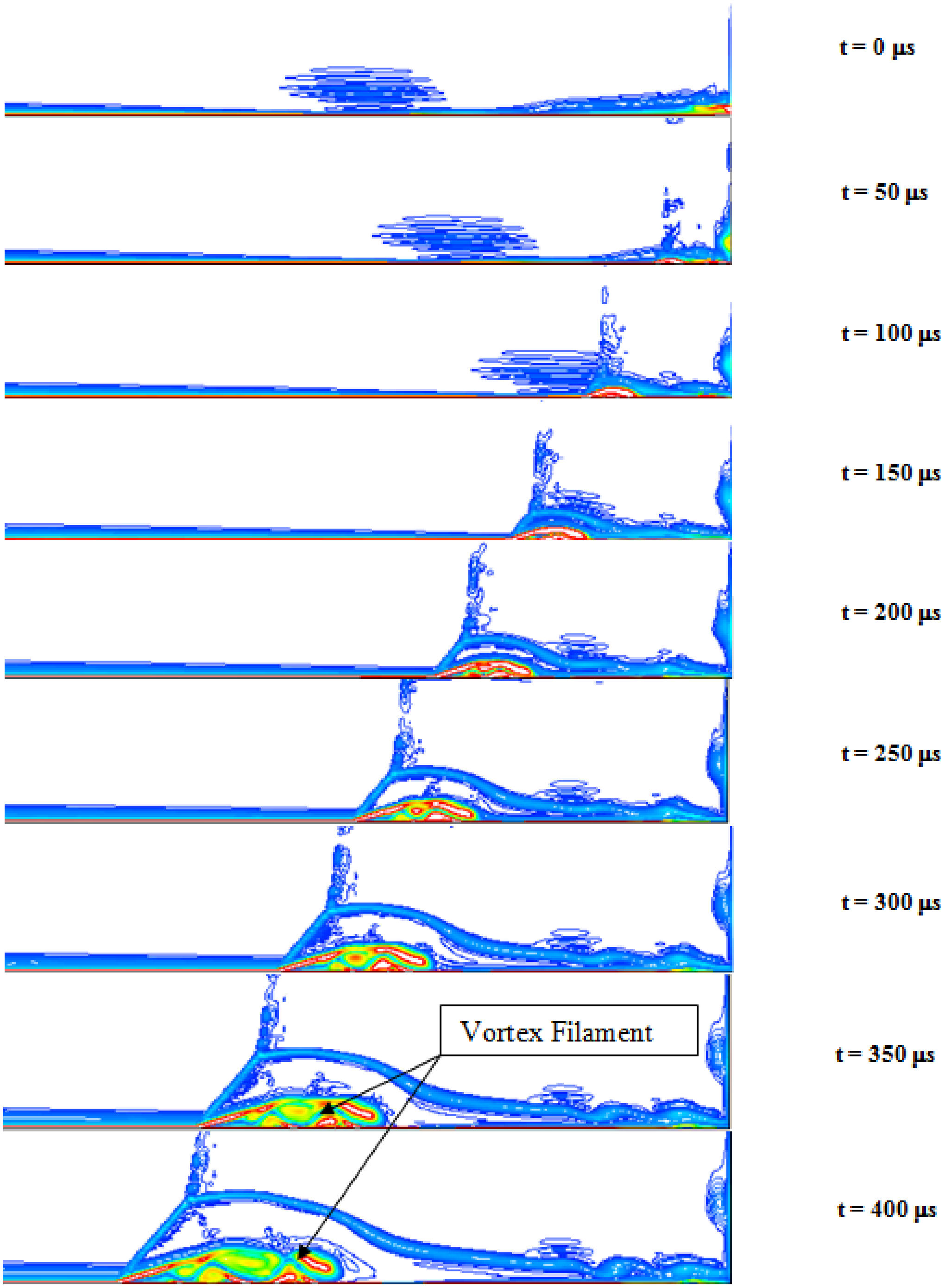
t = 0 μs
t = 50 μs
t = 100 μs
t = 150 μs
t = 200 μs
t = 250 μs
t = 300 μs
Vortex Filament
t = 350 μs
t = 400 μs

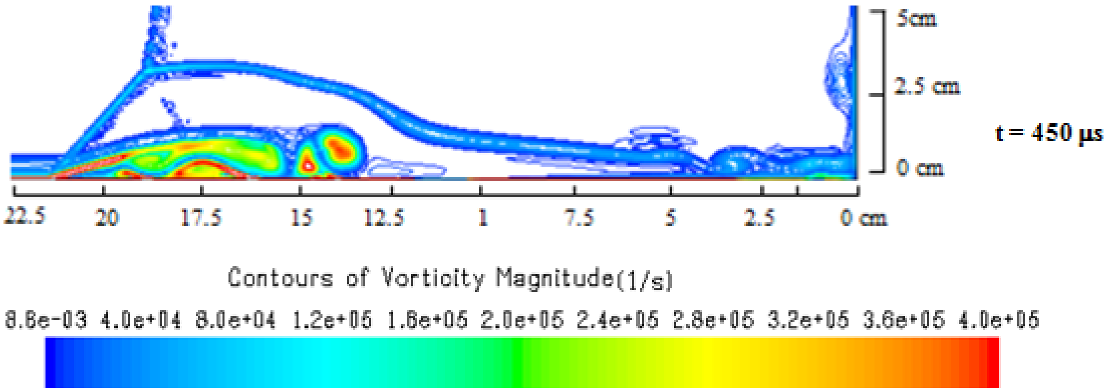

b)

Figure 55: The filled (a) and non-filled (b) vorticity contours showing the time evolution of the bifurcation structure in the endwall region of the shock tube at the conditions behind the reflected shock wave of T_5= 950 K and P_5 = 1 atm in Air Test Gas

As the vortices continue to interact with the boundary layer, they get repulsed out of the boundary layer due to their high entropy. Consequently, the vortices are deformed giving birth to a vortex filament which elongates in the direction of the slip line due to the shear stresses between the boundary layer fluid and the core flow. This result is illustrated in the vorticity contours in Figure 55 where the vortex filament becomes evident at 400 μs. Eventually, the vortex filament breaks, and the co-rotating vortical structures with the same vorticity-sign merge together. The vortical structures look more elongated than discrete, organized structures. Similar flow structures and observations have been reported in the studies of Daru and Tenaud (51) (112). At 450 μs, the biggest vortical structure on the far right of the interaction zone is completely expelled out of the boundary layer due to the increased entropy of the eddy structure and the decreased entropy at the wall. This process is repeated, and the next vortical structure on the far right of the interaction zone looses entropy and bursts out. Eventually there are no more vortices remaining in the boundary layer, which loses its structure and the flow finally reattaches at the wall. Also illustrated in the vorticity contours is the slip line breakup due to entropy changes as the reflected shock is traveling downstream. Smaller-structure vortices are also present in the corners of the endwall. This effect is due to the countercurrent jets which formed at the early stages of the bifurcation structure development and upon the sudden interaction of the boundary layer with the endwall which resulted in the flow displacement in a rolled up fashion.

The supersonic shear layer and embedded vortices impact the slip line which gets deformed, and small oblique shocks called shocklets are formed on its surface and on the tail shock causing the deformation of the tail shock (52). Consequently, the main portion of the reflected shock is also curved at the triple point. This result is evident from the iso-contour lines at the later stages of the interaction in Figure 51, Figure 52, and Figure 54. In addition, the outer edge of the slip line is deflected, and as a result mixing is promoted between the flow in the separation region and the unaffected region thus potentially causing more vortices to form (52).

Pseudo Shock Train

The time evolution of the bifurcation structure in the shock tube beyond a distance of 22.5 cm and up to 65 cm from the endwall is illustrated by the means of the temperature flow fields as shown in Figure 56. The temperature profiles are shown from a time frame of 700 μs to 1.26 ms. The entrainment of the bifurcation structure downstream the shock tube is accompanied by the continuous displacement of the inviscid fluid behind the normal reflected shock and the growth of the bifurcation structure. This eventually induces pseudo shock trains. The shock train although more obvious from the pressure flow fields, can also be depicted by the temperature flow fields given in Figure 56. This behavior has also been reported in the numerical studies of

Weber et al. (44), Wilson et al. (43), and in the experiments of Strehlow and Cohen (118) when the displacement becomes too large as is the cases of 900 μs through 1.26 ms right before the reflected shock-contact surface interaction. The pseudo shock train structure acts as a compression mechanism and turns the unaffected portion of the flow behind the normal reflected shock parallel to the shock tube side walls. These flow structures are a strong function of the flow area and become more pronounced in the case of large flow displacements in conjunction with reduced flow area and are typical of narrow channels (44) as mentioned by Fokeev and Gvozdeva (15) and Brossard and Charpentier (119).

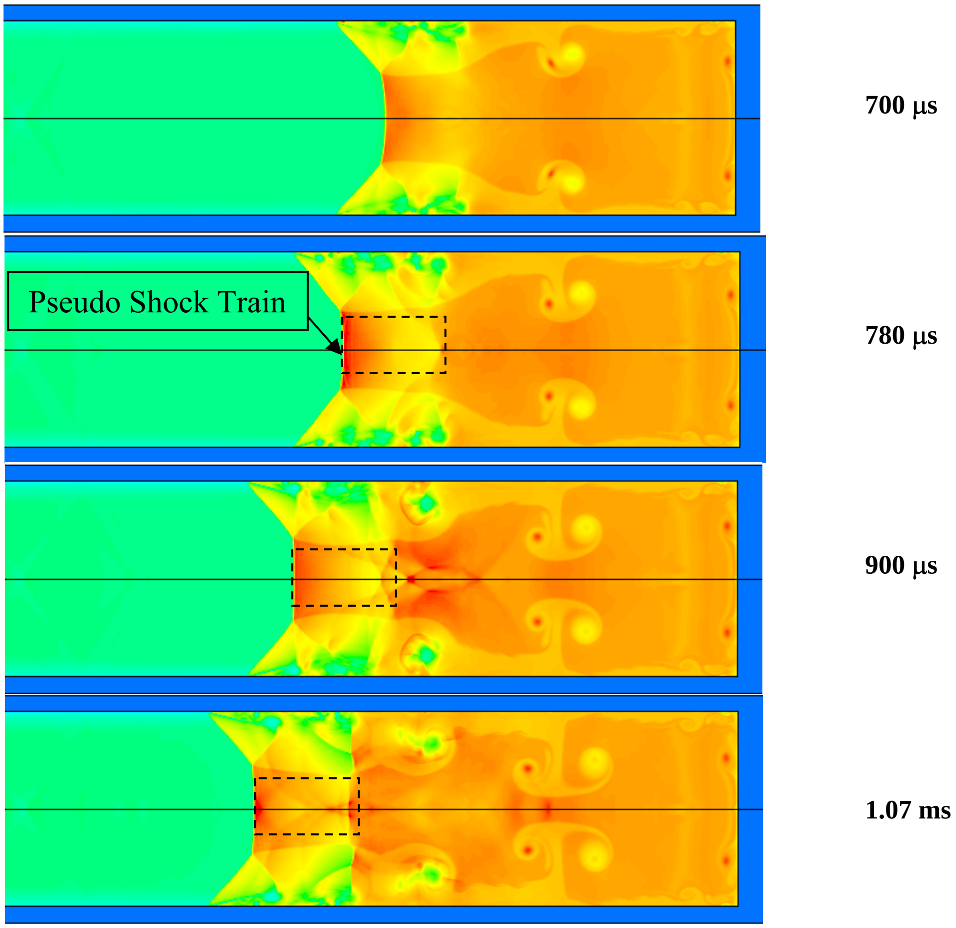

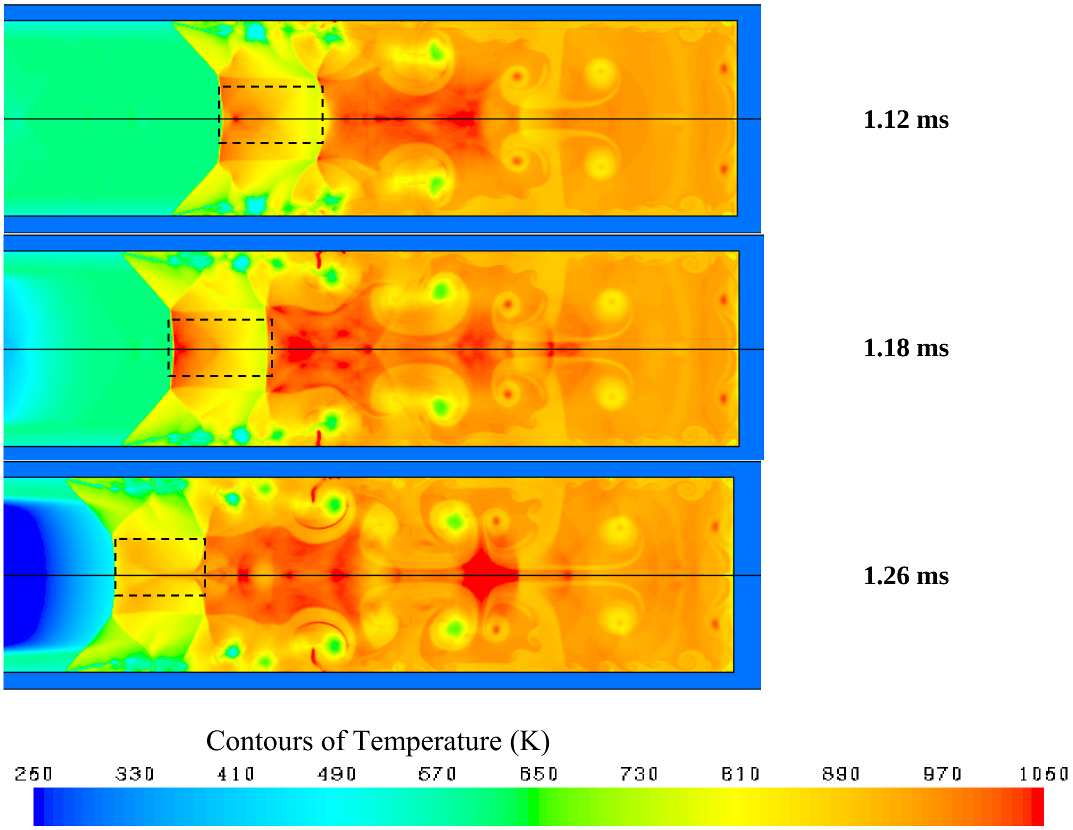

Figure 56: Temperature contours showing the time evolution of the bifurcation structure and the formation of the pseudo shock train behind the moving reflected shock up to 65 cm from the endwall. The time frames are given on the right side of the contours

Bifurcation Foot Height and Angle

The angle of the bifurcated foot on the other hand remains constant and it is measured to be around 55 degrees from the simulation results. Other studies which measured the angle of the bifurcated foot at similar conditions to this study, with air being the test gas and the incident-shock Mach number equal to 2.6, reported values of 45 deg (44). Experimental measurements yielded slightly higher results of at least 50 degrees, as in the study of Matsuo et al. (13) for the same test conditions. Theoretical models which are developed based on isothermal wall conditions as in the studies of Mark (9) and Davies and Wilson (27) predicted results slightly less than the experiments, between 46 and 48 deg. The measured bifurcated foot angle from the simulation results herein of about 55 degrees is in close agreement with the experimental measured values (13) rather than the theoretical and numerical predictions of previous studies (44) (9).

The simulation results demonstrate that the height of the bifurcated foot increases with increasing distance from the endwall. In Petersen and Hanson experimental investigations of the bifurcation phenomenon, it was noted that for locations relatively close to the endwall, the size of the bifurcated foot varies linearly with distance from the endwall and for locations relatively far from the endwall, the height of the bifurcated foot varies at a lower rate (26). This is in agreement with this study's simulation results. Other studies investigated the influence of different parameters on the bifurcated foot height. In particular, the effect of the Reynolds number on the size of the interaction zone delimited by the foot height was studied. Daru and Tenaud observed that the triple point or bifurcation height is strongly dependent on Re such that the height of the bifurcated foot increases with increasing Re, while the bifurcated foot angle is independent of the Re number (52) (51). This is consistent with Marks' (9) predictions based on a inviscid flow assumption, however Weber et al. concluded that the bifurcated foot height increases and the bifurcation angle decreases with decreasing Re due to the thicker boundary layer at lower Re numbers (44). In other studies, it was shown that the bifurcation structure does not depend on the pressure (26) (51) while the dependency on the specific heat ratio is significant with the bifurcated foot height increasing with decreasing specific heat ratio (26). Therefore, it is expected to see stronger interactions and larger-sized bifurcation zones in diatomic and polyatomic gas mixtures than in monatomic mixtures.

Weber et al. explained that the discrepancy between experimental and numerical results is mainly due to the adiabatic wall assumption adopted by the majority of the numerical simulation studies which yield higher boundary layer temperatures and therefore under predict the bifurcation foot angle (44). Weber et al. simulated the bifurcation structure with both the isothermal and adiabatic conditions and concluded that with the isothermal condition, the size of the bifurcation zone and the viscous region is smaller, and the temperature under the bifurcated foot is lower than the adiabatic case (44).

In this study, the numerical simulation uses a conjugate heat transfer model which is expected to yield more accurate results than the adiabatic and isothermal wall assumptions since it is the closest representation of the experimental conditions. The result of a 55-degree bifurcated foot angle determined herein is in agreement with the Weber et al. (44) observations. The conjugate heat transfer model results in a weaker reflected shock wave due to the energy loss to the side and end walls. Consequently, the side wall temperature drops and the boundary layer is thinner. This yields a weaker interaction of the reflected shock with the boundary layer and the viscous region delimited by the slip line and side wall is much smaller. Specifically, the interaction of the incident shock with the endwall does not produce an instantaneously well defined lambda-shock structure due to the more pronounced heat losses in the endwall region as can be seen from the early interaction stages of the reflected shock with the boundary layer near the endwall. In fact, the lambda-like structure is well developed only after 100 μs of elapsed time from the shock reflection. In addition, the conjugate solution leads to smaller and fewer vortices than the results in the studies of Weber et al. (44) and Daru and Tenaud (51) (53) (52). Moreover, the reattachment shock, responsible for the pressure overshoot at the end of the interaction zone, is not as strong as in the adiabatic simulations of other studies (44) (51) (53) (52).

Laminar Vs Turbulent Modeling of Bifurcation

The boundary layer in the current simulations was assumed to be laminar, and no turbulence model was adopted to consider the turbulent nature of the flow field in the shock tube. Time averaged Navier-Stokes equations in combination with a second-order-accurate scheme tend to produce a damping effect which masks the bifurcation structure completely. That is why the majority of studies investigating the bifurcation phenomenon have assumed a laminar boundary layer. The only studies which employed an explicit RANS turbulent model and which the authors are aware of either focused on the interaction of the reflected shock with the contact surface and the resulting driver gas contamination mechanism (40) or the resulting bifurcation structure was not well resolved as is observed herein (59) (120) (121).

Figure 57 and Figure 58 give the temperature, pressure, and vorticity contours from both the laminar and turbulent solutions in Nitrogen test gas at the conditions of 1700K, 17 atm, and 900K, 2.5 atm respectively. The laminar solution is given on the left while the turbulent solution is given on the right. The Bifurcation is well resolved in the laminar flow fields which appear to be highly non-uniform while the converse is true in the turbulent flow fields which display somewhat more uniform profiles and a less resolved bifurcation structure.

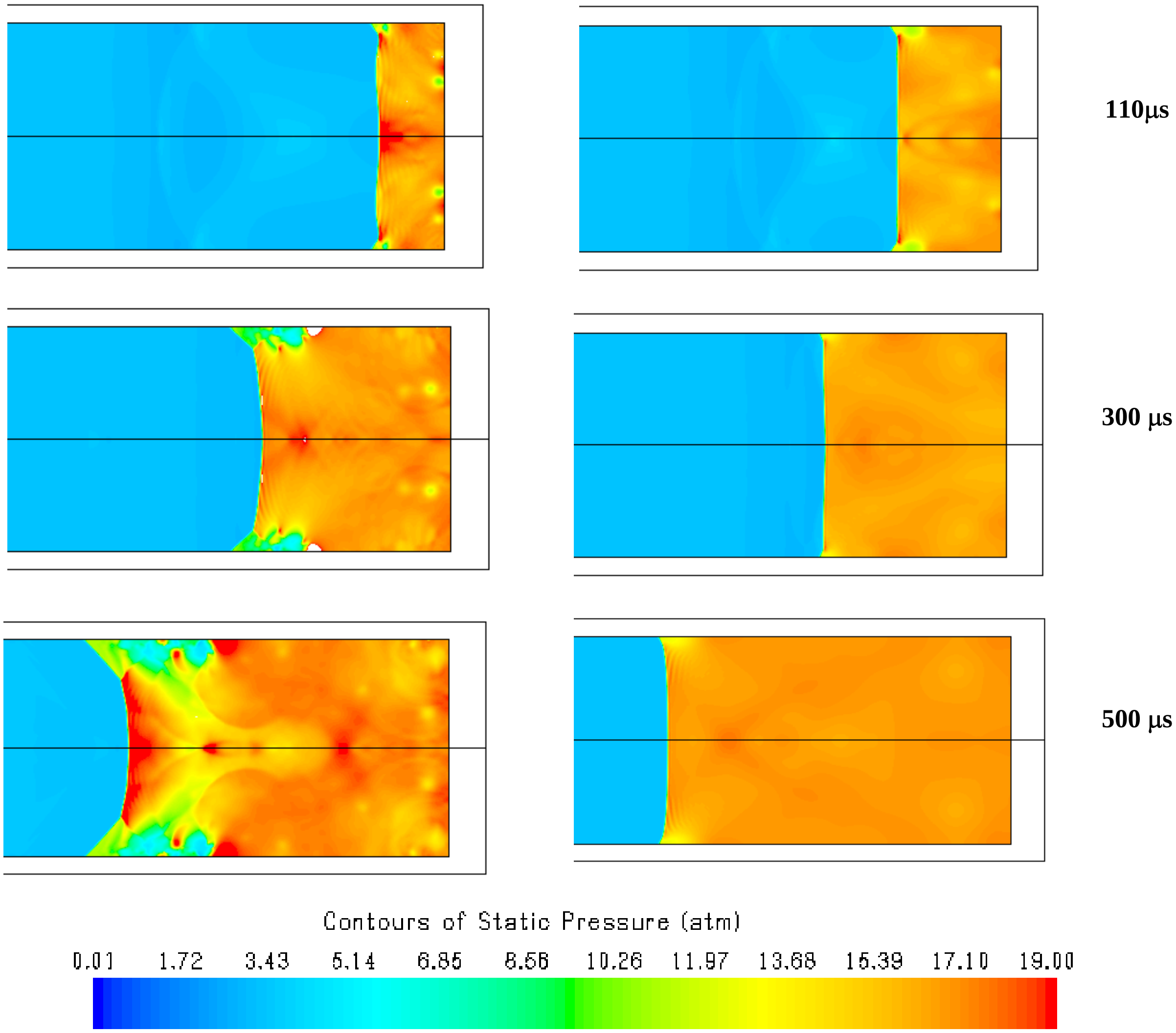
110μs
300 μs
500 μs
Contours of Static Pressure (atm)
0.01
1.72
3.43
5.14
6.85
8.56
10.26
11.97
13.68
15.39
17.10
19.00

a)

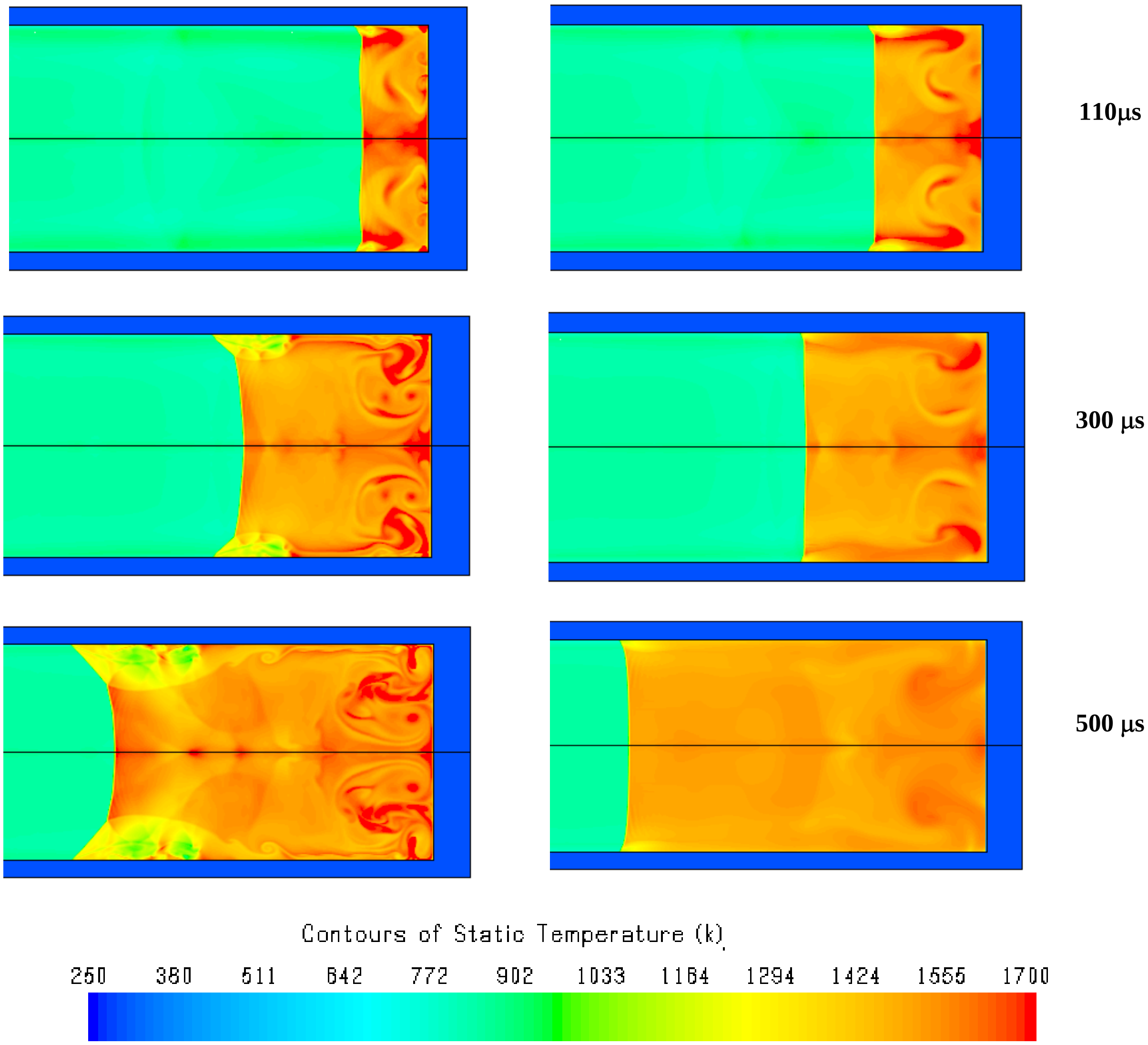
110µs
300 µs
500 µs
Contours of Static Temperature (k)
250
380
511
642
772
902
1033
1164
1294
1424
1555
1700

b)

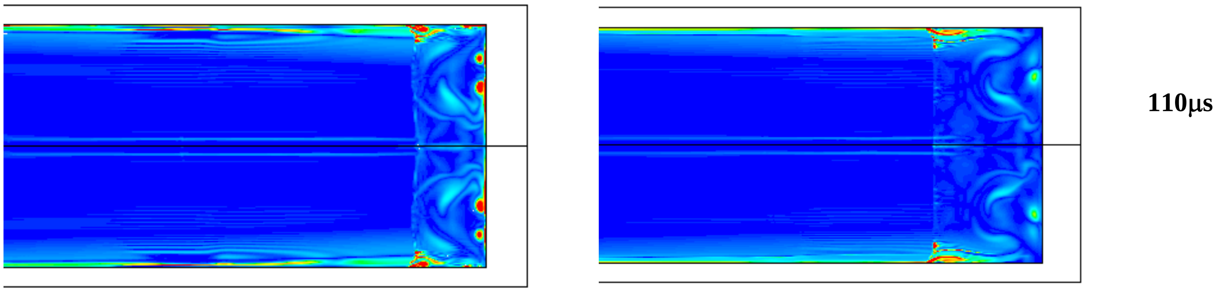
110µs

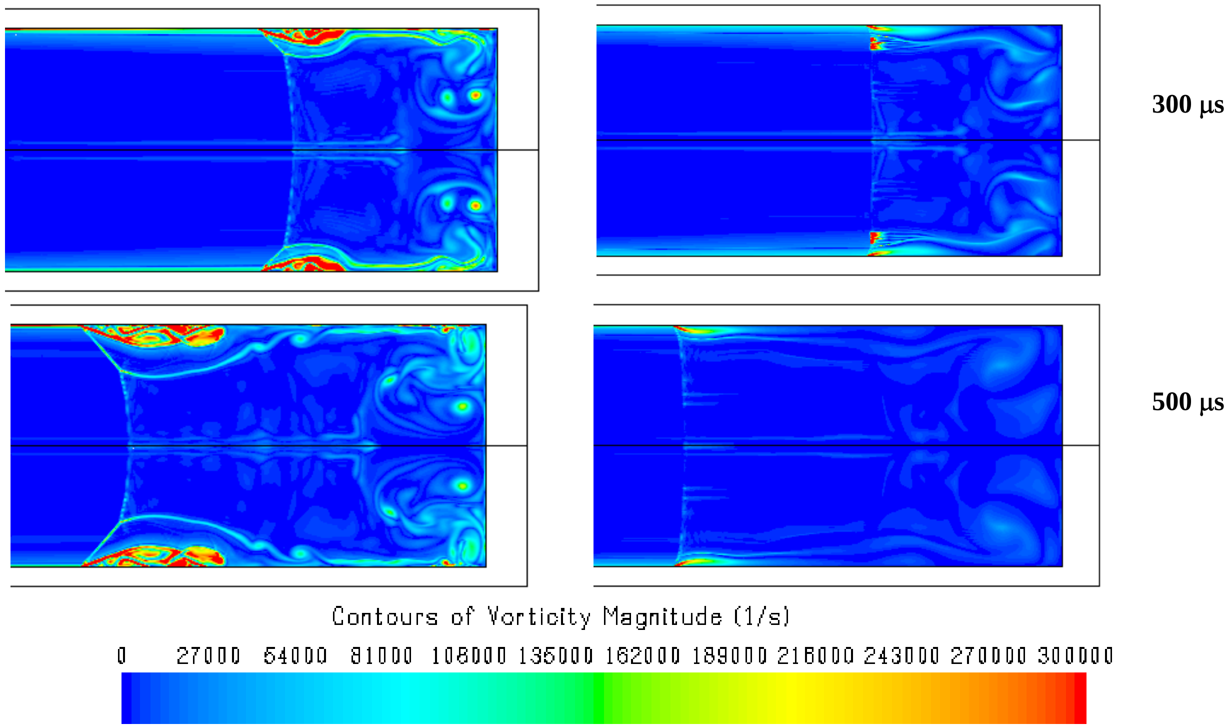

c)

Figure 57: Viscous Laminar (left) and Turbulent (right) simulations in Nitrogen test gas at the conditions of 1700 K, 17 atm showing the flow fields of a) pressure (atm), b) temperature (K), and c) vorticity (1/s) behind the reflected shock wave

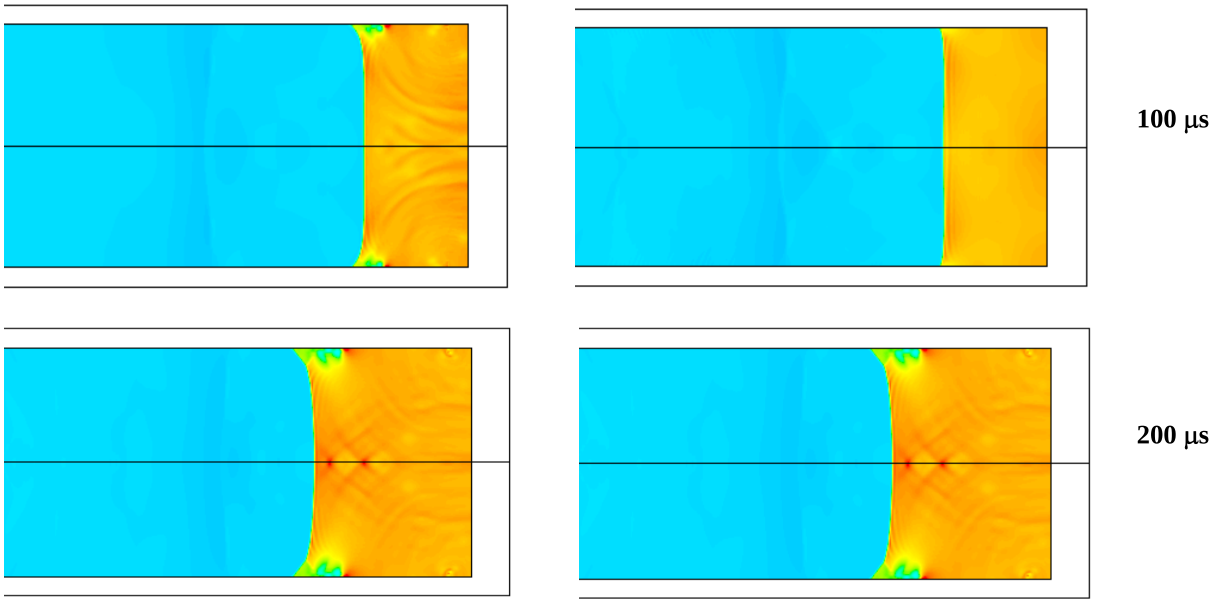

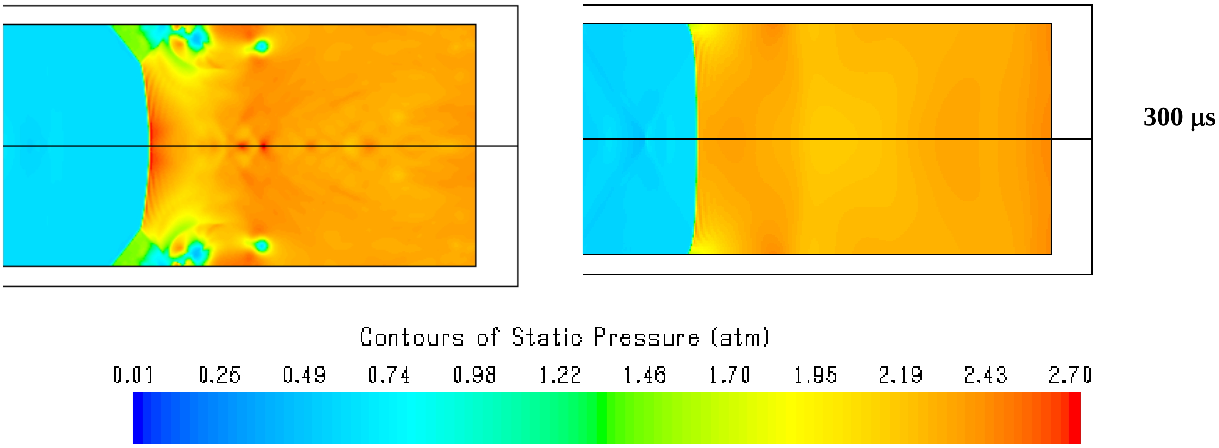
300 μs
Contours of Static Pressure (atm)
0.01
0.25
0.49
0.74
0.98
1.22
1.46
1.70
1.95
2.19
2.43
2.70

a)

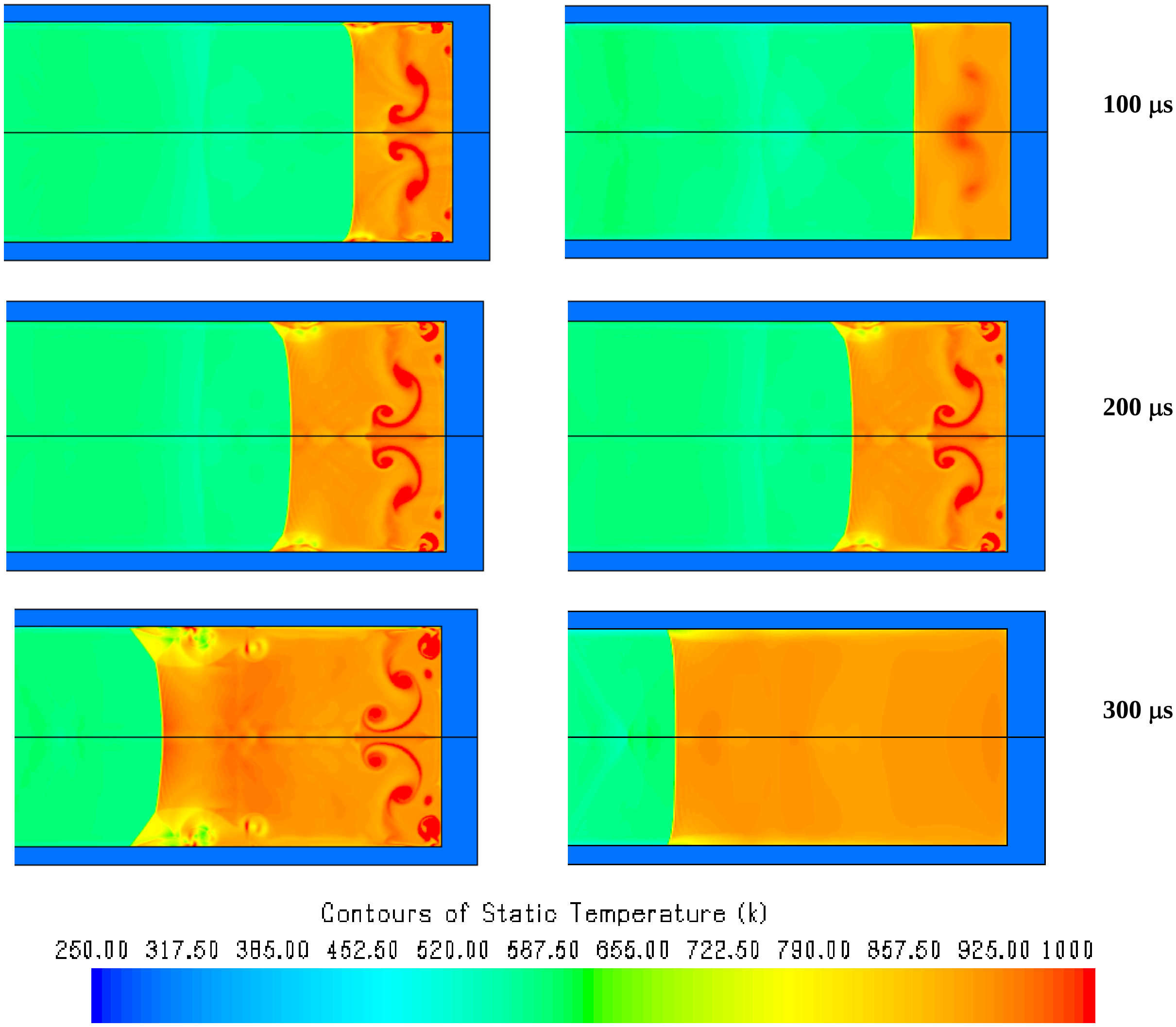
100 μs
200 μs
300 μs
Contours of Static Temperature (k)
250.00
317.50
385.00
452.50
520.00
587.50
655.00
722.50
790.00
857.50
925.00
1000

b)

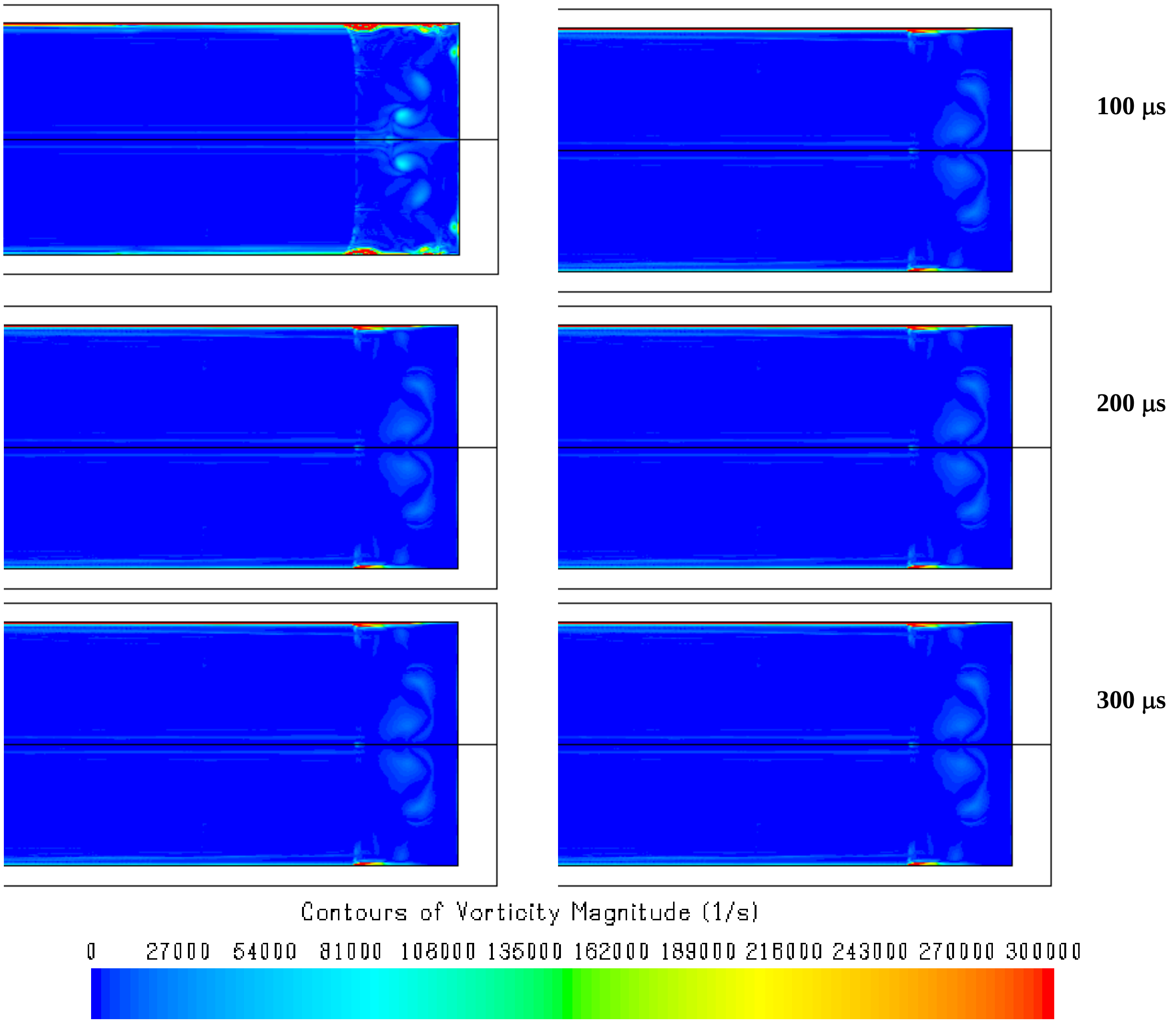

c)

Figure 58**:** Viscous Laminar (left) and Turbulent (right) simulations in Nitrogen test gas at the conditions of 950 K, 2.5 atm showing the flow fields of a) pressure (atm), b) temperature (K), and c) vorticity (1/s) behind the reflected shock wave

The lack of resolution of the bifurcation structure when turbulence URANS model is employed is linked to the weaker interactions when a turbulent boundary layer is assumed, as noted by Mark (9) and Strehlow and Cohen (10). The flow in the turbulent boundary layer is much more energetic than in the laminar boundary layer, which enhances the mixing process at the shear layer level between the viscous region and the flow behind the main reflected shock rendering the flow more uniform and causing the viscous structures to damp out. Consequently, the details of the bifurcation structure can no longer be resolved appropriately, leading to a wrong representation of the results. A laminar model has been shown to be more appropriate for the modeling of the bifurcation phenomenon, especially if resolving the details of the interaction process are of interest.

It is important to note that the bifurcation simulations obtained herein were acquired by the means of a 2nd order accurate space and time scheme in conjunction with the AUSM+ flux discretization scheme. The interaction zone was well resolved, and the details of the bifurcation structure were well captured; while in nature, achieving such high-resolution results can only be made possible with the means of high-resolution schemes of at least fourth-order accurate and higher (44) (52) (112) (51) (54) (55) (56). This behavior confirms the robustness of this study's numerical model in combination with the correct boundary conditions and mesh resolution. The boundary conditions were well represented throughout the entire simulation of the shock tube, while in the majority of previous shock-tube numerical studies only the endwall region was modeled due to the expensive numerical resources associated with modeling the complete shock-tube geometry. All these factors contributed to accurate results which can serve as valuable information for the validation of experimental and numerical shock tube studies.

Driver Gas Contamination

Background

Among the mechanisms responsible for the non-ideal behaviors in the shock tube is driver gas contamination phenomenon which has been investigated experimentally (122) (123), theoretically (27) (28), and numerically (40) (57) (58) (121) (59) (46) (76) (38) (39). Davies and Wilson (27) and Stalker and Crane (28) used Mark's theory and showed that the bifurcated structure provides a mechanism for driver gas contamination and developed analytical models for predicting the premature arrival of driver gas to the endwall region.

Davis and Wilson (27) developed analytical expressions to calculate arrival times of driver gas to endwall. Numerical simulations have also provided reliable information about the contamination process which is of great concern in high enthalpy shock tunnels in particular (40) (57) (58) (121) (59) (46) (76) (38) (39).

In particular, Gooze et al. (40) performed axi-symmetric simulations model driver gas contamination. The boundary layer was modeled as turbulent using the Baldwin-Lomax eddy viscosity model in addition the diaphragm opening was simulated with an iris model. Two operating conditions were examined; an over-tailored and an approximately tailored operation. It was found that bifurcation provides a mechanism for driver gas contamination along the shock tube walls. Interestingly enough, it was also found that bifurcation can prevent driver gas contamination through the vortices shed by the bifurcation structure which inhibit the driver gas from traveling to the endwall section. Chue et al. (121) performed numerical computations to examine the effects of driver gas contamination in the NASA-HYPULSE shock tube facility with a detonation driver shock tunnel. The complete shock facility was modeled using a 3-D mesh with a shock tube diameter of 15.24 cm. Two conditions were analyzed in air test gas. The driver gas is a mixture consisted of stoichiometric hydrogen-oxygen and Argon mixture. The wall boundary layer was assumed to be turbulent and the Baldwin–Lomax algebraic model was applied.

Contact Surface/Reflected Shock/Bifurcation Interactions

Figure 59 shows the numerical solution simulating the contact surface- reflected shock interactions. Pressure (a), temperature (b), and He mole fraction (c) flow fields are presented at different time instances, notably from a time of 460 ms to about 2.1ms since shock reflection off the endwall. The times are given in the upper right corner of the pressure flow fields. The presented pressure and temperature contours aid in tracking the evolution of the bifurcated structure and its role in initiating the driver gas contamination process. He mole fraction flow fields describe the amount of the driver gas in the vicinity of the interaction before and after the encounter of the contact surface with the reflected shock. Ideally the contact surface, which appears to take on a convex form when viewed from downstream the shock tube endwall, is expected to maintain its shape even upon its interaction with the reflected shock. However, when the non-ideal effects are accounted for in the shock tube simulations and notably the bifurcation phenomenon which occurs in diatomic and polyatomic driven gas mixtures, the contact surface shape is greatly distorted which can promote mixing and leakage of the driver gas to the driven mixture, hereby changing the properties of the test gas and its kinetics behavior.

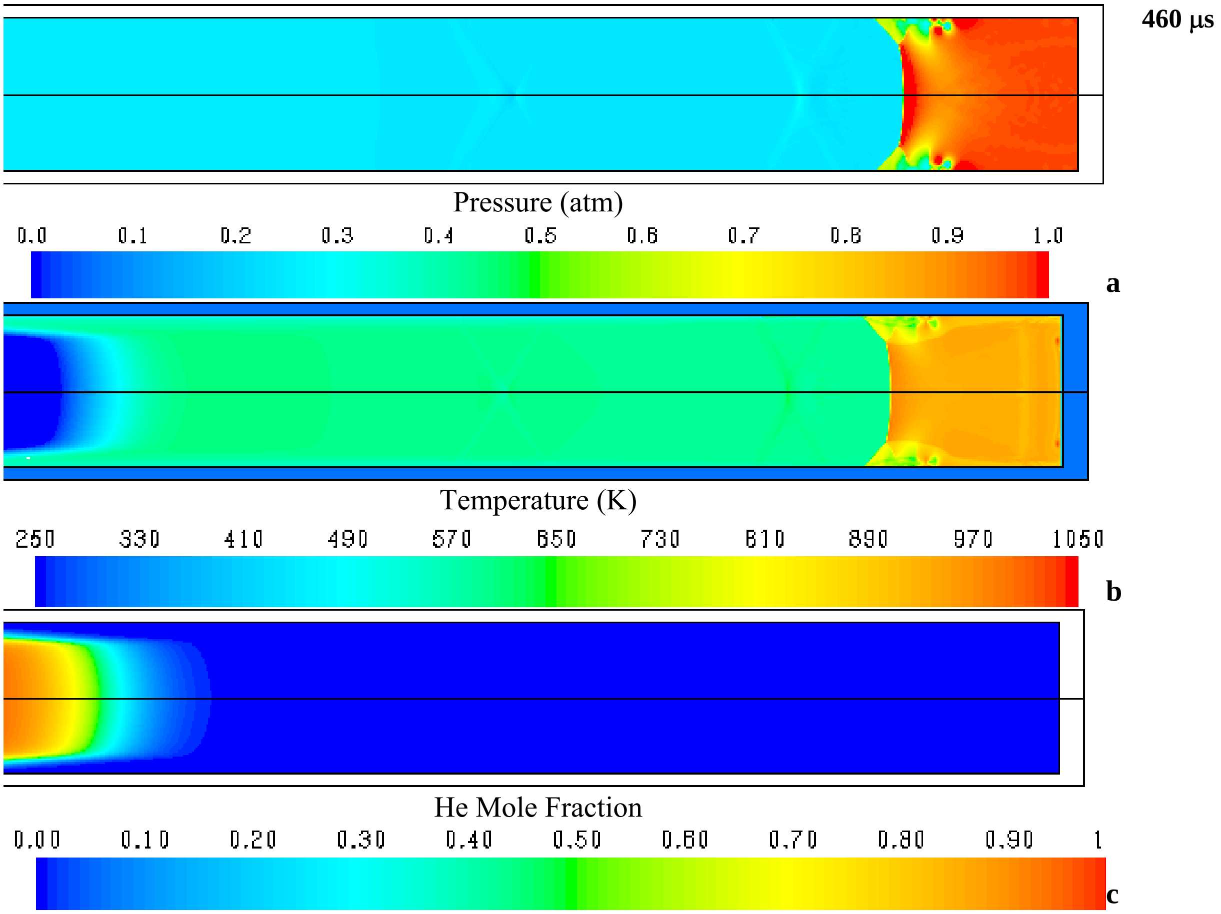
460 µs
Pressure (atm)
0.0
0.1
0.2
0.3
0.4
0.5
0.6
0.7
0.8
0.9
1.0
a
Temperature (K)
250
330
410
490
570
650
730
810
890
970
1050
b
He Mole Fraction
0.00
0.10
0.20
0.30
0.40
0.50
0.60
0.70
0.80
0.90
1
c

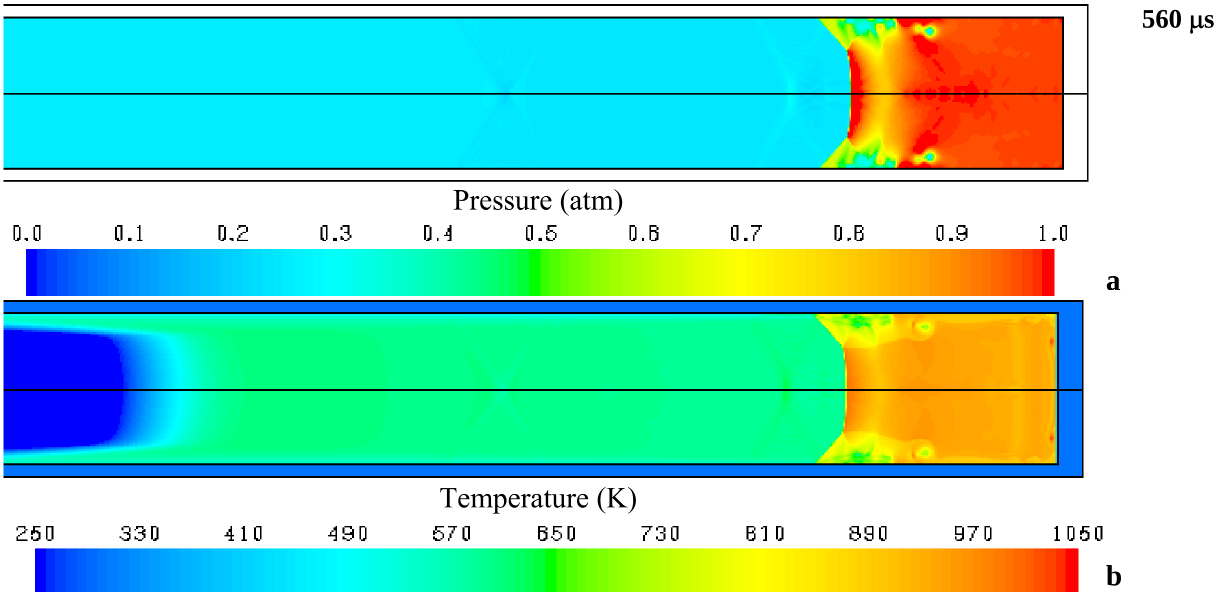
560 µs
Pressure (atm)
0.0
0.1
0.2
0.3
0.4
0.5
0.6
0.7
0.8
0.9
1.0
a
Temperature (K)
250
330
410
490
570
650
730
810
890
970
1050
b

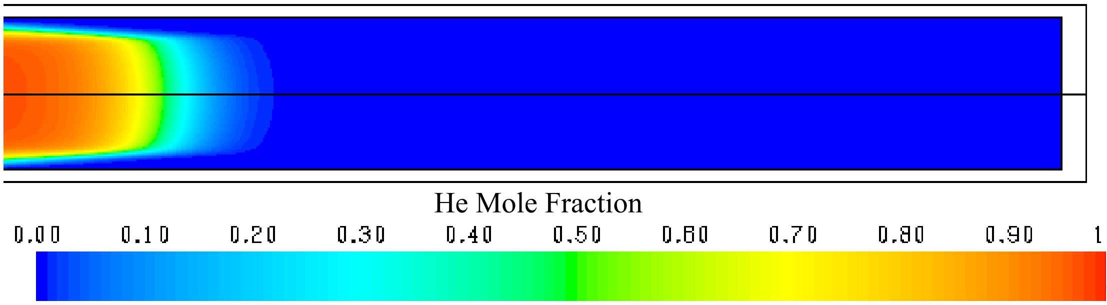

c

760 μs

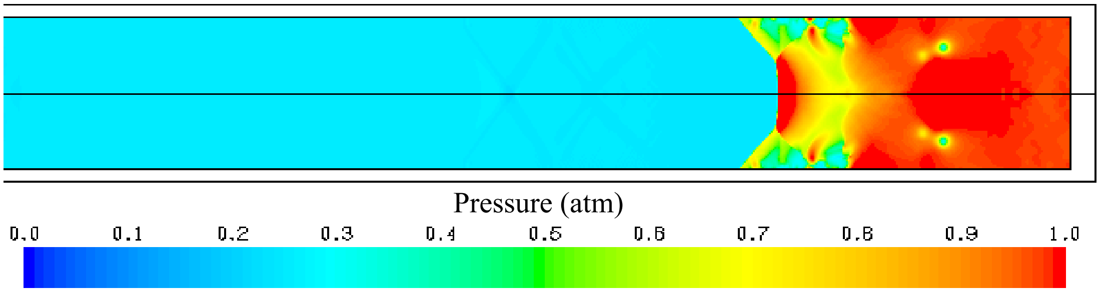

a

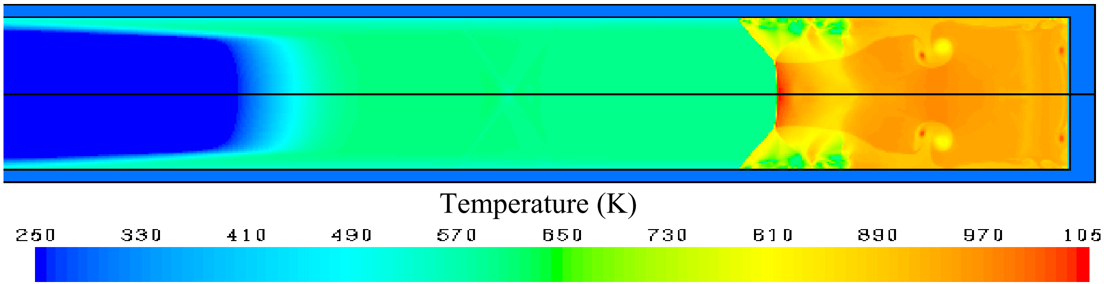

b

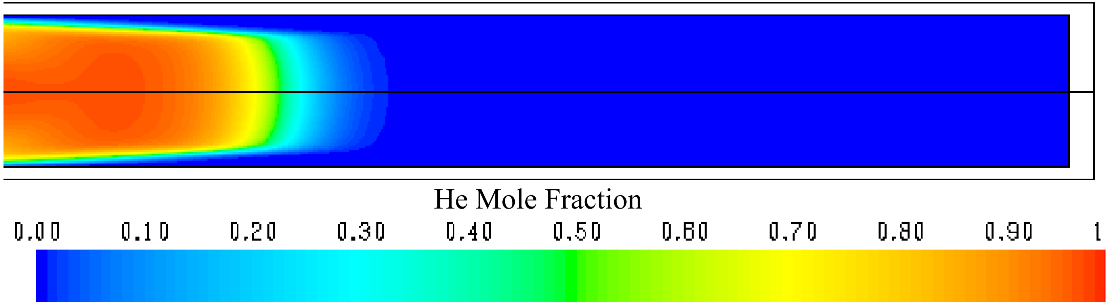

c

960 μs

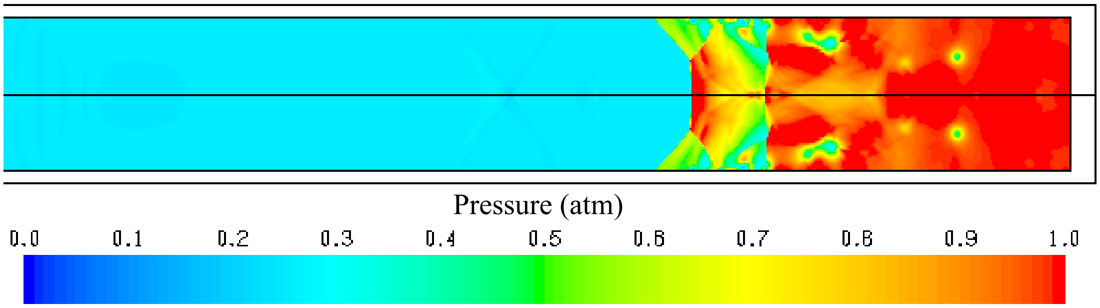

a

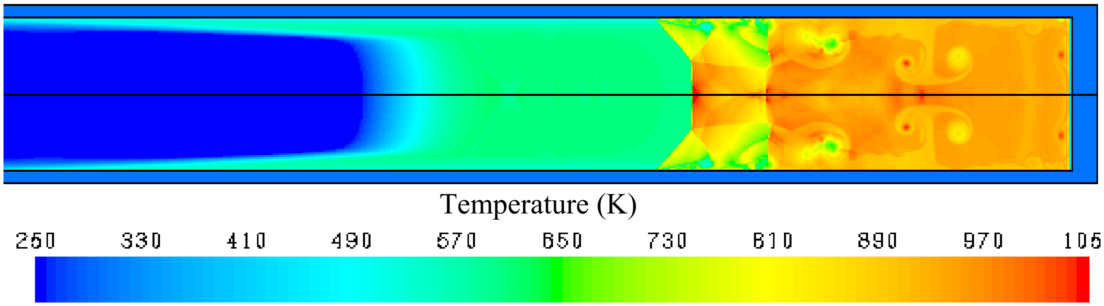
Temperature (K)
250
330
410
490
570
650
730
810
890
970
105

b

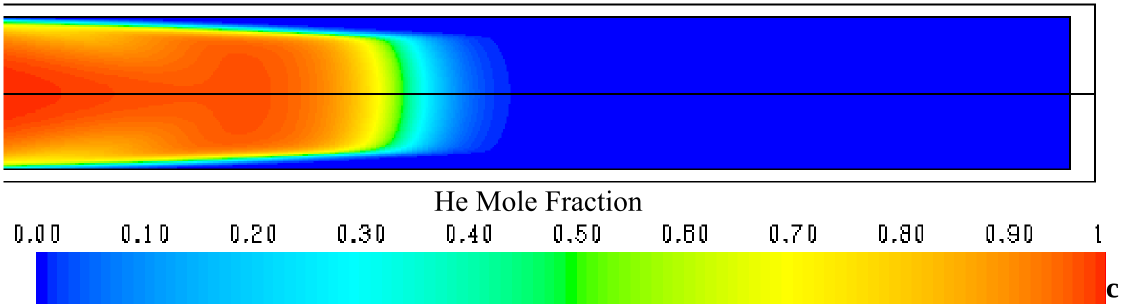
He Mole Fraction
0.00
0.10
0.20
0.30
0.40
0.50
0.60
0.70
0.80
0.90
1

c

1.11 ms

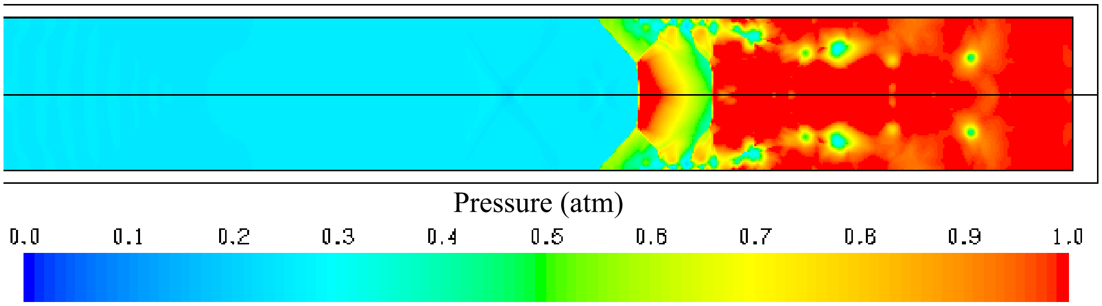
Pressure (atm)
0.0
0.1
0.2
0.3
0.4
0.5
0.6
0.7
0.8
0.9
1.0

a

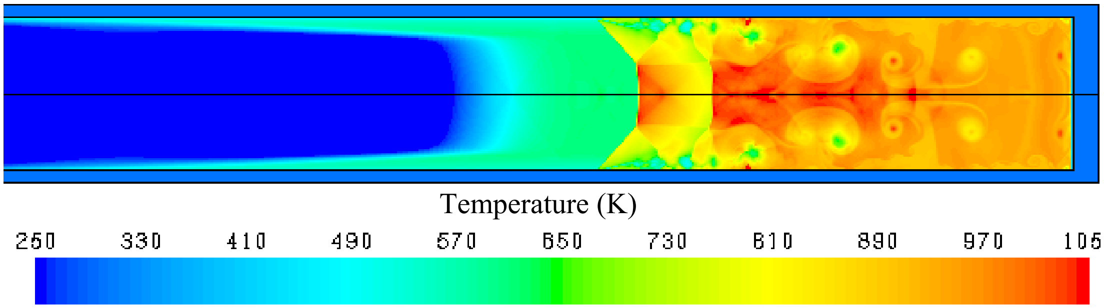
Temperature (K)
250
330
410
490
570
650
730
810
890
970
105

b

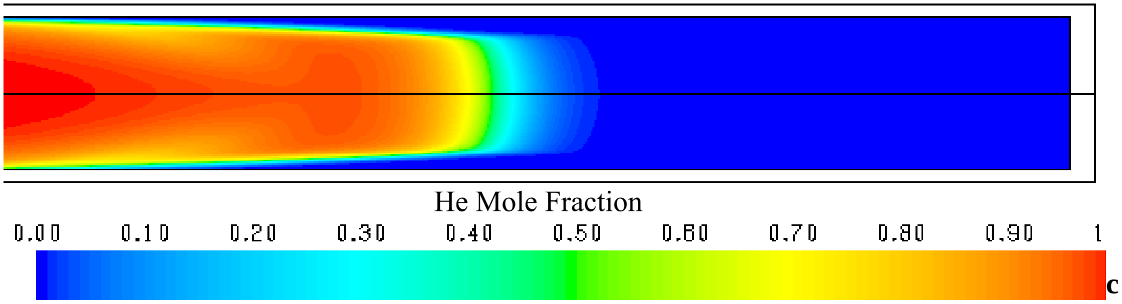
He Mole Fraction
0.00
0.10
0.20
0.30
0.40
0.50
0.60
0.70
0.80
0.90
1

c

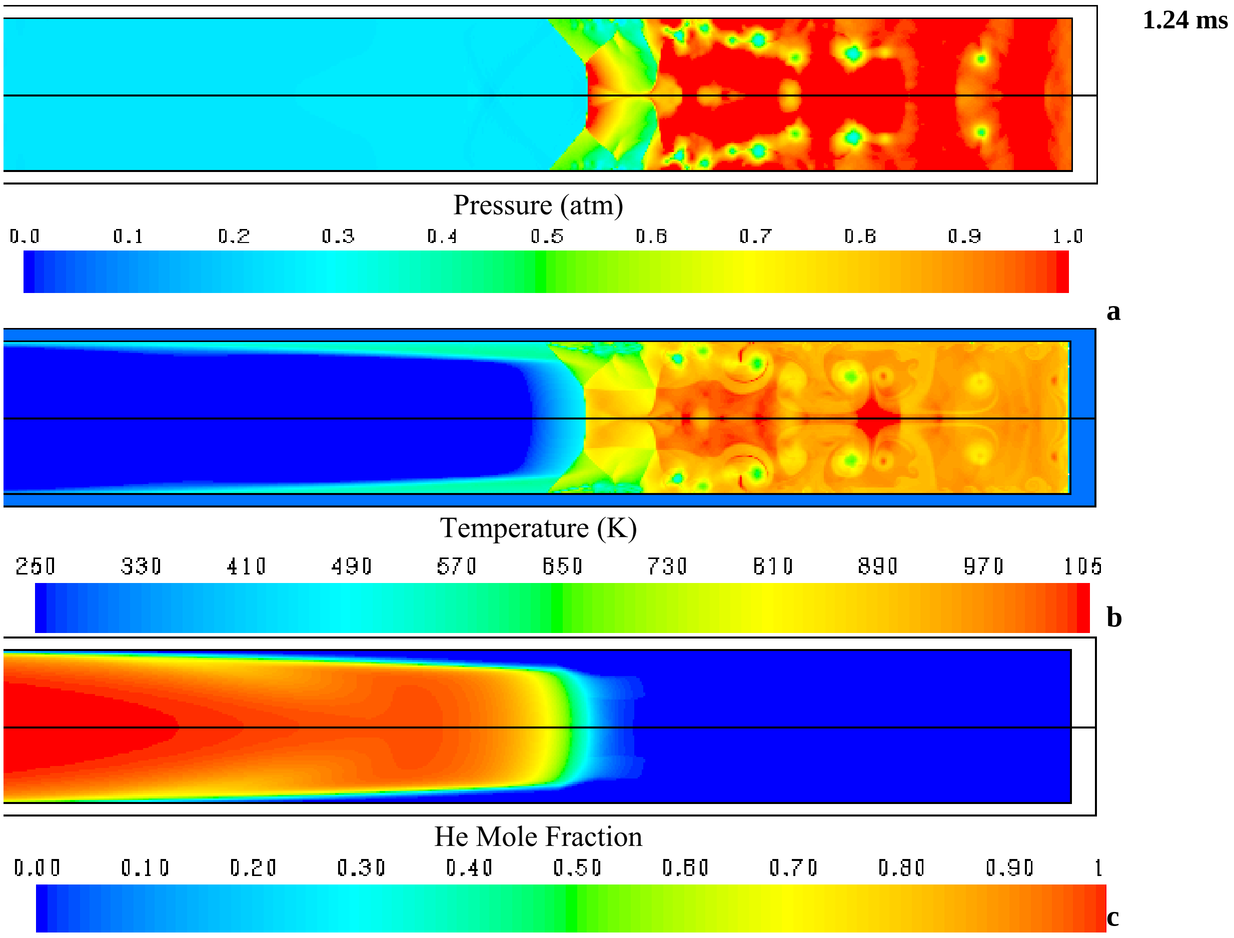
1.24 ms
Pressure (atm)
0.0
0.1
0.2
0.3
0.4
0.5
0.6
0.7
0.8
0.9
1.0
a
Temperature (K)
250
330
410
490
570
650
730
810
890
970
105
b
He Mole Fraction
0.00
0.10
0.20
0.30
0.40
0.50
0.60
0.70
0.80
0.90
1
c

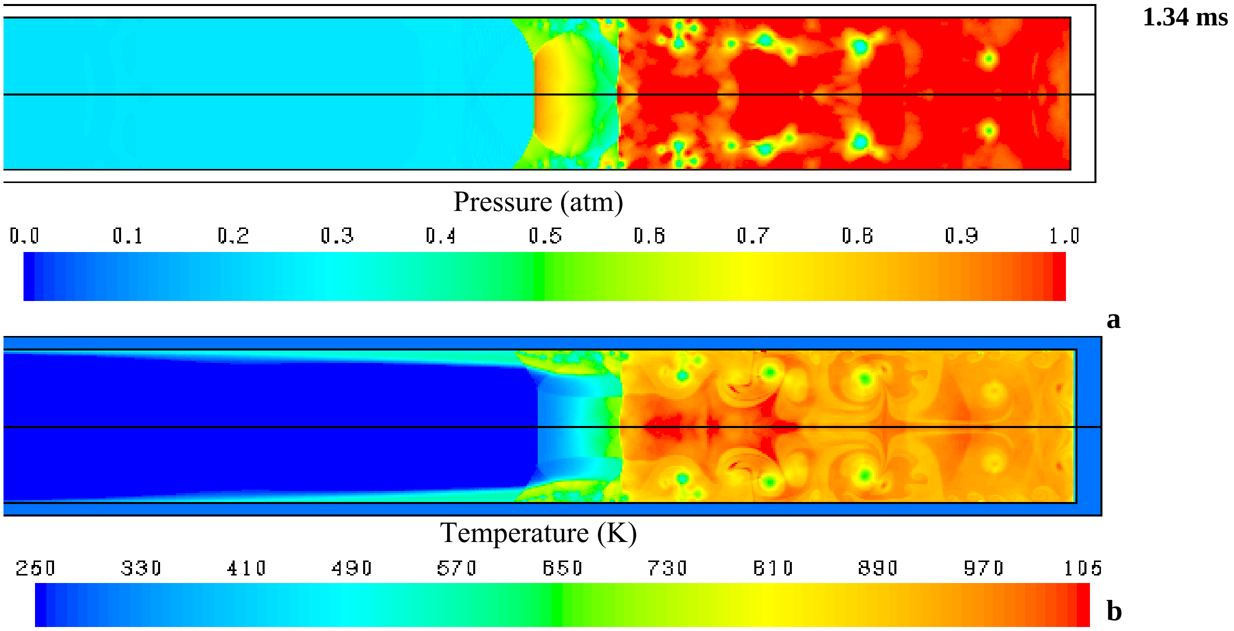
1.34 ms
Pressure (atm)
0.0
0.1
0.2
0.3
0.4
0.5
0.6
0.7
0.8
0.9
1.0
a
Temperature (K)
250
330
410
490
570
650
730
810
890
970
105
b

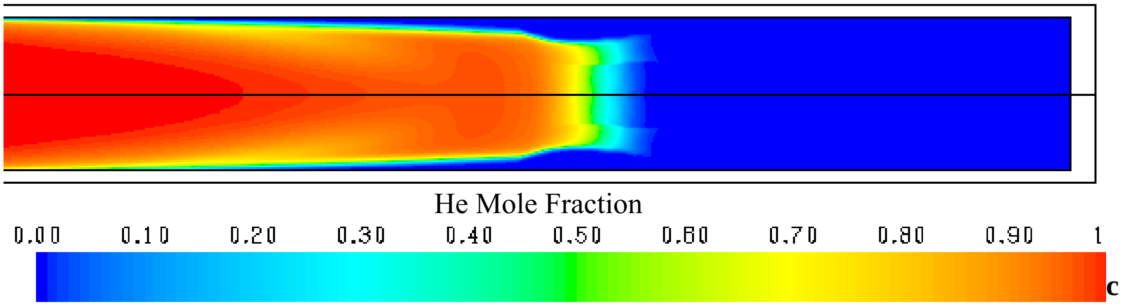

c

1.42 ms

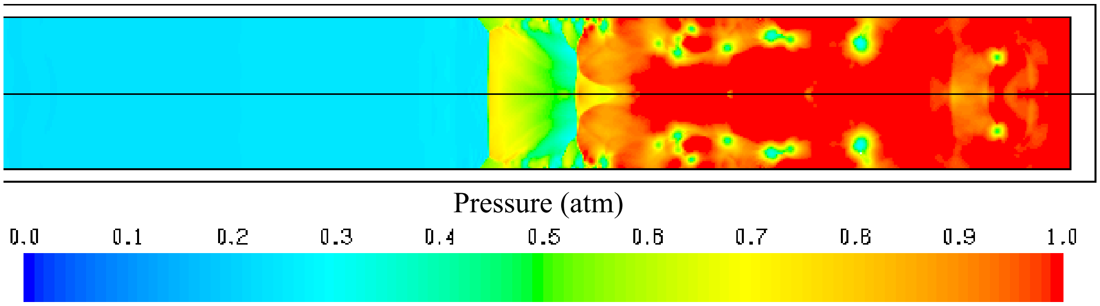

a

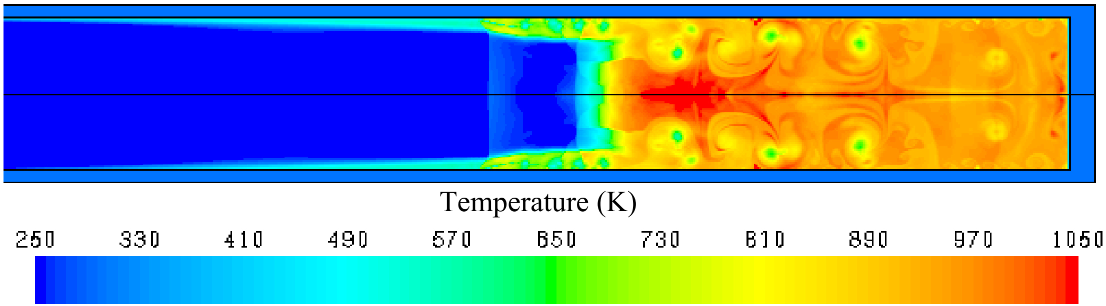

b

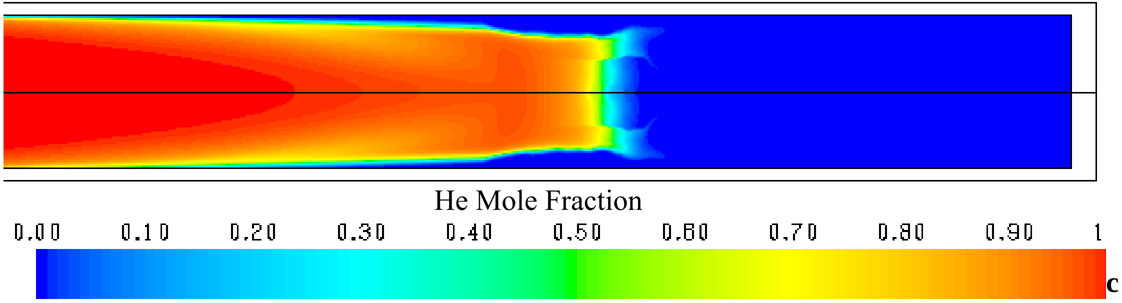

c

1.52 ms

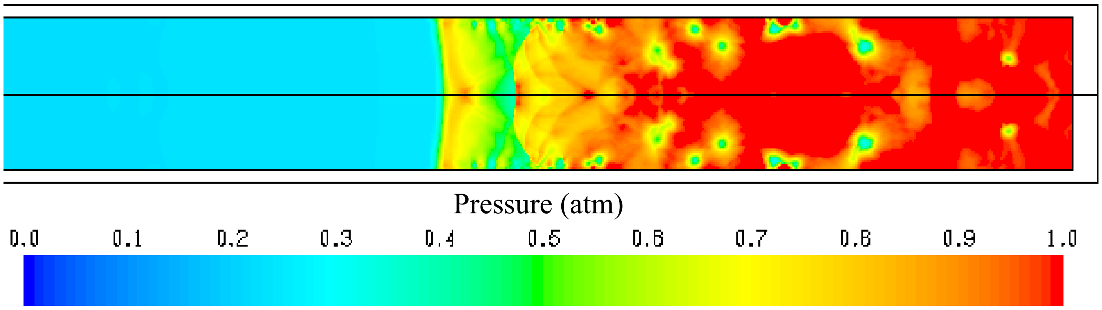

a

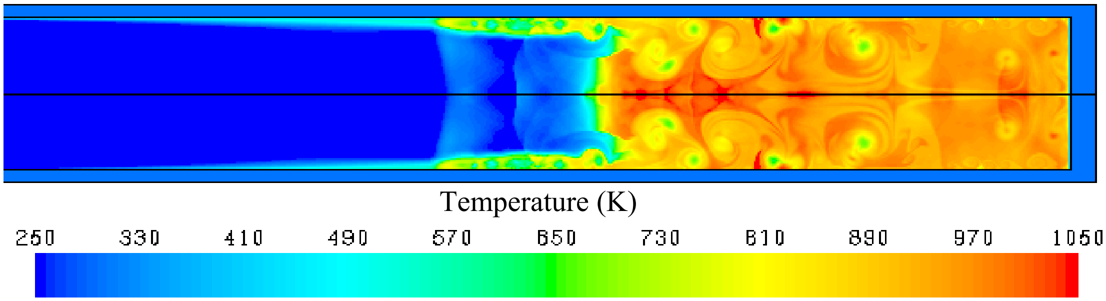
Temperature (K)
250 330 410 490 570 650 730 810 890 970 1050

b

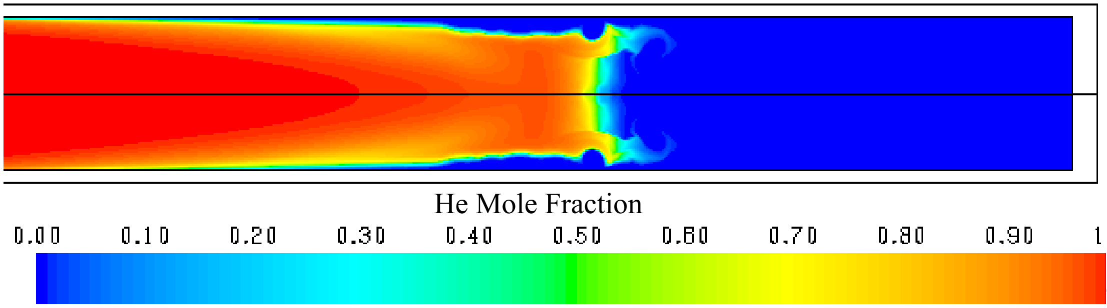
He Mole Fraction
0.00 0.10 0.20 0.30 0.40 0.50 0.60 0.70 0.80 0.90 1

c

1.62 ms

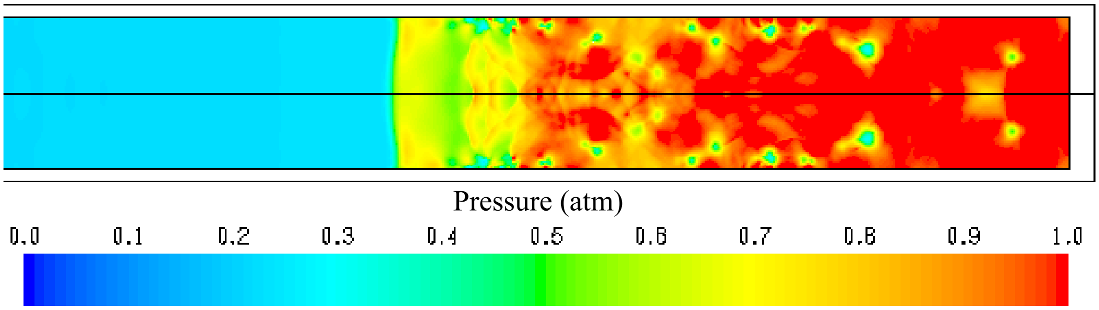
Pressure (atm)
0.0 0.1 0.2 0.3 0.4 0.5 0.6 0.7 0.8 0.9 1.0

a

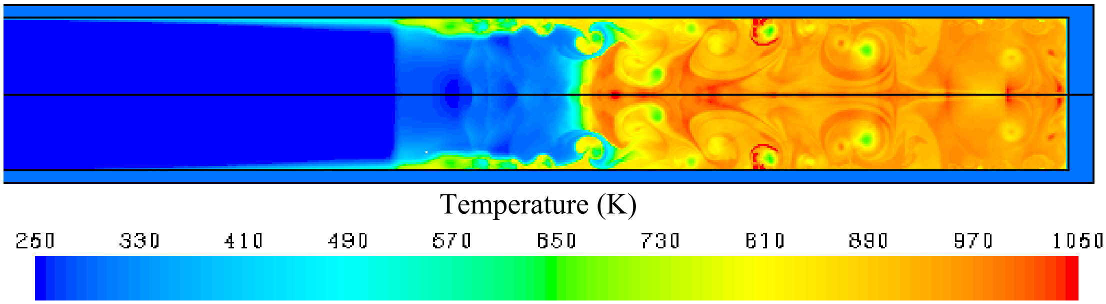
Temperature (K)
250 330 410 490 570 650 730 810 890 970 1050

b

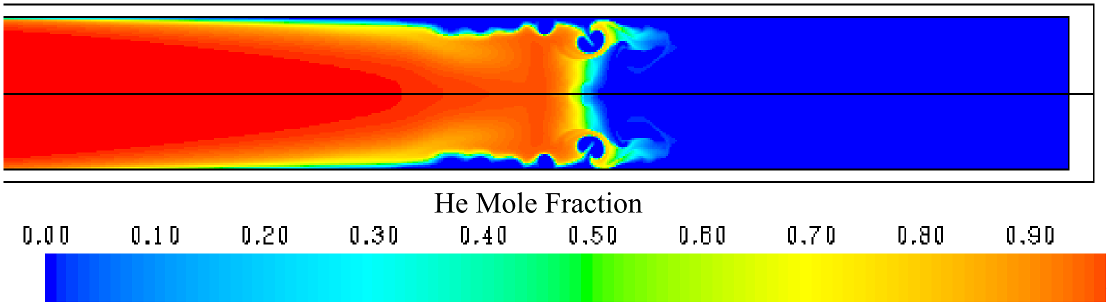
He Mole Fraction
0.00 0.10 0.20 0.30 0.40 0.50 0.60 0.70 0.80 0.90

c

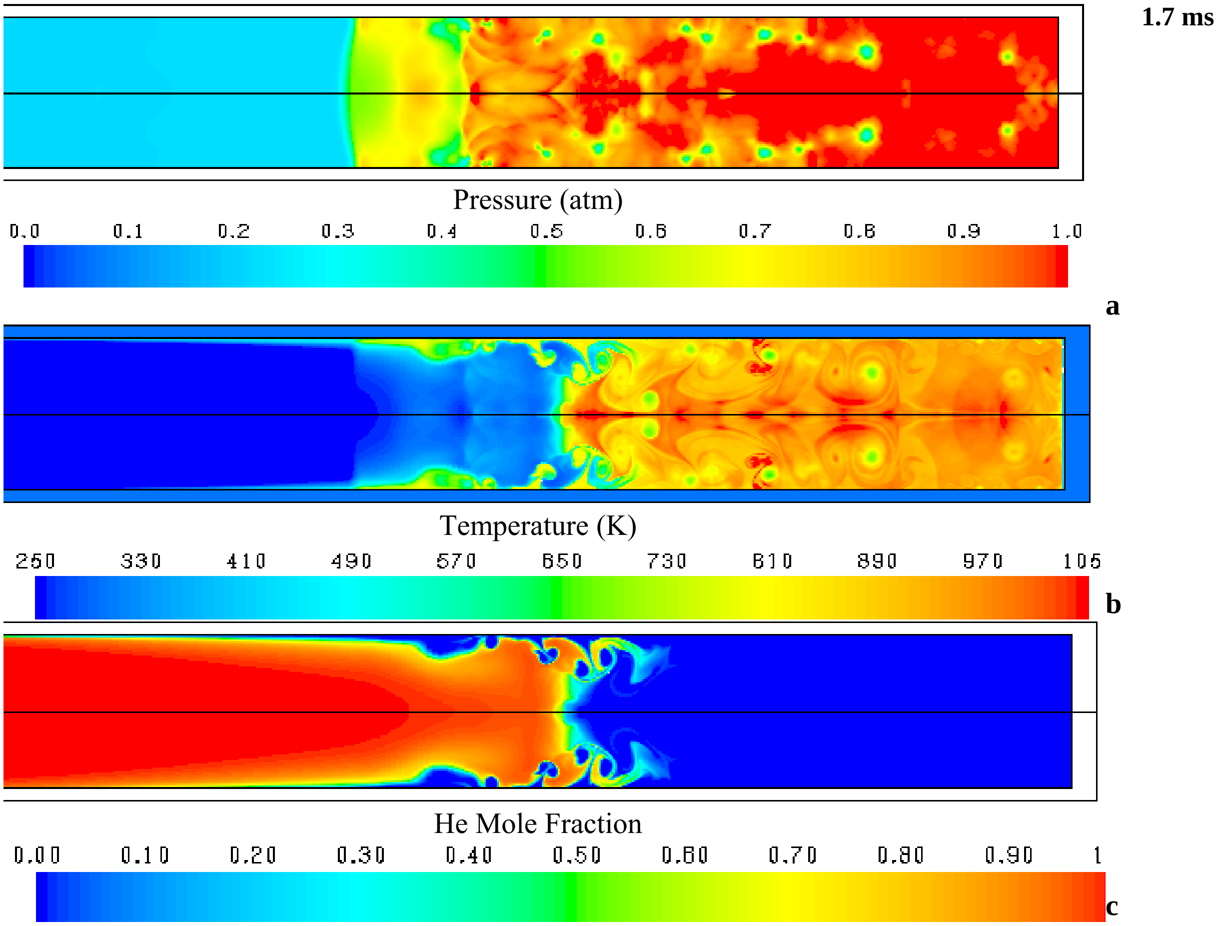
1.7 ms
Pressure (atm)
0.0 0.1 0.2 0.3 0.4 0.5 0.6 0.7 0.8 0.9 1.0
a
Temperature (K)
250 330 410 490 570 650 730 810 890 970 105
b
He Mole Fraction
0.00 0.10 0.20 0.30 0.40 0.50 0.60 0.70 0.80 0.90 1
c

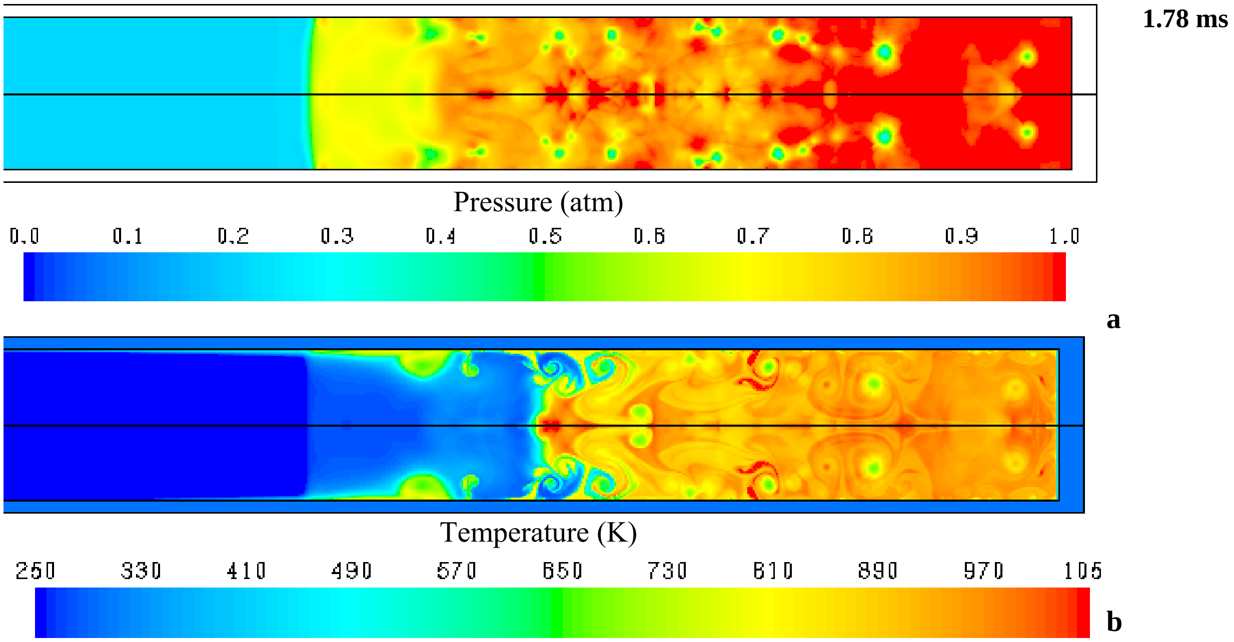
1.78 ms
Pressure (atm)
0.0 0.1 0.2 0.3 0.4 0.5 0.6 0.7 0.8 0.9 1.0
a
Temperature (K)
250 330 410 490 570 650 730 810 890 970 105
b

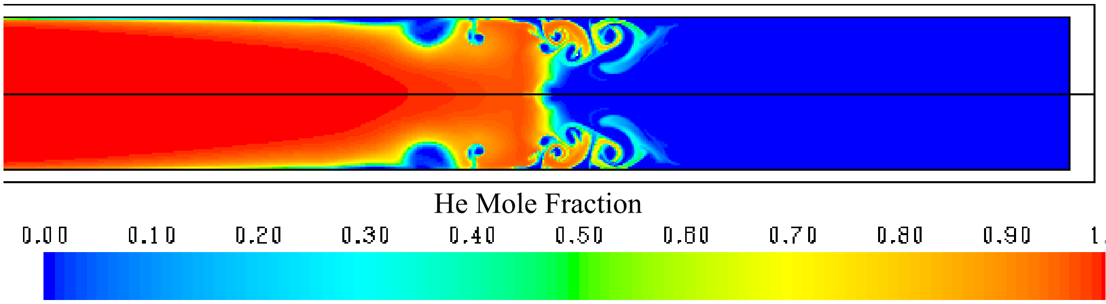

c

1.95 ms

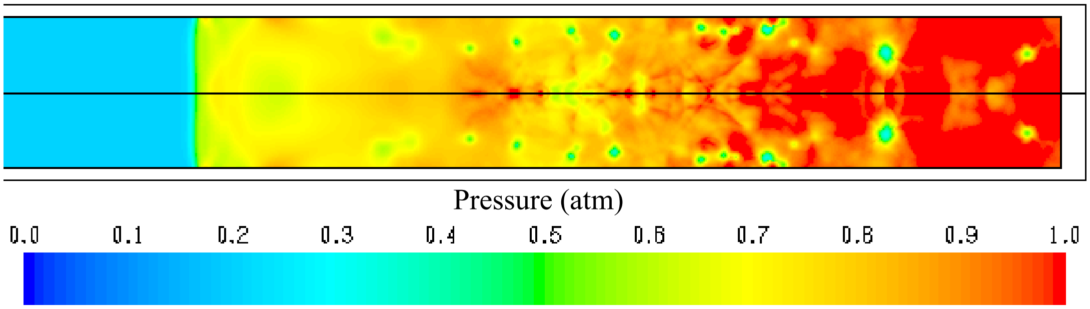

a

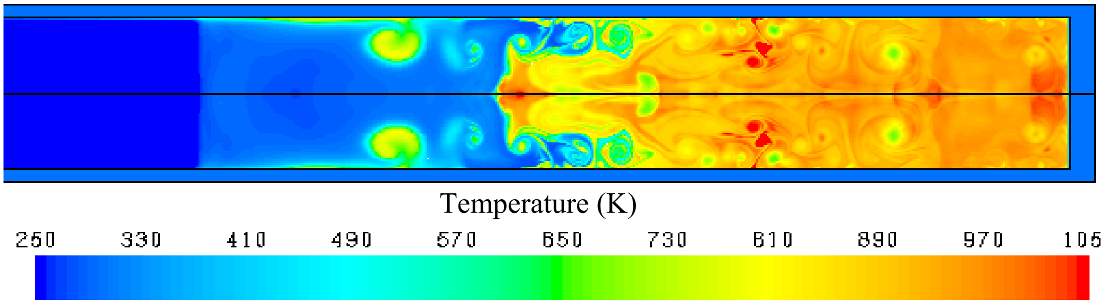

b

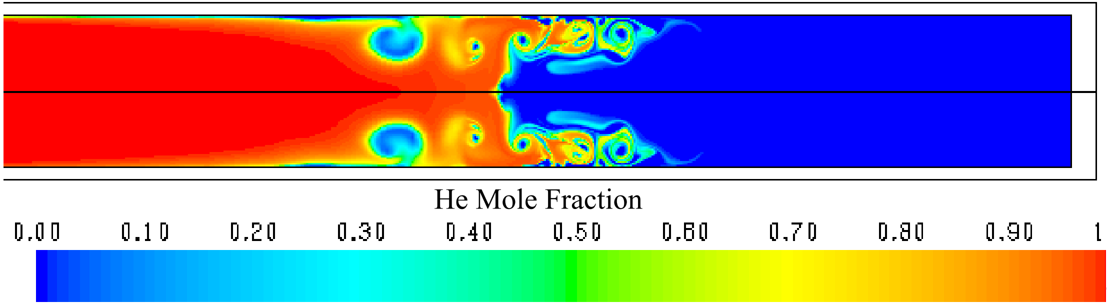

c

2.03 ms

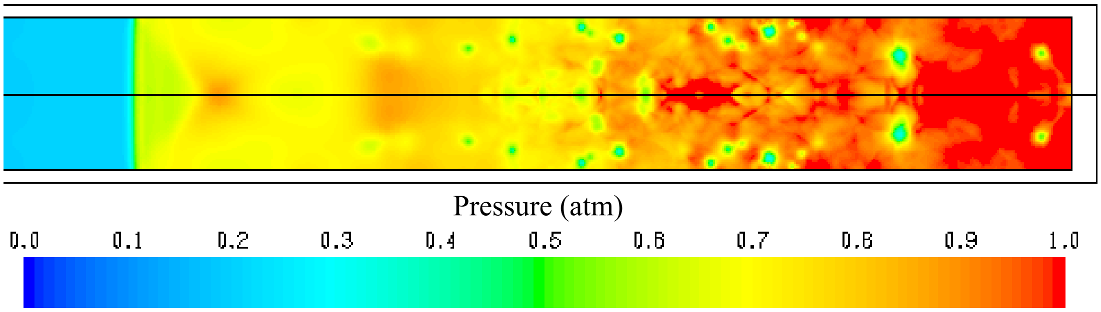

a

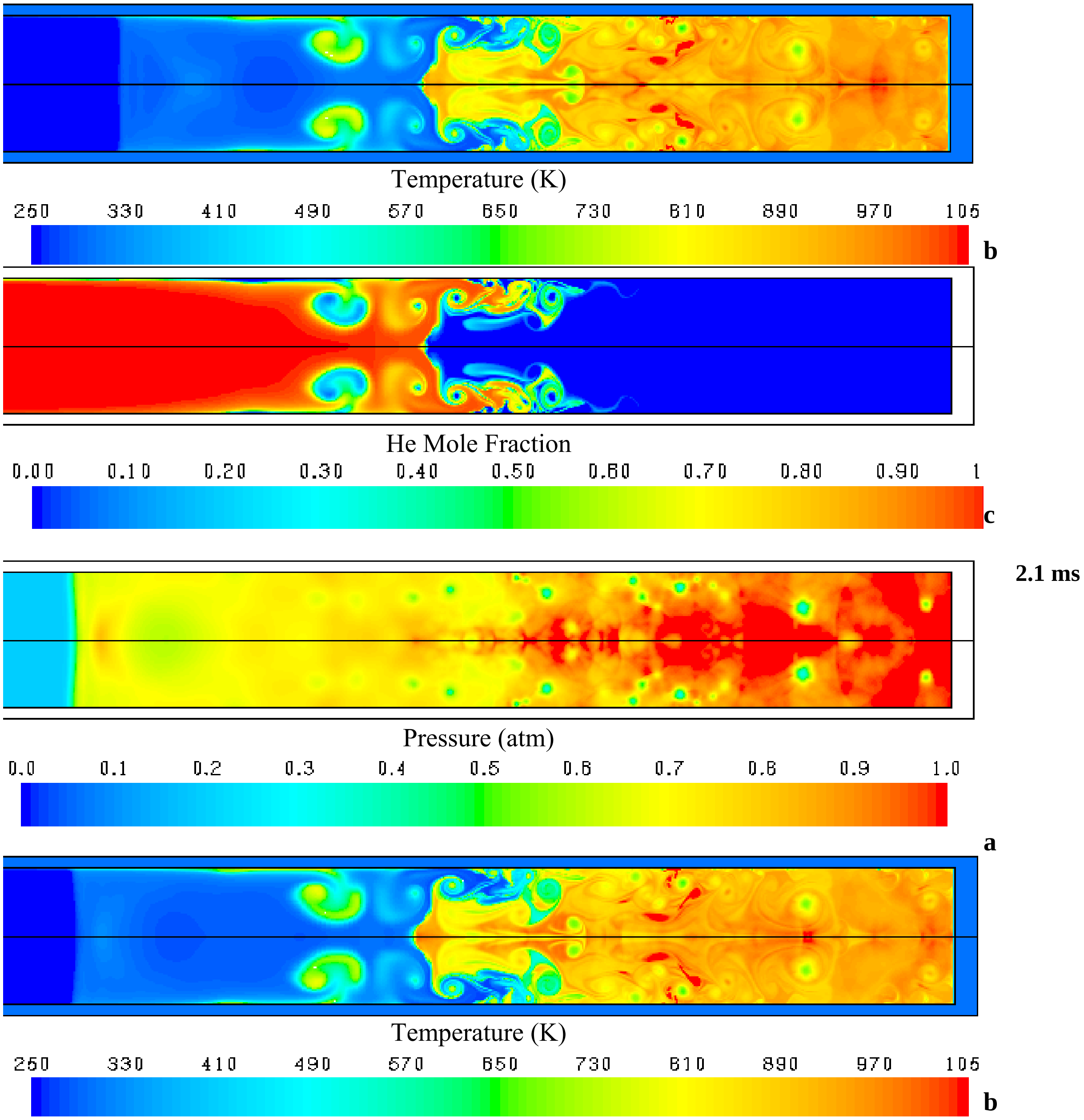
Temperature (K)
250 330 410 490 570 650 730 810 890 970 105
b
He Mole Fraction
0.00 0.10 0.20 0.30 0.40 0.50 0.60 0.70 0.80 0.90 1
c
2.1 ms
Pressure (atm)
0.0 0.1 0.2 0.3 0.4 0.5 0.6 0.7 0.8 0.9 1.0
a
Temperature (K)
250 330 410 490 570 650 730 810 890 970 105
b

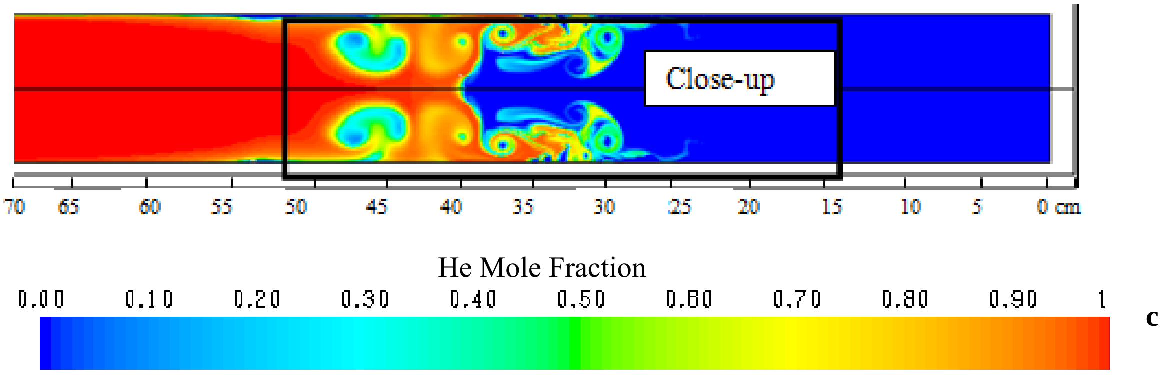

Figure 59: Viscous simulations of driver gas contamination showing a) temperature (K), b) pressure (atm), and c) He mole fraction flow fields before and after reflected shock – contact surface interaction. Conditions behind the reflected shock are 950K, 1 atm in Air test gas. Corresponding times since shock reflection are given in the upper Left corner of the pressure flow fields.

At 460 µs, way before the contact surface interacts with the reflected shock; the contact surface appears as an elongated tongue propagating into the driven gas. The same observation has been reported by Gooze et al. (40) who attributed this to the assumption of an iris diaphragm rupture. The contact surface continues to propagate in the driven gas towards the shock tube endwall, and the reflected shock advances in the opposite direction. The interaction starts around 1.24 ms as illustrated by the pressure and temperature flow fields which show the alignment of the reflected shock with the contact surface. The first encounter does not result in a significant distortion of the contact surface shape mainly because the interaction occurs with the normal portion of the reflected shock. As the reflected shock advances forward, the contact surface starts to interact with the bifurcated foot, and the driver gas is displaced towards the center of the shock tube to allow for the driven gas underneath the bifurcated foot to pass along the shock tube side walls. This fluid displacement is captured between 1.34 and 1.42 ms. The bifurcated shock structure loses its strength and coherence and the cold fluid jetting along the side walls becomes less pronounced. The interaction continues and becomes more pronounced as the vortices shed by the bifurcated foot encounter the driver gas. The interaction with the first vortical structure lagging behind the bifurcated foot takes place at 1.52 ms and results in a swirling motion of the driver gas on the outside edges of the contact surface. More vortices approach the driver gas as the reflected shock advances forward resulting in intensified swirling motions of the driver gas and mixing with the driven gas along the peripheries. By 2.1 ms, the contact surface shape is greatly distorted and the driver gas contaminates the driven gas which is no longer a mixture of 100% air. Figure 60 shows a close up of the He mole fractions in the shock tube before and after the interaction of the contact surface with the reflected shock. The vortices shed by the bifurcated foot provide a mechanism for driver gas contamination along the shock tube side walls and center with more driver gas convecting towards the center than the side walls. Simulations reported by Gooze et al have shown that vortices generated by the bifurcated reflected shock prevent the jetting of the driver gas along the wall and convect driver gas away from the shock tube wall (40), while Cambier et al. observed that jetting of the contact surface occurs near the wall (38). In this study, it is observed that driver gas contamination occurs along the shock-tube side walls and the center with more driver gas convecting to the center.

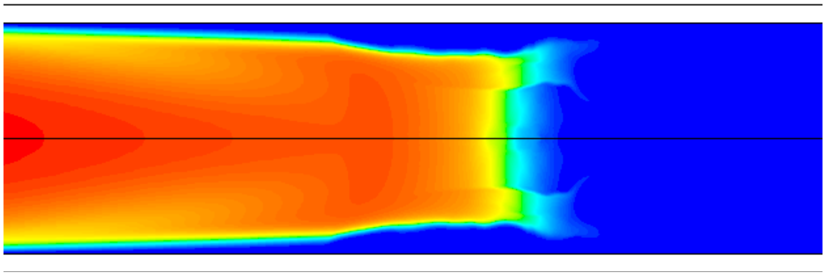

1.42 ms

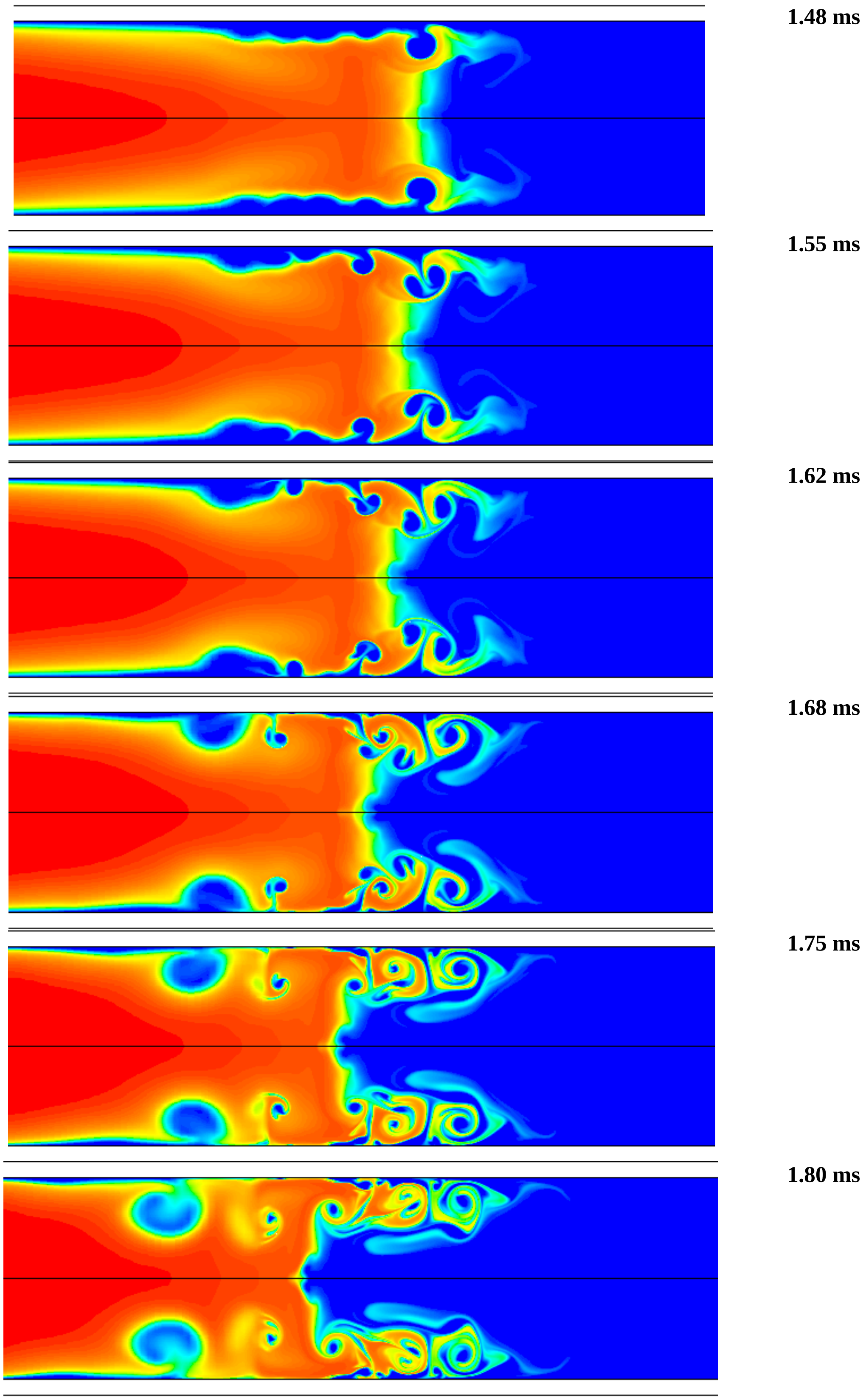
1.48 ms
1.55 ms
1.62 ms
1.68 ms
1.75 ms
1.80 ms

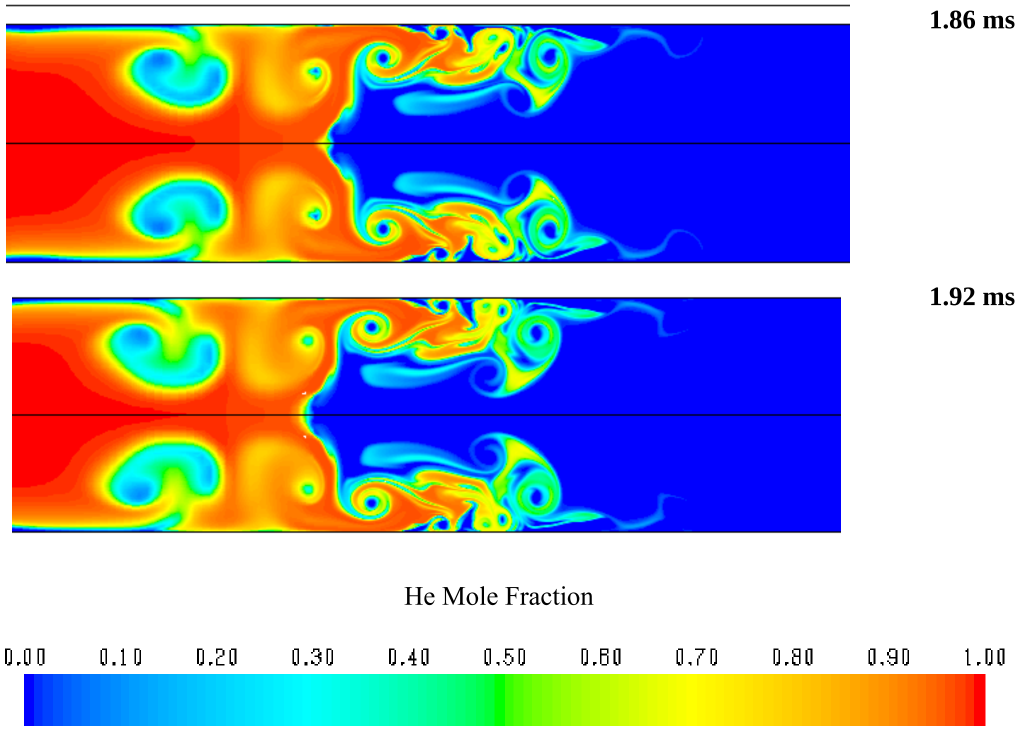

Figure 60: A Close-up on the Contact surface - reflected shock interaction between 1.4 and 2.1 ms since shock reflection showing the He mole fractions. Conditions of the driven gas are 950 K, 1 atm and Air test gas. Conditions of the driven gas are 300 K, 0.4 atm, and He gas. Corresponding times since shock reflection are given in the upper Left corner of each frame.

After the reflected shock and the bifurcation structure and vortices have completely passed through the contact surface which at this point in time has stopped moving forward towards the endwall, the driver gas has no other means of reaching the endwall region and therefore driver gas contamination cannot be sustained. The vortices shed by the bifurcated foot which first acted as a mechanism of driver gas jetting, have also helped in convecting the driver gas away from the side walls towards the center in a clockwise direction, although there exist minor traces of the driver gas along the side walls at the later stages of the interaction but nothing major to constitute a potential of endwall contamination. As a measure of preventing driver gas contamination, addition of annular gas-bleed arrangements in the shock tube (124) and particle trap arrangement on the shock tube centerline (59) have been investigated.

The driver gas contamination not only affects the mixture composition of the driven gas but also the temperature flow fields of the driven gas which experience a further decrease in temperature due to mixing with the colder fluid of the driver gas and the side wall boundary layer. Figure 61 depicts the temperature flow fields in the vicinity of the interaction and the resulting decrease in temperature due to mixing of the driven gas with the colder driver gas. Results are shown for times between 1.56 and 1.75 ms.

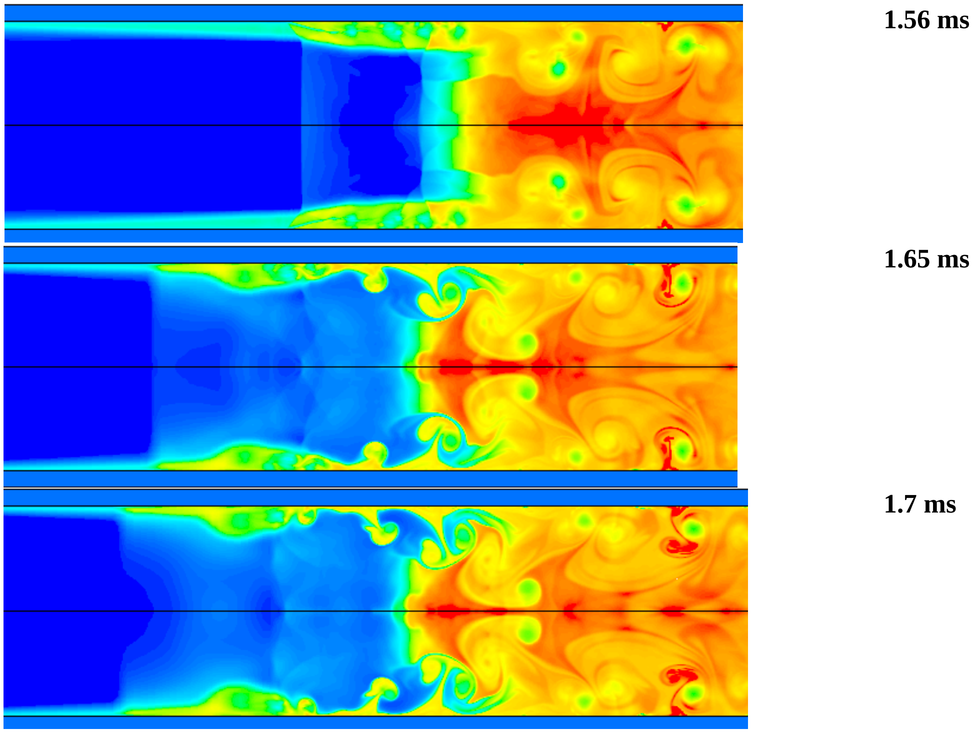

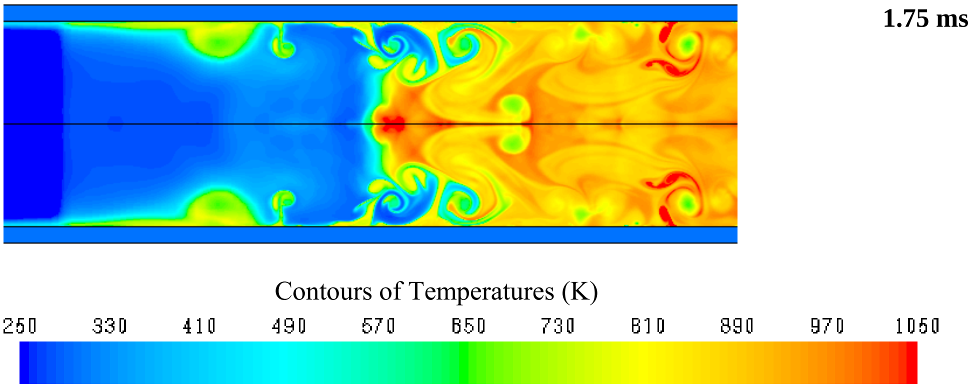

Figure 61: A Close-up on the Contact surface - reflected shock interaction between 1.56 and 1.75 ms since shock reflection showing the temperature flow fields. Temperature has significantly dropped from 950 K to an average of 890 K due to mixing of colder driver gas with the hot driven gas. Corresponding times since shock reflection are given in the upper Left corner of each frame.

In addition to the bifurcated structure being the major mechanism responsible for driver gas contamination, local instabilities on the contact surface level known as the Richtmeyer-Meshkov instability (RMI) can enhance this process. The Richtmeyer-Meshkov instability develops when an interface between two fluids of different densities known here as the contact surface is subjected to shock waves (125) (126).

From the bifurcation results presented herein, it has been shown how the continuous displacement of the viscous region and inviscid flow adjacent to the boundary layer from the bifurcated structure can lead to the formation of small shock waves notably along the slip line and the bifurcated foot and as a result mixing is promoted between the flow in the separation region and the unaffected region. These shock waves can in turn interact with the contact surface along the reflected shock wave and as a result vorticity is produced. These vortices can then enhance the mixing process on the contact surface level and therefore enhance driver gas contamination. The mixing process caused by the vortices generated on the contact surface has been defined as turbulent mixing phenomenon (TM), which has been investigated by numerous studies (22) (18) (20) (19).

CHAPTER FIVE: NON-REACTIVE MODEL VALIDATION

The CFD shock tube model has been validated with experimental measurements. CFD simulations were obtained for both the inviscid and viscous solutions at the conditions provided in Table 9. The experimental pressure profiles were obtained at a location 1.6 cm from the endwall using the equipment detailed by de Vries et al. (2).

Table 9: Test conditions used for the numerical model validation with experimental results

Mixture number	Composition[a]	T_5 (K)	P_5 (atm)
1	100% Ar	800	1
		1500	20
2	100% N_2	950	2.5
		1600	17

[a] Driver gas is He

Inviscid Model Validation

Side wall pressure profiles were monitored for both the CFD model and experimental shock-tube runs. The side wall pressure trace from the inviscid model solution and the experimental results for the two Argon cases in Table 9 are provided in Figure 62. The pressure is normalized relative to P_1 to allow for a direct comparison with the experimental results and to correct for the small pressure offset between the model and the experiment due to the slightly different target conditions. For the comparison of the wave timing, the incident-shock Mach number and test temperature are of primary important, with the pressure having a secondary effect (on the viscous solution), so matching the exact pressures between experiment and model is not necessary.

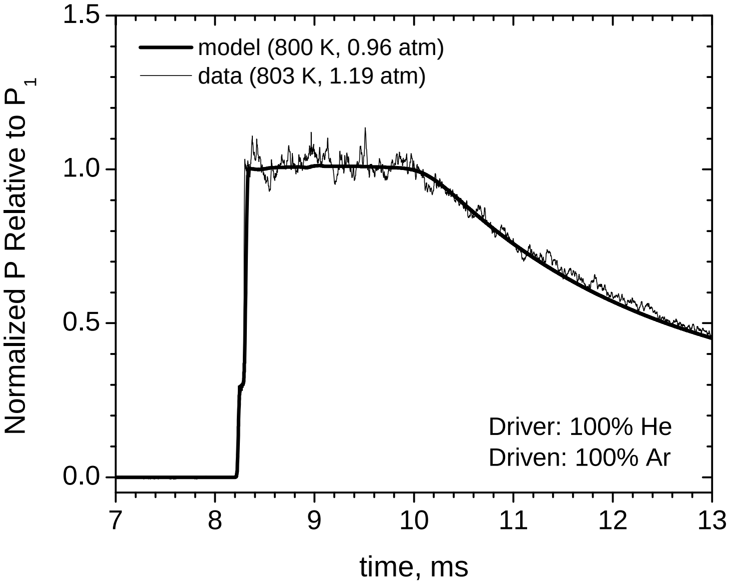

a)

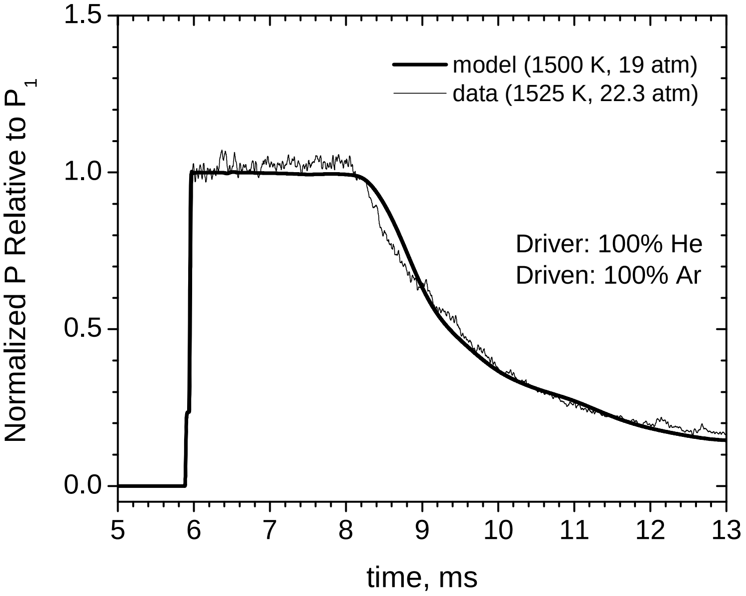

b)

Figure 62: Inviscid numerical model validation with experimental data in Ar test gas at a) T = 800 K, P = 1 atm and b) T = 1500 K, P = 20 atm. The inviscid model has shown to be in very good agreement with the experimental results with the experiment producing slightly higher pressure due to the viscous boundary layer effects which are not accounted for in the inviscid solution.

Overall, the agreement between the CFD model and the experimental measurements for the inviscid argon cases in Figure 62 is very good. The CFD model is able to reproduce the timing of the incident and reflected shock wave passages in perfect agreement with the experimental measurements. The timing of the expansion fan arrival to the endwall which brings the test time to an end is accurately predicted by the CFD model. The inviscid solution however does not capture the experimental pressure oscillations due to the non inclusion of the viscous boundary layer effects.

Viscous Model Validation

Figure 63 compares the measured pressure profiles from the sidewall location for the two Nitrogen test gas runs (Table 9) with the results from the viscous laminar and turbulent solutions respectively. The overall timing of the waves is captured; with the laminar solution displaying slightly more oscillations than the turbulent solution. For the lower-pressure case (Figure 63 a), the viscous model seems to be in a good agreement with the experiment and the timing of the waves is properly captured by both the laminar and turbulent solutions. For the higher-pressure case (Figure 63b), both solutions pick up the compression hump from the interaction of the reflected shock wave with the contact surface at a time of about 1 ms after the passage of the reflected shock; although the timing is a little later than in the experiment as predicted by the turbulent solution. The expansion wave timing is well captured by the laminar solution, however it is under-predicted by the turbulent solution by about 0.5 ms and the strength of the expansion process is over-predicted slightly.

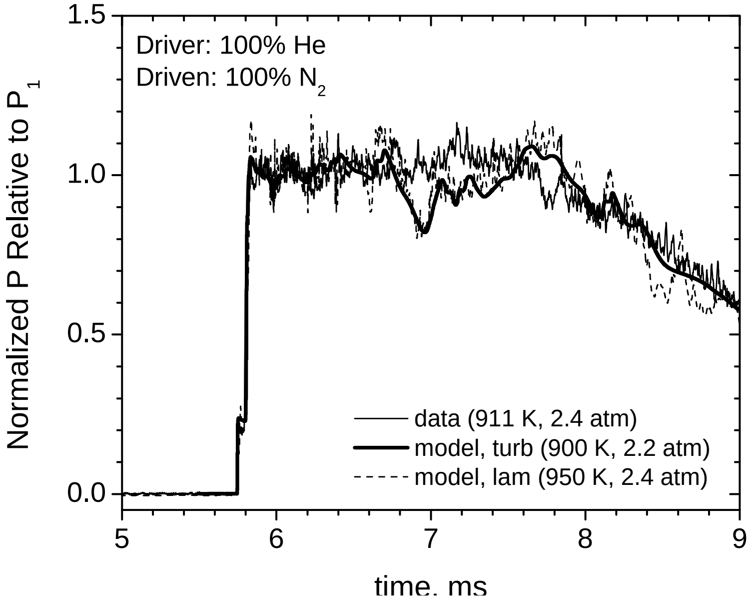

a)

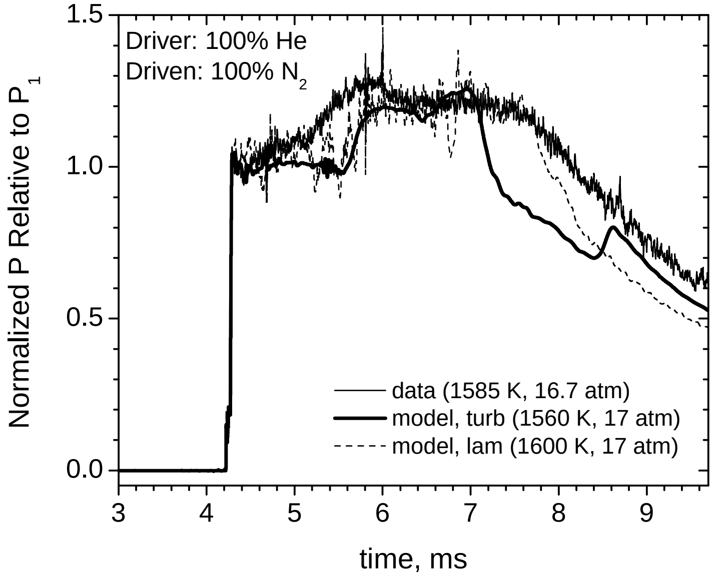

b)

Figure 63: Viscous Laminar numerical model comparison with shock-tube experimental data in N2 test gas at a) T = 950 K, P = 2.4 atm and b) T = 1600 K, P = 17 atm

Overall, the non-reactive viscous numerical model has shown to be capable of reproducing the major flow phenomena associated with unsteady flow behavior in shock tubes including the incident-shock propagation and reflection as well as the arrival of the expansion fan at the endwall. The test time which is defined as the period over which the flow properties behind the reflected shock wave are steady, has been accurately simulated and validated with experimental shock-tube data. The laminar solution is showing a better agreement with the experimental results than the turbulent solution. This is mainly due to the misrepresentation of the shock-tube flow fields when a RANS turbulence model is adopted. Consequently, the non-idealities which impact the flow properties behind the reflected shock wave are not accounted for properly in the turbulent solution.

CHAPTER SIX: COMBUSTION MODELING

Introduction

So far, the flow was assumed as non-reactive and emphasis was placed on developing a robust multi-dimensional, time-dependent numerical model of the shock tube capable of simulating the major flow non-idealities. The combustion model which is developed from the non-reactive baseline solution aims at coupling the shock-tube fluid mechanics with the chemical kinetics in an attempt to model the ignition process behind the reflected shock wave and to gain insight on the extent of non-ideal behavior in diluted and undiluted fuel-air mixtures. As such, the ignition process will be simulated in the vicinity of a highly disturbed flow characterized by bifurcation, vortical structures, and heat transfer effects. In this study, attention is given to the modeling of the combustion process of a Hydrogen-air and Hydrogen-Oxygen-Argon mixtures at conditions representative of the power generation gas turbine industry; notably high pressure and intermediate temperatures. The section which follows provides some background on reactive flow modeling in shock tubes.

Background

Reactive flow simulations in the shock tube have been investigated in two-dimensional, three-dimensional, and axi-symmetric models. Combustion modeling focused on the ignition behind the reflected shock and its role in initiating the deflagration to detonation transition phenomena. Takano (127) performed simulations for detonation initiation behind a reflected shock wave in a Hydrogen-Oxygen-Argon mixture by solving the 2D thin-layer Navier-Stokes equations through a method which combines the FCT scheme, the Crank-Nicolson scheme, and a chemical calculation step. The chemical model consisted of two progress parameters to take into account the induction reactions as well as the exothermic reactions. Loth et al. (128) performed 2D numerical simulations of gas detonation using a flux Corrected Transport scheme (FCT) and a two step induction model coupled with an energy release equation which was simulated with a point implicit finite element scheme. The end wall section of 40 cm was considered. Brown and Thomas (129) performed 2D simulations of shock reflection with the presence of an obstacle in Argon, air, Propane-air, Propane-Oxygen-Argon, and Ethylene-Oxygen-Argon mixtures. Through their simulation results, it was shown that ignition can be induced by the interaction of the reflected shock with an obstacle which can then promote detonation. Chang and Kailasanath (130) numerically studied the shock wave traveling through a multiphase media in a 6 m inviscid axi-symmetric model and used an energy release model and captured behavior similar to detonation. Gui et al. (131) performed axi-symmetric simulation by solving the Navier–Stokes equations with detailed chemistry to simulate laminar spherical CH_4/air flame perturbation by incident and reflected shock waves reflected from a planar or concave wall. Chue et al. (121) performed three-dimensional numerical computations to examine the effects of driver gas contamination in the NASA HYPULSE facility with a detonation driver shock tunnel in hydrogen-oxygen- argon mixture. The Kang–Dunn finite rate chemical kinetics model was used to describe the reacting flow.

Perhaps the most comprehensive research of reactive flow modeling of the shock tube is that of Oran and Gamezo (132) which focused on the deflagration to detonation (DDT) phenomenon. Reactive flow modeling was made possible by solving the time dependent Navier-Stokes equations in an Ethylene-air mixture. It was found that shock flame interactions and the resulting turbulent flame brush, hot spots, boundary layer effects, and mach stems provide a mechanism for DDT through the Zeldovich gradient mechanism. Also, the turbulent flame brush affects the nonreactive nearby material and may trigger hot spots and ignition which in turn can lead to DDT. In addition to flame shock interaction as a mechanism for DDT, flame-flame interaction, turbulent mixing of hot products with the reactant mixture, and direct shock ignition can generate reactivity gradients thus triggering DDT.

Moreover, Shock-Flame interactions and DDT phenomena have been the interest of Khokhlov and Oran (133) (134) (135) (136) (137) and Kholkhov et al. (138). Khokhlov and Oran (133) (134) adopted the 2D reactive Navier-Stokes equations and simulated the interaction of a shock wave and expanding flame front through the Richtmeyer-Meshkov instability, the formation of a flame brush, and the deflagration to detonation transition in an Acetylene–air mixture. It was found that the turbulence generated by pressure fluctuations from continuous flame front and shock interactions may induce hot spot formations which can transition to detonation by the means of the gradient mechanism. Kholkhov et al. (138) simulated the interaction of a shock wave and a sinusoidally perturbed premixed flame by solving the reactive Navier-Stokes equations for a stoichiometric Acetylene-air mixture. It was discovered that the interaction results in enough vorticity to increase the flame surface area and heat release without over-stretching and extinguishing the flame and that the heat release rate increase by a factor of two from 2D to 3D simulations. Oran and Kholkhov (137) performed multidimensional numerical simulations to simulate the deflagration to detonation transition resulting from incident shock waves interactions with laminar flame. Reactive Navier-Stokes equations were solved for an Acetylene air mixture over a wide range of test conditions. The interaction of the shock wave with the laminar flame result into the formation of rarefactions, secondary shocks, and contact surfaces further distorting the flame surface, which leads to the development of the turbulent flame brush and pressure fluctuations. Consequently, hot spots and spontaneous waves through the gradients in the induction times form, inducing the deflagration to detonation transition.

Also, boundary layer effects on the formation of induction time gradients in the shock tube were studied by Gamezo et al. (139) (140) (141) (142) (139) (143) and Oran et al. (144). Gamezo et al. (140) (139) investigated the initiation of detonation in confined and unconfined premixed gaseous systems by solving the two-dimensional Reactive Navier-Stokes equations and using an explicit second order Eulerian Godunov-type method. The combustion process was assumed to occur in a one-step Arrhenius expression. Gamezo et al. (141) simulated the interactions of a premixed flame with incident and reflected shocks in a rectangular shock tube by solving the three-dimensional reactive Navier–Stokes equations. The turbulent features were well captured by the model on different scales. No sub-grid model was adopted and the modeling of the turbulent energy dissipation relied on numerical viscosity. It was learned that the flame which is close to the bifurcated foot as a result of reflected shock/boundary layer interaction gets entrained in the recirculation zone which acts as a flame holder thus attaching it to the shock tube side wall. This in turn provides a mechanism for detonation. In addition and as a result of boundary layer/reflected shock interaction, the accelerated burning and mach stems promote hot-spot formation and eventually accelerate the deflagration-to-detonation transition. Gamezo et al. (142) performed two-dimensional reactive Navier-Stokes numerical simulations in Ethylene-air mixture to study the effects of wakes behind obstacles on shock-flame interactions and deflagration-to-detonation transition in shock-tube experiments. It was found that a bifurcation structure forms due to the velocity gradient in the wake. In the case the wake is large enough, the flame is entrained under the bifurcated foot and is accelerated in the recirculation zone. As the bifurcation structure grows in size, the oblique shocks reflect off the side walls of the shock tube forming mach stems which can induce hot spots, more flames, and trigger detonation.

In other studies, the flame effects on the deflagration to detonation in the shock tube containing an obstacle has been investigated by Gamezo et al. (145) and Vaagsaether et al. (146). Gamezo et al. (145) studied the phenomena of flame acceleration and deflagration-to-detonation transition in channels with obstacles placed along the length of the computational channel by solving the 2D and 3D reactive Navier–Stokes equations. The reaction of a stoichiometric Hydrogen/air mixture was modeled by a one-step Arrhenius rate expression. The obstacles reproduced the major mechanism in reactive mixtures such as choking flames, and detonations. The simulations results showed that the expansion of the hot combustion gases result in flow acceleration while flame propagation depicted by an increase in the heat release rate is caused by shock–flame interactions, Richtmeyer–Meshkov instability, Rayleigh–Taylor instability, Kelvin–Helmholtz instability, and flame–vortex interactions. Vaagsaether et al. (146) simulated Flame acceleration and deflagration to detonation transition (DDT) in a circular 4 m long tube with a diameter of 10.7 cm using a numerical code based on a flux limiter centered method for hyperbolic differential equations. The energy source term was calculated by a Riemann solver for the inhomogeneous Euler equations for the turbulent combustion and a two-step reaction model for hydrogen–air at 1 atm. The transport equations were filtered for large eddy simulation (LES) and the sub-filter turbulence was modeled by a transport equation for the turbulent kinetic energy. The flame tracking was handled by the G-equation for turbulent flames. The modeled shock tube was fitted with an obstruction with circular opening 1m down the tube from the ignition point. It was learned that the obstruction creates high pressures in the ignition end of the tube and very high gas velocities behind the obstruction opening. Therefore, the flame experiences a detonation to deflagration transition DDT in the supersonic jet created by the obstruction.

The studies described above have provided significant understanding of reactive flow modeling in the shock tube. However, more emphasis has been given to the deflagration to detonation transition phenomena and the preceding mechanisms that lead to it. In addition, all these studies employed simplified kinetics models describing the combustion process with two reactions at the most due to the increased computational resources associated with the adoption of a detailed kinetics mechanism. Consequently, the combustion process depends greatly on the assumptions associated with fast chemistry. This study however focuses on the ignition initiation after shock-reflection and the effect of the non-idealities on premature auto-ignition. In order to accurately model the reactive flow fields in the shock tube, the chemistry needs to be described by the means of a detailed kinetics mechanism. As such, this study employs a chemical kinetics mechanism comprising of 19 reactions and 11 species for Hydrogen oxidation. The increased computational time was overcome with the use of parallel computing.

As a first part towards extending the shock tube fluid mechanics model to account for reactive modeling of Hydrogen combustion, an overview on the combustion model governing equations and chemistry models is presented and the Hydrogen chemical kinetics mechanism comprising of 19 elementary reactions and 10 species is incorporated into the CFD solver FLUENT. Next, the combustion simulation results are provided. The modeled conditions behind the reflected shock wave consist of diluted Hydrogen/Oxygen/Ar mixture at the conditions of

1600 K and 1.2 atm and an undiluted Hydrogen/Air mixture at the conditions of 800 K and 35 atm.

Combustion Model

H_2 Chemical Kinetics Mechanism

Combustion modeling requires the coupling of the Navier Stokes equations and the chemistry which necessitates increased computational resources in order to resolve all the relevant scales. In shock tube devices, the flow is characterized to be turbulent indicating that the interaction between the chemical kinetics and turbulence can be significant. The modeling of such complex flow fields requires extensive computational resources, whose cost increases with the number of species in the chemical kinetics mechanism. As such, reduced mechanisms are often used in order to alleviate the problem associated with increased computational cost. In this respect, a reduced H_2/O_2 chemical kinetics mechanism (147) is incorporated into the CFD solver FLUENT. The mechanism is valid for a wide range of conditions, temperatures between 298 and 2700 K, pressures between 0.05 and 87 atm, and equivalence ratios between 0.2 and 6. The kinetics model has been validated against ignition delay times, flame speeds, and species compositions experimental data. Table 10 provides the H_2/O_2 reaction mechanism which consists of 10 species and 19 reversible elementary reactions.

Table 10: Reduced kinetics mechanism for Hydrogen oxidation (147)

		$K(T) = A\,T^{n}\exp(-E/RT)$		
Number	Reactions	A (cm, mol, s)	n	E_a (cal/mol)
1	H+O2 = O+OH	1.92E+14	0	1.64E+04
	REV	5.48E+11	0.39	-2.93E+02
2	O+H2 = H+OH	5.08E+04	2.67	6.29E+03
	REV	2.67E+04	2.65	4.88E+03
3	OH+H2 = H+H2O	2.16E+08	1.51	3.43E+03
	REV	2.30E+09	1.4	1.83E+04
4	O+H2O = OH+OH	2.97E+06	2.02	1.34E+04
	REV	1.47E+05	2.11	-2.90E+03
5	H2+M = H+H+M	4.58E+19	-1.4	1.04E+05
	REV	1.15E+20	-1.68	8.20E+02
	Efficiency Factors: H2=2.5, H2O=12.0			
6	O2+M = O+O+M	4.52E+17	-0.64	1.19E+05
	REV	6.17E+15	-0.5	0.00E+00
	Efficiency Factors: H2=2.5, H2O=12.0,AR=0.83			
7	OH+M = O+H+M	9.88E+17	-0.74	1.02E+05
	REV	4.71E+18	-1	0.00E+00
	Efficiency Factors: H2=2.5, H2O=12.0, AR=0.75			
8	H2O+M = H+OH+M	1.91E+23	-1.83	1.19E+05
	REV	4.50E+22	-2	0.00E+00
	Efficiency Factors: H2=0.73, H2O=12.0, AR=0.38			
9	H+O2(+M) = HO2(+M)	1.48E+12	0.6	0.00E+00
	LOW	3.48E+16	-4.11E-01	-1.12E+03
	TROE/ a= 0.5, T*** = 1E-30, T* = 1E+30, T** = 1.0E+100			
	Efficiency Factors: H2=1.3, H2O=14.0, AR=0.67			
10	HO2+H = H2+O2	1.66E+13	0	8.23E+02
	REV	3.16E+12	0.35	5.55E+04
11	HO2+H = OH+OH	7.08E+13	0	2.95E+02
	REV	2.03E+10	0.72	3.68E+04
12	HO2+O = OH+O2	3.25E+13	0	0.00E+00
	REV	3.25E+12	0.33	5.33E+04
13	HO2+OH = H2O+O2	2.89E+13	0	-4.97E+02
	REV	5.86E+13	0.24	6.91E+04
14	H2O2+O2 = HO2+HO2	4.63E+16	-0.35	5.07E+04
	REV	4.20E+14	0	1.20E+04
	Duplicate: H2O2+O2 = HO2+HO2	1.43E+13	-0.35	3.71E+04

	REV	1.30E+11	0	-1.63E+03
15	H2O2(+M) = OH+OH(+M)	2.95E+14	0	4.84E+04
	REV	3.66E+08	1.14	-2.58E+03
	LOW	1.20E+17	0	45500
	TROE/ a= 0.5, T*** = 1E-30, T* = 1E+30, T** = 1.0E+100			
	Efficiency Factors: H2=2.5, H2O=12.0, AR=0.64			
16	H2O2+H = H2O+OH	2.41E+13	0	3.97E+03
	REV	1.27E+08	1.31	7.14E+04
17	H2O2+H = H2+HO2	6.03E+13	0	7.95E+03
	REV	1.04E+11	0.7	2.40E+04
18	H2O2+O = OH+HO2	9.55E+06	2	3.97E+03
	REV	8.66E+03	2.68	1.86E+04
	H2O2+OH = H2O+HO2	1.00E+12	0	0.00E+00
	REV	1.84E+10	0.59	3.09E+04
19	Duplicate: H2O2+OH = H2O+HO2	5.80E+14	0	9.56E+03
	REV	1.07E+13	0.59	4.05E+04

Species : H, H_2, O, O_2, OH, H_2O, N_2, HO_2, H_2O_2 , and AR

Chemistry Model

In this study, the combustion process is assumed as premixed, and the species mass fractions are obtained from the species transport equation given by:

$$\frac{\partial(\rho Y_i)}{\partial t} + \nabla.(\rho \vec{v} Y_i) = -\nabla.\vec{J_i} + R_i \tag{54}$$

Where R_i is the net rate of species production by chemical reaction. $\vec{J_i}$ is the diffusion flux of species i and is given by the equation below following Fick's Law:

$$\vec{J_i} = -(\rho D_{i,m})\nabla Y_i - D_{T,i}\frac{\nabla T}{T} \tag{55}$$

Where $D_{i,m}$ is the mass diffusion coefficient for species j and $D_{T,i}$ is the thermal diffusion coefficient. For turbulent flows, the diffusion flux of species i is given by:

$$\vec{J_i} = -\left(\rho D_{i,m} + \frac{\mu_t}{Sc_t}\right)\nabla Y_i - D_{T,i}\frac{\nabla T}{T} \tag{56}$$

Where Sc_t is the turbulent Schmidt number and has a value of 0.7 and μ_t is the turbulent viscosity. Then the energy transport equation for viscous flows previously defined herein is given by:

$$\frac{\partial(\rho E)}{\partial t} + \nabla.[\vec{V}(\rho E + p)] = \nabla.[k_{eff}\nabla T - \sum_j h_j J_j + (\bar{\bar{\tau}}_{eff}.\vec{V})] + R_i \tag{57}$$

The chemical source term R_i can be obtained by any of the four chemistry models available in FLUENT. These models include the laminar finite rate model, the Eddy Dissipation model, the Eddy-Break-up model, and the Eddy Dissipation Concept model.

Finite Rate Model

In the Laminar finite rate model, the chemical source term R_i is computed from the Arrhenius rate expressions defined in the chemical kinetics mechanism. And the chemical source term is given by:

$$R_i = M_{w,i} \sum_{r=1}^{N_R} \hat{R}_{i,r} \tag{58}$$

Where $M_{w,i}$ is the molecular weight of species i, $\hat{R}_{i,r}$ is the Arrhenius molar rate of creation and destruction of species i. For a reversible reaction, $\hat{R}_{i,r}$ is given by:

$$\hat{R}_{i,r,kinetic} = \Gamma\left(\nu''_{i,r} - \nu'_{i,r}\right)\left(K_{f,r} \prod_{j=1}^{N} C_{j,r}{}^{\left(\eta'_{j,r}\right)} - K_{b,r} \prod_{j=1}^{N} C_{j,r}{}^{\left(\nu''_{i,r}\right)}\right) \tag{59}$$

Where Γ is the third body net effect on the reaction rate. $\nu''_{i,r}$ and $\nu'_{i,r}$ are the product and reactant stoichiometric coefficients, respectively. $K_{f,r}$ and $K_{b,r}$ are the forward and backward rate constants, respectively, $C_{j,r}$ is the molar concentration of species I, and $\eta'_{j,r}$ is the product rate exponent. The forward rate constant $K_{f,r}$ is given by:

$$K_{f,r} = A\,T^{n}\exp\left(-\frac{E}{RT}\right) \tag{60}$$

Where A is the pre-exponential factor, n is the temperature exponent, E is the activation Energy in (J/kgmol), and R is the universal gas constant in (J/Kmol-K). Note that the units for energy given in Table 10 are in cal/mol, however the units are converted properly once the mechanism is read into FLUENT. The backward rate constant $K_{b,r}$ is given by:

$$K_{b,r} = \frac{K_{f,r}}{K_r} \tag{61}$$

And K_r the equilibrium constant given by:

$$K_r = \exp\left(\frac{\Delta S_r^0}{R} - \frac{\Delta H_r^0}{RT}\right)\left(\frac{P_{atm}}{RT}\right)^{\sum_{i=1}^{N}(\nu''_{i,r}-\nu'_{i,r})} \tag{62}$$

Where the term $\frac{\Delta S_r^0}{R} - \frac{\Delta H_r^0}{RT}$ denotes the change in Gibbs free energy with S_r^0 and H_r^0 being the entropy and enthalpy at the standard state, respectively.

Eddy-Dissipation Model

The Eddy Dissipation model is the typical example of a “mixed is burnt” combustion model and is popular for its simplicity, steady convergence, and implementation. The first attempt to develop the model is due to Spalding, (148) whose idea was to replace the chemical time scale of a one-step reaction by the turbulent time scale, eliminating the influence of chemical kinetics. The model was then improved by Magnussen and Hjertager, (149) who called it the eddy-dissipation model.

The Eddy Dissipation model (EDM) assumes that the reaction is limited by micro-mixing, meaning that the chemical kinetic times are fast compared to the mixing times. The Eddy Dissipation Model relates the rate of combustion to the rate of dissipation of eddies and expresses the rate of reaction by the mean concentration of a reacting species, the turbulent kinetic energy, and the rate of dissipation of this energy. The Eddy dissipation model reaction rate is given by:

$$R_{i,mixing} = 4\nu'_{i,r} M_{w,i} \rho \frac{\varepsilon}{k} min\left(\frac{Y_R}{\nu'_{R,r} M_{w,R}}\right) \tag{63}$$

In this model, an ignition source is not necessary to start combustion, which makes this model not acceptable for the modeling of premixed combustion.

Eddy Break-up Model

Several attempts have been made for finite-rate chemistry correction of the Eddy Dissipation (ED) combustion model, (150) (151) and now, the eddy dissipation model is used in a form that allows for finite-rate chemistry. This new form of the ED model has been used in combustion simulations with encouraging results (152) (151) (153) (154). The chemical source term is computed from the minimum of the mixing rate and the Arrhenius rate as such:

$$R_i = \min\left(R_{mixing}, R_{kinetic}\right) \tag{64}$$

At equilibrium conditions, the model automatically reduces to the Magnussen –Hjertager (149) model.

Eddy Dissipation Concept (EDC)

The description of the turbulence-chemistry interactions represents one of the most difficult tasks in turbulent combustion and it becomes necessary to adopt a robust model that accounts for both the chemistry and the turbulence such as the Eddy Dissipation Concept (EDC) model. Not to be mistaken for the Eddy Dissipation model (EDM), the Eddy-Dissipation-Concept (EDC) model accounts for detailed chemistry in turbulent flows (155) (156). Reaction is then assumed to take place in fine turbulent scales over the time scale τ which is proportional to the kolmogorov time scale,

$$\tau = 0.4082\sqrt{\frac{\nu}{\varepsilon}} \equiv t_{kolmogorov} \tag{65}$$

The time scale constant is equal to 0.4082. This constant can be adjusted in FLUENT either to accelerate or slow down the reaction. Decreasing the time scale constant will result in an acceleration of the reaction while increasing it slows down the reaction process. The fine scale length fraction γ given by:

$$\gamma = 2.1377\left(\frac{\varepsilon\nu}{k^2}\right)^{1/4} \equiv \; Re_t^{-1/4} \tag{66}$$

Where, 2.1377 is the volume fraction constant, and ν is the kinematic viscosity. The chemical source term R_i is then given by:

$$R_i = \frac{\gamma^2}{\tau}(Y_i^* - Y_i) \tag{67}$$

Where Y_i^* is the fine scale species mass fraction reacting over the time τ.

The EDC model can become computationally demanding when the chemical mechanism used contains multiple reactions and species mainly due to the nonlinearity of the chemical kinetics mechanism which renders the direct integration method cumbersome. FLUENT overcomes this problem and uses ISAT (In-Situ Adaptive Tabulation) to integrate the reactions (157) Reducing the computational time as opposed to direct integration.

The chemistry models which are used to model ignition behind the reflected shock wave in this study are the laminar finite rate model in the case of laminar flow fields and the Eddy-Dissipation Concept (EDC) Model in the case of turbulent flow fields. Although the Eddy Dissipation Concept model in conjunction with a RANS turbulence model is more likely to provide a realistic representation of the turbulence-chemistry interactions in the shock tube flow fields, the failure of the RANS turbulence models to resolve the non-idealities and notably the bifurcation phenomenon in the non-reactive model suggested that the laminar finite rate model would be more suitable for the reactive shock tube flow field simulations. Nonetheless, combustion results from both the laminar finite rate and EDC chemistry models are obtained and analyzed.

Reactive Model Test Conditions

Numerical simulations were performed for multiple initial conditions across the diaphragm by varying the driver-to-driven pressure ratios to achieve the conditions of interest behind the reflected shock wave. Due to the increased computational time associated with modeling the shock wave propagation all the way to the endwall with the full reactive model setup activated, at first only the flow properties behind the incident shock wave were used as an estimate for the conditions behind the reflected shock wave, and once the results converged to the conditions of interest, full simulations were obtained. Table 11 and Table 12 provide a summary of the numerical simulations performed in the reactive flow model for a diluted Hydrogen mixture in Argon (mixture 3) and an undiluted Hydrogen/Air mixture (mixture 4). Plots of the pressure ratio across the diaphragm versus the temperature behind the incident shock wave are also provided in Figure 64 and Figure 65 for mixtures 3 and 4, respectively. Table 13 provides the conditions for which the entire shock tube model was simulated. These conditions were used to investigate ignition behind the reflected shock wave as seen in the shock-tube experiments.

Table 11: Summary of the numerical simulations performed in the reactive flow model for a diluted Hydrogen mixture in Argon (Mixture 3)

T_2 (K)	P_2 (atm)	P_1 (atm)	P_4 (atm)	P_4/P_1
600	0.5	0.11	3	27.27
700	0.6	0.11	4	36.36
730	0.15	0.03	1.2	40.00
775	0.4	0.06	2.7	45.00
950	0.3	0.04	3.2	80.00

Table 12: Summary of the numerical simulations performed in the reactive flow model for an undiluted Hydrogen/Air mixture (Mixture 4)

T_2 (K)	P_2 (atm)	P_1 (atm)	P_4 (atm)	P_4/P_1
400	0.25	0.11	1	9.09
450	3.5	1	15	15.00
475	6.2	1.7	34	20.00
500	7.5	1.8	45	25.00
540	9	1.8	64	35.56
580	10	1.8	90	50.00
600	11	1.7	120	70.59
600	8	1.3	91	70.00

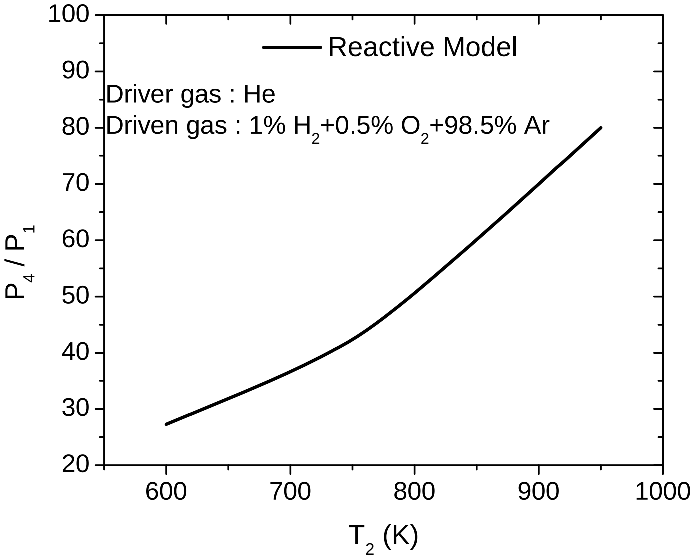

Figure 64: Diaphragm pressure ratios P_4/P_1 required to generate temperatures behind the incident shock wave in the range of 600-950 K for a diluted Hydrogen/O_2 mixture in Ar

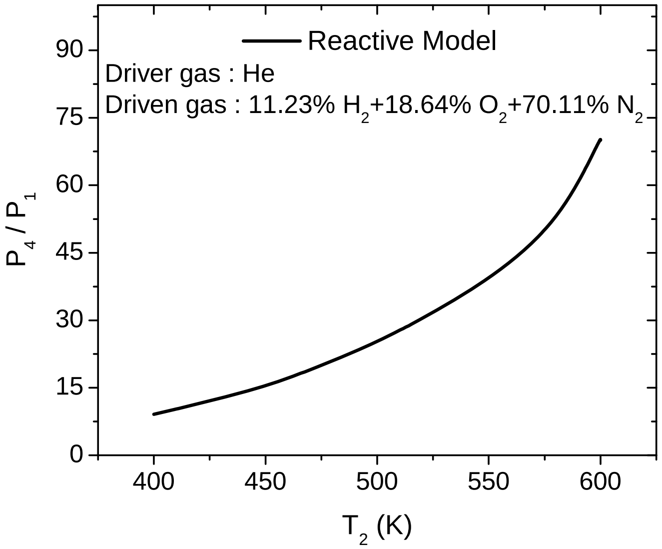

Figure 65: Diaphragm pressure ratios P_4/P_1 required to generate temperatures behind the incident shock wave in the range of 400-600 K for an undiluted Hydrogen/Air mixture

Table 13: Test gas mixtures and range of test conditions used in the validation study of the axi-symmetric model

Mixture number	Composition[a]	T_5 (K)	P_5 (atm)
3	1% H_2 + 0.5% O_2 + 98.5% Ar	1600	1
4	11.23% H_2 + 18.64% O_2 + 70.11% N_2	850-1000	35-45

[a] Driver gas is He

Ignition Delay Time Simulations

Reactive Simulations are to be performed for the mixtures given in Table 13. In order to detect ignition, the flow properties including pressure, temperature, and species mole fractions need to be monitored at various locations in the shock-tube test region. Figure 66 shows a schematic of the shock tube test region with the different monitor points at which the flow field profiles were obtained.

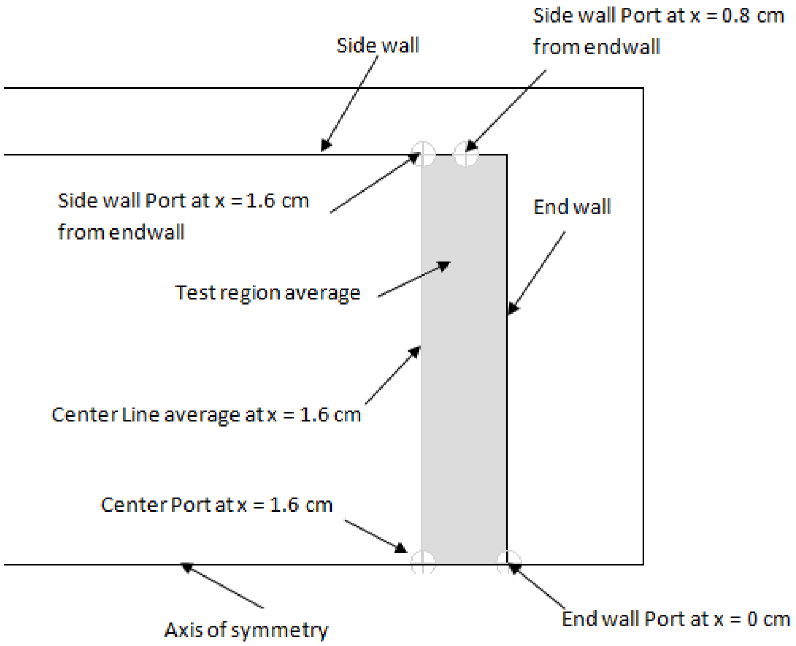

Figure 66: Schematic of the shock-tube endwall section showing the various locations at which the flow properties are monitored for the purpose of ignition detection.

At first, both the laminar finite rate and Eddy Dissipation Concept turbulent models are used in the simulations in order to investigate the influence of the two models on the initiation of the combustion process and also to allow for a direct comparison between the results achieved by the laminar and turbulent reactive models. Figure 67 gives the temperature (a) and pressure (b) flow fields obtained with the laminar finite rate (left) and the turbulent Eddy Dissipation Concept models at the conditions of 1000 K and 45 atm for the undiluted Hydrogen mixture #4. Both models depict ignition initiation and the resulting pressure wave from the exothermic reaction, however the turbulent model seems to be under-predicting the intensity of the ignition process compared to the laminar model. This result is consistent with the laminar versus turbulent solution previously obtained with the non-reactive viscous model where it has been shown that the RANS turbulence models fail to accurately represent the shock-tube non-idealities and their impact on the ignition mechanism. Chemical reaction in experimental shock tubes occurs under turbulent conditions. Perhaps a sub-grid model such as LES would be more appropriate to represent the turbulent nature of the shock-tube flow fields without suppressing the flow non-uniformities associated with viscous effects as the RANS model do.

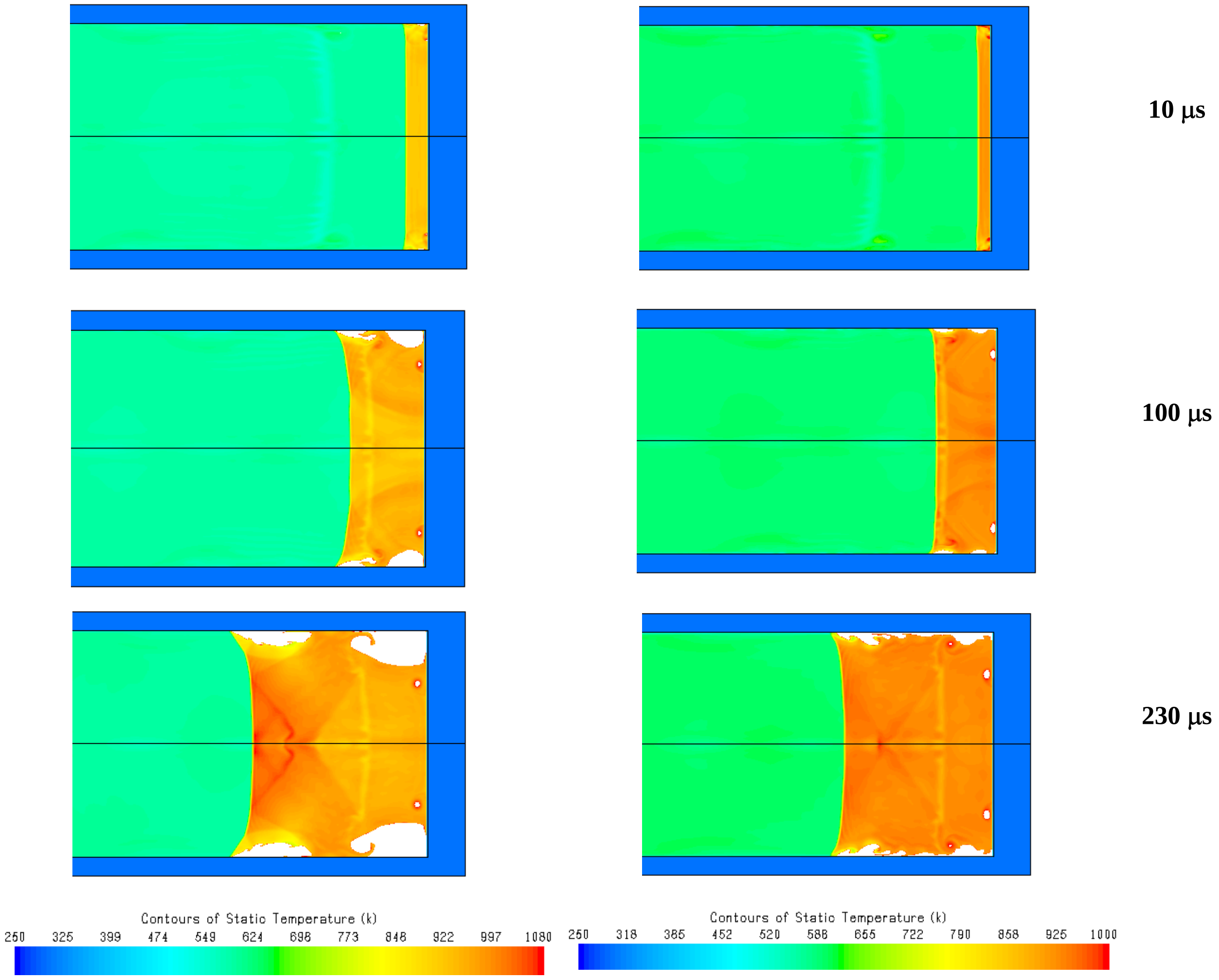

a)

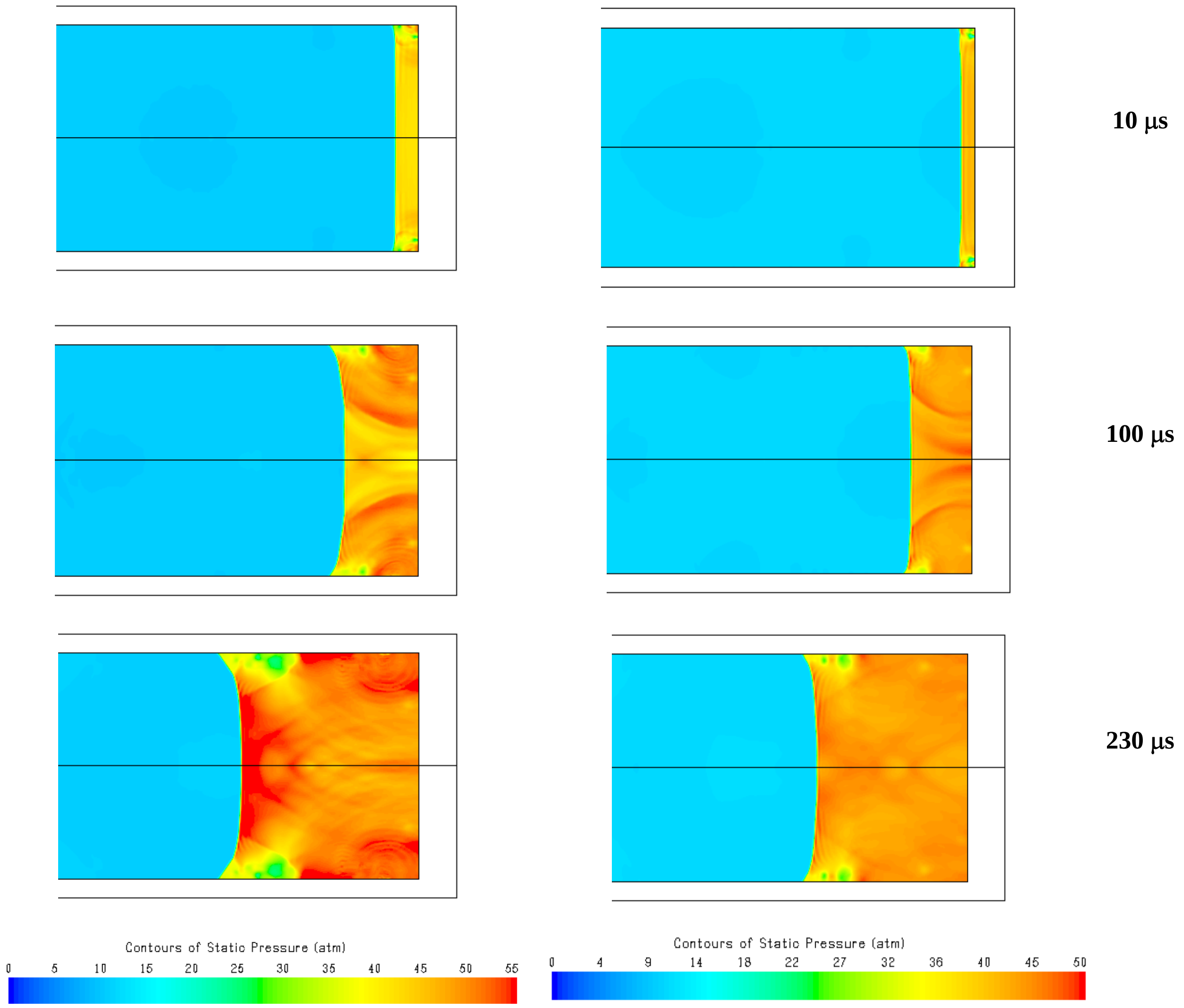

b)

Figure 67: Reactive Laminar (left) and Turbulent (right) simulations in undiluted Hydrogen/Air mixture showing the flow fields of a) temperature (K) and b) pressure (atm) behind the reflected shock wave at conditions near 1000 K and 45 atm . White areas depict flames with temperatures of 2000 K and 3500 K for the turbulent and laminar solutions, respectively.

Detonation Modeling

Detonation phenomenon occurs as a result of the Zeldovich gradient mechanism (158). Another process by which detonation occurs is when the reaction wave emerging from two merging flames develops into a detonation wave. This has been observed by Gamezo et al. (140) in numerical simulations involving very high thermo-conductivity such that the detonation wave thickness is less than the flame thickness and the thickness of the non-reacted material between the two merging flames.

In case detonation takes place, the reactive pressure fields should be able to detect the reaction front resulting from the hot spot explosion and the resulting shock wave (134). There are two conditions which need to exist for the initiation of detonation through the Zeldovich gradient mechanism (158). First, the appropriate induction time gradient represented by the localized non uniform hot spots needs to exist and second, the emerging reaction wave from the reaction zone has to have the same velocity as the shock wave originating from the reaction zone (132). The first condition ensures that a reaction wave will develop and propagate, and the second condition is necessary for the reaction wave to transition to a detonation wave. The second condition to satisfy the transition to detonation is that the reaction wave and the shock wave velocities emerging from the hot spot have to match. In the case where the shock wave originating from the reaction zone is traveling faster than the reaction wave itself, the two waves are not coupled and a transition to detonation does not occur (132). In the case that detonation does not take place, the reaction zone develops into a flame (132) which grows in surface and generates more pressure waves that cause more non-uniformities in the flow fields. As a result, new hot spots appear which in turn can develop into flames if they survive long enough. Also transition to detonation does not occur if the reaction wave speed is less than the speed of sound (137).

Detonation is more likely to be captured under increased grid resolution. Studies which simulated the transition to detonation phenomenon successively employed grid sizes as small as 0.02 mm while in this study; the minimum grid size was limited to 0.1 mm due to increased computational resources associated with increased grid resolution. On the other hand, the temporal variations were fully resolved with time scale as low as 0.01 μs

It is important to note that the studies which captured the transition to detonation phenomenon did not account for the heat losses to the shock-tube walls and often assumed adiabatic walls (139) (145) (140) (142) (133) (138) (135) (134) (132) (137) (159) (136). Consequently, the temperature in the test region can be over-predicted and the transition to detonation event can be exaggerated. While in this study, the heat transfer effects were accounted for by the means of a conjugate heat transfer model and the temperatures in the test region were accurately modeled.

Another factor which can affect the detection of a detonation event is the chemistry model used to model the combustion process. Due to the increased computational cost associated with detailed chemistry modeling, chemistry is often represented with a one- or two-step reaction model (139) (145) (140) (142) (133) (138) (135) (134) (132) (137) (159) (136). This simplification could result into the under-prediction of the gradient induction time in the hot spots and therefore the misrepresentation of the gradient mechanism responsible for detonation initiation. While in this study, a more detailed mechanism comprising of 19 reactions was employed. As such, the chemical times are ensured to be better represented. All of the factors mentioned herein need to be considered when modeling detonation in the reactive flow fields.

Recommendations

The chemistry-turbulence interactions play an important role in the initiation of the combustion process behind the reflected shock wave. Accurate representation of the shock-tube turbulent reactive flow fields can be obtained by the means of a sub-grid model such as LES in combination with a robust chemistry model such as the EDC model. On the other hand, the detailed modeling of detonation requires the simulation of the complex flame-shock-vortical interactions and the understating of the role the gradient mechanism plays in initiating detonation. The detailed modeling of the reactive shock-tube flow fields should be performed with the full consideration of the following factors.

a) Full resolution of the temporal and spatial scales which should be on the order of 0.01 μs and 0.01 mm respectively for typical shock-tube problems.

b) Accounting for the turbulence-chemistry interactions by the means of the EDC chemistry model and a sub-grid model such as LES.

c) Adoption of a more detailed reaction mechanism rather than a one or two-step reaction model to describe the chemistry

d) Accounting for the heat losses from the shock-tube hot gas to the shock-tube walls by the means of conduction, convection, and radiation. Note that radiation was not accounted for in the current study.

e) Optimization of the computational resources through the options of parallelization and ISAT (in Situ Adaptive Tabulation). ISAT is available with the EDC chemistry model that comes with the CFD solver FLUENT.

Such an effort would require few months of analysis and computational efforts. Perhaps this can be pursued in a future study.

CONCLUSIONS

Axi-symmetric inviscid, viscous, and reactive models have been developed to simulate the complete geometry of the high-pressure shock-tube facility at Texas A&M University. The simulations were carried out with the commercial CFD solver FLUENT. The model equations were discretized in space and time following the control volume approach and utilizing a density-based explicit solver. The flow domain was represented with a structured mesh. The AUSM+ flux vector splitting scheme was used to compute the flux vectors. Grid adaption was used to resolve regions with the steepest gradients, notably shock and contact discontinuities. This approach improved the accuracy of the solution and reduced the smearing effect associated with the numerical dissipation. Also, a grid-refinement study showed that an adequate resolution of the flow field has been achieved.

The first part of the shock-tube modeling study assumed the flow is inviscid and concentrated on developing a robust numerical model to be used as a baseline for the more-complex viscous solution. The convective terms were discretized in space following three schemes: 1/2nd order blending upwind, 2nd order upwind, and third-order MUSCL schemes to investigate the impact of increasing the scheme resolution on the accuracy and stability of the inviscid solution. It was not possible to achieve a solution free of unphysical numerical oscillations with the high-resolution schemes, while the 1st/2nd order blending and second-order schemes provided a more stable solution that is in very good agreement with the 1-D theory.

The incident shock wave Mach numbers were determined from the velocities and flow properties of the traveling shock wave and compared with the 1-D ideal theory. It was found that the model under-predicts the incident-shock velocities when the same initial pressure ratio between the model and the ideal theory is applied. Whereas velocity simulations reported in other numerical studies, in which the gradual opening of the diaphragm was modeled, were highly over-predicted. The reason for the discrepancy was attributed partly to the fact that the current model does not take into account the gradual opening of the diaphragm which has been shown to cause an acceleration of the incident shock wave, and partly to the fact that the ideal theory assume equal diameters between the driver and driven tubes. The discrepancy was overcome by matching the incident-shock velocity between the model and the 1-D theory or the experiment regardless of the initial pressure ratio across the diaphragm.

The inviscid flow fields behind the reflected shock wave were simulated for a wide range of test conditions; $700 \text{ K} < T_5 < 2528 \text{ K}$ and $0.9 \text{ atm} < P_5 < 15 \text{ atm}$ in both Ar and N_2 test gases which were then validated with the 1-D ideal theory. The inviscid numerical model reproduced the major processes occurring in the shock tube. The arrival of the expansion fan to the endwall depicted by the decrease in the test pressure was also well captured.

In the second part of the shock tube study, the effects of the viscous boundary layer were taken into account. This addition allowed for the modeling of the non-ideal behaviors in the shock tube represented mainly by the low-pressure high-velocity phenomenon in the shock tube nozzle downstream the diaphragm, heat transfer effects from the shock-tube hot gas to the shock-tube walls, the interaction of the reflected shock wave with the boundary layer induced by the incident shock, and the interaction of the bifurcated shock structure with the contact surface.

The strange behavior observed in the shock-tube nozzle downstream the diaphragm characterized by a steep pressure drop following the pressure rise from the incident shock wave is attributed to the shock formation and transmission which occurs at a much faster rate than the pressure wave propagation in the nozzle, resulting in an over-expanded flow region lagging behind the incident shock wave. The time-accurate solutions were able to reproduce this transient phenomenon and model the pressure drop accordingly. The low-pressure high-velocity phenomenon in the nozzle section is a physical behavior which should not be misinterpreted for the nonphysical spurious oscillations attributed to the accuracy of the numerical scheme employed. Future experimental shock-tube studies are underway to investigate the presence of the low-pressure high-velocity region in the shock-tube nozzle section.

The heat transfer effects from the shock-tube hot gas to the shock-tube cold walls were modeled by the means of a conjugate heat transfer model. The conditions of 800 K and 1 atm in Ar test gas behind the reflected shock-wave and under the extended test times of 15 ms and 17 ms obtained by the laminar and turbulent models respectively provided the extreme conditions yielding the maximum heat transfer from the shocked hot gas to the cold shock-tube walls. The extension of the test times beyond few milliseconds was achieved through the tailoring of the driver gas with a mixture composition of 40% C_3H_8 + 60 % He such that the interaction of the reflected shock wave with the incoming contact surface would result into a compression wave whose magnitude matches the magnitude of the reflected shock. As a result, uniform pressure condition are achieved behind the reflected shock wave for an extended time of 15 ms. The test time is ended by the arrival of expansion fan or the contact surface expansion wave to the endwall followed by the head expansion wave. The average gas temperature solution achieved with the conjugate heat transfer CFD model was compared to the 1-D analytical conduction solution T(r , t) (32). The jump in the average gas temperature immediately after the shock tube walls come into contact with the hot gas was well captured by the CFD model with the jump being more pronounced in the CFD model due to the stronger convective forces which are not modeled by the conduction solution. Also the CFD model was found to exhibit a lesser decrease in the average gas temperature compared to the conduction analytical due to the presence of the viscous dissipation term in the energy equation represented in the CFD model which reduces the overall effect of heat transfer, notably after the passage of the reflected shock wave, resulting in a lower heat loss by the conjugate CFD models when compared to the conduction-only model. Although the pressure and Mach number flow fields at the worst test condition of 800 K, 1 atm, and 15 ms of test time remained uniform behind the reflected shock wave, the thermal boundary layer along the shock-tube walls depicted a strong temperature gradient from the thermal boundary layer notably in the shock-tube endwall corners which could have an effect on the mechanism by which ignition is initiated.

Shock bifurcation is considered to be one of the major mechanisms responsible for non-ideal behavior in shock tubes for chemical kinetic studies. Bifurcation causes a major flow disturbance in the endwall region which affects the flow uniformity in therein. Bifurcation simulations were performed for a test gas mixture of Air at the average test conditions behind the reflected shock of 950 K and 1 atm. The interaction zone was well resolved, and the details of the bifurcation structure were well captured, while in nature, achieving such high resolution results can only be made possible with the means of high resolution schemes of at least fourth order accurate and higher.

The effects of bifurcation on the endwall flow properties were well characterized. In particular, it was noted that upon the passage of the bifurcation structure over the port of measurement, placed 16 mm from the endwall, the side wall pressure profiles displayed strong pressure oscillations due to the embedded vortices and unstable shear layer in the separation zone adjacent to the side wall. Twenty microseconds after the shock reflection, the flow is turned parallel to the shock-tube side wall, and the pressure is of the same condition as the flow compressed by the normal portion of the reflected shock. By this time, the bifurcation structure has completely passed, and the pressure profile over the port of measurement has become completely uniform.

However, the temperature profiles reported a different behavior. The axi-symmetric flow fields have shown the development of hot jets and small-structure vortices near the endwall corners due to the sudden movement of the hot endwall fluid in a rolled up direction. This result is due to the countercurrent jets which formed at the early stages of the bifurcation structure development and upon the sudden interaction of the boundary layer with the endwall, resulting in flow displacement in a counterclockwise direction. The hot jets are about 100 K higher than the average flow temperature. This could present a concern for chemical kinetics measurements because even after the complete passage of the interaction zone over the port of measurement, these hot jets remain in the corners of the endwall and present a potential for local autoignition at conditions which are different from the assumed values. In addition to the hot jets at the shock-tube endwall corners, cold jets carrying the colder fluid from the boundary layer fluid impinge on the slip line and the side and end walls in an oscillatory motion impacting the local flow properties in the entire endwall region. The monitored average and local temperature and pressure profiles have shown strong gradients in the endwall region due the oscillatory motion of the supersonic wall jet and the side wall temperature has significantly dropped. This decrease in temperature is further enhanced by the heat transfer effects captured by the conjugate heat transfer model.

The conjugate heat transfer model is expected to yield more-accurate results than the adiabatic and isothermal wall assumptions since it is the closest representation of the experimental conditions. The weaker interaction at the early stages of the bifurcation structure formation is due to the more-pronounced energy loss to the side and endwalls and therefore the thinner boundary layer captured by the conjugate heat transfer model.

The bifurcation phenomenon should not present a concern for chemical kinetics measurements when the kinetic measurements are taken after the complete passage of the bifurcation structure over the port of measurement and when the flow properties have become uniform again. However, this statement does not hold valid when local disturbances remain in the endwall region even after the complete passage of the bifurcation structure and over a time of interest to kinetics measurements. Care should be taken when quantifying the endwall local flow field properties which appear to deviate significantly from the overall endwall average properties and notably the temperature profiles. Assuming the flow properties are uniform when a bifurcation phenomenon is likely to occur in diatomic and polyatomic test gas mixtures can impact the interpretation of chemical kinetics measurements.

The interaction of the bifurcated shock structure with the contact surface was also investigated. The simulated flow fields revealed that the first encounter between the bifurcated shock and the contact surface does not result in a significant distortion of the contact surface shape mainly because the interaction occurs with the normal portion of the reflected shock. As the reflected shock advances forward, the contact surface starts to interact with the bifurcated foot and the driver gas is displaced towards the center of the shock tube to allow for the driven gas underneath the bifurcated foot to pass along the shock tube side walls. This causes the bifurcated shock structure to lose its strength and coherence and the cold fluid jetting along the side walls becomes less pronounced. The interaction becomes more pronounced as the vortices shed by the bifurcated foot encounter the driver gas which gets locally swirled and mixes with the nearby driven gas therefore contaminating the driven gas. As such, the vortices shed by the bifurcated foot provide a mechanism for driver gas contamination along the shock tube side walls and center. At the same time the clockwise motion of the vortical structures help convect the driver gas away from the side walls towards the center of the shock tube. It was concluded that the interaction of the contact surface with the bifurcated shock does result into the contamination of the driven gas by the driver gas; however the contamination does not progress towards the test region which remains unaffected for the entire time of simulation.

The robustness and accuracy of the non-reactive axi-symmetric shock-tube model was confirmed through validation with shock-tube experimental data although with slight room for improvement. The boundary conditions were well represented by the entire simulation of the shock-tube facility instead of modeling only the shock-tube endwall region, and the adoption of a conjugate heat transfer model further enhanced the credibility of the results. The non-ideal effects were well quantified and accurately modeled. The results obtained herein should serve as valuable information for the validation of experimental and numerical shock tube data.

The study was then extended to account for chemical reaction behind the reflected shock wave in order to quantify the shock-tube test time reduction as a result of the non-uniformities in the reactive flow fields. As such, the robust non-reactive model served as a baseline for the rather more complex reactive shock-tube model. Chemistry was described by the means of a 10 species 19 elementary reaction chemical kinetics mechanism for Hydrogen oxidation. The reaction rates and combustion source term were obtained with the laminar finite rate and Eddy Dissipation Concept (EDC) models assuming the combustion process is perfectly premixed. Spatial and temporal resolution was achieved with time steps as low as 1e-8 sec. It was found that the RANS models under-predict the reaction process while the laminar model exaggerates it. Perhaps a subgrid model such as LES would be more appropriate for the shock-tube reactive flow field simulations. Robust reactive simulations are to be obtained in a future study by the means of the turbulent-Eddy Dissipation Concept (EDC) model in conjunction with the LES subgrid model. As such, the turbulence-chemistry interactions would be resolved and the reactive shock-tube flow fields would be accurately represented.

APPENDIX: SHOCK RELATIONS EXAMPLE

For any given initial conditions in the shock tube

$Ru := 8314 \cdot \frac{J}{K \cdot mol}$

$atm = 1.013 \times 10^5\ Pa$

Driven Gas

$1 = Ar$

$\rho 1 := 1.72 \cdot \frac{kg}{m^3}$

$M1 := 39 \cdot \frac{kg}{mol}$

$T1 = \frac{P1}{\rho 1 \cdot R1}$

$\gamma 1 := 1.67$

$R1 := \frac{Ru}{M1}$

$P1 := 400 \cdot torr$

$T1 := 300K$

$a1 := \sqrt{\gamma 1 \cdot R1 \cdot T1}$

$a1 = 326.807 \frac{m}{s}$

Driver gas

$4 = He$

$\rho 4 = 0.1625 \frac{kg}{m^3}$ Not Constant

$M4 := 4 \frac{kg}{mol}$

$T4 = \frac{P4}{\rho 4 \cdot R1}$

$\gamma 4 := 1.66$

$R4 := \frac{Ru}{M4}$

$P4a := 100 \cdot atm$

$T4 := 300K$

$a4 := \sqrt{\gamma 4 \cdot R4 \cdot T4}$

$a4 = 1.017 \times 10^3 \frac{m}{s}$

Starting from a given pressure ratio across the diaphragm

Guess P2

$P2 := 13 \cdot \mathrm{atm}$

$$P4 := P2\left[1 - \frac{(\gamma 4 - 1)\left(\frac{a1}{a4}\right)\left(\frac{P2}{P1} - 1\right)}{\sqrt{2\gamma 1 \cdot \left[2\gamma 1 + (\gamma 1 + 1)\left(\frac{P2}{P1} - 1\right)\right]}}\right]^{\frac{-2\gamma 4}{\gamma 1 - 1}}$$

$P4 = 1.008 \times 10^{7}\ \mathrm{Pa}$

Until error between P4 and P4 actual given by P4a is minimum

$$\frac{(P4 - P4a)}{P4a} = -4.915 \times 10^{-3}$$

Pressure ratio across the diaphragm $\frac{P4}{P1} = 189.066$

Pressure Ratio across the incident shock $\frac{P2}{P1} = 24.7$

Incident Shock Properties

$$Ms := \sqrt{\frac{\gamma 1 + 1}{2 \cdot \gamma 1} \cdot \left(\frac{P2}{P1} - 1\right) + 1}$$

$Ms = 4.466$

Velocity of shock and gas ahead of the shock tube $w := Ms \cdot a1$

$w = 1.46 \times 10^{3}\ \frac{m}{s}$

Temperature across the incident shock

$$T = \frac{T2}{T1}$$

$$T := \frac{P2}{P1} \cdot \left(\frac{\frac{\gamma 1 + 1}{\gamma 1 - 1} + \frac{P2}{P1}}{1 + \frac{\gamma 1 + 1}{\gamma 1 - 1} \cdot \frac{P2}{P1}}\right)$$

$T2 := T1 \cdot T$

$T2 = 2.138 \times 10^{3}\ K$

Density across the incident shock

$$\rho = \frac{\rho2}{\rho1} \qquad \rho := \frac{1 + \frac{\gamma1 + 1}{\gamma1 - 1} \cdot \frac{P2}{P1}}{\frac{\gamma1 + 1}{\gamma1 - 1} + \frac{P2}{P1}}$$

$$\rho2 := \rho \cdot \rho1 \qquad \rho2 = 5.962 \frac{kg}{m^3}$$

Velocity of the induced mass motion behind shock, relative to lab

$$up := Ms \cdot a1 \cdot \left(1 - \frac{\rho1}{\rho2}\right) \qquad up = 1.038 \times 10^3 \frac{m}{s}$$

$$a2 := \sqrt{\gamma1 \cdot R1 \cdot T2} \qquad a2 = 872.382 \frac{m}{s}$$

$$Mp := \frac{up}{a2} \qquad Mp = 1.19$$

Velocity of Gas behind the shock, relative to the shock

$$u2 := w - up \qquad u2 = 421.066 \frac{m}{s}$$

$$M2 := \frac{u2}{a2} \qquad M2 = 0.483$$

Reflected Shock Properties

Reflected Mach Mr

$$MR = \frac{Mr}{Mr^2 - 1} \qquad MR := \frac{Ms}{Ms^2 - 1} \cdot \sqrt{1 + \frac{\left(Ms^2 - 1\right) \cdot \left(\gamma1 + \frac{1}{Ms^2}\right) \cdot 2 \cdot (\gamma1 - 1)}{(\gamma1 + 1)^2}}$$

$$MR = 0.629 \qquad F(Mr) := MR \cdot \left(Mr^2 - 1\right) - Mr$$

$$F(Mr)\ \text{solve}, Mr \rightarrow$$

$$Mr = 2.1$$

Temperature behind reflected shock

$$T5 := T1 \cdot \frac{\left[2\cdot(\gamma1 - 1)\cdot Ms^2 + (3 - \gamma1)\right]\cdot\left[(3\cdot\gamma1 - 1)\cdot Ms^2 - 2\cdot(\gamma1 - 1)\right]}{(\gamma1 + 1)^2\,Ms^2}$$

$T5 = 4.655\times 10^3\,K$

Pressure behind Reflected shock

$$P5 := P1\cdot\left[2\cdot\frac{\gamma1\cdot Ms^2 - (\gamma1 - 1)}{\gamma1 + 1}\right]\cdot\left[\frac{(3\gamma1 - 1)\cdot Ms^2 - 2\cdot(\gamma1 - 1)}{(\gamma1 - 1)\cdot Ms^2 + 2}\right]$$

$P5 = 6.674\times 10^6\,Pa$

Contact Surface

$P3 := P2 = \left(1.317\times 10^6 Pa\right)$

$u3 := u2 = \left(421.066\frac{m}{s}\right)$

$\rho3 := \rho2 = \left(5.962\frac{kg}{m^3}\right)$

Starting from a given incident shock velocity

$w := 1000\frac{m}{s}$

$a1 = 326.807\frac{m}{s}$

$Ms := \frac{w}{a1}$ $\qquad Ms = 3.06$

$P1 = 5.333\times 10^{4}\,Pa$

$$P2 := P1\cdot\left[1 + \frac{2\gamma 1}{\gamma 1 + 1}\cdot\left(Ms^{2} - 1\right)\right] \qquad P2 = 6.112\times 10^{5}\,Pa \qquad P2 = 6.03\,atm$$

$$P4 := P2\left[1 - \frac{(\gamma 4 - 1)\left(\frac{a1}{a4}\right)\left(\frac{P2}{P1} - 1\right)}{\sqrt{2\gamma 1\cdot\left[2\gamma 1 + (\gamma 1 + 1)\left(\frac{P2}{P1} - 1\right)\right]}}\right]^{\frac{-2\gamma 4}{\gamma 1 - 1}} \qquad P4 = 2.054\times 10^{6}\,Pa \qquad P4 = 20.27\,atm$$

Pressure across the diaphragm

$\frac{P4}{P1} = 38.523$

Pressure across incident shock

$\frac{P2}{P1} = 11.462$

Temperature across the incident shock

$T = \frac{T2}{T1}$

$$T := \frac{P2}{P1}\cdot\left(\frac{\frac{\gamma 1 + 1}{\gamma 1 - 1} + \frac{P2}{P1}}{1 + \frac{\gamma 1 + 1}{\gamma 1 - 1}\cdot\frac{P2}{P1}}\right)$$

$T2 := T1\cdot T$

$T2 = 1.138\times 10^{3}\,K$

Density across the incident shock

$\rho = \frac{\rho 2}{\rho 1}$

$$\rho := \frac{1 + \frac{\gamma 1 + 1}{\gamma 1 - 1}\cdot\frac{P2}{P1}}{\frac{\gamma 1 + 1}{\gamma 1 - 1} + \frac{P2}{P1}}$$

$\rho2 := \rho \cdot \rho1$ $\qquad$ $\rho2 = 5.197 \frac{kg}{m^3}$

Velocity of the induced mass motion behind shock, relative to lab

$$up := Ms \cdot a1 \cdot \left(1 - \frac{\rho1}{\rho2}\right) \qquad up = 669.061 \frac{m}{s}$$

$$a2 := \sqrt{\gamma1 \cdot R1 \cdot T2} \qquad a2 = 636.485 \frac{m}{s}$$

$$Mp := \frac{up}{a2} \qquad Mp = 1.051$$

Velocity of Gas behind the shock, relative to the shock

$$u2 := w - up \qquad u2 = 330.939 \frac{m}{s}$$

$$M2 := \frac{u2}{a2} \qquad M2 = 0.52$$

Reflected Shock

Reflected Mach Mr

$$MR = \frac{Mr}{Mr^2 - 1} \qquad MR := \frac{Ms}{Ms^2 - 1} \cdot \sqrt{1 + \frac{\left(Ms^2 - 1\right) \cdot \left(\gamma1 + \frac{1}{Ms^2}\right) \cdot 2 \cdot (\gamma1 - 1)}{(\gamma1 + 1)^2}}$$

$$MR = 0.713 \qquad F(Mr) := MR \cdot \left(Mr^2 - 1\right) - Mr$$

$F(Mr)$ solve, $Mr \rightarrow$ $\qquad$ $Mr = 2.1$

Temperature behind reflected shock

$$T5 := T1 \cdot \frac{\left[2 \cdot (\gamma1 - 1) \cdot Ms^2 + (3 - \gamma1)\right] \cdot \left[(3 \cdot \gamma1 - 1) \cdot Ms^2 - 2 \cdot (\gamma1 - 1)\right]}{(\gamma1 + 1)^2 Ms^2}$$

$$T5 = 2.258 \times 10^3 \, K$$

Pressure behind Reflected shock

$$P5 := P1\cdot\left[2\cdot\frac{\gamma 1\cdot Ms^2-(\gamma 1-1)}{\gamma 1+1}\right]\cdot\left[\frac{(3\gamma 1-1)\cdot Ms^2-2\cdot(\gamma 1-1)}{(\gamma 1-1)\cdot Ms^2+2}\right]$$

$P5 = 2.616\times 10^6\,Pa$ $P5 = 25.8\,atm$

Contact Surface

$P3 := P2 = \left(6.112\times 10^5\,Pa\right)$

$u3 := u2 = \left(330.939\frac{m}{s}\right)$

$\rho 3 := \rho 2 = \left(5.197\frac{kg}{m^3}\right)$

$\rho 2 = 5.197\frac{kg}{m^3}$

LIST OF REFERENCES

1. **Wright, J. K.** *Shock Tube.* London : Spottiswoode, Ballantyne & Co. Ltd., 1961.

2. **De Vries, J., Aul, C., Barrett, A., Lambe, D., and Petersen, E. L.***"Shock Tube for High-Pressure and Low-Temperature chemical Kinetics Experiments,"* Gottingen, Germany : s.n., July 15-20 2007. Paper No. 0913, 26th International Symposium on Shock Waves.

3. **Duff, R. E.** *"Shock-Tube Performance at Low Initial Pressure,"* 1959, Phys. Fluid, Vol. 2, p. 207.

4. **White, D. R.** *"Influence of diaphragm Openieng Time on Shock Tube flow,".* 1958, J. Fluid Mech, Vol. 4, p. 585.

5. **Miller, C. G. and Jones, J. J.** *"Incident Shock Wave Characterictics in Air, Argon, Carbon Dioxide, and Helium in a Shock Tube with Unheated Helium Driver,"* NASA, Lamgely Research Center Hampton, VA : s.n., 1975. Tech Rep TN D-8099.

6. **Nagamatsu, H. T., Geiger R. E., Sheer, R. E.** *"Hypersonic Shock Tunnel,"* 1959, Am Rocket Society, Vol. 29, p. 332.

7. **Huber, P. W.** *"Note on Hydrogen as a Real Gas Driver for Shock Tubes,"* 1958, J. Aeronautical Sciences, p. 269.

8. **Outa, E., Tajima, K., Hayakawa, K.** "Shock Tube Flow Influence by Diaphragm Opening (Two Dimensional Flow Near the Diaphragm). [book auth.] G. (ed.) Kaminoto. *10th International Symposium on Shock Tubes.* 1975, pp. 312-319.

9. **Mark, H.** "*The Interaction of a Reflected Shock Wave with the Boundary Layer in a Shock Tube,"* 1958, NACA, TM-1418.

10. **Strehlow, R. A. and Cohen, A.** *" Limitations of the Reflected Shock Technique for Studying Fast Chemical Reactions and its Application to the Observation of Relaxation in Nitrogen and Oxygen,"* 1959, J. Chem. Phys., Vol. 30, pp. 257-265.

11. **Center, R.** *"Reflected Shock Interaction with Shock Tube Boundary Layers,"* 1963, Phys. Fluids, Vol. 6, pp. 307-308.

12. **Dyner, H. B.** *"Density Variation due to Reflected Shock-Boundary Layer Interaction,"* 1966, Phys. FLuids, Vol. 9, pp. 879-892.

13. **Matsuo, K., Kawagoe, S., and Kage, K.** "The Interaction of a Reflected Shock Wave with the Boundary Layer in a Shock Tube," *Bull ASME.* 1974, Vol. 17, 110, pp. 1039-1046.

14. **Honda, M., Takayama, K., Onodera, O., Kohama, Y.** "Motion of Reflected Shock Waves in Shock Tube,". [book auth.] G.(ed) Kaminoto. *Modern Developments in Shock Tube Research. Proceedings of the 10th International Shock Tube symposium.* Japan : Shock Tube Research Society, 1975, pp. 320-327.

15. **Fokeev, V. P. and Gvozdeva, L. G.** "Study of Bifurcation of Reflected Shock Waves in Channels of Various Cross-Sections,". [book auth.] Y. (ed.) Kim. *Current Topics in Shock Waves. Proceedings of the 17th International Symposium of Shock Waves and Shock Tubes.* New York : AIP, 1990, pp. 862-866.

16. **Kleine, H., Lyakhov, V., Gvozdeva, L., Gronig, H.** "*Bifurcation of a Reflected Shock Wave in a Shock Tub,"* Springer-Verlag, Berlin, 1991, Proc. 18th International Symposium on Shock, pp. 261-266.

17. **Taylor, G. I.** *"The Instability of Liquid Surfaces when Accelerated in a Direction Perependicular to their Planes,"* London Series A, 1950, Proc. Royal Society, Vol. 201, p. 192.

18. **Jourdan, G., Billiote, M., and Houas, L.** *"Shock Induced Richtmyer-Meshkov Instability in the Presence of a Wall Boundary Layer,"* 1996, Shock Waves, Vol. 6, pp. 1-8.

19. **Houas, L., Jourdan, G., Schwaederle, L., Carrey, R., and Diaz, F.** *" A New Large Cross-Section Shock Tube for Studies of Turbulent Mixing Induced by Interfacial, Hydrodynamic Instability,"* 2003, Shock Waves, Vol. 13, pp. 431-434.

20. **Chebotareva, E. I., aleshin, A. N., Zaytsev, S. G., and Sergeev, S. V.** *"Investigation of Interaction between Reflected shocks and Growing Perturbation on an Interface,"* 1999, Shock Waves, Vol. 9, pp. 81-86.

21. **Houwing, A. F. P., Hornung, H. G., and Sandeman, R. J.** "Investigation of the Distortion of Shock-Fronts in Real Gases," [book auth.] C. E., and , Hall, J. G., (eds) Treanor. *Shock Tubes and Waves: proceedings of the 13th International Symposium on Shock Tubes and Waves.* Niagara Falls : SUNY Press, 1981, p. 176.

22. **Neuvazhayev, V. E.** *" Turbulent Mixing, Induced by the Richtmyer-Meshkov Instability,"* 1994, Shock Waves, Vol. 3, pp. 263-266.

23. **Sturtevant, B. and Slachmuylders, E.** *"End Wall Heat Transfer Effects on the Trajectory of a Reflected Shock Wave,"* 1964, Phys Fluids, Vol. 7, pp. 1201-1207.

24. **Baganoff, D.** *"Experiments on the Wall Pressure History in Shock-Reflection Processes,"* 1965, J. Fluid Mech, Vol. 23, pp. 209-228.

25. **Piva, H. O. and Sturtevant, B.** "Electron Beam Measurements of Density in Shock Waves Reflecting from a Cold Wall," [book auth.] L., Wachman, H. Y., (eds) Thrilling. *Rarefied Gas Dynaimcs.* s.l. : Academic Press, 1969, Vol. 1, pp. 381-395.

26. **Petersen, E. L. and Hanson, R. K.** "*Measurement of Reflected-Shock Bifurcation Over a Wide Range of Gas Composition and Pressure,"* 2006, Shock Waves, Vol. 15, pp. 333-340.

27. **Davies, L. and Wilson, J. L.** *"Influence of Reflected Shock and Boundary-Layer Interaction on Shock Tube Flows"* 1969, Phys. Fluids Suppl. I 12, Vol. 12, pp. I37-I43.

28. **Stalker, R. J. and Crane, K. C. A.***"Driver Gas Contamination in a High Enthalpy Reflected Shock Tunnel,"* 1978, AIAA, Vol. 16, pp. 277-279.

29. **Goldswothy, F. A.** "*The Structure of a Contact Region with Application to the Reflection of a Shock From a Heat-Conducting Wall,"* 1959, J. of Fluid Mech., Vol. 5, pp. 164-176.

30. **Clarke, J. F.** *"The Reflection of a Plane Shock Wave From a Heat-Conducting Wall,"* 1967, Proc Roy Soc Series, Vol. A 299, pp. 221-237.

31. **Keck, J. C.** *"Thermal Boundary Layer in a Gas Subject to a Time Dependent Pressure,"* 1981, Lett. Heat Mass Transfer, Vol. 8, pp. 313-319.

32. **Frazier, C., Kassab, A., and Petersen, E. L.** *"Wall Heat Transfer in Shock Tubes at Long Test Times,"* Gottingen, Germany, 2007. 26th, International Symposium on Shock Waves, Paper No. 0910.

33. **Onishi, Y.** *"On Flows Behind Shock Waves Reflected From a Solid Wall,"* 1991, Shock Waves, Vol. 1, pp. 293-299.

34. **Hanel, D. and Gronig, H.** "The Normal Reflection of a Shock Wave from an Accommodating and Absorbing Wall," [book auth.] M. and Fiebig, M. Becker. *Rarefied Gas Dynamics.* PozWahn, Germany : DFVLR Press, 1974, Vol. 1, B 28, pp. 1-9.

35. **Luo, X., Olivier, H., and Hoeijmakers, H. W. M.** *"Wave Induced Thermal Boundary Layers in a compressible Fluid: Analysis and Numerical Simulations,"* 2007, Shock Waves, Vol. 16, pp. 339-347.

36. **Vasil'ev, E. I. and Danil'chuck, E. V.** *" Numerical Solution of the Problem of Shock Tube Flow Development with Transverse Diaphragm Withdrawal,"* 1994, Fluid Dynamics, Vol. 29, No2, pp. 270-276.

37. **Petrie-Repar, P. J. and Jacobs, P. A.** *"A computational Study of the Shock speeds in High-Performance shock Tubes,"* 1998, Shock Waves, Vol. 8, pp. 79-91.

38. **Cambier, J. L.,Tokarcik, S., Prabhu, D. K.** *"Numerical Simulations of Unsteady Flow in a Hypersonic shock Tunnel Facility,"* Nashville, TN, 1992, AIAA 17th aerospace Ground Testing Conference.

39. **Gooze, R. J.** *"Simulation of a Complete Shock Tunnel with Parallel Computer Codes,"* Brisbane, Queensland, Australia : The University of Queensland, 2003. PhD Thesis.

40. **Gooze, R. J, Jacobs, P. A., Buttsworth, D. R.** *"Simulation of a Complete Reflected Shock Tunnel Showing a Vortex Mechanism for Flow Contamination,"* 2006, Shock Waves, Vol. 15, pp. 165-176.

41. **Daru, V., Fernandez, G., and Tenaud, C.** "On CFD to Investigate Bifurcated Shock Wave Pattern," [book auth.] F. (ed.) Houwing. *Procedings of the 21st International Symposium on Shock Waves.* 1997, p. Paper 1950.

42. **Nishida, M. and Lee, M.** "Reflected Shock Side Boundary Layer Interaction in a Shock Tube," [book auth.] B., Shepherd, J., and Hornung, H. (eds.) Sturtevant. *Proceedings of the 20th International Symposium on Shock Waves.* Singapore : World Scientific, 1996, pp. 705-710.

43. **Wilson, G. J., Sharma, S. P., and Gillespie, W. D.** *"Time-Dependent Simulation of Reflected-Shock/Boundary Layer Interaction,"* 1993, AIAA A93-23382.

44. **Weber, Y. S., Oran, E. S., Boris, J. P., Anderson, J. D. Jr.** *"The Numerical Simulation of Shock Bifurcation Near the End Wall of a Shock Tube,"* 1995, Phys. Fluids, Vol. 7, pp. 2475-2488.

45. **Takano, Y.** "Smulations for Effects of Side Wall Boundary Layer on Reflected Shock Flow Fields in Shock Tubes," [book auth.] H. (ed.) Gronig. *Shock Tubes and Waves. Proceedings of the 16th International Symposium on Shock Tubes and Waves.* New York : VCH, 1987, pp. 645-651.

46. **Badcock, K. J.** *" A Numerical Simulation of Boundary Layer Effects in a Shock Tube,"* 1992, Int. J. Num. Methods Fluids, Vol. 14, pp. 1151-1171.

47. **Kaneko, M., Men'shov, I., and Nakamura, Y.** *"Interaction of Reflected Shock Wave with Shock Tube Wall,"* 2004, J. of the Japan society for Aeronautical and Space Sciences, Vol. 52, pp. 153-159 .

48. **Graur I. A., Ivanov M. S., Markelov G. N., Burtschell Y., Valerio E., Zeitoun D.** *"Comparison of kinetic and continuum approaches for simulation of shock wave/boundary layer interaction,"* 2003, Shock Waves, Vol. 12, No 4, pp. 343-350.

49. **Burtschell, Y. and Zeitoun, D. E.** *"Shock/Shock and Shock/Boundary Layer Interactions in an axisymmetric Steady Laminar Flow,"* 2003, Shock Waves, Vol. 12, pp. 487-495.

50. **Bulovich, S. V., Vikolainen, V. E., Zverintsev, S. V., and Petrov, R. L.** *"Numerical Simulation of the Interaction between Reflected Shock Wave and Near-Wall Boundary Layer,"* Pleiades Publishing, 2007, Technical Physics Letters, Vol. 33, No 2, pp. 173–175.

51. **Daru, V. and Tenaud, C.** *"Numerical Simulation of the Viscous Schock Tube Problem by Using a High Resolution Monotonicity-Preserving Scheme,"* 2009, Computers and Fluids, Vol. 38, No 3, pp. 664-676.

52. **Daru, V. and Tenaud, C.** *"Evaluation of TVD high Resolution Schemes for Unsteady Viscous Shocked Flows,"* 2001, Computers and Fluids, Vol. 30, No 1, pp. 89-113.

53. **Daru, V. and Tenaud, C.** "Numerical Simulation of the Shock Wave / Boundary Layer Interaction in a Shock Tube by Using a High Resolution Monotonicity-Preserving Scheme," [book auth.] C. and Zingg, D. W. (eds) Groth. *Computational Fluid Dynamics: Proceedings of the 3rd International Conference on Computational Fluid Dynamics, ICCFD3.* Toronto : Springer Berlin Heidelberg, 2004, pp. 277-282.

54. **Sjogreen, B. and Yee, H. C.** *"Grid Convergence of High Order Methods for Multiscale Complex Unsteady Viscous Compressible Flows,"* 2003, Journal of Computational Physics, Vol. 185, No 1, pp. 1-26.

55. **Kim, K. and Kim, C.** *"Accurate, Efficient and Monotonic Numerical Methods for Multi-Dimensional Compressible Flows. Part I. Spatial Discretization,"* 2005, J. Comput. Phys., Vol. 208, No 2, pp. 527-569.

56. **Kim, K. and Kim, C.** *"Accurate, Efficient and Monotonic Numerical Methods for Multi-Dimensional Compressible Flows. Part II. Multi-Dimensional Limiting Process,"* 2005, J. Comput. Phys., Vol. 208, No 2, pp. 570-615.

57. **Sharma, S. P. and Wilson, G. J.** *"Test Times in Hypersonic Shock Tubes,".* Reno, Nevada, 1995. 33rd AIAA Aerospace Sciences Meeting and Exhibit, AIAA Paper 95-0713.

58. **Wilson, G. J.** *"Numerical Studies of High-Enthalpy Impulse Facilities,"* Pasadena, California : World Scientific Publising Co, 1995. Proceedings of the 20th international Synposium on Shock Waves. Vol. Vol I.

59. **Chue, R. S. M. and Eitelberg, G.** *"Studies of the Transient Flows in High Enthalpy Shock Tunnels,"* 1998, Exp Fluids, Vol. 25, pp. 474-486.

60. **Mirels, H.** *"Laminar Boundary Layer Behind shock Advancing into Stationary Fluid,"* 1955. NACA TN 3401.

61. **Mirels, H.** *"Boundary Layer Behind Shock or Thin Expansion Wave Moving into Stationary Fluid,".* 1956. NACA TN 3712.

62. **Liou, M. S.n and Steffen, C. J.** *" A New Flux Splitting Scheme,"* 1993, Journal of Computational Physics, Vol. 107, pp. 23-39.

63. **Liou, M. S.** *"A Sequel to AUSM: AUSM+,"* 1996, Journal of Computational Physics, Vol. 123, pp. 364-382.

64. **Liou, M. S., and Wada, Y.** *" An Accurate and Robust Flux Splitting Scheme for Shock and Contact Discontinuities,"* 1997, SIAM J. Scientific Computing, Vol. 18, pp. 633-657.

65. **VanLeer, B.** *" Towards the Ultimate Conservative Difference Scheme V; a Second Order Sequel to Godunov's Sequel,"* 1979, J. Comput. Phys., Vol. 32, pp. 101-136.

66. **Daunenhofer, J. F. and Baron, J. R.** *"Grid Adaption for the 2D Euler Equation,"* 1985. AIAA-85-0484.

67. **Rauch, R. D., Batira, J. T., and Yang, N. T. Y.** *"Spatial Adapation Procedures on Unstructed MEshes for Accurate Unsteady Aerodynamic Flow,"* 1991. AIAA-91-1106.

68. **Argow, B. M.** *"Computational analysis of Dense Gas Shock tube Flow,"* 1996, Shock Waves, Vol. 6, pp. 241-248.

69. **Sheng, Y., Sislian, J. P., and Liu, J. J.** *"A Computational Technique for High Enthalpy Shock Tube and Shock Tunnel Flow Simulation,"* 1998, Shock Waves, Vol. 8, pp. 203-214.

70. **Cocchi, J. P., Saurel, R., and Loraud J. C.** *"Treatment of Interface Problems with Godunov-type Schemes,"* 1996, Shock Waves, Vol. 5, pp. 347-357.

71. **Chang, K. S. and Kim, J. K.** *"Numerical Investigation of Inviscid shock Wave Dynamics in an Expansion Tube,"* 1995, Shock Waves, Vol. 5, pp. 33-45.

72. **Cocchi, J. P., Saurel, R., and Loraud, J. C.** *" Some Remarks About the Resolution of High Velocity flows Near Low Densities,"* 1998, Shock Waves, Vol. 8, pp. 119-125.

73. **Satofuka, N.** *" A Numerical Study of Shock Formation in Cylindrical and Two-Dimensional shock Tubes,"* University of Tokyo. Japan, 1970. Tech Rep 451, ISAS.

74. **Jiang, Z., Wang, C., Miura, Y., Takayama, K.** *"Three-Dimensional Propagation of the Transmitted Shock Wave in a Square Cross-Sectional Chamber,"* 2003, Shock Waves, Vol. 13, pp. 103-111.

75. **Loh, C. Y. and Liou, M. S.** *Three-dimensional Steady Supersonic Duct Flow Using Langragian Formulation,"* 1994, Shock Waves, Vol. 3, pp. 239-248.

76. **Wilson, G. J., Sharma, S. P., and Gillespie, W. D.** *"Time-Dependent Simulatio of Reflected-Shock/Boundary Layer Interaction,"* 1993. AIAA A93-23382.

77. **MacCormak, R. W.** *"The Effect of Viscosity in Hyperbolic Impact Cratering,"* 1969. AIAA Paper. pp. 69-354.

78. **Lax, P. D., and Wendroff, B.** *"Systems of Consevation Laws,"* 1960, Commun. Pure Appl Math, Vol. 13, pp. 217-237.

79. **Warming, R. F. and Beam, R. M.** *"Upwind Second Order Difference Schemes and Applications in Aerodynamic Flows"* 1976, AIAA Journal 0001-1452, Vol. 14, No 9, pp. 1242-1249.

80. **Harten, A.** *" High Resolution Schemes for Hyperbolic Conservation Laws"* 1983, J. Comput. Phys., Vol. 49, pp. 357-293.

81. **Godunov, S. K.** *"A Difference Scheme for Numerical Computation of Discontinuous solutions of Hyperbolic Equation,"* 1959, Math. Sbornik, Vol. 47, pp. 271-306.

82. **Boris, J. P. and Book, D. L.** *"Flux-corrected Transport III Minimal Error FCT Algorithms,"* 1976, J. of Comptuational Physics, Vol. 20, pp. 397-431.

83. **Harten, A., Engquist, B., Osher, S., and Chakravarthy, S. R.** *"Uniformly High Order Accurate Essentially Non Oscillatory Scemes III,"* 1987, J. Comput. Phys., Vol. 71, pp. 231-303.

84. **Colella, P. and Woodward, P.** *"The Piecewise Parabolic Method (PPM) for Gas dynamical Simulations,"* 1984, J. Comput. Phys., Vol. 54, pp. 174-201.

85. **Roe, P. L.** *" Approximate Riemann Solvers, Parameter Vectors and Differebce Schemes,"* 1981, J. Compt. Phys., Vol. 43, pp. 357-372.

86. **Schu, C. W., Osher, S.** *" Efficient Implementation of Essentially Non-Oscillatory Shock Capturing Schemes,"* 1988, J. Compt. Phys., Vol. 77, pp. 439-471.

87. **Hirsch, C. B.** *"Numerical Computation of Internal and External Flows"* Elsevier, 2007. fundamentals of computational fluid dynamics.

88. **Toro, E. F.** *"Riemann Solvers and Numerical Methods for Fluid Dynamics" 2nd ed.* Springer-Verlag, 1999.

89. **Godunov, S.** *"Different Methods for Shock Waves" PH. D Dissertation,* Moscow State Univesity, 1954.

90. **Liou, M. S. and Hsu A. T.** *" A Time Accurate Finite Volume High Resolution Scheme for Three Dimensional Navier Stokes Equations,"* 1989. AIAA Paper 89-1994-CP.

91. **Takayama, K. and Sun M.** *" A note on Numerical Simulation of Vortical Structures in Shock Diffraction,"* 2003, Shock Waves, Vol. 13, pp. 25-32.

92. **Whitefield, J. D., Norfleet, G. D., and Wolny, W.** *" Status of Research on a High Performance Shock Tunnel,"* US Air Force, 1966. Tech Rep AEDC-TR-65-272.

93. **Ikui, T., Matsuo, K., and Negi, M.** *" Investigations of the Aerodynamic Characteristics of the Shock tubes,"* 1969, Bulletin JSME, Vol. 12, No 52, pp. 774-782.

94. **Zeitoun, D., Brun, R., and Valetta, M. J.** "Shock Tube Flow Computation Including the diaphragm and Boundary-Layer effects," [book auth.] A., Rom, J. (eds.) Lifshitz. *Proceedings of the 12th Int Symposium on Ahock-Tubes and Waves.* 1979, p. 180.

95. **Alpher, R. A., and White, D. R.** *"Flow in Shock Tubes with Area Change at the Diaphragm Section,"* J. of Fluid Mechanics, 1958, Vol. 3, No 2, pp. 457-470.

96. **Spalart, P. R. and Allmaras, S. R.** *"A One-Equation Turbulence Model for Aerodynamic Flows,"* 1992. AIAA Paper 92-0439.

97. **Launder, B. E. and Spalding, D. B.** *"The numerical computation of turbulent flows"* Computer Methods in Applied Mechanics and Engineering,, 1974, Vol. 3, No 2, pp 269-289.

98. **Yakhot, V., Orszag, S. A.,Thangam, S., Gatski, T. B., and Speziale, C. G.** *"Development of Turbulence Models for Shear Flows by a Double Expansion Technique"* Physics of Fluids A: Fluid Dynamics, 1992, Vols. Vol. 4, No 7, pp 1510-1520.

99. **Shih, T. H., Liou, W. W., Shabbir, A., Yang, Z., and Zhu, J.** *"A New k-e Eddy Viscosity Model for High Reynolds Number Turbulent Flows-Model Development and Validation,"* W. DC : NASA, August 1994. NASA TM-106721, .

100. **Wilcox, D.C.** *"Re-assessment of the scale-determining equation for advanced turbulence models,"* AIAA Journa, 1988, Vols. vol. 26,, pp. pp. 1414-1421.

101. **Menter, F. R.** *"Zonal Two Equation k-ω Turbulence Models for Aerodynamic Flows,"* 1993. AIAA Paper 93-2906.

102. **Launder, B. E., Reece, G. J. and Rodi, W.** *"Progress in the Development of a Reynolds-Stress Turbulent Closure."* Journal of Fluid Mechanics,, 1975, Vols. Vol. 68, No 3, pp. 537-566.

103. http://www.fluentusers.com/fluent/doc/ori/html/ug/node410.htm. [Online]

104. http://www.fluentusers.com/fluent/doc/ori/html/ug/node462.htm. [Online]

105. **Abe, A. and Takayam, K.** *"Numerical simulation and Density Measurement of a Shock Wave Discharged from the Open End of a Shock Tube,"* 1990, Int J of Mech Eng Jpn Soc, Vol. 33, p. 216.

106. **Wang, J. C. T. and Widhopf, G. F.** *" Numerical Simulation of Blast Flow-Fields Using a High Resolution TVD Finite Volume Scheme,"* 1990, Computers and Fluids, Vol. 18, p. 103.

107. **Chang, K. S and Kim, J. K.** *"Blast Dynamics Generated Behind a Strong Shock Wave Discharged from an Open-Ended Shock Tube,"* 1993, J. Comp. Fluid Dynamics, Vol. 2, p. 291.

108. **Konov, A. A., Krymov, G. A.** "*Experimental study of heat transfer behind reflected shock waves propagating in an air-dust medium,"* 1980, In: Problems of convective and radiative-conductive heat transfer. (A80-51792 23-34) Moscow, pp. 196-205.

109. **Riabov, V.V. and Provotorov, V. P.** "*Modeling of heat transfer processes at catalytic materials in shock tube,"* 1995, Journal of Thermophysics and Heat Transfer (ISSN 0887-8722), vol. 9, no. 2, pp. 363-365.

110. **Roberts, G. T., East, R. A., Kilpin, D., Lyons, P., and Sandeman, R. J.** "*Shock tube measurements of convective heat transfer from a high Reynolds number, particle-laden, turbulent, non-steady boundary layer,"* 1986, Shock waves and shock tubes; Proceedings of the Fifteenth International Symposium, Berkeley, CA, July 28-August 2, 1985 (A87-12576 02-34). Stanford, CA, pp. p. 619-625. .

111. **Amadio, A. R., Crofton, M.W., and Petersen, E.L.** "*Test-Time Extension Behind Reflected Shock Waves Using CO2-He and C3H8-He Driver Mixture,"* 2006, Shock Waves, Vol. 16, No 2, pp. 157-165.

112. **Daru, C., and Tenaud, V.** *"High order one-step monotonicity-preserving schemes for unsteady compressible flow calculations,"* 2004, Journal of Computational Physics, Vol. 193, pp. 563–594.

113. **Daru, V., and Tenaud, C.** *"High resolution monotonicity-preserving schemes,"* Sydney, Australia, July 2002. International Conference on Conputational Fluid Dynamics.

114. **Takano, Y.** *"Simulations of bifurcation processes of reflected-shock waves in ionizing argon in a shock tube,"* Pergamon Press, Inc. Tarrytown, NY, USA , 1991, Computers and Fluids , Vols. Vol 19, No 3-4, pp. 387 - 392.

115. **Narayanswami, N., Knight D. D., and Horstman C. C.** *"Investigation of a Hypersonic Crossing Shock Wave/Turbulent Boundary Layer Interaction,"* 1993 , Shock Waves, Vol. 3, pp. 35-48.

116. **Glowacki, W. J., Kuhl, A. L., Glaz, H. M., and Ferguson, R. E.** *" Shock Wave Interaction with High Sound Speed Layer,"* Stanford, Ca : Stanford University Press, 1985. Proceedings of the 15th International Symposium on Shock Waves and Shock Tubes. Edited by Bershader, D. and Hanson, R. p. 188.

117. **Havener, G., Holden, M. S., and Azevedo, D.** *" Preliminary Applications of Holographic Interfetometry to Study Hypersonic Regions of Shock Wave/Boundary Layer Interaction,"* Washington, DC : Institute of Aeronautics and Astronautics, 1987. AIAA Paper No. AIAA-87-1194 .

118. **Strehlow, R. A. and Cohen, A.** "*Comment on Reflected Shock Wave Studies,"* 1958, Journal of Chemical Physics, Vol. 28, pp. 983-985.

119. **Brossard, J. and Charpentier, N.** *"Experimental Study of Shock Wave Reflection in a Narrow Channel,"* Sanford, Ca, 1985. Proceedings of the 15th International Symposium on Shock Waves and Shock Tubes. Edited by Bershader, D., and Hanson, R.,. p. 163.

120. **Chue, R. S. M., Itoh, K.** "Influence of Reflected-Shock/Boundary Layer Interaction on Driver-Gas Contamination in High Enthalpy shock Tunnels" [book auth.] B., Shepherd, J.E., Hornung, H.G Sturtevant. *Procs. 20th Int. Symp. Shock Waves.* Pasadena, C, 1996, pp. 777–782.

121. **Chue, R. S. M., Tsai, C. Y., and Bakos, R. J.** *"Driver Gas Contamination in a Detonation-Driven Reflected-Shock Tunnel,"* 2004, Shock Waves, Vol. 13, pp. 367-380.

122. **Bull, D. and Edwards, D.** *" An Investigation of the Reflcted Shock Interaction Process in a Shock Tube,"* 1968, AIAA J., Vol. 6, pp. 1546-1555.

123. **Dumitrecsu, L., Popescu, C., Brun, R.** " Experimental Studies of the Shock Reflection and Interaction in a Shock Tube," [book auth.] I. (ed) Glass. *Shock Tubes. Proceedings of the 7th International Shock Tube Symposium.* Toronto : University of Toronto Press, 1970, pp. 751-770.

124. **Sudani, N., Valiferdowsi, B., Hornung, H. G.** *"Test Time Increase by Delaying Driver Gas Contamination for Reflected Shock Tunnels,"* 2000, AIAA J., Vol. 38, No 9, pp. 1497-1503.

125. **Meshkov, E. E.** *"Instability of a Shock Wave accelerating Interface Between Two Gases,".* 1969, NASA Technical Translation, Vols. F-13, p. 74.

126. **Richtmyer, R. D.** *" Taylor Instability in shock acceleration of Compressible Fluids,"* 1960, Commmun. Pure Applied Math., Vol. 13, pp. 297-319.

127. **Takano, Y.** “Simulations for Reflected Shock Waves in Combustible Gas in Shock Tube," [book auth.] K., (ed) Takayama. *Proceedings of the 18th International Symposium on Shock Waves and Shock Tubes.* Berlin : Springer-Verlag, 1992, p. 869.

128. **Loth, E., Sivier, S., and Baum, J.** *"Adaptive Unstructured Finite Element Method for Two-Dimensional Detonation Simulations,"* 1998, Shock Waves, Vol. 8, pp. 47-53.

129. **Brown, C.J., and Thomas, G.O.** *"Experimental studies of ignition and transition to detonation induced by the reflection and diffraction of shock waves,"* Shock Waves , 2000. Vol. 10, pp. 23-32.

130. **Chang, E. J. and Kailasanath, K.** *"Shock Wave Interactions with Particles and Liquid Fuel Droplets,"* 2003, Shock Waves, Vol. 12, pp. 333-341.

131. **Gui, M., Fan, B. C. , Dong, G., Ye, J. F.** *"Interaction of a Reflected Shock from a Concave Wall with a Flame Distorted by an Incident Shock,"* 2009, Shock Waves, Vol. 18, pp. 487-494.

132. **Oran, E. S. and Gamezo, V.N.** *"Origins of the Deflagration-to-Detonation Transition in Gas-Phase Combustion,"* 2007, Combustion and Flame, Vol. 148, pp. 4-47.

133. **Khokhlov, A. M., Oran, E. S., and Thomas, G.O.** "*Numerical Simulation of Deflagration-to-Detonation Transition: The Role of Shock–Flame Interactions in Turbulent Flames,"* Combustion and flame, 1999,. Vols. vol. 117, no1-2, pp. pp. 323-339.

134. **Khokhlov, A.M., and Oran, E.S.** "*Numerical Simulation of Detonation Initiation in a Flame Brush: The Role of Hot Spot*," Combustion and Flame, 1999. Vols. 19, No 4, pp. 400-416.

135. **Khokhlov, A.M., and Oran, E.S.** *"Adaptive Mesh Numerical Simulation of Deflagration-to-Detonation Transition: The Dynamics of Hot Spots,"* Reston, VA, 1999. AIAA Fluid Dynamics Meeting, Paper AIAA-99-3439, AIAA, .

136. **Oran, E.S., and Khokhlov, A.M.** "*Numerical Simulation of Deflagration-to-Detonation Transition,"* Reston, VA, 1999. 37th Aerospace Sciences Meeting, Paper AIAA-99-0965,.

137. **Oran, E.S, and Khokhlov, A. M.** "*Deflagrations, Hot Spots, and the Transition to Detonation*" [ed.] Physical and Engineering Sciences, Philosophical Transactions: Mathematical. The Royal Society , 1999. Vols. Vol. 357, No. 1764, pp. 3539-3551.

138. **Khokhlov, A.M., Oran, E.S., Chtchelkanova, A.Y., and Wheeler, J.G.** "*Interaction of a Shock With a Sinusoidally Perturbed Flame"* Combustion and Flame , 1999. Vols. Volume 117, Issues 1-2,, pp. Pages 99-116.

139. **Gamezo, V. N., Khokhlov, A.M., and Oran E.S.** *"Numerical Simulation of Ignition Behind Reflected Shocks"* Oakland CA, 2001, Proceedings of the combustion Institute, Vol. 126, pp. 1810-1826.

140. **Gamezo, V. N., Oran, E.S., and Khokhlov, A. M.** *"Formation of Induction Time Gradients for Detonation Initiation,"* Reno, Nevada : s.n., 2003, 41st Aerospace Sciences Meeting, Paper 2003-1317 AIAA.

141. **Gamezo, V. N., Oran, E. S., and Khokhlov, A. M.** "*Three-dimensional reactive shock bifurcations,"* Proceedings of the Combustion Institute, 2005. Vol. 30, pp. 1841-1847.

142. **Gamezo, V.N.,Khokhlov, A. M., and Oran, E. S.** "*Effects of Wakes on Shock-Flame Interctaions and Deflagration-to-Detonation Transition*," Proceedings of the combustion Institute, 2002. Vol. 29, pp. 2803-2808.

143. **Gamezo, V.N., Khokhlov, A.M., and Oran, E.S.** *"Effects of Boundary Layers on Ignition behind Reflected Shocks,"* 2001, Proceedings of the 18th ICDERS, University of Washington, ISBM 0-9711740-0-8.

144. **Oran, E.S., Gamezo, V.N. , and Khokhlov, A.M.** *"Effects of Boundary Layers and Wakes on Shock–Flame Interactions and DDT,"* Reston, VA, 2002. 40th Aerospace Sciences Meeting, Paper 2002-0776, AIAA.

145. **Gamezo, V. N., Ogawa,T., and Oran, E.S.** "*Numerical simulations of flame propagation and DDT in obstructed channels filled with hydrogen–air mixture,"* Proceedings of the Combustion Institute, 2007. Vol. 31, pp. 2463-2471.

146. **Vaagsaether, K., Knudsen, V., and , Bjerketvedt, D.** "*Simulation of flame acceleration and DDT inH2-air mixture with a flux limiter centered method,"* International Journal of Hydrogen Energy, 2007. Vol. 32 , pp. 2186 – 2191.

147. **Connaire, M. O., Curran, H J., Simmie, J. M., Pitz, W. J. and Westbrook, C.K.** *"A Comprehensive Modeling Study of Hydrogen Oxidation,"* International Journal of Chemical Kinetics, UCRL-JC-152569, 2004, Vol. 36, pp. 603-622.

148. **Spalding, D. B.** "*Development of The Eddy-Break-Up Model of Turbulent Combustion,"* 1976, 16th Symposium on Combustion, Combustion Inst., Pittsburg, PA, pp. 1657-1633.

149. **Magnussen, B. F. and Hjertager, B. H.** "*On Mathematical Models of Turbulent Combustion with Special Emphasis on Soot Formation and Combustion,"* 1976, Proceedings of the Combustion Institute, Vol. 16, pp. 719-729.

150. **Golovitchev, V.I. and Chomiak J.** "*Analysis of Main Assumptions Underlying Extended Eddy Dissipation Model of Turbulent Combustion,"* Scandinavian-Nordic Section of the Combustion Institute.

151. **Peters, A. A. F., and Weber, R.** "*Mathematical Modeling of a 2.25 MWt Swirling Natural Gas Flame. Part 1: Eddy Break-up Concept for Turbulent Combustion; Probability Density Function Approach for Nitric Oxide Formation,"* 1995, Combustion Science and Technology, Vol. 110, pp. 67-101.

152. **Molnar, M., and Marek, C. J.** "*Simplified Two-Time Step Method for Calculating Combustion and Emission Rates of Jet-A and Methane Fuel With and Without Water Injection,"* 2005, AIAA Paper 2005-0549, 43rd Aerospace Sciences Meeting and Exhibit, January 2005.

153. **Magel, H. C., Schneider, R., Risio, B., Schnell, U., and Hein, K. R. G.** "*Numerical Simulation of Utility Boilers with Advanced Combustion Technologies,"* 1995, 8th International Symposium on Transport Phenomena in Combustion, San Fransisco, CA.

154. **Brink, A., Mueller, C., Kilpinen, P., and Hupa, M.** "*Possibilities and Limitations of The Eddy Break-Up Model,"* 2000, Combustion and Flame, Vol. 123, No. 1, pp. pp. 275-279.

155. **Magnussen, B. F.** *"On the Structure of Turbulence and a Generalized Eddy Dissipation Concept for Chemical Reaction in Turbulent Flow,"* St. Louis : Nineteenth AIAA Meeting, 1981.

156. **Gran, I. R. and Magnussen, B. F.** *"A Numerical Study of a Bluff-Body Stabilized Diffusion Flame. Part 2. Influence of Combustion Modeling and Finite-Rate Chemistry,"* Combustion Science and Technology,, 1996. Vol. 119, p. 191.

157. **Pope, S. B.** *"Computationally Efficient Implementation of Combustion Chemistry Using In-Situ Adaptive Tabulation,"* Combustion Theory and Modeling, , 1997. Vol. 1, pp. 41-63.

158. **Zeldovich, Y. B., Librovich, V. B., Makhviladze, G. M., and Sivashinsky, G. I.** *"On the Development of Detonation in Non-Uniformly Preheated Gas,"* Astronautica Acta, 1970, Vol. 15, p. 313.

159. **Oran, E.S., Gamezo, V.N., and Khokhlov, A.M.** "*Effects of Boundary Layers on Ignition Behind Reflected Shocks,"* 2001, Proceedings of the 18th ICDERS, University of Washington, ISBM 0-9711740-0-8.